A systematic study of phonon dynamics at the 2D limit and beyond: an *ab-initio* view of ultrafast diffuse scattering

PhD Dissertation

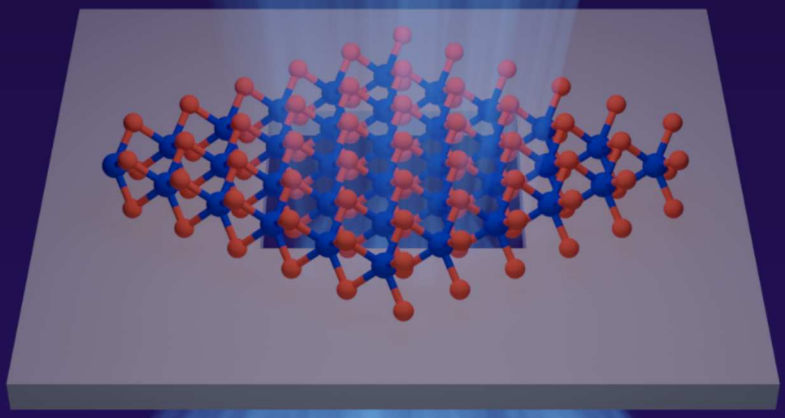

Tristan Britt

Department of Physics, Centre for the Physics of Materials

McGill University, Montréal

December 2023

A thesis submitted to McGill University in partial fulfillment of the requirements of the degree of Doctor of Philosophy

IMPRINT

A systematic study of phonon dynamics at the 2D limit and beyond: an ab-initio *view of ultrafast diffuse scattering*

Published by McGill University.

COLOPHON

This thesis was typeset using LaTeX and the `memoir` documentclass. It is based on Aaron Turon's thesis *Understanding and expressing scalable concurrency*[1], `classicthesis`[2] by André Miede and `tufte-latex`[3], based on Edward Tufte's *Beautiful Evidence*.

The bibliography was processed by Biblatex. All graphics and plots are made with PGF/Ti*k*Z, the `matplotlib` library of `python`, and `Blender`.

Matthew Carter's Charter acts as both the text and display typeface. Monospaced text uses Jim Lyles's `Bitstream Vera Mono` ("Bera Mono"), while mathematical notation utilizes Diego Puga's `mathpazo`[4].

[1] https://people.mpi-sws.org/~turon/turon-thesis.pdf
[2] https://bitbucket.org/amiede/classicthesis/
[3] https://github.com/Tufte-LaTeX/tufte-latex
[4] https://www.ctan.org/pkg/mathpazo

Everything should be made as simple as possible,

but not simpler.

—Albert Einstein

Contents

List of Figures

List of Tables

List of Abbreviations

1L	monolayer	80
2D	two dimensional	79
ARPES	angle-resolved photoemission spectroscopy	144
BBO	β-BaB_2O_4	21
BE	Bose-Einstein	52
BSE	Bethe-Salpeter equation	89
BZ	Brillouin zone	32
CPA	chirped pulse amplifier	20
CVD	chemical vapour deposition	84
CW	continuous wave	19
DFPT	density functional perturbation theory	127
DFT	density functional theory	41
DOS	density of states	53
ED	electrochemical deposition	84
EOM	equation of motion	64
EPC	electron-phonon coupling	6
ETL	electron transporting layer	81
FD	Fermi-Dirac	52
FOM	figure-of-merit	137
GGA	generalized gradient approximation	95
HTL	hole transporting layer	81
IR	irreducible representation	114
IRF	impulse response function	10
LBJ	Laval-Born-James	183
LDA	local density approximation	95

List of Symbols

Physics Constants

ϵ_0 Vacuum electric permittivity

$8.854\,187 \cdot 10^{-12}$ F-m^{-1}

m_e Electron rest mass

$9.109\,383 \cdot 10^{-31}$ kg

c Speed of light in a vacuum

$299\,792\,458$ m-s^{-1}

h Planck constant

$6.626\,070\,15 \cdot 10^{-34}$ J-Hz^{-1}

Number Sets

$\mathbb{Z}$ Integer numbers

$\mathbb{C}$ Complex numbers

$\mathbb{R}$ Real numbers

Indices

α, β, γ Cartesian indices

κ, i, j, k Atomic indices

ν Phonon branch index

h, k, l Miller indices

m, n Electronic band index

p Unit cell index in supercell

Momentum-space Quantities

$\aleph_{\mathbf{q}\nu}$ Phonon momentum- and branch-resolved value of the quantity $\aleph$

$\aleph_{n\mathbf{k}}$ Electron momentum- and band-resolved value of the quantity $\aleph$

$\mathbf{G}$ Reciprocal lattice vector

$\mathbf{H}$ Bragg peak

$\mathbf{k}$ Electron momentum

$\mathbf{Q}$ Scattering vector / momentum transfer

$\mathbf{q}$ Phonon momentum

Real-space Quantities

$\boldsymbol{\tau}_{p\kappa}$ Atomic position of the κ^{th} atom in the p^{th} unit cell

$\boldsymbol{\varepsilon}_{\mathbf{q}\nu\kappa}$ Momentum- and branch-resolved atomic eigendisplacement of the κ^{th} atom

$\mathbf{x}$ Real space 3-vector

$\Delta\boldsymbol{\tau}_{p\kappa}$ Atomic displacement of the κ^{th} atom in the p^{th} unit cell

Miscellaneous

ℓ Azimuthal angular momentum quantum number

$\equiv$ "is congruent to"

$\Im$ Imaginary component of a complex quantity

μ Chemical potential

μ_k Relative atomic mass

∇ Laplacian operator $\nabla \triangleq \sum_i \partial_{ii}^2$

ω Angular frequency

Ω_{BZ} Dimensionality-based measure of the BZ

ϕ, φ Phase

$\Re$ Real component of a complex quantity

θ Angle

$\triangleq$ "is defined to be equal to"

ε Electronic energy

f Radial frequency

m_k Absolute atomic mass

s Spin quantum number

Abstract

The development of new and interesting technologies is one of the strongest inspiration for materials science, from heat shields for spacecraft re-entering Earth's orbit, to smaller transistors for use in mobile devices, to new light emitting diodes for television screens. To understand novel materials, though, requires equally sophisticated tools with which one can characterise them. The structure of a material, and the ways in which the structure responds to various stimuli, is often difficult or impossible to directly observe on the time- and length scales most relevant to the changes. To this aim, this thesis expands on the usage of ultrafast elastic and inelastic scattering as a means through which one can understand not only the dynamics of a crystal's lattice, but also the electronic system, and the formation dynamics of more complicated collective excitations and quasiparticles like phonons and polarons.

I start by showing that on state-of-the-art instruments, ultrafast electron diffuse scattering is realizable on systems at the limits of dimensionality, namely 2D samples. What's more, having shown that such experiments are feasible, I, with collaborators, develop the recently posited theory needed to simulate and quantitatively replicate the experimental signatures found in these experiments. We do this on monolayer molybdenum disulfide, a system with complicated many-body interactions, strongly susceptible to its environment, to illustrate the power of the theoretical results developed.

Knowing that our lab can make such sensitive measurements, I extend the current theory to illustrate how these experiments are, while blind to the electronic system of a material, still able to sensitively detect spin- and valley-tronic effects like chiral phonons in materials where they are present.

Finally, to further illustrate the utility of inelastic diffuse scattering, I reconcile conflicting accounts of previously acquired scattering data on the thermoelectric material tin selenide, where these hypocritical interpretations are adjoined by the discovery

of two independent processes in the material: an electron-phonon coupling strength with a unique momentum-space signature, as well a strongly anharmonic lattice that results in pronounced three-phonon and four-phonon scattering processes. We validate these conclusions by developing the novel formalism of polaron diffuse scattering in the benchmark wide-gap ionic insulator lithium fluoride.

Abergé

Le développement de technologies nouvelles et intéressantes est l'une des plus grandes sources d'inspiration pour la science des matériaux, qu'il s'agisse de boucliers thermiques pour les vaisseaux spatiaux rentrant en orbite terrestre, de transistors plus petits utilisés dans les appareils mobiles ou de nouvelles diodes électroluminescentes pour les écrans de télévision. Cependant, pour comprendre les nouveaux matériaux, il faut des outils tout aussi sophistiqués pour les caractériser. La structure d'un matériau et la façon dont cette structure change en fonction de divers stimuli sont souvent compliquées à comprendre sur les minuscules échelles de temps et de longueur des changements en question. Dans ce but, cette thèse développe l'utilisation de la diffusion élastique et inélastique ultrarapide comme moyen de comprendre non seulement la dynamique du réseau cristallin, mais aussi le système électronique et des objets plus complexes tels que les défauts localisés et d'autres quasiparticules.

Je commence par montrer qu'avec les instruments les plus modernes, la diffusion diffuse ultrarapide d'électrons est réalisable sur des systèmes à la limite de la dimensionnalité, à savoir des échantillons 2D. De plus, après avoir montré que de telles expériences sont réalisables, je développe, avec des collaborateurs, la théorie récemment postulée nécessaire pour simuler et reproduire quantitativement les signatures expérimentales trouvées dans ces expériences. Nous le faisons sur le disulfure de molybdène monocouche, un système avec des interactions complexes à plusieurs corps, fortement sensible à son environnement, afin d'illustrer la puissance des résultats théoriques développés.

Sachant que notre laboratoire peut effectuer des mesures aussi sensibles, j'élargis la théorie actuelle pour illustrer comment ces expériences, bien qu'aveugles au système électronique d'un matériau, sont toujours capables de détecter de manière sensible les effets troniques de spin et de vallée tels que les phonons chiraux dans les matériaux où ils sont présents.

Enfin, pour illustrer davantage l'utilité de la diffusion diffuse inélastique, je réconcilie des comptes-rendus contradictoires de données de diffusion acquises précédemment sur le matériau thermoélectrique séléniure d'étain, où ces interprétations hypocrites sont adjointes à la découverte de deux processus indépendants dans le matériau : une force de couplage électron-phonon avec une signature unique de l'espace-temps, ainsi qu'un réseau fortement anharmonique qui entraîne des processus de diffusion prononcés à trois et quatre phonons. Nous validons ces conclusions en développant le nouveau formalisme de la diffusion diffuse de polarons dans l'isolant ionique à grand écart de référence qu'est le fluorure de lithium.

Acknowledgments

There are a lot of people who have contributed to my ability to produce this thesis. I have to start first and foremost with my grandfather, the nuclear physicist who inspired in me the quest to figure out how the world works. My search to find new knowledge without a doubt came from him, and I'd like to imagine that if he had the chance, this thesis would have been a delight for him to read. *Requiescat in pace*. In a similar vein, the support from my parents has been a constant on which I can rely during my time in academia. Their reassurance and motivation gave me the needed boost to persevere through it all and come out on top.

There have been many people who professionally have guided me and given me the tools to succeed throughout this PhD. Chief among these is my advisor, Prof. Bradley Siwick, whose positive attitude and trust in me throughout my time at McGill provided a space in which I could thrive and find a true sense of satisfaction as I discovered new and interesting things about the world. His expertise in the results of this thesis really allowed me to complete excellent work that has been very well received. Here's to hoping the gun does not crash again! ⚡

As issues with the administration of McGill and its facilities became apparent towards the middle of my degree, resulting in my pivot into exclusively theoretical work, I must thank my collaborator Junior Professor Fabio Caruso in Kiel, Germany, whose technical experitise and advice concerning the first-principles calculations in this thesis fostered my needed progress to complete a degree worthy of a true physicist. The coordination of these two professors, in addition to the guidance of Xiaoyang Zhu (X.Y.Z.) at Columbia University, as well as his students Qiuyang Li and Nicholas Olsen, is what made my work on monolayers possible. Cheers! 🔬

With regards to the execution of my degree, there were many people at McGill who indirectly helped with my work, including but not limited to Jean-Marc Gauthier, our front-

man in the onslaught of HVAC related issues to McGill facilities, and Pascal Bourseguin, chief machinist at our machine shop who supervised the flawless production of the custom hardware needed to operate the instrument over its various configurations throughout the years. ♨️🗜️

None of this work would have also been possible without the help and support of my coworkers, and, I'm glad to say, my friends: Laurent René de Cotret, Martin Otto, Dallas Strandell, and the latest and greatest of the Siwick Lab, Laurenz Kremeyer and Sebastian Hammer. Prost! 🍻

There are obviously non-physics related contributors to my ability to produce this thesis, namely the chosen family I've found since living in Montréal: Alyssa Guerra, Kailee Hopkins, Hannah Lieberman and Adam Pedersen, Emma Vadot and Madde Macdonald, Alyshah Walji, Arthur Scialom, Lamiah Adamjee, Anna de Waal, and others. Their support and validation over the years here in Québec are what have sustained me through the best and worst of my degree, and without them, I'm not sure what would have become of me. I have much love for you all, and don't you forget it. 👪

I could not have solved all the problems I encountered throughout my PhD without my cat Nala, who let me "rubber duck" with her countless times, and whose gentle love calmed me down and provided focus to my life. If only she could read this! 🐱

Last but certainly not least is my parner Anaïs. She has been so much more to me than just another PhD student with whom I could sympathise and vent regarding the toils of acquiring a doctoral degree. Her support and confidence in me have, to understate it, allowed me to trust in myself and in my skills, to accel in my endevours, and to *carpe diem* like never before. She has seen me through the best and worst of my degree, and has continued to, relentlessly, demonstrate compassion, empathy, and affection that have helped me shine through it all. *Je n'aurais pas pu terminer cette diplôme sans toi, et j'espere que tu sais étendue de mon amour pour toi, mon bb chat.* ❤️

Contribution to original knowledge

I solemnly affirm, under oath and with unwavering honesty, that the entirety of my doctoral dissertation was meticulously and exclusively crafted by my own intellect, effort, and dedication. I unequivocally assert that no external assistance, whether it be in the form of writing, research, or data analysis, was sought or received in the creation of this scholarly work. All ideas, arguments, interpretations, and conclusions presented within the dissertation are the result of my independent research and critical thinking, and external contributions from my collaborators are accredited as appropriate in the following section. I attest to the authenticity of the data collected, the integrity of the methodology employed, and the originality of the entire content. I do hereby declare, under penalty of perjury, that the statements made in this document are true and accurate to the best of my knowledge and belief.

Date

Signature

Contribution of authors and agencies

The contribution of co-authors to the new physics outlined in this thesis are encapsulated in the set of publications [Nano Lett. 2022, 22, **12**, 4718-4724], [Phys. Rev. B **107**, 214306], and []. The specific contributions are as follows.

These works were supported by the Natural Sciences and Engineering Research Council of Canada (NSERC, RGPIN/06001-2019 and EQPEQ/473095-2015), the Fonds de Recherche du Québec-Nature et Technologies (FRQNT, 2022-PR-301243, 318480), the Canada Foundation for Innovation (CFI, CFI-LOF 23261), and a McGill Fessenden Professorship, in addition to the Sony Corporation. Prof. Siwick (B.J.S.) and Prof. Zhu (X.Z.) conceived the research of the experimental monolayer works. X.Z. acknowledges support for sample preparation by the Materials Science and Engineering Research Center (MRSEC) through US-NSF grant DMR-2011738. N.O. and Taketo Handa, supervised by X.Z., performed PL measurements verifying the number of layers of the sample. I performed the experiments with assistance from Laurent René de Cotret, Martin Otto, Syed Ali Hassan, and I computed the phonon dispersion, equilibrium one-phonon structure factors, and electronic bandstructure. The samples were prepared by Qiuyang Li. First-principles calculations based on the TDBE were performed by Fabio Caruso (F.C.), who acknowledges funding from the Deutsche Forschungsgemeinschaft (DFG)-Projektnummer 443988403. The dynamic diffuse scattering intensities and MSD were computed by Marios Zacharias, who acknowledges financial support from the program ΜΕΤΑΔΙΔΑΚΤΩΡ of the Cyprus University of Technology. We acknowledge that the results of this research have been achieved using the DECI resource Prometheus at CYFRONET in Poland with support from the PRACE aisbl.

The chiral phonon work was additionally supported by Quantum Photonics Quebec (PQ2), and a McGill Fessenden Professorship. B.J.S. conceived the research, and I conducted the research, developing the theory and performing the DFT and diffuse

scattering calculations. We also acknowledge stimulating conversations with F.C. and his students motivating the interpretation of these results.

The polaronic materials research was conceived by B.J.S., and conducted by myself, with technical supervision under F.C.

Part I

PROLOGUE

1

Introduction to Ultrafast Experiments

"Intellectual men who quickly wolf down whatever nourishment
is necessary for their bodies with a kind of disdain
may be very rational and have a noble intelligence,
but they are not men of taste."
—Charles-Augustin de Coulomb

The history of material science is a continually evolving story, dating back to antiquity. It is so central to our understanding of the developement of the modern age that the critical epochs in history are named after the advances in materials during that time (the Stone age, Bronze age, the Iron age, the Golden[1] age, etc.). For most of scientific history, the choice of material for a given application was based on external properties: gold is shiny, gemstones are pretty, etc. However, with the advent and subsequent development of condensed matter physics, experimentalists began to probe materials for an ever increasing variety of reasons: how readily electrons drift through the material when an electric field is applied, how tightly atoms are bound together, how willing a material is to ionize, and more, adding more complex descriptions of materials, like superconductivity. Most critically, we have also begun to consider a final aspect of materials: their size.

Given the ever decreasing length scales in which novel materials of interest lie, the approaches needed to even view these materials were forced to improve. Optical mi-

[1]This is the familial name for the age of modern computing.

croscopy, the oldest of the scientific imaging techniques originating in Europe in the early 1600's [1], used to be entirely suffient for a quantitative record of the behaviour of a sample. From the inspection of metal welds, to the counting of cultured cells in a Petri dish, it was amazing how far the humble compound microscope brought science. Yet, there are hard limits to these devices: (i) only dark or refractive objects can be well imaged, and (ii) diffraction-limited viewing dramatically affects the magnification such microscopes can provide. Even neglecting both these effects, there are fundamental constraints on what human eyes can even detect! As scientific inquiry surpassed the length and energy scales afforded by the technology of the time, new ways to "see" had to be developed.

While many other flavours of optical microscopy had been invented to combat these issues, or to circumvent them all together, the fundamental limit that visible light can only provide around $0.2\,\mu$m of spatial resolution stands the largest of obstacles to overcome in our quest to see smaller and smaller. The ability to see on macro-, micro-, nanoscales and beyond came with the advent of the electron microscope. Sparked by the observation [2] and subsequent theoretical explanation [3] of the photoelectric effect from metals, the electrons that were "ripped" from the metal surface were placed inside electric fields of static voltage that would provide an acceleration s. t. the de Broglie wavelengths of the electrons were smaller than the diffraction limit of optical microscopy. This opened up new avenues of exploration for science. This wavelength, determined by the acceleration voltage, can be written:

$$\lambda_{\mathrm{dB}} = \frac{hc}{\sqrt{eV(2m_e c^2 + eV)}} \quad . \tag{1.1}$$

which, for a typical TEM voltage of 100 keV is 3.87 picometers. While the precise historical origins of the electron microscope are unclear [4], the advantages it brings are not. In addition to spatial resolution with atomic granularity, the penetration depths of the electron beams began exceeding the thickness of samples, allowing for the development of transmission electron microscopy (TEM). This approach focuses an electron beam with suffi-

cient energy through a sample. The transmitted electrons are offset in phase and energy relative to before the illumination of the sample. This beam, now rich in information about the sample, is magnified and imaged on a viewing screen, usually a phosphor scintillator. By rastering the beam over the surface, known as scanning transmission electron microscopy (STEM), we can even further enrich the images obtained in such an approach. Lo and behold, there is now an approach for achieving sub-atomic spatial resolution. With such an advance in microscopy, the upper bound on what we could see was quickly dissolving.

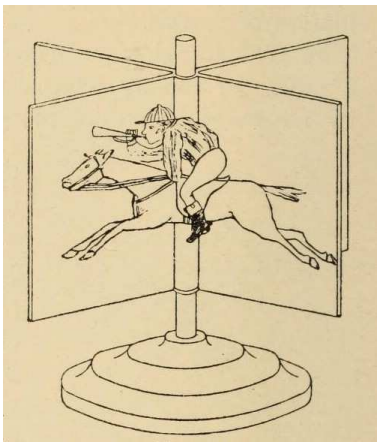

An illustration of a four-panel animator, taken from [5].

The ability to inspect such small length scales opened up questions about dynamics: now that we can see small, can we see fast? While equilibrium views of a material are valuable, and not always easily understood, there is an entirely new dimension to consider in the study of materials: time. The typical picture for time-resolved studies originates with the zootrope, a device used to create "animations" by quickly displaying sequential frames to create the illusion of continuous motion.

The question of "can we peak into fast-happening processes" arises pretty naturally from the study of the material world; nothing is static. Whether one's concerned with the passage of time on gargantuan scales like cosmology or evolution, or on much quicker scales like the morning commute to the lab, time consistently marches forward, and the world with it. The smaller length scale to which one investigates, the quicker things tend to move, and the harder it gets to "see".

1.1 WHAT ARE WE DOING?

The goal of this work is to unravel the behaviour of materials on some of the smallest length and time scales modern transmission electron microscopy can afford, developing on and extending current theories of (in)elastic scattering to the 2D limit and beyond. We show that such extensions are physically realizable. We aim, more specifically, to untangle the complex (potentially many-body) interactions found in exotic quantum materials, with a focus on the coupling of the charges inside the material to its atomic arrangement. This so called electron-phonon coupling (EPC) is a central concern in materials physics generally, providing the fundamental origin of phenomena as diverse as conventional superconductivity [6], charge-density waves [7] and soft-mode phase transitions [8], playing an important role in determining both charge and thermal transport properties. This thesis aims to be a "how-to" guide to understand phonons, their dynamics, and EPC by means of ultrafast diffuse scattering in atypical condensed matter systems, starting from elemental quantum mechanics, and progressing to more advances concepts such as anharmonicity and the breakdown of the phonon formalism.

Assuming that, at the worst case, atoms only vibrate with the equivalent energy of room temperature ($300\,\mathrm{K} \simeq 25\,\mathrm{meV}$), this still gives us a vibrational period of $(6\,\mathrm{THz})^{-1} \simeq 0.16$ picoseconds (ps, 10^{-12} s). This means that in order to view atomic motion, experiments require a time-resolution on the order of femtoseconds (fs, 10^{-15} s). For electron microscopy, this means that the imaging electrons need to be emitted in pulses, with each pulse having femtosecond time duration. Yet, as read-out times of electronics cannot be this quick, we apply integration techniques as we describe in Section 1.1.2. Such experiments that can achieve these time resolutions are given the moniker *ultrafast*. While other approaches focus on imaging in real space, like the compound microscope, we focus herein on the corresponding *diffraction*. This is a momentum-resolved view of the same information, with an interpretation more closely tied to the *scattering* processes

inside the material.

Definition 1 (Diffraction)**.** The change in direction (momentum) and energy of the electrons in a beam as a result of scattering from the instantaneous interatomic potential of a material. The intensity of electrons at a given scattering angle and energy at a given plane of (x, y) coordinates is what is known as a *diffraction pattern*. Recording these changes in energy and momentum close to the scattering plane is called *Fresnel* diffraction, while at larger distances is a *Fraunhofer* diffraction pattern.

Historically, the first attempts to understand quantum dynamics came from Schrödinger's equation, the first quantitative relationship between the intrinsic energies of a system Ψ to its time evolution. For a matrix A residing in the Lie algebra of a complex Hilbert space[2] $\mathfrak{g}(n, \mathbb{C})$, for $\psi_0 \in \mathbb{C}$, the function $\Psi(t) \triangleq e^{tA}\psi_0$ for all times $t \in \mathbb{R}$ is the unique solution of the differential equation:

$$\frac{d\Psi(t)}{dt} = A\Psi(t) \tag{1.2}$$

for $\Psi(0) = \psi_0$. Setting $A \triangleq -i\hat{\mathcal{H}}/\hbar$ brings us to Schrödinger's equation:

$$i\hbar\partial_t\Psi(\mathbf{x}, t) = \hat{\mathcal{H}}\Psi(\mathbf{x}, t) \tag{1.3}$$

where $\hat{\mathcal{H}}$ is the operator called the *Hamiltonian* describing the energy of the system, and $(\mathbf{x}, t)$ describes the space and time coordinates of the system. Such a description proved extremely powerful in answering many open questions in quantum mechanics at the time, and is the lens through which we can understand *most* of the phenomena in this work. We develop further the Schrödinger picture of Eq. (1.3) in Section 2.1.

[2]Briefly, the space $\mathbb{C}^n$ becomes a Hilbert space with the conjunction of the inner product $\langle\varphi|\psi\rangle \triangleq \sum_{j=1}^{N}(\varphi^j)^\dagger\psi^j$ and the norm $||\psi|| \triangleq \sqrt{\langle\psi|\psi\rangle}$. The Lie algebra of this space is the coordinate space representation of the real observables in the complex Hilbert space, see [9].

1.1.1 *A Ginzburg-Landau approach*

In these experiments, a material is photoexcited with an ultrafast optical pulse, which induces changes in the electronic and structural properties of the material. The state of the material across its phase diagram can be described by an *order parameter*.

Definition 2 (Order Parameter)**.** Describes the degree of order across boundaries in the phase diagram of a given system. It is common for the order parameter to be null for one phase (typically above the critical point), and range continuously to unity elsewhere in the phase diagram.

The study of this order parameter near a phase transition is called *Ginzburg-Landau theory*, which, while historically applied first to superconducting systems, yields meaningful insights into the material systems studied in these works[3]. The extension of the theory to the time domain, thus studying the dynamics of the order parameter following photoexcitation, for example, is very useful to understand ultrafast scattering experiments.

When we photoexcite strongly, the material is placed far from equilibrium. We can drive phase transitions and change the properties of the material dramatically by the optical pulse, initiating nonequilibrium dynamics with a laser pulse by impulsively driving carrier excitations or phonon excitations. Intuitively, the order parameter of a system can be thought to lie, in equilibrium, at a minimum in the free energy landscape. Photoexcitation will "roll the ball up the hill" to place the order parameter elsewhere in free energy over time. Once excited, the system is then free to relax to other minima in free energy. The existence of multiple minima is, in general, possible, allowing for competing ground states, or even *metastable* phases, represented by local minima in the free energy landscape that are not thermally accessible, and can only be reached through techniques like photoexcitation. These dynamics are illustrated in Figure 1.1,

[3] This is a complex topic on its own, and lies outside the scope of this thesis. We mention only the key aspects of the theory as it pertains to the studies herein.

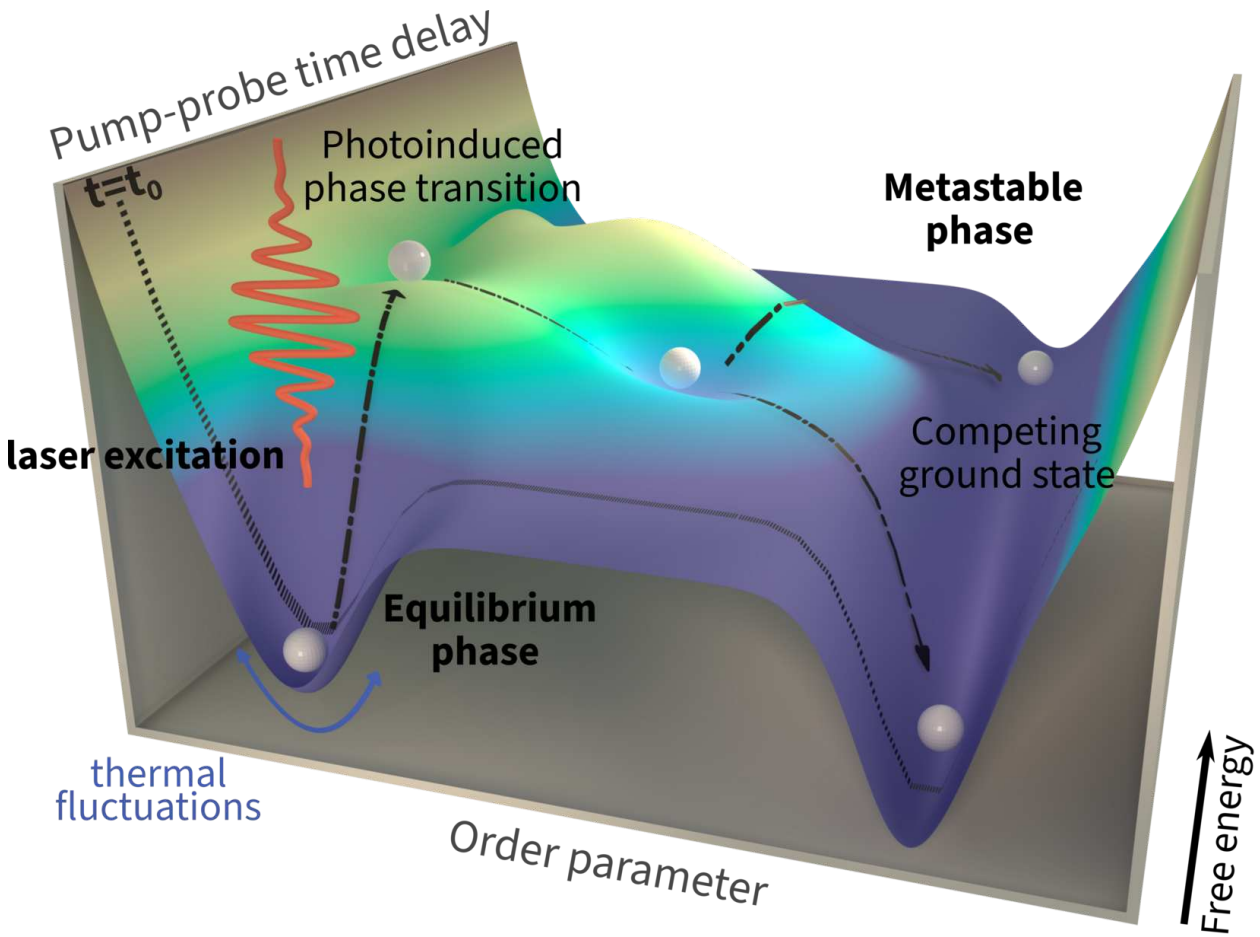

FIGURE 1.1: Order parameter dynamics in Ginzburg-Landau theory. Photoexcitation by the optical pulse will shift the free energy surface as a function of time following photoexcitation. This adjustment of the free energy allows for the order parameter to begin relaxing to different minima than thermal equilibrium, potentially relaxing to competing global minima (ground states), or to metastable phases that do not exist on equilibrium phase diagrams. Figure created for Ref. [10].

and as the order parameter moves throughout the free energy surface, we follow the resulting nonequilibrium lattice dynamics with the observables available through electron scattering, namely lattice structure and phonon distribution. In Chapter 2, we will discuss further how ultrafast scattering recovers these observables.

1.1.2 *The Pump-Probe Scheme*

The pump-probe scheme is a powerful experimental spectroscopic approach that relies on two key ingredients that are called, understandably, the pump and the probe. The pump is the method through which the material is excited, often optical. The probe

is the method through which the instantaneous state of the system is recorded. While optical in optical spectroscopy, in this specific application, the probe corresponds to the pulse train of ultrafast electron or x-ray bunches. The heart of the idea is the following: expose the system to the excitation, then after some time delay, image the state of the system. By iterating over the time delays, and therefore taking many images, one is able to reconstruct a "movie" of the system dynamics, in much the same way as the zootropes of centuries past. The utility of this approach is that it discretizes the continuous-time behaviour of the system response in a way that is repeatable, offering multiple measurements of the system response at every time delay, thus improving data quality. To this point, by "repeatable" we mean that the system is assumed to be re-equilibrated before the arrival of the next pump pulse, allowing for equivalent measurements every pump-probe cycle.

1.2 TIME-RESOLUTION IN ULTRAFAST ELECTRON DIFFRACTION

Theoretical developments made in this thesis that rely on any "ultrafast" descriptions would seem highfalutin if there was no experimental means through which one could probe such theories. To this point, we briefly synopsize what it means for ultrafast electron diffractometers to have short time resolution, as well as the means through which short time resolution is achieved[4].

1.2.1 *Impulse Response Function*

We start by considering the impact of the instrumentation itself on the time resolution of the ultrafast electron diffraction (UED) experiment, quantifying its response as a function of time with the impulse response function (IRF). Unfortunately, every aspect of

[4]The ability to produce ultrafast packets of x-rays is, stated without proof, possible, and presents various pros and cons compared to electron bunches, but is outside the pervue of this work. Enthused readers are encouraged to read Ref [11].

the measurement process does not happen instantaneously. For example, the electron bunches are packaged into discrete pancakes, Gaussian distributed in time, with finite spatial dimension. Further, each of the electro-optics used to manipulate such an electron beam have finite response times, increasing the temporal spread of the system IRF.

At this point, we have multiple responses to consider: (i) the instrument, (ii) the probe, (iii) the pump, and (iv) the sample itself. By pumping the sample at time $t = 0$, and by probing at some time-delay $t = \tau$, UED measures the order parameter of the system as a function of time via the observables of UED. The measured function is an effective response owing to the finite response of the instrument, corresponding to a convolution between the instrument IRF and the true system response. The illustration of the pump-probe scheme in the repeatable UED experiment is shown in Figure 1.2.

1.2.2 *Spacecharge considerations*

To achieve ultrafast time resolution via electron diffraction, the imaging electron bunch must be temporally focused s. t., at the time it arrives at the sample, the bunch is as short in duration as possible. The unfortunate complication here is that, due to the spatial localization of the electrons, the internal Coulomb potential energy can be very large in ultrashort electron bunches. Left alone, this potential energy quickly gets converted to kinetic energy, resulting in a "space-charge explosion" that rapidly reduces the available time resolution of the probe. One can easily imagine a few factors that will affect the rate of this explosion:

1. The beam current / number of electrons per bunch, as less bodies in the multi-body interactions will reduce the upper limit on the interal Coulomb potential energy

2. The brightness and collimation of the beam, as in theory it is possible to produce a "pancake" of charge (dimensions transverse to the direction of propagation are much larger than the dimension in the direction of propagation), s. t. the electrons are only "close" in a single dimension

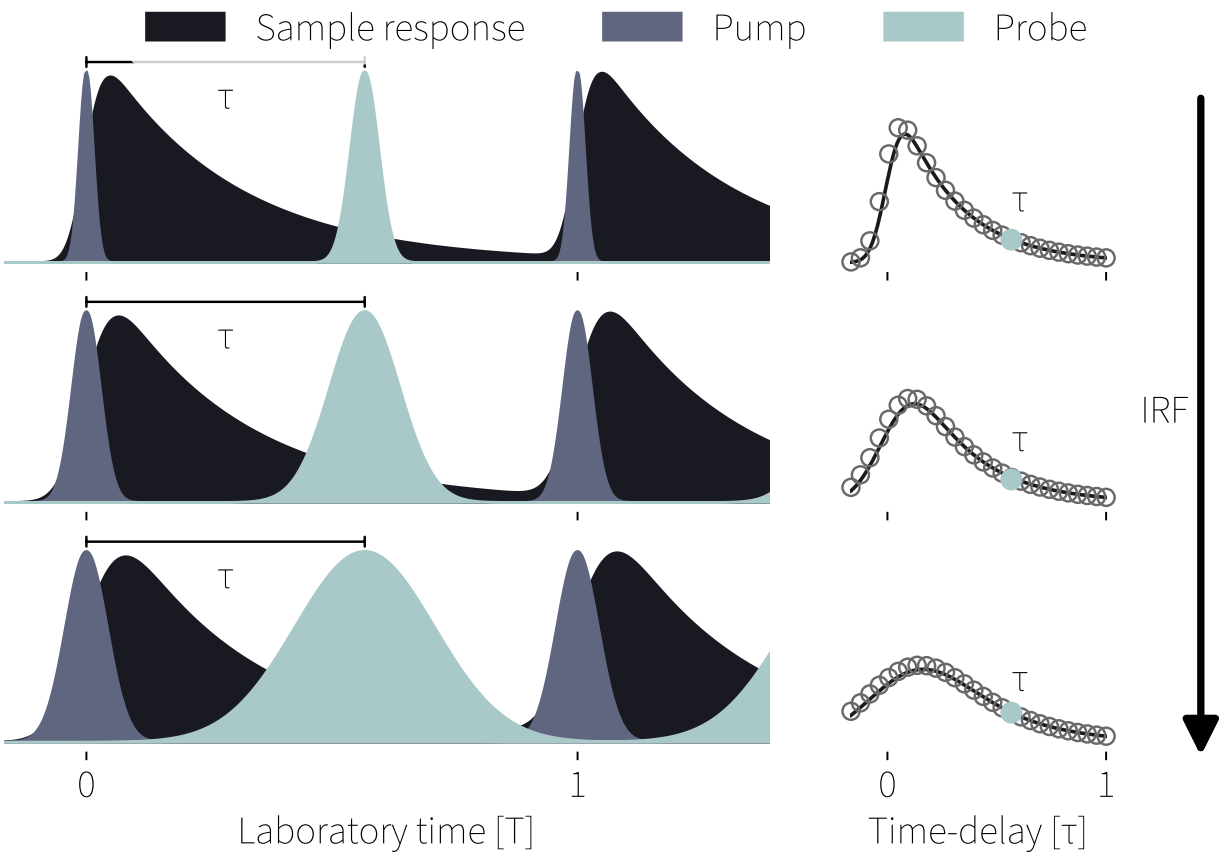

FIGURE 1.2: Pump-probe resolution as a function of IRF. The plots illustrate increasing values of pump, probe, and instrument IRF in the direction of the arrow. It is clear that for large values of IRF, fast system responses become entirely impossible to map out with sufficient resolution, necessitating that for quick phenomena that all contributions must be minimized, while for slow effects (picosecond time scales) high IRF may be sufficient. Adopted from [12].

- For example, at 100 keV, 100 fs bunches have transverse extents of $\sim$ 3 mm, with an axial dimension of 15 μm

3. The average energy of the electron bunch, since at relativistic energies the electrons will see the retarded potential of the other charges less than at non-relativistic energies

To quickly see how these factors impact the electrostatic potential energy (U in the lab frame, U' in the rest frame of the electron bunch), we can define the internal Coulomb

potential energy:

$$U' = e^2 \left(\frac{N}{M}\right)^2 \sum_{i}^{M-1} \sum_{j>i}^{M} \frac{1}{|\mathbf{r}'_i - \mathbf{r}'_j|} \tag{1.4}$$

where we have N electrons (thus total charge $Q = -Ne$), M macroparticles from which we sample to determine the potential energy[5], and we assume the beam is monochromatic with a single relativistic factor γ. For high M, this will converge to a simple geometric parameter (the average inverse distance between electrons in the bunch relative to the center of mass of the bunch), with $\sigma \triangleq \langle 1/\mathbf{r}'_{ij} \rangle$, and thus $U' = Q^2\sigma$. Taking $\mathbf{r}'_{ij} \triangleq \left[(x'_i - x'_j)^2 + (y'_i - y'_j)^2 + (z'_i - z'_j)^2\right]^{1/2}$, and assuming Gaussian distribution in each spatial dimension, namely $\langle (z'_i - z'_j)^2 \rangle = \sigma_z'^2$ etc., it can be shown that [13] $\langle 1/\mathbf{r}'_{ij} \rangle = \ln(\sigma'_z/\sigma_r)/3\sigma'_z$.

Note 1.1

This can also be seen more exactly by the more rigorous treatment of spacecharge forces which utilizes what is known as the KV distribution, from which the equation of motion for the bunch envelope can be written as:

$$\partial_{tt}^2 \sigma_x + k_x^2(z)\sigma_x - \frac{\epsilon_n^2}{\gamma^2 \sigma_x^3} - \frac{I}{\gamma^3 I_A(\sigma_x + \sigma_y)} = 0 \tag{1.5}$$

with $k_x \triangleq a_x/\gamma\beta^2c^2m$ being "space-charge factor" in x, and ϵ the RMS beam emittance [14].

We can therefore write the average potential energy (relative to the rest mass) as:

$$u' = \frac{U'}{Nm_ec^2} \approx \frac{I}{I_A\gamma} \ln(\gamma\sigma_z/\sigma_r) \tag{1.6}$$

where $I = Qc/\sqrt{2\pi}\sigma_z$ is the peak beam current, and $I_A = m_ec^3/e$ is the Alfvén current. The critical feature here is two fold: (i) the upper limit is directly proportional to the peak beam current (and thus number of electrons), and (ii) it is inversely proportional to the beam energy (via the Lorentz factor γ). This suggests that, for high electron count

[5] While a seemingly unnecessary complication, the introduction of macroparticles into the description of space-charge effects is critical for the simulation of high bunch charge pulses, and therefore our simulations of the UED beamline at McGill University, making it a worthwhile discussion.

low-energy bunches, the probing electron beam will be susceptible to the highest space-charge forces, which is unfortunately the regime in which most UED setups operate. It is therefore necessary, for electron beams with nonrelativistic energies, to have a secondary mechanism through which the space-charge forces are corrected, providing a temporal focus to the electron bunch and thus short time resolution.

1.2.3 *RF compression*

There are multiple schemas that have been developed to combat the space-charge problem. It is worth mentioning that some research institutions elect to mute with space-charge problem by using relativistic electron beams ($\langle T \rangle > 1\,\mathrm{MeV}$), where the facilities, power consumption, and manual labor required to maintain such a beam solve the space-charge problem with *cash*. Barring this exception, the three most frequently used techniques to combat the Coulomb explosion are:

- electrostatic mirrors [15], a simple approach where an electric field is generated s. t. the electrons will experience a force roughly antiparallel to the direction of incidence
  - The penetration depth of the higher energy electrons in the bunch will be greater than the lower energy electrons, resulting in a tuning of bunch duration at some focal point in reflection of the electrostatic mirror
- achromatic bending magnet [16], providing the same time-of-arrival correction as the electrostatic mirror except by adjusting the time of flight of various energy electrons via a displacing magnetic field that translates the electron beams tranverse to the direction of propagation and then back again[6]
- RF fields, where the correcting electric field is axial (inline with the beam)

[6] Although, this technique works only for relativistic electron beams.

We focus herein on the RF compression approach, as it, in addition to being the approach we have developed, overcomes the tedious alignment of the electrostatic methods and provides robust long-term stability as we describe.

In the absence of external fields, it can be shown that an ultrafast electron bunch will autoinduce a linear chirp in its axial momentum [17] (c.f. Figure 1.3), which will be the dominant manifestation of the Coulomb repulsion on the distance scales relevant here. To correct for this linear chirp in momentum, one should ideally apply an electric field that satisfies the following properties:

- The i^{th} electron with $z_i' > \langle z' \rangle$ (and therefore higher energy) will see a negative change in axial momentum
- The j^{th} electron with $z_j' < \langle z' \rangle$ (and therefore lower energy) will see a positive change in axial momentum
- The field should be entirely axial ($E_r = 0$) in order to act properly as a compression field and not impact the beam emittance
- The change in axial momentum Δp_z should be much less than the average axial momentum of the bunch $\langle p_{iz} \rangle$ to not change the energy of the beam
- Each electron bunch should sample only one oscillation of the compression field

This inversion of the axial momentum chirp with such a field can be achieved with the TM_{010} standing mode, whose field expressions can be written in cylindrical coordinates as the solution to the Maxwell's Equations in a pillbox cavity:

$$E_z = E_0 J_0 \left(x_{01} r / R \right) \sin\{\omega_{010} t + \varphi\} \tag{1.7a}$$

$$B_\phi = E_0 J_1 \left(x_{01} r / R \right) \cos\{\omega_{010} t + \varphi\} / c \tag{1.7b}$$

where r is the radial coordinate, R the radius of the pillbox cavity, E_0 the field strength, and c the speed of light. The radial dependence is entirely captured by the Bessel functions

of the first kind J_n, with the corresponding first zero of the Bessel function of the first kind $x_{01} \approx 2.4048$, from which we can write an expression for the resonant frequency of this mode $\omega_{010} = kc = {}^{x_{01}c}/_{R}$. To take into account the finite axial dimension of any real cavity, we provide a modulation of the axial electric field strength with the double normalized `erf` acceleration profile outside the pillbox of length L:

$$E_0 \longrightarrow E_0(z) = \frac{E_0}{2\mathrm{erf}({}^{L}/_{2\sqrt{2}})} \left\{ \mathrm{erf}\left(\frac{z + {}^{L}/_{2}}{\sqrt{2}} \right) - \mathrm{erf}\left(\frac{z - {}^{L}/_{2}}{\sqrt{2}} \right) \right\} \quad . \tag{1.8}$$

which is the most accurate approximation with closed-form analytic expression, allowing for easy integration into numerical simulation techniques.

It is now clear how we can design such a cavity to perform pulse compression using the TM_{010} mode. Firstly, create a cavity with suffient radius s. t. the field oscillation frequency is much quicker than the arrival frequency of the electron bunches; each bunch must sample only the linear regime of the sinusoidal driving field. Secondly, choose a phase offset φ (relative to the peak electric field strength) s. t. the electrons in the front of the bunch see the a negative electric field (thus providing positive work to the electrons and negative axial momentum offset), and that electrons in the back see an accelerating positive electric field. This can be explicitly seen by identifying the momentum transfer from the cavity to the electrons at an arrival time t as:

$$\begin{aligned}
\Delta p_z &= -e \int_{\mathbb{R}} E_z(z,t)\, dt = -\frac{e}{c\langle\beta_z\rangle} \int_{\mathbb{R}} E_0(z) \sin\left(\frac{\omega_{010}(z - \langle z_i\rangle)}{c\langle\beta_z\rangle} + \varphi \right) dz \\
&\overset{v_z \approx c\langle\beta_z\rangle}{=} -\frac{e}{v_z} \int_{\mathbb{R}} E_0(z) \left[\cos\left(\frac{\omega_{010} z}{v_z} \right) \cos\left(-\frac{\omega_{010}\langle z_i\rangle}{v_z} - \varphi \right) \right. \\
&\qquad \left. - \sin\left(\frac{\omega_{010} z}{v_z} \right) \sin\left(-\frac{\omega_{010}\langle z_i\rangle}{v_z} - \varphi \right) \right] \\
&= -\frac{e}{v_z} E_0 L_{\mathrm{cav}} \left[\cos\varphi \cos\left(\frac{\omega_{010}\langle z_i\rangle}{v_z} \right) + \sin\varphi \sin\left(\frac{\omega_{010}\langle z_i\rangle}{v_z} \right) \right] \\
&\approx -\frac{e}{v_z} E_0 L_{\mathrm{cav}} \left[\cos\varphi + \frac{\omega_{010}\langle z_i\rangle}{v_z} \sin\varphi \right]
\end{aligned} \tag{1.9}$$

where we apply the coordinate transform $t = {}^{(z - \langle z_i\rangle)}/_{2c\langle\beta_z\rangle}$, all the unprimed variables denote either the axial velocity $c\langle\beta_z\rangle$ or average position of the electron bunch $\langle z_i\rangle$ in the

lab frame. These two conditions require the following of the relative phase: the phase φ of the compression field should be chosen s. t. the $E_z(\langle z_i \rangle) = 0$. We note that we have defined the effective cavity length:

$$L_{\text{cav}} \triangleq \frac{1}{E_0} \int_{\mathbb{R}} E_0(z) \cos\left(\frac{\omega_{010} z}{v_z}\right) dz \tag{1.10}$$

which allows for ready determination of the focusing "power"[7] $\mathcal{P}_{010}$ of such a mode, defined as the inverse of the temporal focal distance f_{010}:

$$\mathcal{P}_{010} \triangleq f_{010}^{-1} = -\frac{1}{p_z} \frac{\partial \Delta p_z}{\partial \langle z_i \rangle} = \frac{e E_0 L_{\text{cav}} \omega_{010}}{m v_z^3} \sin\varphi \quad . \tag{1.11}$$

We can visualize the dynamics of the pulse compression in Figure 1.3. Firstly, the linearly chirped pulse enters the cavity. Secondly, the phase has been adjusted s. t. the zero-crossing of the electric field is at $\langle z_i \rangle$. This means the fast electrons receive a negative chirp, while the slow electrons receive a positive chirp. As the sample propagates, the applied changes in axial momentum will correct the chirp at a particular point after the cavity, the temporal focus, where the pulse is at its shortest duration possible. At this point, we are essentially back to photoemission conditions, where the transverse dimensions of the bunch are much much larger than the axial dimension.

1.2.3.1 *Long-term stability of RF compression*

There are a few hidden assumptions in this compression protocol. First, not only does one need an electric signal to drive the TM_{010} mode that is synchronized in some way to the arrival times of the electron bunches, but secondly, this signal must be phase stable lest the applied chirp correction not be constant between bunches over long time scales. To evaluate the necessary phase stability for long-term consistency of bunch compression, we find the rate of change of the time-of-flight for the bunch as a function

[7] Power in the sense of a measure of ability, but not a true power in units of watt.

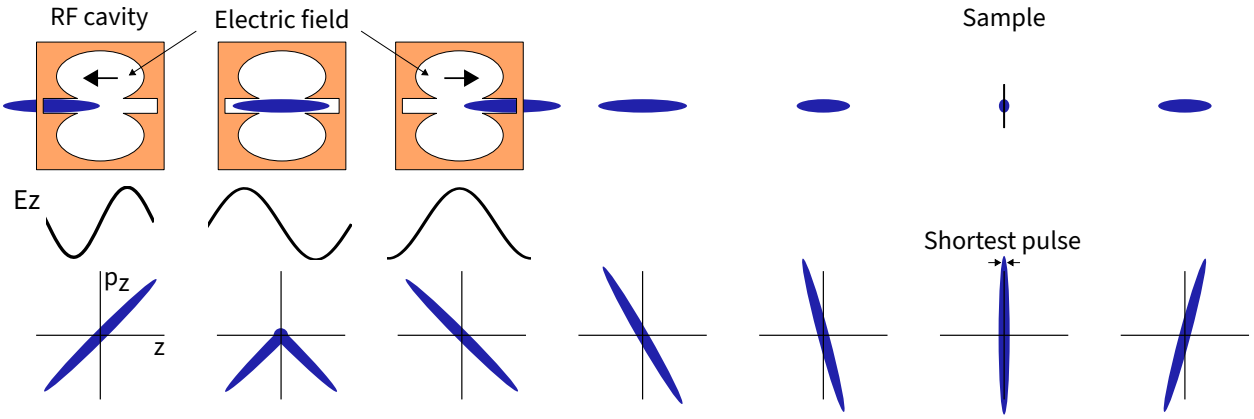

FIGURE 1.3: Schematic of RF pulse compression using a standing TM_{010} mode. At various stages, the electric field inside the cavity is rendered below to illustrate the field phase at that point in the compression. The pulse enters the cavity s. t. $E_{010}(\langle z_i \rangle) = 0$, ensuring the fast electrons see negative work to decellerate and the slow electrons see positive work to accelerate. The cavity corrects the linear chirp in axial momentum precisely at some point (the temporal focus) post compression. After the temporal focus, the dynamics of the bunch are again dominated by space-charge interactions. Adopted from [12].

of driving field phase φ

$$\begin{aligned}\frac{dt}{d\varphi} = \frac{dL/v_z}{d\varphi} = -\frac{L}{v_z^2}\frac{dv_z}{d\varphi} = \frac{L}{f_{010}\omega_{010}}\left[\frac{\omega_{010}\langle z_i\rangle}{v_z}\sin\left(\frac{\omega_{010}\langle z_i\rangle}{v_z}\right) + \cos\left(\frac{\omega_{010}\langle z_i\rangle}{v_z}\right)\right] \\ = \frac{L}{f_{010}\omega_{010}}\left[1 + \frac{3}{2}(\omega_{010}\tau)^2 + \frac{1}{6}(\omega_{010}\tau)^3 + \cdots\right]\end{aligned} \tag{1.12}$$

where $\tau = \langle z_i \rangle / v_z$ is the RMS arrival time of the electrons in the bunch in the lab frame, aka the pulse duration. For typical S-band cavities (for example $\omega_{010} \approx 2\pi \times 3$ GHz), we find the first-order jitter of the compression to be 53 fs/mrad, necessitating mrad stability of the input driving signal phase with respect to the electron pulse arrival times for ultrafast applications.

1.3 APPARATUS

Having briefly perused the needed considerations to realize an instrument capable of probing the theory in this thesis, the ultrafast electron diffractometer at McGill University that is, in principle, capable of performing such experiments is described in the following.

Note 1.2

The following describes the state of the instrument at the time of the experiments performed in this work. The current state of the instrument is upgrade with respect to many technologies.

Generation of ultrafast pulses

To first generate an ultrafast pulse from a continuous wave (CW) input, we utilized the passive modelocking approach of a resonator cavity. In this approach, a saturable absorber, which introduces loss to the intracavity radiation (large for low intensities, but much less for high intensity short pulses), generates self-amplitude modulation of the light inside the cavity. Therefore, a short pulse has loss modulation since the high peak intensity saturates the absorber more than the lower intensity tails. The result is that a circulating pulse saturates the gain to the point of compensating for the loss of the pulse itself, and any other low-intensity light experiences more loss than gain, and is not transmitted out of the cavity [18]. To mimic the saturable absorber in our case, we utilise the Kerr lens modelocking approach, where the fast saturable absorber is simulated by the Kerr lens, inducing the following change in the index of refraction:

$$\Delta n(r,t) \triangleq n_2 I(r,t) \tag{1.13}$$

where n_2 is the nonlinear refractive index, and $I(r,t)$ is the pulse intensity. The combination of the Kerr lens with a hard aperture inside the cavity results in a reduction in laser mode area for high intensities at the aperature, thus becoming an artificial saturable absorber[8]. We can quickly see how the self focusing works as follows:

$$I(x,y) = I_0 \exp\left(-\frac{x^2+y^2}{w^2}\right) \overset{(x^2+y^2)\ll w^2}{\longrightarrow} \approx I_0\left(1-2\frac{x^2+y^2}{w^2}\right)$$

$$\implies n(x,y) = n + n_2 I(x,y) \approx n_p - \Delta n_p \frac{x^2+y^2}{w^2}$$

where $\Delta n_p \triangleq n_2 I_0$ and $n_p = n + \Delta n_p$.

[8] It is artificial in the sense that the Kerr effect does not itself produce absorption.

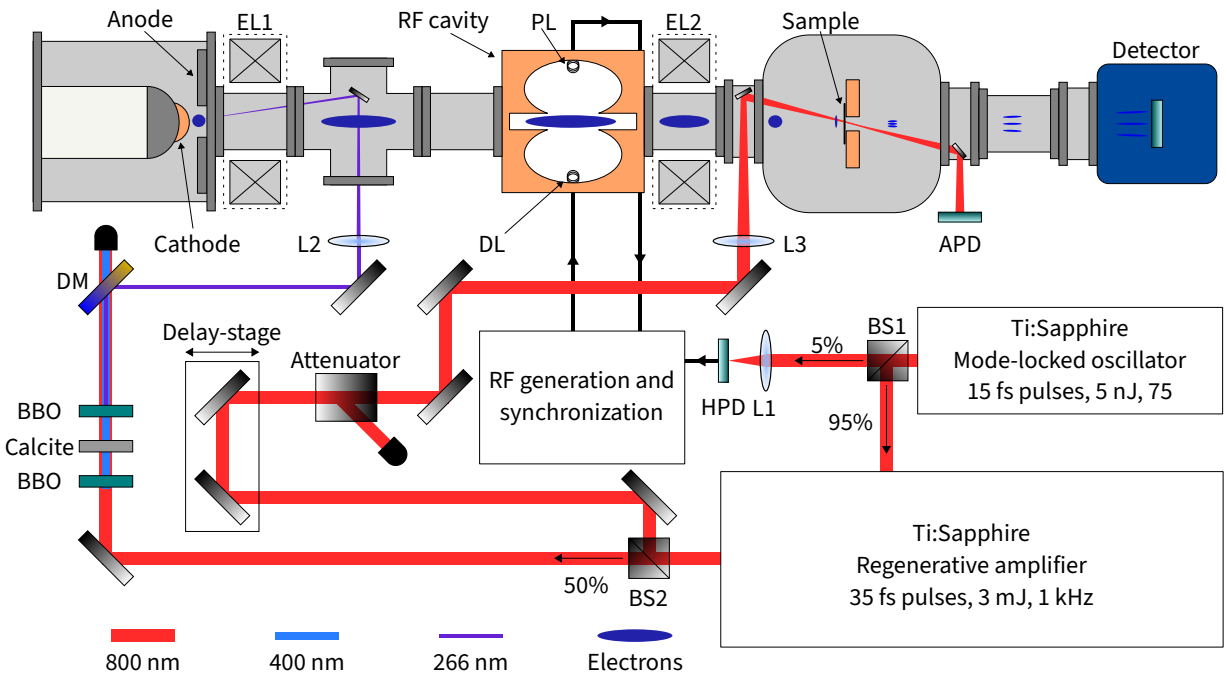

FIGURE 1.4: The schematic of the ultrafast electron column at McGill University. A modelocked oscillator generates low-power short pulses of light that are then passed to CPA to produce high-power short pulses. The resulting beam is sent across the table, split into a pump line that directly photoexcites the material, and a probe line that is upconverted to UV-C light. This UV-C light is used to generate the ultrafast electron bunches used to image the samples.

▸ AMPLIFICATION OF ULTRAFAST PULSES

Unfortunately owing to the relative tight difference in gain and loss in such a cavity in a few passes, the output pulses from (passively) modelocked oscillators are low in power. To this aim, we employ a chirped pulse amplifier (CPA) to amplify the ultrafast pulses. A full description of the technology is not relevant here, but suffice to say, we use a commercial amplified femtosecond laser system with a Ti:sapph gain medium. We use a central wavelength of 800 nm with 35 fs pulse duration, 3 mJ pulse energy, at a 1 kHz repetition rate.

▸ GENERATION OF PUMP AND PROBE BEAMS

Now having the amplified short pulses, we then split the output into two beams: the pump and the probe beams, used to stimulate electronic transitions in the material and image the instantaneous state of the lattice respectively. The pump beam is usually left

as is to utilize the 800 nm excitation for the sample. The probe beam, however, must be processed in order to successfully create illumination conditions on the photocathode to generate the ultrafast electron bunches. To this aim, we utilize the ability of nonlinear crystals to produce higher harmonics from ultrafast pulses. First, the 800 nm pulse is incident on the first non-linear crystal β-BaB_2O_4 (BBO). The crystal has a second-order $\chi^{(2)}$ reponse, where the pulse induces a second-harmonic polarization response in the material that then reradiates as light at twice the incident frequency:

$$E(2\omega) \propto P^{(2)}(2\omega) = \chi^{(2)} E(\omega) E(\omega) \tag{1.14}$$

Now having colinear 800 nm and 400 nm beams, we retard the 400 nm pulses via a calcite plate s. t. the pulses of both colours arrive at the same time at a second BBO (polarized orthogonally with respect to the other), to instantiate Type II sum frequency generation of the two pulses, producing 256 nm UV-C light. This UV light is well above the work function of the copper photocathode ($\Phi_{\mathrm{Cu}} \simeq 4.16\,\mathrm{eV}$), and is thus suitable to photoemit electrons for the probe beam at an energy $\hbar\omega_{266\,\mathrm{nm}} - \Phi_{\mathrm{Cu}}$ [19]. Ideally, the bandwidth of the ultrafast pulse will be the only factor that can modulate the energy spread of the resulting electrons, but, as surfaces are never atomically level, there will be competing affects such as step defects, multi-faceting, and impurities that will impact the chromaticity of the beam [20]. Yet, once the beam is generated, it is accelerated in a constant 90 kV DC field to impart a de Broglie wavelength shorter than atomic distances.

The optical path lengths of the beams must be carefully chosen s. t. the incident 800 nm optical pulse arrives to the sample at the same instance (in lab time) as the electron probe pulse, remembering to take into account the difference in propagation time of the electrons in the beam at the given acceleration voltage. This allows for the identification of "time-zero" in pump-probe experiments. Knowing where this crossing is allows for the fine-tune delay of the pump signal to perform time-resolved experiments. The pump line is delayed with respect to the probe by a delay stage (0.01 mm spatial resolution) s. t.

the pump arrives earlier than the probe by a given amount, making the electron bunches probe the material at that particular delay time following photoexcitation.

▸ GENERATION OF RF SIGNALS + SYNCHRONIZATION TO THE LASER PULSE TRAIN

In order to derive an electrical signal that is inherently synchronized to the optical pulse train, we can take a sampled portion of the beam from the modelocked oscillator ($\sim$5 % in power) and shine it onto a photodiode, thus converting the optical signal to an electrical one. Unfortunately, this generates a signal with a fundamental tone of the repetition rate of the oscilallator (around 75 MHz). Since an RF compression field requires each electron bunch to sample the linear regime of a single cycle of the RF field, the resonant frequency of the cavity $\omega_{010} = x_{01}c/R$ must at least be greater than this fundamental tone, and the synchronization requirement further means that whatever electric signal we generate must be a harmonic of this fundamental tone. If the cavity was driven using the fundamental tone, the cavity must then have a radius $R = x_{01} \cdot 3 \times 10^8/(2\pi \times 75 \times 10^6) \approx$1.52 m! Such a cavity is entirely impossible to realize, especially for electron beams $100\times$ smaller than the cavity. For this fundamental tone, we finally approach reasonable cavity dimensions at the 40^{th} harmonic $\approx$ 2.998 GHz, resulting in a cavity radius of a much more realistic 3 mm. Such a small cavity is also much easier to drive at the target powers needed for RF compression (around 100 W of CW driving).

While the illumination of the photodiode with the oscillator light does produce a frequency comb (a clock signal at every harmonic of the fundamental tone), the spectral content of the electric signal at such high harmonics will be low, providing issues in amplification to the necessary driving strengths. After bandpass filtering the frequency comb to isolate the 40^{th} harmonic (illustrated in Figure 1.5), it is amplified to high power to be able to drive the RF compression field strongly enough. It is first, however, passed through a synchronization system that uses active PID control to phase lock the driving signal to a reference value determined by the initial phase difference of drive and pickup

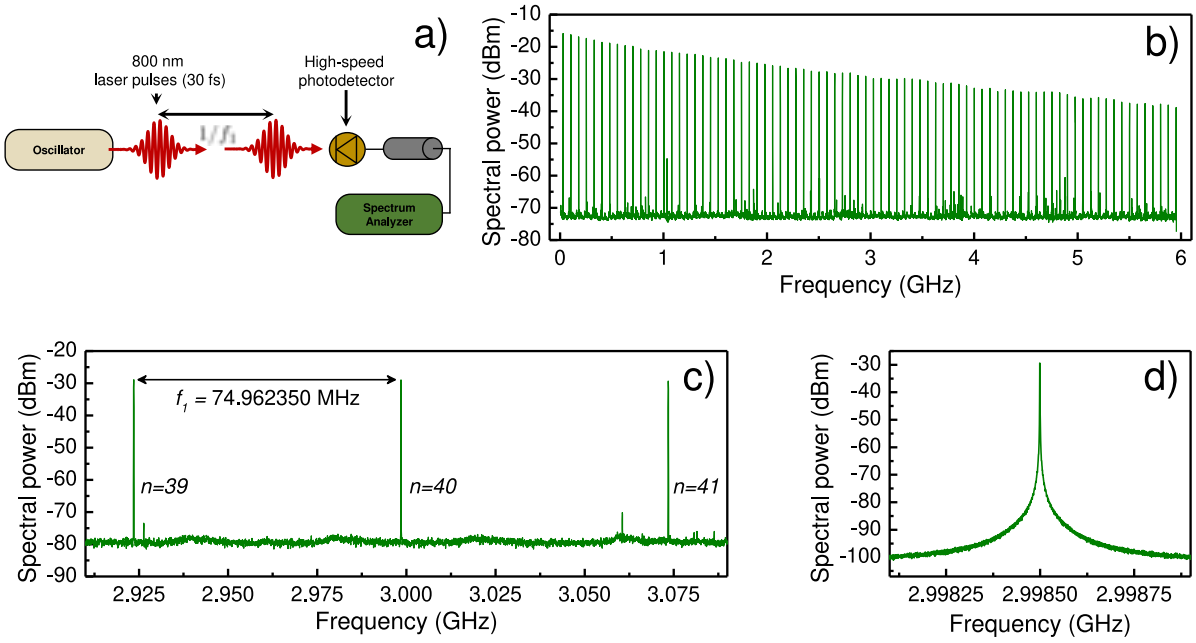

FIGURE 1.5: The measured frequency comb from the modelocked oscillator in the UEDS lab at McGill University, reprinted with permission from [21]. The experimental setup used to generate the pulses (a) shines the oscillator output onto a high-bandwidth Si photodetector. This generates an electrical frequency comb (b) of the harmonics of the fundamental tone ($\sim$ 75 MHz). Magnifying into the S-band illustrates the harmonics around the 3 GHz tone (c), which is rendered in high resolution with 500 kHz bandwidth in panel (d).

signals at the beginning of an experiment. The diagram of the cavity used in this thesis is given in Figure 1.6.

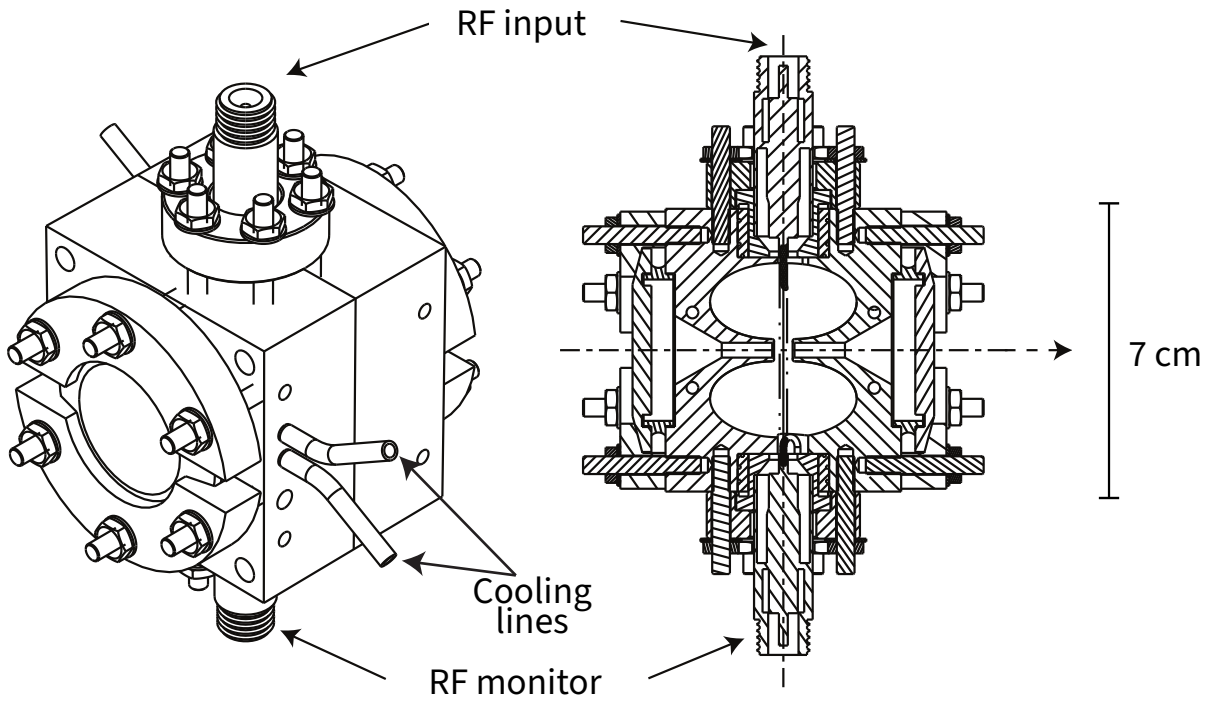

FIGURE 1.6: Schematic of the compression cavity used in the UEDS work of this thesis. The amplified, phase-jitter corrected, driving signal is deposited into the input port on the top of the device. The energy is deposited into the EM field from the RF signal by means of a drive loop, received by a pickup loop at a relative angle so as to maximize the coupling. At the powers used to drive this cavity (~ 100 W CW), the copper bulk will heat and expand. Cooling lines are machined into the block to control the device temperature and minimize thermal expansion, thus retaining the target resonant frequency for the TM_{010} mode.

1.4 OVERVIEW

This thesis aims to further develop the capabilities of UED and ultrafast electron diffuse spectroscopy (UEDS), specifically regarding the utility of these experiments in probing materials down to the 2D limit, and open a new window on previously unseen phonon-related phenomena using these techniques. In Chapter 2, we develop the theory of (in)elastic scattering from a quantum mechanical view, and discuss its shortcomings. We then describe the tools from DFT needed to progress towards a more rigorous description of such scattering in Chapter 3. To begin making the connection between *ab-initio* approaches and experimental time-resolved studies, we advance to a first-principles description of phonon dynamics in Chapter 4, and finally make the connection to the experimental observables of UED and UEDS in Chapter 5.

Having the needed background, we begin discussing the primary results of this thesis. In Part III, we start by experimentally validating the theory in the material 1L-MoS_2 in Chapters 6 and 7, showing accurate and precise UEDS experiments are physically realizable at the 2D limit. We continue in Chapter 8 by showing that such experiments are able to sensitively detect spin- and valley-tronic effects, such as chiral phonons, in systems where they exist. The final part of this thesis, Part IV, studies polaronic materials, and discovers their diffuse scattering signatures. We first discuss conflicting interpretations of existing UEDS data on the thermoelectric material SnSe in its room temperature phase in Chapter 9, and proceed to validate our theoretical results on the the benchmark wide-gap ionic insulator LiF, and apply our new-found knowledge to the alleged polaronic material SnSe in Chapter 10.

2

Electron Scattering Theory

"Gentlemen, we have run out of money. It's time to start thinking."
—Ernest Rutherford

Before diving head first into the (admittedly detailed) theory of *ab-initio* treatments of ultrafast scattering, we start from a quantum mechanical picture to see how far we can get from what one might expect out of Schrödinger's equation for billiard ball scattering of an electron off a potential. Miraculously, we can get very far with the tools provided to us by Sakurai and others.

2.1 LIPPMANN-SCHWINGER FORMALISM

The relativistic nature of electrons in the limit of scattering necessitates the Schrödinger wavefunction picture, where the key properties of the electron, namely its momentum $\mathbf{k}$ and energy ε, are written in terms of the wavefunction Ψ. Assignment of the momentum operator of the electron as $\hat{\mathbf{p}} = -i\hbar\partial_{\mathbf{x}}$ and tentative prescription of the particle's kinetic energy as $\hat{T} = (\hat{\mathbf{p}})^2 = -\hbar^2\nabla^2_{\mathbf{x}}/2m_e$ allows us to write the time dependence of the wavefunction via the energy operator $i\hbar\partial_t$ as:

$$i\hbar\partial t\Psi(\mathbf{x},t) = \left[\frac{-\hbar^2}{2m_e}\nabla^2_{\mathbf{x}} + V(\mathbf{x},t)\right]\Psi(\mathbf{x},t) \tag{2.1}$$

where we include an arbitrary potential energy landscape seen by the electron as $V(\mathbf{x}, t)$. The solution of Eq. (2.1) is crucial in determining predictive behaviour for the electron in a given environment.

2.1.1 *Electrons in free space*

Electrons propogating in real space see no external potential energy, i. e. $V(\mathbf{x}, t) \equiv 0$, leading to a separable equation of the form:

$$i\hbar\partial_t \Psi(\mathbf{x}, t) = -\frac{\hbar^2}{2m_e}\nabla_{\mathbf{x}}^2 \Psi(\mathbf{x}, t) \quad . \tag{2.2}$$

As such, the energy of the system will remain constant, meaning that the eigenproblem will be characterized by eigenstates $\{\Psi_n\}$ and eigenenergies $\hbar\omega_n \triangleq E_n$, where E_n is the total energy of the given eigenfunction. In this way, we separate the wavefunction into spatio-temporal components $u_n(\mathbf{x})$ and $e^{-i\omega_n t}$, where $u_n(\mathbf{x})$ satisfies the Helmholtz equation $\left[\nabla_{\mathbf{x}}^2 + k_n^2\right] u_n(\mathbf{x}) = 0$, and $k_n \equiv 2m_e E_n \hbar^2$ is the *wavevector* associated with the electron momentum $\mathbf{p}_n^2/\hbar^2$. Separation of variables a second time allows for the decomposition of the spatial wavefunction into each physical dimension as $u_n(\mathbf{x}) = u_n^x(\mathbf{x}\cdot\hat{\mathbf{x}})u_n^y(\mathbf{x}\cdot\hat{\mathbf{y}})u_n^z(\mathbf{x}\cdot\hat{\mathbf{z}})$, allowing us to realise wavfunctions of the following form:

$$\Psi_n(\mathbf{x}, t) = e^{-i\omega_n t}u_n(\mathbf{x}) = \prod_{i=1}^{3} \mathcal{A}_j e^{i(\mathbf{k}_n\cdot\hat{\mathbf{e}}_j)(\mathbf{x}\cdot\hat{\mathbf{e}}_j)} = \mathcal{A}e^{i(\mathbf{k}_n\cdot\mathbf{x}-\omega_n t)} \tag{2.3}$$

2.1.2 *Electrons in potential*

Lemma 2.1. *The expectation of an electron in an initial state $|\Psi\rangle$ scattering from a potential $\hat{V}$ and being detected in a final state $\langle\mathbf{k}_f|$ in the first Born-Oppenheimer approximation can be written [22] as:*

$$\langle\mathbf{k}_f|\hat{V}|\Psi\rangle = \langle\mathbf{k}_f|\left[\sum_{n\geq 1}\hat{V}\left(\frac{\hat{V}}{E_i - \hat{H}_0 + i\epsilon}\right)^{n-1}\right]|\mathbf{k}_i\rangle = \langle\mathbf{k}_f|\hat{V}|\mathbf{k}_i\rangle + \mathcal{O}(\hat{V}^2)$$

The plane-wave solutions, in the absence of an external potential, break down in solid state systems. The electrons in condensed matter are exposed to not only other

electrons, but the nuclei as well, moving quickly owing to finite temperature thermal motion. This entangled state of affairs requires a more involved look into the behaviour of the Schrödinger equation. For the sake of electron scattering, we consider only the projection of the complete wavefunction onto the detection plane, given by the state $\langle \mathbf{x}|$, as this is what will be detected in the real experiment. To this aim, we adopt the *Lipmann-Schwinger formalism*, which allows for decomposition of the projection $\langle \mathbf{x}|\Psi\rangle$ into physically intuitive terms. To start, we assume a local potential $\langle \mathbf{x}'|\hat{V}|\mathbf{x}''\rangle = V(\mathbf{x}')\delta(\mathbf{x}' - \mathbf{x}'')$ and, using[1] $\langle \mathbf{x}|\mathbf{k}\rangle = e^{i\mathbf{k}\cdot\mathbf{x}}/L^{3/2}$, we arrive at the Lipmann-Schwinger Equation:

$$\begin{aligned}\langle \mathbf{x}|\Psi\rangle &= \langle \mathbf{x}|\mathbf{k}_i\rangle - \frac{2m_e}{\hbar^2}\int d^3\mathbf{x}' V(\mathbf{x}')\langle \mathbf{x}|\Psi\rangle \frac{e^{i|\mathbf{k}_i||\mathbf{x}-\mathbf{x}'|}}{4\pi|\mathbf{x}-\mathbf{x}'|} \\ &= \frac{1}{L^{3/2}}\left[e^{i\mathbf{k}_i\cdot\mathbf{x}} + \underbrace{\frac{e^{ik_f r}}{r}\left(-\frac{m_e L^2}{2\pi\hbar^2}\right)\langle \mathbf{k}_f|\hat{V}|\Psi\rangle}_{\triangleq f(\mathbf{k}_f,\mathbf{k}_i)}\right] \end{aligned} \tag{2.4}$$

where we make use of the fact that the scattering potential is far from the imaging plane $e^{i|\mathbf{k}||\mathbf{x}-\mathbf{x}'|} \approx e^{ikr}e^{-i\mathbf{k}_i\cdot\mathbf{x}'}$ with $r \triangleq |\mathbf{x}-\mathbf{x}'|$ and $k \triangleq |\mathbf{k}|$.

Lemma 2.2. *Small displacement of Fourier Transform is a phase shift.*

Proof.

$$\mathcal{F}[h(\mathbf{x}+\mathbf{y})] = \frac{1}{2\pi}\int d\mathbf{x}' e^{-i\mathbf{q}\cdot(\mathbf{x}'+\mathbf{y})}h(\mathbf{x}') = \frac{e^{-i\mathbf{q}\cdot\mathbf{y}}}{2\pi}\int d\mathbf{x}' e^{i\mathbf{q}\mathbf{x}'}h(\mathbf{x}') = e^{-i\mathbf{q}\cdot\mathbf{y}}\mathcal{F}[h(\mathbf{x})]$$

■

So what is this f? Ignoring the first term of Eq. (2.4), which describes the unscattered electon beam, this f is a probability density of scattering from an initial momentum state $\mathbf{k}_i$ to a final state $\mathbf{k}_f$ in terms of the arbitrary external scattering potential. This scattering form factor is thus crucial to the interpretation of the Lippmann - Schwinger equation. To this end, we approximate the expectation of the wavefunction Ψ in the

[1] The derivation assumes a particle in an infinitesmial box, which will be taken to be infinitely large at the final limit.

scattering potential $\hat{V}$ at a final momenta state $\mathbf{k}_f$ using Lemma 2.1:

$$f(\mathbf{k}_f, \mathbf{k}_i) \propto \langle \mathbf{k}_f | \hat{V} | \mathbf{k}_i \rangle = \int d\mathbf{x}' \langle \mathbf{k}_f | \hat{V} | \mathbf{x}' \rangle \langle \mathbf{x}' | \mathbf{k}_i \rangle$$
$$\propto \int d\mathbf{x}' \frac{e^{i(\mathbf{k}_i - \mathbf{k}_f)\cdot \mathbf{x}'}}{L^3} V(\mathbf{x}') \propto \widetilde{V}(\mathbf{Q} = \mathbf{k}_f - \mathbf{k}_i) \tag{2.5}$$

where we clearly see that the scattering form factor is related to the Fourier transform of the scattering potential. The intensity of the scattered beam then can be written (carrying the proper constants) as:

$$I(\mathbf{Q}) = |\langle \mathbf{x} | \Psi \rangle|^2 = \left| \frac{e^{ikr}}{r} f(\mathbf{k}_f, \mathbf{k}_i) \right|^2 = \frac{1}{r^2} \left| f(\mathbf{k}_f, \mathbf{k}_i) \right|^2 = \frac{m_e^2}{4\pi^2 \hbar^4 r^2} \left| \tilde{V}(\mathbf{Q}) \right|^2 \tag{2.6}$$

where the onus now lies on applying the scattering potential resembling that seen by the electrons in a solid state condensed matter system. For a single atom, in a semi-classical picture, we assume its potential is only Coulomb like, namely:

$$V_\kappa(\mathbf{x}) = -\frac{Z_\kappa e^2}{|\mathbf{x}|} + \sum_{i=1}^{Z} \frac{e^2}{|\mathbf{x} - \mathbf{x}_i|} \tag{2.7}$$

with Z_κ the atomic weight, $\mathbf{x}$ a displacement from the ionic core, and $\mathbf{x}_i$ the classical position of the i^{th} electron. Obviously this approximation is hardly valid for most systems, but numerical implementations of computing the potential energy landscape associated with energetic electrons have been well developed; chief among these is the Hatree-Fock method [23, 24, 25] and the use of pseudopotentials [26, 27, 28, 29]. To determine the atomic form factor, i. e. the Fourier transform of this potential, to high degree of precision, we note that light atoms are spherically symmetric, and can be approximated using the "sum of Gaussians" method, the parameters of which, for a 10-parameter (5 Gaussian) fit, are tabulated in Ref [30].

$$f_e(\mathbf{Q}) = \sum_{i=1}^{n} a_i \exp(-b_i \mathbf{Q}^2) \tag{2.8}$$

Note 2.1

It is worth emphasizing here that we can readily tabulate x-ray scattering form factors f_x from the electron form factors f_e via the Mott-Bethe formula [31, 32], namely:

$$f_e(\mathbf{Q}) = \frac{2m_e e^2}{\hbar^2 \mathbf{Q}^2}[Z - \frac{m_e c^2}{e^2} f_x(\mathbf{Q})] \approx \frac{3.779}{\mathbf{Q}^2}(Z - 3.54 \times 10^4 f_x(\mathbf{Q}))$$

showing a $\sim 10^5$ enhancement in scattering of electrons.

Putting the pieces together viz a viz Lemma 2.2 and Note 2.1.2, we find the scattering intensity resulting from the interatomic potential of a crystal:

$$\widetilde{V}_c(\mathbf{Q}) = \mathcal{F}\left[\sum_\kappa V_{a\kappa}(\mathbf{x} - \mathbf{r}_\kappa)\right] = \sum_\kappa f_{e,\kappa}(\mathbf{Q}) e^{-i\mathbf{Q}\cdot\mathbf{r}_i} \tag{2.9a}$$

$$\implies I_0(\mathbf{Q}) = |\langle \mathbf{x}|\Psi\rangle|^2 \propto \left|\sum_\kappa f_{e,\kappa}(\mathbf{Q}) e^{-i\mathbf{Q}\cdot\mathbf{r}_\kappa}\right|^2 \tag{2.9b}$$

2.2 THE RECIPROCAL LATTICE

At the heart of diffraction is the concept of a *reciprocal lattice*.

Definition 3 (Reciprocal lattice)**.** The reciprocal lattice of the real-space "direct" lattice, defined by lattice vectors $\{\mathbf{a}_i\}$ in a real vector space V, is the dual space[2] V^* spanned by the reciprocal lattice vectors $\{\mathbf{b}_j\}$ for an inner product $g : V \times V \to \mathbb{R}$, $g(\mathbf{a}_i, \mathbf{b}_i) = 2\pi\delta_{ij}$.

Stated without proof [33, 34] is that the dual lattice in $\mathbb{R}^n$ has reciprocal lattice vectors determined by:

$$\mathbf{b}_i = 2\pi \frac{\epsilon_{\sigma^1 i \ldots \sigma^n i}}{\omega(\mathbf{a}_i, \ldots, \mathbf{a}_n)} g^{-1}(\mathbf{a}_{\sigma^{n-1} i} \lrcorner \ldots \mathbf{a}_{\sigma^1 i} \lrcorner \omega) \tag{2.10}$$

[2]The definition of dual lattice here that corresponds directly to the reciprocal lattice of solid state physics is the Pontryagin duality (and the associated volume measure), not in its typical usage as duals of quadratic forms on the vector space nor as the vector space of linear transformations with images in the ground field.

where ϵ is the Levi-Cevita tensor in $\mathbb{R}^n$, $\omega : V^n \to \mathbb{R}$ is the volume form, g^{-1} is the inverse of the vector space isomorphism of the inner product $\hat{g} : V \to V^* \mid \hat{g}(v)(w) = g(v,w)$, and $\lrcorner$ denotes inner multiplication. Here, σ is a permutation matrix whose rows iterate over cyclic permutations of indices 1 to n. In three dimensions, we find that the reciprocal lattice vectors are given as:

$$\mathbf{b}_1 = \frac{\mathbf{a}_2 \times \mathbf{a}_3}{\mathbf{a}_1 \cdot (\mathbf{a}_2 \times \mathbf{a}_3)} \tag{2.11}$$

and analgously for cyclic permutations of the indices. An example of a 2D reciprocal lattice is given in Figure 2.1. We can further construct the reciprocal points $\mathbf{H}$, the locations of the fundamental frequencies of the Fourier transform of the atomic potential, as linear combinations of the reciprocal lattice vectors.

Definition 4 (Reciprocal points)**.** Points in reciprocal space $\mathbf{H}$ are defined as $\mathbf{H} = (h,k,l) \cdot (\mathbf{b}_1, \mathbf{b}_2, \mathbf{b}_3)$, with $h,k,l \in \mathbb{Z}$. The integer coefficients h,k,l are known as the *Miller indices*, named after their inventor [35].

Definition 5 (Brillouin zone)**.** The reciprocal space can be divided into regions that compartmentalize the wavevectors $\mathbf{q}$ into physically distinct segments. The unit of discretization of the reciprocal space is called the Brillouin zone (BZ), the primitive cell of reciprocal space. It can be technically defined as the Wigner-Seitz cell of the reciprocal lattice, and can be practically determined by Voronoi decomposition of the reciprocal points. The complete range of wavevectors $\mathbf{q}$ allowed s. t. $\mathbf{q} \in$ BZ is called the *reducible* BZ, while the reduction of this space by all symmetries of the point group of the crystal is called the *irreducible* BZ.

For large crystals, we make a transformation of the atomic positions $\mathbf{r}_i \to \boldsymbol{\tau}_{p\kappa} = \mathbf{R}_p + \mathbf{x}_\kappa$ s. t. Eq. (2.9a) becomes:

$$I_0(\mathbf{Q}) = \frac{m_e^2}{4\pi^2\hbar^4 r^2}\left|\sum_{p\kappa} f_{e,\kappa}(\mathbf{Q}) e^{-i\mathbf{Q}\cdot(\mathbf{R}_p+\mathbf{x}_\kappa)}\right|^2 = \frac{N_p^2 m_e^2}{4\pi^2\hbar^4 r^2}\left|\sum_{\mathbf{H}}\sum_{\kappa} f_{e,\kappa}(\mathbf{Q}) e^{-i\mathbf{Q}\cdot\mathbf{x}_\kappa}\delta(\mathbf{q}-\mathbf{H})\right|^2 \tag{2.12}$$

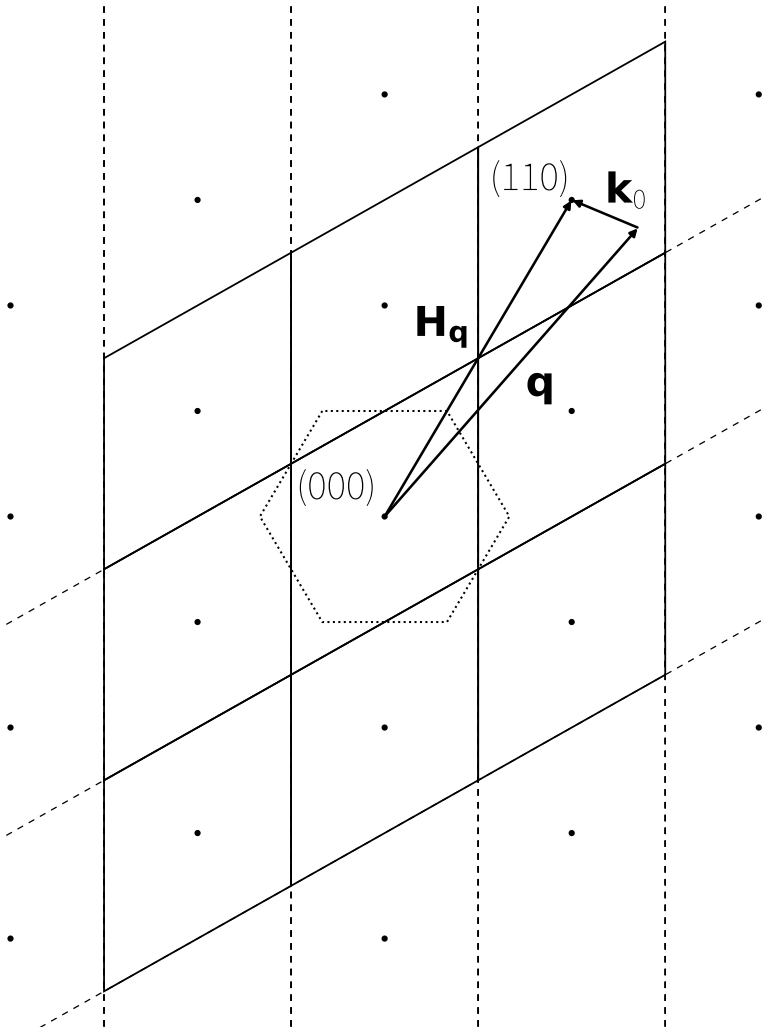

FIGURE 2.1: The corresponding 2D reciprocal lattice of a hexagonal real lattice. Given in the solid lines are the primitive rhomboidal reciprocal unit cell, and the dashed line gives the hexagon corresponding to the Wigner-Seitz reciprocal unit cell. Reflections are labelled by the integer combinations of $\{\mathbf{b}_i\}$ needed to obtain the given reflection. Vectors correspond to the Bragg peaks $\mathbf{H_q}$, the momentum transfer $\mathbf{k}_0$, and the scattering vector $\mathbf{q}$.

where we used the large crystal limit provided by Lemma 2.3 [36].

Lemma 2.3. *A sum of exponentials in the large crystal limit is a sum of delta functions evaluated at the reciprocal points.*

Proof. The Poisson summation formula says [37] that, for a well-behaved function

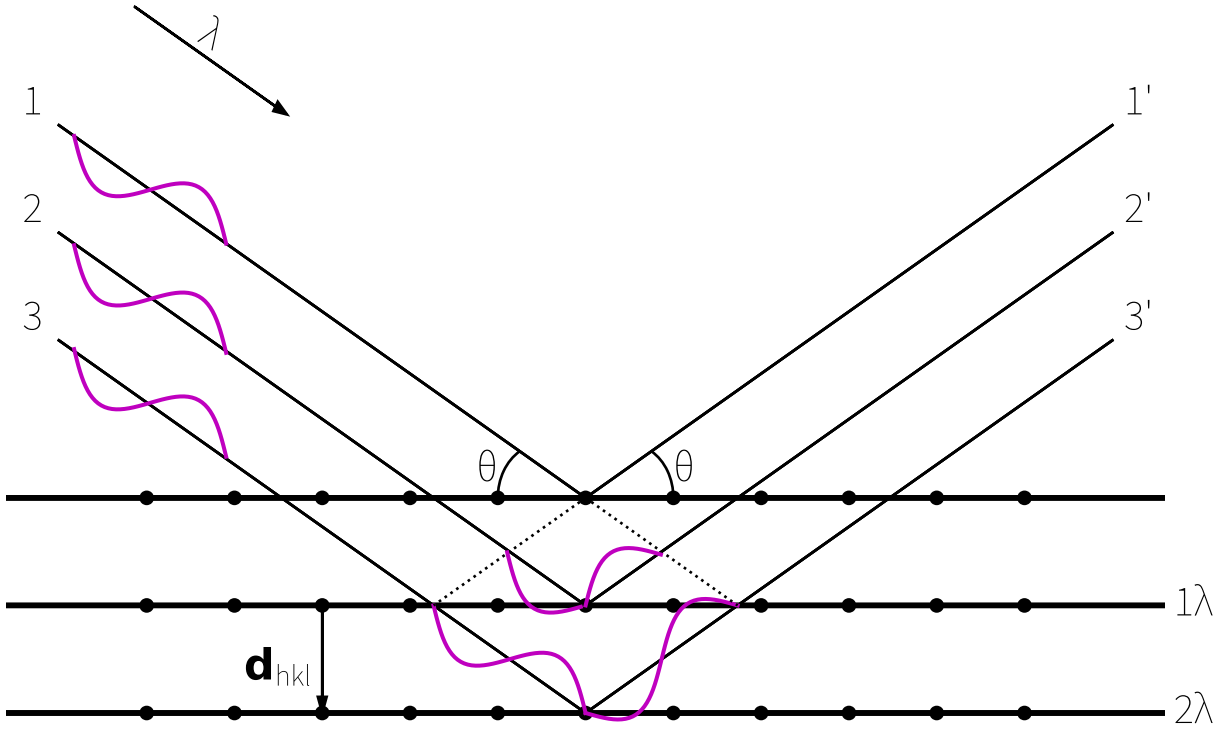

FIGURE 2.2: A schematic illustration of reflections of incident light on a cubic lattice, showing how integer divisions of the wavelength are reflected off the lattice for a given angle of incidence and interplanar distance d_{hkl}.

$f : \mathbb{R}^n \to \mathbb{R}$ and a full-rank lattice $M \subseteq \mathbb{R}^n$:

$$\sum_{\mathbf{x}\in M} f(\mathbf{x}) = \frac{1}{\operatorname{covol}(M)} \sum_{\mathbf{y}\in M^*} \mathcal{F}[f(\mathbf{x})](\mathbf{y})$$

where M^* is the dual lattice, and $\operatorname{covol}(M) = \operatorname{vol}(\mathbb{R}^n/M)$ is the volume of the fundamental domain of M. Specializing to large crystals in $\mathbb{R}^3$ ($\operatorname{covol}(M) = N_p$) for $f(x) = \delta(x)$, we can show:

$$\sum_{m=1}^{N_p} e^{-i\mathbf{q}\cdot\mathbf{R}_m} \overset{N_p\to\infty}{\longrightarrow} N_p \sum_{\mathbf{H}} \delta(\mathbf{q} - \mathbf{H})$$

■

2.2.1 *Bragg's law*

We note that the primary information used in deriving Eq. (2.12) was the fact that the frequencies of the Fourier-transformed atomic potentials is strongest at the Bragg peaks, made manifest in the delta function constraint. To this end, we note that for an incident electron of wavevector $\mathbf{k}_i$ and final wavevector $\mathbf{k}_f$ that the scattering form factor $f(\mathbf{k}_f, \mathbf{k}_i)$ is maximum when $\hat{V}(\mathbf{k}_f - \mathbf{k}_i)$ is maximum, namely that:

$$\Delta\mathbf{k} \triangleq \mathbf{k}_f - \mathbf{k}_i = h\mathbf{b}_1 + k\mathbf{b}_2 + l\mathbf{b}_3 \triangleq \mathbf{H} \quad . \tag{2.13}$$

This is known as the *Laue condition*, and describes that elastic scattering happens only when the electron momentum transfer is equivalent to a reciprocal point $\mathbf{H}$. This can be related to the canonical form of Bragg's Law by noting that, for elastic scattering, $|\mathbf{k}_i| = |\mathbf{k}_f| = 2\pi/\lambda$, where λ is the de Broglie wavelength, and thus:

$$\frac{1}{d_{hkl}} = |\mathbf{H}| = \frac{2\pi}{\lambda}|\hat{\mathbf{k}_f} - \hat{\mathbf{k}_i}| = \frac{2\pi \sin\vartheta}{\lambda} \tag{2.14}$$

where d_{hkl} is the interplanar distance of the corresponding Miller plane. This yields the original form of Bragg's law:

$$\frac{2\pi \sin\vartheta}{\lambda} = \frac{1}{d_{hkl}} \tag{2.15}$$

which removes the three dimensionality of the original constraint, but was historically motivated by exploration of polycrystalline samples, where such information is less critical for a heuristic analysis. A schematic illustration of this law is shown in Figure 2.2.

2.2.2 *Ewald sphere*

We can determine a geometric interpretation of Bragg's law by recognising that elastic scattering will only be possible for momentum transfers $\mathbf{Q}$ that fall on a sphere in reciprocal space of radius $|\mathbf{Q}| = 2\pi/\lambda$, shown for 100 kev electrons and 13 keV x-rays in Figure 2.3. The concept of the Ewald sphere allows us to re-package our understanding of peak brightness in diffraction patterns. Bragg peaks can be thought of as "rods" in the normal

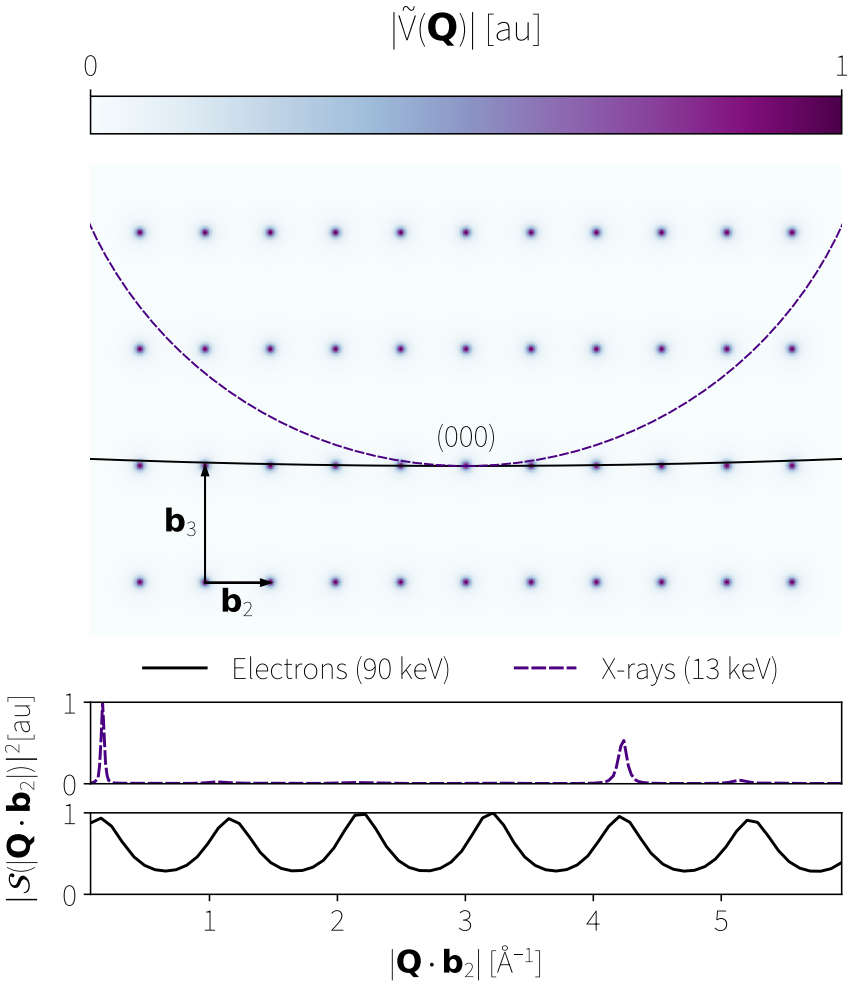

FIGURE 2.3: The Geometric intepretation of Bragg's Law, showing that the incident energy of the scatter determines the 2D slice through reciprocal space of which diffraction will be representative. The image shows the Fourier transform of the interatomic potential, with the Ewald sphere for electrons and soft x-rays. The bottom panels show the apparent intensity on the imaging plane resulting from the increased intersection of the Bragg peaks and the Ewald sphere for each probe as a function of scattering vector in the $\hat{\mathbf{b}}_2$ direction. The Bragg peaks intersect with the Ewald sphere of the electrons much more than the Ewald sphere of the x-ray, resulting in more peaks being visible by the electron probe.

direction[3], and finite momentum resolution effects will loosen the δ-fcn constraint of Eq. (2.12). Together, these imply that the points that are bright in the image are those rods that "cut" through the Ewald sphere; the less the sphere intersects the rods, the less intense those peaks are in the diffraction.

[3]In low energy electrons, or thin samples, this results from the constructive intereference of the diffraction of the crystal layers in the direction along the illumination axis.

2.3 SCATTERING CROSS SECTION

We hereunto relied on Lemma 2.1 to discuss only single scattering of the probing electron. In principle, there are multiple opportunities for the electron to scatter from the apparent potential energy landscape. We codify our justification in Appendix A for using only the Born-Oppenheimer approximation as such by examining the $n = 2$ term of the propagtor, where we show:

$$\frac{d\sigma_2}{d\Omega} < \frac{1}{a}\left(\frac{d\sigma_1}{d\Omega}\right)^2 \quad . \tag{2.16}$$

For most materials, where $[a] \sim$ Å, the relative liklihood of multiple scattering is therefore low.

2.4 OUTLOOK

Here we can proceed no further without making connections to first-principles ideas, namely moving to the quasiparticle phonon picture. Yet, we can appreciate how far quantum mechanics alone took us. Not only do we now know the behaviour of elastic scattering, and under what conditions features in diffraction patterns appear, but also the conditions required for single scattering. The elastic scattering information here has been the focus of UED since its conception, and still contains rich information to be discovered or understood. We make corrections to the present theory in Chapter 5, where we include more atomistic descriptions of condensed matter systems to complete the first-principles approach to inelastic diffuse scattering used in this thesis.

Part II

AN *AB-INITIO* VIEW OF ULTRAFAST SCATTERING AND DYNAMICS

3

Density Functional Theory

"The first principle is that you must not fool yourself,
and you are the easiest person to fool."
—Richard Feynman

Owing to the in-depth *ab-initio* calcuations in this thesis, it is worth while to review density functional theory (DFT) and how it can be used to calculate parameters of interest such as electronic band structures and phonon dispersions. That being said, the overview and complete description of computational quantum chemistry is very much out of the pervue of this thesis, and does not serve the purposes herein. The description here is limited to a minimal view to give the reader an elementary grasp on the computational methods used in these works.

Historically, the first method through which we could compute electronic band structure was the Hartree-Fock method [23, 24], where wavefunctions can only be computed for single electrons, removing all correlations between electrons from different atoms, energies, orbitals with various degrees of hybridization, etc. Overcoming these limitations was finally made possible in 1964 with the realization of the two Hohenberg-Kohn theorems [38], stated below.

Theorem 3.1. *The external potential is a unique functional of the electron density* $n(\mathbf{r})$*. Mainly, if two systems of electrons, each trapped in a potential* $v_1(\mathbf{r})$ *and the other in* $v_2(\mathbf{r})$*, have the same*

ground-state density $n(\mathbf{r})$, then $v_2(\mathbf{r}) - v_1(\mathbf{r})$ is necessarily constant.

Theorem 3.2. *The functional that derives the ground-state energy gives the lowest energy if and only if the input density is truly the ground-state density. Namely, for any N electrons in a potential $v(\mathbf{r})$, there is a functional $F[n]$ of the electron density for which, $E_{v,N}[n] = F[n] + \int v(\mathbf{r})n(\mathbf{r})d^3\mathbf{r}$ is minimal at the ground-state, with E the system energy, As such, $\min E_{v,N}[n] = E_{\text{gs}}$.*

Immediately following these theorems is the fact that the ground-state density uniquely determines the potential, and thus all (potentially many-body) properties of the system. To begin computing such a ground-state density, we start by determining the dominant interaction mechanisms between the electrons and the rest of the system. Obviously, there will be the Coulomb interaction for the density interacting with the nuclei V^{en}, as well as the Coulombic self-interactions called the Hartree energy V^{H}. We further need, however, terms to take into account electron antisymmetry (exchange effects) and electron correlation effects V^{xc}. We finally will need to include a kinetic energy term where the density corresponds to a wavefunction consisting of a single Slater determinant[1]. In such a picture, we arrive at Kohn-Sham DFT [39], where we can define the total Hamiltonian as a function of the atomic coordinates $\boldsymbol{\tau}_{p\kappa}$ of the form:

$$\underbrace{\left[-\frac{\hbar^2}{2m_e}\nabla^2 + V^{\text{KS}}\left(\mathbf{r};\left\{\boldsymbol{\tau}_{p\kappa}\right\}\right)\right]}_{\mathcal{H}^{\text{KS}}}\psi_n(\mathbf{r}) = \varepsilon_n\psi_n(\mathbf{r}) \quad . \tag{3.1}$$

Here, V^{KS} is the sum of nuclear, Hartree, and exchange-correlation energies:

$$V^{\text{KS}} = V^{\text{en}} + V^{\text{H}} + V^{\text{xc}} \tag{3.2a}$$

$$V^{\text{en}}\left(\mathbf{r};\left\{\boldsymbol{\tau}_{p\kappa}\right\}\right) = \sum_{p\kappa\mathbf{R}} V_\kappa(\mathbf{r} - \mathbf{r}_{p\kappa} - \mathbf{R}) \tag{3.2b}$$

$$V^{\text{H}}\left(\mathbf{r};\left\{\boldsymbol{\tau}_{p\kappa}\right\}\right) = \frac{e^2}{4\pi\epsilon_0}\sum_{\mathbf{R}}\int_{\text{sc}}\frac{n\left(\mathbf{r}';\left\{\boldsymbol{\tau}_{p\kappa}\right\}\right)}{|\mathbf{r} - \mathbf{r}' - \mathbf{R}|}d\mathbf{r}' \tag{3.2c}$$

[1]Such terminology refers only to the fact that one electron corresponds to one molecular orbital in the non-interacting "single-particle electron" limit. This step is very similar to standard Hartree-Fock theory.

$$V^{\mathrm{xc}}\left(\mathbf{r};\{\boldsymbol{\tau}_{p\kappa}\}\right) = \left.\frac{\delta E^{\mathrm{xc}}[n]}{\delta n}\right|_{n\left(\mathbf{r};\{\boldsymbol{\tau}_{p\kappa}\}\right)} \tag{3.2d}$$

where $\mathbf{R}$ is a direct lattice vector of the supercell. We have now a single-particle description of the wavefunctions, their energies, and the total system energy based on densities, expressed as:

$$n(\mathbf{r}) = 2\sum_i \psi_i^*(\mathbf{r})\psi_i(\mathbf{r}) \quad . \tag{3.3}$$

The first of the potentials here is the electron-lattice potential. It is the sum of the individual atomic potentials V_κ with respect to the nuclei. In a classical picture, V_κ is a Coulomb interaction of the form:

$$V_\kappa(\mathbf{r}) = -\frac{e^2}{4\pi\epsilon_0}\frac{Z_\kappa}{|\mathbf{r}|} \tag{3.4}$$

where Z_κ is the atomic number of the atom. Owing to the divergence of the Coulomb potential at $|\mathbf{r}| = 0$, such a potential clearly cannot be physical for small distances as matter does not spontaneously implode. To correct for this, we implore the *pseudopotential* method. Pseudopotentials are nonlocal due to explicit individual characterization of angular momentum channels (spherical harmonics) [40], but such considerations are left to the reader.

Definition 6 (Pseudopotential)**.** By replacing the nuclear charge with the ionic charge (the difference between the nuclear charge and some number of core electrons described by the pseudopotential), we create a function that resembles Eq. (3.4) at large $|\mathbf{r}|$ but remaining finite at $|\mathbf{r}| \sim 0$ that can take into account the effective potential of core electrons, while still retaining the key features and behaviour of covalent electrons.

Next is the Hartree potential V^{H}, describing the Coulomb repulsion between the electron being considered in one of the Kohn-Sham equations and the total electron density defined by all the electrons. This includes a self-interaction owing to the fact that the electron under consideration is also a part of the total electron density. This self interaction is unphysical, and hence, a correction is applied in the final potential V^{xc}, the

exchange-correlation potential. This is an in-depth topic in its own right, and interested readers are encouraged to read Ref [41]. It is, simply put, the functional derivative of the exchange-correlation energy functional as in Eq. (3.2d), itself a phenomenological choice based on the particular system of interest. There are various levels of approximations taking into account local and non-local effects. Some of these are listed in Note 3.

Note 3.1

Given below are XC functionals at different orders of approximation. Here, n is the electron density, τ the kinetic energy density, and $E_{\text{HF}}^{\text{xc}}$ is the Hatree-Fock exchange energy.

XC func.	Inclusions	
LDA	n	local electron density
GGA	∇n	electron density + slope
metaGGA	$\tau + \nabla^2 n$	kinetic energy + curvature
hybridGGA	$E_{\text{HF}}^{\text{xc}}$	KS orbitals

3.1 ELECTRONIC BAND STRUCTURE

To determine the ground state electron density, we can iterate over the Kohn-Sham equations by Algorithm 1. There are many details that have been skipped in this description, such as the ideal choice of initial trial guess for the density, how to update the wavefunctions should the density after the next iteration not be the ground state, etc. In practice, the convergence criterion is expressed as a difference in energy between successive iterations of the algorithm instead of exact identity between two densities. Furthermore, many of these calculations, such as the solving of the eigenproblem in Eq. (3.1) and the evaluation of the energy functional in Eq. (3.1), happen in momentum space (the Fourier transform of these equations). The conversion introduces many advantages, such as an

Algorithm 1 Ground-state electron density optimization

Precondition:
initial guess for the density $n_0(\mathbf{r})$ OR initial guess for wavefunctions $\{\psi_{i0}(\mathbf{r})\}$, a differential energy tolerance $\Delta E_{\text{tol}}^{\text{DFT}}$,
Postcondition: Single-particle ground-state electron wavefunctions $\{\psi_i(\mathbf{r})\}$

```
function GROUND-STATE DETERMINATION({ψ_i0(r)}, ΔE_tol^DFT)
    for all i ∈ [1, N] do
        Update ψ_{i+1}(r) ← solution of Kohn-Sham equation Eq. (3.1)
        Compute n_{i+1}(r) ← determine equivalent density from Eq. (3.3)
        if n_i(r) ≡ n_{i+1}(r) then
            n_KS(r) = n_{i+1}(r) ← Ground-state density reached
            return n_KS(r)
        else
            Update {ψ_i(r)} ← Use of optimization method (Newton, Secant, etc)
```

increase in computational efficiency and data management, at the cost of increasing the complexity of a complete description of the theory. As such, we do not discuss it further in this thesis. Suffice it to say, Kohn-Sham DFT allows for the computatation of reciprocal space electron wavefunctions $\{\psi_{n\mathbf{k}}\}$ and their eigenvalue energies $\varepsilon_{n\mathbf{k}}$.

3.1.1 *Maximally Localized Wannier Functions*

Owing to their relevancy and usage in the practical implementations to solutions of these equations, we take the time to briefly mention maximally-localized Wannier functions (MLWF) [42, 43]. In these simulations, the periodicity of the system necessitates the usage of Bloch states that are also periodic with the lattice, for example explicitly writing the eigenfunctions of the DFT Hamiltonian:

$$\psi_{n\mathbf{k}}(\mathbf{r}) = N_p^{1/2} u_{n\mathbf{k}}(\mathbf{r}) e^{i\mathbf{k}\cdot\mathbf{r}} \tag{3.5}$$

where $u_{n\mathbf{k}}$ is a lattice-periodic function, normalized to one in the crystal unit cell while the wavefunction is normalized to one in the supercell of the calculation. The Wannier functions are then defined by:

$$\phi_{n\mathbf{R}}(\mathbf{r}) = \frac{N_p^{1/2}}{\Omega_{\text{BZ}}} \int_{\text{BZ}} d^3\mathbf{k} e^{-i\mathbf{k}\cdot\mathbf{R}} \psi_{n\mathbf{k}}(\mathbf{r}) \tag{3.6}$$

for BZ volume Ω_{BZ} and number of $\mathbf{k}$-grid points N_p. Since Bloch states are only defined up to a variance in the phase, the identification of "ideal" Wannier functions corresponds to finding the phases of the Bloch states that give the most convenient basis set of real-space functions in which to work. This usually equates to the MLWFs, where $\phi_{n\mathbf{R}}$ is highly localized around $\mathbf{R}$. The minimization of spread of these MLWF is according to some procedure outside the scope of this work. Nonetheless, what results are a set of molecular orbital-like functions $\{\phi_{n\mathbf{R}}\}$ localized in real space that allow us to directly visualize the electronic wavefunctions computed in Algorithm 1, as well as offering a more convenient basis set to interpolate electronic bandstructure, for example. Such functions are implemented in many software suites.

Note 3.2

The following sections discuss the concepts of a *phonon*, as well as *electron-phonon coupling*, which have been hereunto undefined. We provide a more rigorous description of these concepts as they become relevant in Sections 4.3.1, 5.1.1, 7.1.2, 8.1 and 10.2.

3.2 VIBRATIONAL DISPERSION

To determine the allowed ways of movement of the crystal, we need to, in some sense, determine the force that will drive such motion. Writing the energy of the system $E^{\mathrm{DFT}} = \langle \psi_{n\mathbf{k}} | \mathcal{H}^{\mathrm{KS}} | \psi_{n\mathbf{k}} \rangle$ as in Eq. (3.1), we can find the equivalent force via the Hellman-Feynman Theorem by considering variations with respect to some atomic displacements $\Delta\boldsymbol{\tau}_{p\kappa}$:

$$F = -\frac{\partial E^{\mathrm{DFT}}}{\partial \Delta\boldsymbol{\tau}_{p\kappa}} = -\left\langle \frac{\partial \psi_{n\mathbf{k}}}{\partial \Delta\boldsymbol{\tau}_{p\kappa}} \middle| \mathcal{H}^{\mathrm{HS}} \middle| \psi_{n\mathbf{k}} \right\rangle - \left\langle \psi_{n\mathbf{k}} \middle| \mathcal{H}^{\mathrm{HS}} \middle| \frac{\partial \psi_{n\mathbf{k}}}{\partial \Delta\boldsymbol{\tau}_{p\kappa}} \right\rangle - \left\langle \psi_{n\mathbf{k}} \middle| \frac{\partial V^{\mathrm{KS}}}{\partial \Delta\boldsymbol{\tau}_{p\kappa}} \middle| \psi_{n\mathbf{k}} \right\rangle \quad . \tag{3.7}$$

With $\langle\psi_{n\mathbf{k}}|$ as the ground state, the first two terms of Eq. (3.7) will vanish[2], leaving us with the following harmonic expansion of the energy of the system:

$$E^{\mathrm{DFT}}[\{\psi_{n\mathbf{k}}\},\{\Delta\boldsymbol{\tau}_{p\kappa}\}] = E_0^{\mathrm{DFT}}\left[\left\{\psi^0_{n\mathbf{k}}\right\}\right] + \frac{1}{2}\sum_{\substack{\kappa\alpha p\\ \kappa'\alpha' p}} \underbrace{C_{\kappa\alpha p,\kappa'\alpha' p'}}_{\text{force constants}} \left(\Delta\boldsymbol{\tau}_{p\kappa}\right)^{\alpha}\left(\Delta\boldsymbol{\tau}_{p'\kappa'}\right)^{\alpha'} + \mathcal{O}(\Delta\boldsymbol{\tau}^3) \quad . \tag{3.8}$$

Here, the second order force constants and corresponding forces can be expressed [44] as:

$$\begin{aligned} C_{\kappa\alpha p,\kappa'\alpha' p'} &= \frac{\partial^2 E^{\mathrm{DFT}}}{\partial\Delta\boldsymbol{\tau}^{\alpha}_{p\kappa}\partial\Delta\boldsymbol{\tau}^{\alpha'}_{p'\kappa'}} \\ &= \left\langle \frac{\partial\psi_{n\mathbf{k}}}{\partial\Delta\boldsymbol{\tau}_{p\kappa}}\middle|\frac{\partial V^{\mathrm{KS}}}{\partial\Delta\boldsymbol{\tau}_{p\kappa}}\middle|\psi_{n\mathbf{k}}\right\rangle + \left\langle \psi_{n\mathbf{k}}\middle|\frac{\partial V^{\mathrm{KS}}}{\partial\Delta\boldsymbol{\tau}_{p'\kappa'}}\middle|\frac{\partial\psi_{n\mathbf{k}}}{\partial\Delta\boldsymbol{\tau}_{p'\kappa'}}\right\rangle - \left\langle \psi_{n\mathbf{k}}\middle|\frac{\partial^2 V^{\mathrm{KS}}}{\partial\Delta\boldsymbol{\tau}_{p\kappa}\partial\Delta\boldsymbol{\tau}_{p'\kappa'}}\middle|\psi_{n\mathbf{k}}\right\rangle \end{aligned} \tag{3.9a}$$

$$\left(F^{pp'}_{\kappa}\right)^{\alpha} = -\sum_{\kappa',\alpha'} C_{\kappa\alpha p,\kappa'\alpha' p'}\left(\Delta\boldsymbol{\tau}_{p'\kappa'}\right)^{\alpha'} \quad . \tag{3.9b}$$

We note finally that the Fourier transform of these constants is what is known as the *dynamical matrix* [45], whose components are given by:

$$\left(\mathcal{D}^{\kappa\kappa'}_{\mathbf{q}}\right)_{\alpha\alpha'} \triangleq \tilde{C}_{\kappa\alpha,\kappa'\alpha'}(\mathbf{q})/\sqrt{\mu_\kappa\mu_{\kappa'}} = \frac{1}{N_p\sqrt{\mu_\kappa\mu_{\kappa'}}}\sum_p C_{\kappa\alpha 0,\kappa'\alpha' p}e^{i\mathbf{q}\cdot\mathbf{R}_p} \quad . \tag{3.10}$$

This elucidates the pathway through which we are able to compute vibrational dispersion. By displacing the lattice by a small amount[3], performing a self-consistent calculation to determine the new electronic density and take the numerical derivative, therefore computing the interatomic force constants, we can generate the dynamical matrix at a particular momentum $\mathbf{q}$. From here, we perform standard eigenproblem solving techniques to solve Eq. (5.2) for the atomic displacements and their associated energies. The scheme to generate such dynamical matrices and related quantities is illustrated in Algorithm 2.

[2] This is because $\left\langle \psi_{n\mathbf{k}}\middle|\mathcal{H}^{\mathrm{KS}}\middle|\frac{\partial\psi_{n\mathbf{k}}}{\partial\Delta\boldsymbol{\tau}_{p\kappa}}\right\rangle = \varepsilon_{n\mathbf{k}}\langle\psi_{n\mathbf{k}}|\frac{\partial\psi_{n\mathbf{k}}}{\partial\Delta\boldsymbol{\tau}_{p\kappa}}\rangle = 0$.

[3] Each atom can be moved in any of the Cartesian directions, meaning there will be a total of $3N_{\mathrm{at}}$ modes of movement of the lattice.

Algorithm 2 Density functional perturbation calculations

Precondition:
equilibrium electronic wavefunctions $\{\psi^0_{n\mathbf{k}}\}$,
Postcondition: Vibrational dispersion with frequencies $\omega_{\mathbf{q}\nu}$ and displacements $\varepsilon_{\mathbf{q}\nu\kappa}$

```
function DFPT({ψ⁰_nk})
    for all i ∈ [1,2,3] do                          ▷ Cartesian indices
        for all κ ∈ [1, N_atoms] do                 ▷ Iterate over each atom
            Displace atom κ in direction i by small amount h_iκ
            Solve for new electronic wavefunctions by Algorithm 1
            Determine interatomic force constants for h_iκ
    Fourier interpolate to determine q-space force constants
    Generate Eq. (5.2) for arbitrary momentum
    Diagonalize Eq. (5.2) to determine frequencies and eigendisplacements
return ω_qν, ε_qνκ
```

Note 3.3

These calculations are extremely expensive owing to the many self-consistent calculations necessary at each atomic perturbation, in addition to the expensive solutions of the dynamical matrix calculations. As such, the dominant technique is to take advantage of the benefits of the Fourier transform. Since the momentum-space interatomic force constants uniquely define the dynamical matrix, by computing the momentum space force constants on a coarse grid in $\mathbf{q}$-space and transforming them to $\mathbf{r}$-space, we can Fourier interpolate back to $\mathbf{q}$-space with arbitrary density in momentum space, allowing for easy determination of energies and displacements at arbitrary momenta.

There are two assumptions in these derivations: (i) the harmonic approximation, allowing for the truncation of Eq. (3.8) to second order in the atomic displacements, and (ii) the Born-Oppenheimer adiabatic approximation, made when calculating the interatomic force constants with the electrons in the ground state. Moving beyond the harmonic approximation is treated more in Chapter 6 of this thesis.

3.3 ELECTRON-PHONON COUPLING

In order to determine the strength of EPC in materials, we will need to first determine explicitly the electron-phonon Hamiltonian in the framework of DFT. In such calculations, explicit supercells are often needed to obtain accurate results. To this aim, we must reformulate the KS Hamiltonian now including the electron-phonon interaction. Starting with Eq. (3.5), we expand the Kohn-Sham potential of Eq. (3.2a) to first order in the atomic displacements:

$$\begin{aligned} V^{\mathrm{KS}}\left(\{\boldsymbol{\tau}_{p\kappa}\}\right) &= V^{\mathrm{KS}}\left(\left\{\boldsymbol{\tau}^0_{p\kappa}\right\}\right) + \sum_{p\kappa\alpha} \frac{\partial V^{\mathrm{KS}}}{\partial \Delta\boldsymbol{\tau}^{\alpha}_{p\kappa}} \Delta\boldsymbol{\tau}^{\alpha}_{p\kappa} \\ &= V^{\mathrm{KS}}\left(\left\{\boldsymbol{\tau}^0_{p\kappa}\right\}\right) + N_P^{-1/2} \sum_{\mathbf{q}\nu} \Delta_{\mathbf{q}\nu} V^{\mathrm{KS}} \left(\hat{a}_{\mathbf{q}\nu} + \hat{a}^{\dagger}_{-\mathbf{q}\nu}\right) \end{aligned} \tag{3.11}$$

where we have defined the following as in [46]:

$$\Delta_{\mathbf{q}\nu} V^{\mathrm{KS}} = e^{i\mathbf{q}\cdot\mathbf{r}} \Delta_{\mathbf{q}\nu} v^{\mathrm{KS}} \tag{3.12a}$$

$$\Delta_{\mathbf{q}\nu} v^{\mathrm{KS}} = l_{\mathbf{q}\nu} \sum_{\kappa\alpha} \left(\mu_0/\mu_\kappa\right)^{1/2} \left(\boldsymbol{\varepsilon}^{\kappa}_{\mathbf{q}\nu}\right)^{\alpha} \partial_{\kappa\alpha\mathbf{q}} v^{\mathrm{KS}} \tag{3.12b}$$

$$\partial_{\kappa\alpha\mathbf{q}} v^{\mathrm{KS}} = \sum_p e^{-i\mathbf{q}\cdot(\mathbf{r}-\mathbf{R}_p)} \frac{\partial V^{\mathrm{KS}}}{\partial \Delta\boldsymbol{\tau}^{\alpha}_{p\kappa}}\bigg|_{\mathbf{r}-\mathbf{R}_p} \tag{3.12c}$$

where $l_{\mathbf{q}\nu} = \left[\hbar/(2\mu_0\omega_{\mathbf{q}\nu})\right]^{1/2}$ is the zero-point displacement amplitude of the mode ν at wavevector $\mathbf{q}$, with μ_0 being a simple reference mass to ensure consistent dimensions[4]. Combining Lemma 2.2, Eq. (3.5), and Eq. (3.12), we arrive at the electron-phonon Hamiltonian.

$$\hat{\mathcal{H}}^{\mathrm{ep}} = N_p^{-1/2} \sum_{\mathbf{k},\mathbf{q}} \sum_{mn\nu} g^{\nu}_{mn}(\mathbf{k},\mathbf{q}) \hat{c}^{\dagger}_{m\mathbf{k}+\mathbf{q}} \hat{c}_{n\mathbf{k}} \left(\hat{a}_{\mathbf{q}\nu} + \hat{a}^{\dagger}_{-\mathbf{q}\nu}\right) \tag{3.13}$$

where $\hat{c}$ and $\hat{c}^{\dagger}$ are the Fermionic annihilation and creation operators. We define the EPC matrix elements in terms of the periodic components of the Bloch wavefunction (c.f. Eq. (3.5)) as:

[4] It is usually taken to be the proton mass.

$$g^{\nu}_{mn}(\mathbf{k},\mathbf{q}) = \left\langle u_{m\mathbf{k}+\mathbf{q}} \left| \Delta_{\mathbf{q}\nu} v^{\mathrm{KS}} \right| u_{n\mathbf{k}} \right\rangle \tag{3.14}$$

The techniques implemented to compute such matrix elements, as well as couplings second-order in the atomic displacements are detailed and cumbersome. Interested readers are encouraged to peruse Ref [46].

4

Ab-initio dynamic theory

"Elegance should be left to shoemakers and tailors."
—Ludwig Boltzmann

In order to start examining the microscopic states of the lattice following photoexcitation, we first must consider the behaviour of the electronic system and the lattice. A common way is by ascribing them as heat baths resting at temperatures T_{el} and T_{ph} respectively [47]. Before, we treated phonons in a single "particle" picture, but as real systems populate each of these quasiparticles *en masse*, we pivot to a statistical view of their resulting dynamics.

Assuming an isotropic static coupling between these two heat sinks, g_{el} and g_{ph}, we can show that the energy transfer between them for a sufficiently small temperature difference will be linear during the time interval Δt. Writing the energy of each bath as $E = CT$, where C is the specific heat of the bath, and imposing energy conservation ($\Delta E_{\mathrm{el}} = -\Delta E_{\mathrm{ph}}$ and thus $g_{\mathrm{el}} = g_{\mathrm{ph}} \triangleq g$[1]), we find the coupled first order differential equations, as a function of pump-probe delay time τ, to describe the combined system in the two temperature model (TTM):

$$\frac{\partial T_{\mathrm{el}}}{\partial \tau} = \frac{g}{C_{\mathrm{el}}} \left(T_{\mathrm{ph}} - T_{\mathrm{el}} \right) \tag{4.1a}$$

[1]This coupling will have units of $\left[\text{energy} \times (\text{temperature} \times \text{time})^{-1}\right]$.

$$\frac{\partial T_{\text{ph}}}{\partial \tau} = \frac{g}{C_{\text{ph}}} \left(T_{\text{el}} - T_{\text{ph}} \right) \quad . \tag{4.1b}$$

In this regime, the coupling g aims to restore thermal equilibrium ($T_{\text{el}} = T_{\text{ph}}$), and in the static coupling limit, Eq. (4.1) admits exponential solutions (rise for the heat sink, decay for the heat source). Indeed, to successfully model the ultrafast photoexcitation of the sample, we can include source terms into Eq. (4.1b) of the form $Ae^{-|\tau|\Delta\nu}\theta_{\text{H}}(\tau)$, where τ is reminiscent of the pump-probe delay time and $\Delta\nu$ is the bandwidth of the ultrafast pulse (implying a pulse duration of $1/\Delta\nu$). In such a scheme, we can determine analytical expressions of the temperatures of each bath in the form:

$$T_{\text{el}}(\tau) = -\frac{b_1}{\Delta\nu} e^{-\tau\Delta\nu} - b_2\gamma^{-1}e^{-\gamma\tau} + b_3 \tag{4.2a}$$

$$T_{\text{ph}}(\tau) = T_{\text{el}}(\tau) + \frac{C_{\text{el}}}{g}\left[(b_1 - A)e^{-\tau\Delta\nu} + b_2 e^{-\gamma\tau} \right] \quad . \tag{4.2b}$$

4.1 TWO-TEMPERATURE MODEL

Now having explicit expressions for the temperatures of each system in the TTM, we begin to slowly remove approximations and make Eq. (4.2) as technically accurate as possible. In a thermalized regime, the occupation of a given electronic or vibrational eigenstate will be given by the Fermi-Dirac (FD) or Bose-Einstein (BE) distributions respectively.

$$f_{n\mathbf{k}}(\mu, T_{\text{el}}) = [e^{(\varepsilon_{n\mathbf{k}} - \mu)/k_B T_{\text{el}}} + 1]^{-1} \tag{4.3a}$$

$$n_{\mathbf{q}\nu}(T_{\text{ph}}) = [e^{\hbar\omega_{\mathbf{q}\nu}/k_B T_{\text{ph}}} - 1]^{-1} \tag{4.3b}$$

with μ the chemical potential. We have now made the connection to first-principles calculations. Following the computational procedures outlined in Chapter 3, we determine electronic band structures $\varepsilon_{n\mathbf{k}}$ and phonon frequencies $\omega_{\mathbf{q}\nu}$ that allows for immediate calculation of these occupation distribution functions[2]. By integration over electronic

[2]The determination of the chemical potential μ is discussed in Section 4.3.

(vibrational) momenta $\mathbf{k}$ ($\mathbf{q}$), we determine the appropriate density of states (DOS) $D_{\text{el}}(\varepsilon)$ ($D_{\text{ph}}(\omega)$). We then write expressions for the electron and phonon heat capacities as:

$$C_{\text{el}}(T) = \int_{\infty}^{\infty} d\varepsilon D_{\text{el}}(\varepsilon)\varepsilon \frac{\partial f(\mu, \varepsilon, T_{\text{el}})}{\partial T_{\text{el}}} \tag{4.4a}$$

$$C_{\text{ph}}(T) = \int_{0}^{\infty} d(\hbar\omega) D_{\text{ph}}(\omega)\hbar\omega \frac{\partial n(\omega, T_{\text{ph}})}{\partial T_{\text{ph}}} \quad . \tag{4.4b}$$

Owing to the nontrivial temperature dependence of these capacities, the coupled system Eq. (4.2) requires careful numerical integration techniques, such as Runge-Kutta time stepping. While the strength of the EPC is technically given with full electron momentum, phonon momentum, electron band, and phonon branch resolution via Section 3.3 and Eq. (3.14), owing to the expensive computation of retaining such momentum resolution throughout the time propagation, we can approximate this coupling constant through the second moment of the phonon spectrum $\langle\omega^2\rangle$ and the isotropically averaged coupling strength to the electronic system λ. These are determined entirely by the *Eliashberg function* $\alpha^2F(\Omega)$:

$$\lambda\langle\omega^2\rangle = 2\int \Omega\alpha^2F(\Omega)d\Omega \tag{4.5}$$

Definition 7 (Eliashberg function)**.** This is the probability of an electronic state transiting to and from the state $n\mathbf{k}$ by interaction with a phonon mode at frequency ω. We define the momentum resolved coupling strength:

$$\lambda_{\mathbf{q}\nu} \propto \frac{1}{\pi}\frac{\Pi''_{\mathbf{q}\nu}}{\omega^2_{\mathbf{q}\nu}} \tag{4.6}$$

where Π'' is the imaginary component of the phonon self-energy determined by the interaction vertex of the coupled Hamiltonian in Eq. (3.13). From here, we can then write the Elaishberg function in terms of these coupling strengths as [48]:

$$\alpha^2F(\omega) = \frac{1}{2}\sum_{\nu}\int \frac{d\mathbf{q}}{\Omega_{\text{BZ}}}\omega_{\mathbf{q}\nu}\lambda_{\mathbf{q}\nu}\delta\left(\omega - \omega_{\mathbf{q}\nu}\right) \tag{4.7}$$

We then write the isotropically averaged coupling strength g (in metals) as [49]:

$$g = \frac{\pi k_B}{\hbar D_{\mathrm{el}}(\varepsilon_{\mathrm{F}})} \lambda \langle \omega^2 \rangle \int_{-\infty}^{\infty} D_{\mathrm{el}}^2(\varepsilon) \left(-\frac{\partial f(\mu, \varepsilon, T_{\mathrm{el}})}{\partial \varepsilon} \right) d\varepsilon \tag{4.8}$$

where ε_{F} is the Fermi level. This now completely describes the TTM, but these results do present their own drawbacks and approximations.

Most immediately seen is the fact that we have imposed that the electronic and vibrational distribution functions at all time steps can be described by FD or BE statistics at elevated electronic temperature T_{el} and effective lattice temperature T_{ph} (therefore assumed to be thermalized). This implies that the TTM is not suited at all to describe non-equilibrium lattice dynamics, nor early stage electron dynamics ($\lesssim 100$ fs), hot carrier generation ansiotropic throughout the BZ, or electron-electron / electron-plasmon scattering. This makes the application of the TTM limited to (semi-)metals or materials with short electron thermalization times, completely excluding semiconductors or other gapped systems.

4.2 NONTHERMAL LATTICE MODEL

We can extend the number of heat sinks that are included in such a framework to produce the nonthermal lattice model (NLM). By now ascribing an effective temperature to a certain partition of the phonon modes, we can rewrite the coupled set of N_g differential equations as:

$$\frac{\partial T_{\mathrm{ph}}^{\nu}}{\partial \tau} = \frac{g_{\nu}}{C_{\mathrm{ph}}^{\nu}} (T_{\mathrm{el}} - T_{\mathrm{el}}^{\nu}) + \sum_{\nu'} \frac{T_{\mathrm{ph}}^{\nu'} - T_{\mathrm{ph}}^{\nu}}{\tau_{\nu\nu'}} \tag{4.9a}$$

$$\frac{\partial T_{\mathrm{el}}}{\partial \tau} = \sum_{\nu}^{N_g} \frac{g_{\nu}}{C_{\mathrm{el}}} (T_{\mathrm{ph}}^{\nu} - T_{\mathrm{el}}) + S(\tau) \tag{4.9b}$$

where $S(\tau)$ is the "heat" source, C_{ph}^{ν} the phonon heat capacity obtained by limiting the DOS to only include phonon mode ν, and g_{ν} likewise the coupling strength limiting the phonon spectrum to include only mode ν. In this way, we can describe anisotropic

coupling to N_g heat baths, where $1 \leq N_g \leq \nu_{\max}$. To roughly account for the phonon-self interaction, we compute the decay time constant of the ν^{th} subgroup by its interaction with the vibrations in the ν'^{th} subgroup $\tau_{\nu\nu'}$ [50]. This approach has been successfully employed previously [51], but still presents drawbacks, namely in the arbitrariness of the partitioning of the vibrational system. For materials with few atoms in its unit cell, these coupled system of equations is relatively inexpensive, but for large systems, the NLM becomes untractable. Furthermore, the NLM does not take into account momentum anisotropy in either the coupling strengths g or the phonon lifetime $\tau_{\nu\nu'}$. In order to overcome these limitations, we move to an exact scheme that allows for the retention of arbitrary electron and phonon momentum resolution, time resolution, and phonon mode resolution.

4.3 TIME-DEPENDENT BOLTZMANN EQUATION

The time dependence of the electronic and vibrational occupations can be modelled via the time-dependent Boltzmann equation (TDBE) [52]. In this scheme, initial temperatures of each degree of freedom, T_0^{el} and T_0^{ph} respectively, are used to initialize the electron and phonon occupancies, $f_{n\mathbf{k}}$ and $n_{\mathbf{q}\nu}$, to the FD and BE distributions. Propagating the system according to Eq. (4.10) allows direct determination of these occupations with arbitrary time and momentum resolution.

$$\frac{\partial f_{n\mathbf{k}}}{\partial \tau} = \Gamma_{n\mathbf{k}}^{\text{e-ph}}(f_{n\mathbf{k}}, n_{\mathbf{q}\nu}; \tau) \tag{4.10a}$$

$$\frac{\partial n_{\mathbf{q}\nu}}{\partial \tau} = \Gamma_{\mathbf{q}\nu}^{\text{ph-e}}(n_{\mathbf{q}\nu}, f_{n\mathbf{k}}; \tau) + \Gamma_{\mathbf{q}\nu}^{\text{ph-ph}}(n_{\mathbf{q}\nu}; \tau) \tag{4.10b}$$

Here, $\Gamma^{\text{x-y}}(\tau)$ are the collision integrals used to describe the scattering rates of coalescing and emissive processes in and between the electronic and vibrational systems[3]

[3]Electron-electron scattering is not expected to contribute in the physical or virtual system, as the

for a propagation time τ. Including the phonon-phonon interactions explicitly takes into account the available phase space for anharmonic phonon scattering processes, while the phonon-electron term describes the transfer of energy to the lattice from the excited carriers relaxing to equilibrium.

In order to solve the coupled Eq. (4.10), we start by specifying initial conditions for the electron and phonon occupations, satisfying FD and BE statistics $f^0_{n\mathbf{k}}(\mu, T^0_{\text{el}})$ and $n^0_{\mathbf{q}\nu}(T^0_{\text{ph}})$. The chemical potential μ is solved self-consistently by the following relation for a given carrier concentration:

$$n_0 = \frac{1}{\Omega_{\text{BZ}}} \sum_m^{\text{cond}} \int d\mathbf{k} f^0_{m\mathbf{k}}(\mu, T^0_{\text{el}}) \tag{4.11}$$

where n_0 is the concentration of photo-excited carriers, and the sum extends over the conduction manifold[4]. The TDBE is then propagated by explicitly computing the electron-phonon and phonon-electron collision integrals, whereas phonon-phonon scattering is accounted for in the relaxation time approximation (RTA) [53].

4.3.1 *Electron-phonon coupling revisited*

In order to derive the scattering rates resulting from EPC, we start from the bosonic annihilation and creation operators $\hat{a}_{\mathbf{q}\nu}$ and $\hat{a}^\dagger_{\mathbf{q}\nu}$ discussed more in Section 5.1.1 and the expression of the electron-phonon Hamiltonian from Eq. (3.13). To continue further, we recall that the phonon occupancy operator is defined as $\hat{N}_{\mathbf{q}\nu}$, with eigenvalues $n_{\mathbf{q}\nu}$, related to the eigenstate $|\chi\rangle$ of the phonon Hamiltonian:

$$\hat{\mathcal{H}}^{\text{ph}} = \sum_{\mathbf{q}\nu} \hbar\omega_{\mathbf{q}\nu} \left[\hat{a}_{\mathbf{q}\nu}\hat{a}^\dagger_{\mathbf{q}\nu} + 1/2\right] \quad . \tag{4.12}$$

Recalling that the Kohn-Sham wavefunctions $|\psi_{n\mathbf{k}}\rangle$ are eigenstates of the electronic Hamiltonian from Chapter 3, we express, in the Born-Oppenheimer approximation, the initial state $|i\rangle$ as a Hartree-like product $|i\rangle = |\psi_i\rangle|\chi_i\rangle$, and likewise for the final state. In

electron occupation at each step can be reasonably described by a FD distribution [52].

[4] This formula is readily extended to hole concentrations, with the sum going over the valence manifold instead.

such a framework, we write the corresponding matrix elements of the electron-phonon Hamiltonian in Eq. (3.13) as:

$$\left\langle f \left| \mathcal{H}^{\mathrm{e-ph}} \right| i \right\rangle = N_p^{-1/2} \sum_{\mathbf{k},\mathbf{q}} \sum_{mn\nu} g^{\nu}_{mn}(\mathbf{k},\mathbf{q}) \left\langle \psi_f \left| \hat{c}^{\dagger}_{m\mathbf{k}+\mathbf{q}} \hat{c}_{n\mathbf{k}} \right| \psi_i \right\rangle \left\langle \chi_f \left| \hat{a}_{\mathbf{q}\nu} + \hat{a}^{\dagger}_{-\mathbf{q}\nu} \right| \chi_i \right\rangle \quad . \tag{4.13}$$

Fermionic matrix elements will be nonzero only if the initial and final states differ in occupation from $n\mathbf{k}$ to $m\mathbf{k}+\mathbf{q}$, namely that $\langle \psi_f | \hat{c}^{\dagger}_{m\mathbf{k}+\mathbf{q}} \hat{c}_{n\mathbf{k}} | \psi_i \rangle = \left[f_{n\mathbf{k}}(1 - f_{m\mathbf{k}+\mathbf{q}}) \right]^{1/2}$. Likewise, boson statistics shows that $\langle \chi_f | \hat{a}_{\mathbf{q}\nu} | \chi_i \rangle = \sqrt{n_{\mathbf{q}\nu}}$ and $\langle \chi_f | \hat{a}^{\dagger}_{-\mathbf{q}\nu} | \chi_f \rangle = \sqrt{n_{-\mathbf{q}\nu} + 1}$ provided the initial and final states differ in occupation from $\pm\mathbf{q}\nu$ so that $n^f_{\mathbf{q}\nu} = n^i_{\mathbf{q}\nu} \mp 1$. Such considerations describe phonon absorption processes. By using Fermi's golden rule, we can now determine the transition rate of such systems.

$$\begin{aligned} \Gamma^{i\to f} = \Gamma^{\mathrm{ph-e}}_{\mathrm{abs}} &= \frac{2\pi}{\hbar} \left| \langle f | \hat{\mathcal{H}}^{\mathrm{e-ph}} | i \rangle \right|^2 \delta\left(E^{\mathrm{tot}}_f - E^{\mathrm{tot}}_i \right) \\ &= \frac{4\pi}{\hbar} \sum_{mn} \int \frac{d\mathbf{k}}{\Omega_{\mathrm{BZ}}} |g^{\nu}_{mn}(\mathbf{k},\mathbf{q})|^2 f_{n\mathbf{k}}(1 - f_{m\mathbf{k}+\mathbf{q}}) n_{\mathbf{q}\nu} \delta(\varepsilon_{n\mathbf{k}} + \hbar\omega_{\mathbf{q}\nu} - \varepsilon_{m\mathbf{k}+\mathbf{q}}) \quad . \end{aligned} \tag{4.14}$$

We likewise create the scattering transition probability for emissive processes:

$$\Gamma^{\mathrm{ph-e}}_{\mathrm{em}} = \frac{4\pi}{\hbar} \sum_{mn} \int \frac{d\mathbf{k}}{\Omega_{\mathrm{BZ}}} |g^{\nu}_{mn}(\mathbf{k},\mathbf{q})|^2 f_{n\mathbf{k}}(1 - f_{m\mathbf{k}+\mathbf{q}})(n_{\mathbf{q}\nu} + 1) \delta(\varepsilon_{n\mathbf{k}} - \hbar\omega_{\mathbf{q}\nu} - \varepsilon_{m\mathbf{k}+\mathbf{q}}) \tag{4.15}$$

as well as likewise create an expression for the electron-phonon collision integral $\Gamma^{\mathrm{e-ph}}_{n\mathbf{k}}$ [52]. These collision integrals are given by Eq. (4.16) below:

$$\begin{aligned} \Gamma^{\mathrm{e-ph}}_{n\mathbf{k}}(f_{n\mathbf{k}}, n_{\mathbf{q}\nu}; \tau) = \frac{2\pi}{\hbar} \sum_{m\nu} \int \frac{d\mathbf{q}}{\Omega_{\mathrm{BZ}}} |g^{\nu}_{mn}(\mathbf{k},\mathbf{q})|^2 \\ \times \Big\{ (1 - f_{n\mathbf{k}}) f_{m\mathbf{k}+\mathbf{q}} \delta(\varepsilon_{n\mathbf{k}} - \varepsilon_{m\mathbf{k}+\mathbf{q}} + \hbar\omega_{\mathbf{q}\nu})(1 + n_{\mathbf{q}\nu}) \\ + \quad (1 - f_{n\mathbf{k}}) f_{m\mathbf{k}+\mathbf{q}} \delta(\varepsilon_{n\mathbf{k}} - \varepsilon_{m\mathbf{k}+\mathbf{q}} - \hbar\omega_{\mathbf{q}\nu}) n_{\mathbf{q}\nu} \\ - \quad f_{n\mathbf{k}}(1 - f_{m\mathbf{k}+\mathbf{q}}) \delta(\varepsilon_{n\mathbf{k}} - \varepsilon_{m\mathbf{k}+\mathbf{q}} - \hbar\omega_{\mathbf{q}\nu})(1 + n_{\mathbf{q}\nu}) \\ - \quad f_{n\mathbf{k}}(1 - f_{m\mathbf{k}+\mathbf{q}}) \delta(\varepsilon_{n\mathbf{k}} - \varepsilon_{m\mathbf{k}+\mathbf{q}} + \hbar\omega_{\mathbf{q}\nu}) n_{\mathbf{q}\nu} \Big\} \end{aligned} \tag{4.16a}$$

$$\Gamma^{\mathrm{ph-e}}_{\mathbf{q}\nu}(n_{\mathbf{q}\nu}, f_{n\mathbf{k}}; \tau) = \frac{4\pi}{\hbar}\sum_{mn}\int \frac{d\mathbf{k}}{\Omega_{\mathrm{BZ}}}|g^{\nu}_{mn}(\mathbf{k},\mathbf{q})|^2 f_{n\mathbf{k}}(1 - f_{m\mathbf{k}+\mathbf{q}}) \times \Big[\delta(\varepsilon_{n\mathbf{k}} - \hbar\omega_{\mathbf{q}\nu} - \varepsilon_{m\mathbf{k}+\mathbf{q}})(n_{\mathbf{q}\nu}+1) - \delta(\varepsilon_{n\mathbf{k}} + \hbar\omega_{\mathbf{q}\nu} - \varepsilon_{m\mathbf{k}+\mathbf{q}})n_{\mathbf{q}\nu}\Big] \quad . \tag{4.16b}$$

It is important to note that Eq. (4.16) directly depend on the amplitude of the EPC matrix elements, namely $|g^{\nu}_{mn}(\mathbf{k},\mathbf{q})|^2$, where m, n index the Kohn-Sham electronic eigenstates. Therefore, any renormalization of the EPC strength will directly affect the propagation of the TDBE and the subsequent simulated diffraction intensity.

4.3.2 *Phonon-phonon coupling*

The phonon self-interacting Hamiltonian can be prescribed to the anharmonicities arising from the lattice and is expressed, up to three-phonon processes, as [54]:

$$\hat{\mathcal{H}}^{\mathrm{ph-ph}} = \sum_{n>2}\left\{\frac{1}{n!}\sum_{\{\nu_i\}}\Psi^{\nu_1\nu_2\cdots\nu_n}_{\mathbf{q}_1\mathbf{q}_2\cdots\mathbf{q}_n}\prod_i^n\int\frac{d\mathbf{q}_i}{\Omega_{\mathrm{BZ}}}\left[\hat{a}_{\mathbf{q}_i\nu_i} + \hat{a}^{\dagger}_{-\mathbf{q}_i\nu_i}\right]\right\} \xrightarrow{n=3} \frac{1}{3!}\sum_{\mathbf{q}\mathbf{q}'\mathbf{q}''}\sum_{\nu\nu'\nu''}\Psi^{\nu\nu'\nu''}_{\mathbf{q}\mathbf{q}'\mathbf{q}''}\left[\hat{a}_{\mathbf{q}\nu} + \hat{a}^{\dagger}_{-\mathbf{q}\nu}\right]\left[\hat{a}_{\mathbf{q}'\nu'} + \hat{a}^{\dagger}_{-\mathbf{q}'\nu'}\right]\left[\hat{a}_{\mathbf{q}''\nu''} + \hat{a}^{\dagger}_{-\mathbf{q}''\nu''}\right] \tag{4.17}$$

where $\Psi^{\nu\nu'\nu''}_{\mathbf{q}\mathbf{q}'\mathbf{q}''}$ is the 3-phonon scattering matrix elements of coalescing (emission) processes. The evaluation of the expectations of these bosonic operators is tedious but analagous to the previous derivations. We can express the phonon-phonon scattering probability as follows:

$$\Gamma^{\mathrm{ph-ph}}_{\mathbf{q}\nu}(n_{\mathbf{q}\nu};\tau) = \frac{2\pi}{\hbar}\sum_{\nu\nu'}\int\frac{d\mathbf{q}'}{\Omega_{\mathrm{BZ}}}\left|\Psi^{\nu\nu'\nu''}_{\mathbf{q}\mathbf{q}'\mathbf{q}''}\right|^2 \times \Big\{[(n_{\mathbf{q}\nu}+1)(n_{\mathbf{q}'\nu'}+1)n_{\mathbf{q}''\nu''} - n_{\mathbf{q}\nu}n_{\mathbf{q}'\nu'}(n_{\mathbf{q}''\nu''}+1)] \times \delta(\omega_{\mathbf{q}\nu} + \omega_{\mathbf{q}'\nu'} - \omega_{\mathbf{q}''\nu''})\delta^{\mathbf{H}}_{\mathbf{q}\mathbf{q}'-\mathbf{q}''} + \frac{1}{2}\left[(n_{\mathbf{q}\nu}+1)n_{\mathbf{q}'\nu'}n_{\mathbf{q}''\nu''} - n_{\mathbf{q}\nu}(n_{\mathbf{q}'\nu'}+1)(n_{\mathbf{q}''\nu''}+1)\right] \times \delta(\omega_{\mathbf{q}\nu} - \omega_{\mathbf{q}'\nu'} - \omega^{\mathbf{q}''\nu''})\delta^{\mathbf{H}}_{\mathbf{q}-\mathbf{q}'-\mathbf{q}''}\Big\} \tag{4.18}$$

4.3.2.1 *Relaxation time approximation*

This collision integral, while technically accurate, is not open to interpretation in terms of understanding the degree of anharmonicity in the lattice for a given material. To extract a set of physically meaningful values, we compute the phonon-phonon collision integral $\Gamma^{\text{ph}-\text{ph}}_{\mathbf{q}\nu}$ in the RTA. In this manner, we can express this collision integral as:

$$\Gamma^{\text{ph}-\text{ph}}_{\mathbf{q}\nu}(n_{\mathbf{q}\nu};\tau) \simeq \frac{n_{\mathbf{q}\nu}(\tau) - n^{\text{eq}}_{\mathbf{q}\nu}(\tau)}{\tau^{\text{ph}-\text{ph}}_{\mathbf{q}\nu}} \tag{4.19}$$

where n^{eq} is the equilibrium distribution that arises at the effective temperature of the lattice at time τ. Its time dependence arises from the constant exchange of energy between the vibrational and electronic systems, leading to changes in average temperature of the lattice. Furthermore, $\tau^{\text{ph}-\text{ph}}_{\mathbf{q}\nu}$ is the phonon-phonon relaxation time at equilibrium, defined [55]:

$$\begin{aligned}\frac{1}{\tau^{\text{ph}-\text{ph}}_{\mathbf{q}\nu}} = \frac{\hbar\pi}{4}\sum_{\nu'\nu''}\int\frac{d\mathbf{q}'}{\Omega_{\text{BZ}}}\Big|\Psi^{\nu\nu'\nu''}_{\mathbf{q}\mathbf{q}'\mathbf{q}''}\Big|^2_+ (n_{\mathbf{q}'\nu'} - n_{\mathbf{q}''\nu''})\delta(\omega_{\mathbf{q}\nu} + \omega_{\mathbf{q}'\nu'} - \omega_{\mathbf{q}''\nu''})\delta^{\mathbf{G}}_{\mathbf{q}+\mathbf{q}'-\mathbf{q}''} + \\ \Big|\Psi^{\nu\nu'\nu''}_{\mathbf{q}\mathbf{q}'\mathbf{q}''}\Big|^2_- (n_{\mathbf{q}'\nu'} + n_{\mathbf{q}''\nu''} + 1)\delta(\omega_{\mathbf{q}\nu} - \omega_{\mathbf{q}'\nu'} - \omega_{\mathbf{q}''\nu''})\delta^{\mathbf{G}}_{\mathbf{q}-\mathbf{q}'-\mathbf{q}''}\end{aligned} \tag{4.20a}$$

$$\left(\Psi^{\nu\nu'\nu''}_{\mathbf{q}\mathbf{q}'\mathbf{q}''}\right)_\pm = \sum_{i\in\text{u.c.}}\sum_{j,k}\sum_{\alpha\beta\gamma}\Phi^{\alpha\beta\gamma}_{ijk}\frac{(\boldsymbol{\varepsilon}_{\mathbf{q}\nu i})^\alpha\ (\boldsymbol{\varepsilon}_{\pm\mathbf{q}'\nu' j})^\beta\ (\boldsymbol{\varepsilon}_{-\mathbf{q}''\nu'' k})^\gamma}{\sqrt{\mu_i\mu_j\mu_k}} e^{\pm i\mathbf{q}'\cdot\mathbf{R}_j} e^{-i\mathbf{q}''\cdot\mathbf{R}_k} \tag{4.20b}$$

$$\begin{aligned}\Phi^{\alpha\beta\gamma}_{ijk} = \frac{\partial^3\mathcal{H}^{\text{KS}}}{\partial r^\alpha_i r^\beta_j r^\gamma_k} &\simeq \frac{1}{2h}\left[\frac{\partial^2\mathcal{H}^{\text{KS}}}{\partial r^\beta_j \partial r^\gamma_k}(r^\alpha_i = h) - \frac{\partial^2\mathcal{H}^{\text{KS}}}{\partial r^\beta_j \partial r^\gamma_k}(r^\alpha_i = -h)\right] \\ &\simeq \frac{1}{4h^2}\big[-F^\gamma_k(r^\alpha_i = h, r^\beta_j = h) \quad + F^\gamma_k(r^\alpha_i = h, r^\beta_j = -h) \\ &\qquad + F^\gamma_k(r^\alpha_i = -h, r^\beta_j = h) - F^\gamma_k(r^\alpha_i = -h, r^\beta_j = -h)\big]\end{aligned} \tag{4.20c}$$

where $(\varepsilon_{\mathbf{q}\nu i})^\alpha$ the α^{th} component of the atomic eigendisplacement of the i^{th} atom at momentum $\mathbf{q}$ in mode ν, and Φ the third-order interatomic force constant. $\mathcal{H}^{\text{KS}}$ is the Kohn-Sham DFT Hamiltonian, as in Eq. (3.1), of the perturbed system (/ Eq. (3.8)), and r^α_i

the α^{th} component of the displacement from equilibrium of the i^{th} atom[5], with F_k^γ the γ component of the force felt on atom k under component-wise displacements of atoms i and j by $\pm h$, with $h \ll 1$.

Note 4.1

Most phonon calculations use the adiabatic approximation, which necessitates that the many-body force constants form a real and symmetric matrix, guaranteeing all eigenvalues (and those phonon frequencies) are real. This directly corresponds to sharp resonances in the dynamical matrix, and phonons are meaningful long-lived excitations of the system. Going beyond the adiabatic approximation is essential for metals owing to the divergences of the dielectric function at $\mathbf{q} \sim \Gamma$, and introduces frequency renormalization and linewidth broadening [46].

The third-order force constants are indicative of the lowest order term in the imaginary term of the phonon self-energy $\Im\Sigma_{\mathbf{q}\nu}^{\text{ph}-\text{ph}}$, and are thus the first higher-order term than the harmonic approximation.

4.4 SUMMARY

To briefly recapitulate the various methods of simulating phonon dynamics, we visualize the coupling paradigms of each method in Figure 4.1. The TTM will provide insight for systems where a scalar coupling between the electronic and vibrational system is sufficient, where the extension of this scalar coupling to multiple phonons via the NLM provides finer-grained information on the internal channels of equilibration. Should a scalar coupling be insufficient, a momentum-resolved coupling must be established, and can then be used to provide a precise view into the available energy transfer mechanisms across phonon modes, and across the BZ.

[5] These force constants are determined by resolving an irreducible set of atomic displacements from which to compute the full anharmonic matrix.

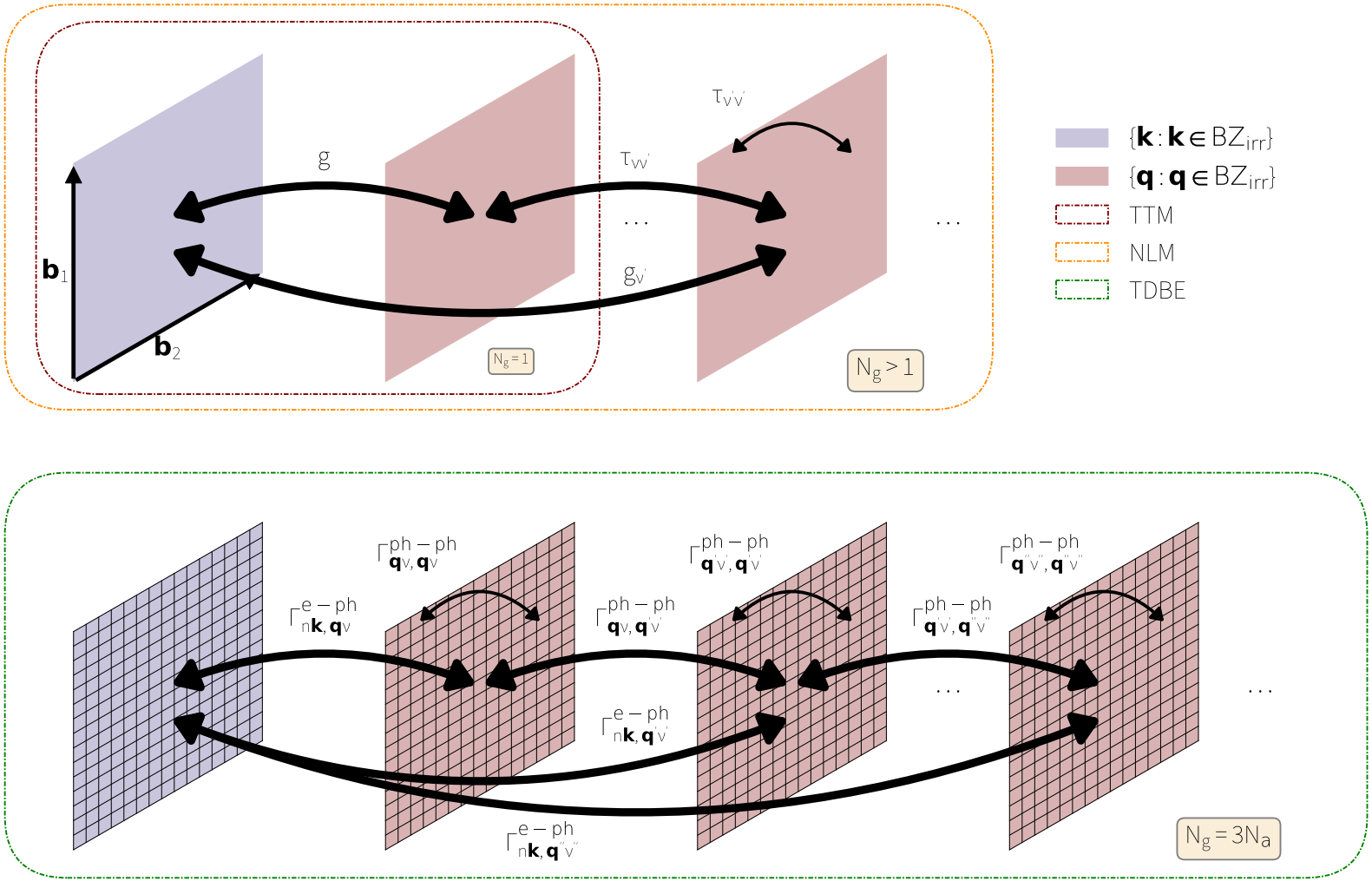

FIGURE 4.1: Comparison of different lattice models for electron-phonon coupled dynamics shown for a hexagonal reciprocal lattice (illustrated in its primitive rhomboidal reciprocal space unit cell, with 2D reciprocal lattice vectors $\mathbf{b}_1$ and $\mathbf{b}_2$). Black arrows indicate couplings between different electronic or phononic systems, and couplings for a given model are only those entirely contained in a given bounding box.

5

First-principles approach to UED

"But science and everyday life cannot and should not be separated."
—Rosalind Franklin

Now having a way to track the changes in phonon occupancy following excitation, our goal is to discover how these arbitrary occupations of phonons manifest in the diffuse scattering patterns that are experimentally accessible. Our description of ultrafast scattering ended with elastic Bragg scattering, where we uncovered the Laue condition, as well as concepts such as single-scattering conditions in thin films. To expand the description to *ab-initio* ideas, we expand our notions of scattering to the phonon normal mode formalism, which, while discussed previously, is described more precisely in the following.

5.1 QUANTUM FIELD THEORETIC APPROACH TO VIBRATIONS ON A LATTICE

Within the first Born-Oppenheimer approximation, real material systems do not have clamped nuclei, meaning that they vibrate owing to finite temperature. As such, particular vibrational modes are occupied with Bosonic statistics. In the normal mode approximation, we ascribe these vibrations to oscillations in independent harmonic oscillators

called *phonons*. As bosons, these quasiparticles can be described in a field theoretic picture, characterized by annihilation and creation operators a and $a^\dagger$ respectively. In the following section, we focus on the contribution of these lattice waves to the diffraction patterns resulting from single electron scattering. This thesis does not concern itself multiple scattering effects such as Kikuchi lines [56], either from thick samples or thin samples with heavy atoms.

5.1.1 *Second quantization of lattice waves*

The atom κ, located in the p^{th} unit cell, is displaced from its position in thermal equilibrium $\boldsymbol{\tau}_{p\kappa} = \mathbf{R}_p + \mathbf{x}_\kappa$ by a vector $\Delta\boldsymbol{\tau}_{p\kappa}$. We recast Eq. (2.9a) into:

$$\begin{aligned}
|f^{(1)}(\mathbf{Q})|^2 &= \left| -\frac{m_e}{\hbar^2}\hat{V}(\mathbf{Q}) \right|^2 = \frac{m_e^2}{\hbar^4}\hat{V}(\mathbf{Q})\hat{V}^\star(\mathbf{Q}) \\
&= \frac{m_e^2}{\hbar^4}\sum_{\kappa,\kappa'}\sum_{p,p'} f_{e,p}(\mathbf{Q}) f_{e,p'}(\mathbf{Q}) e^{-i\mathbf{Q}\cdot(\boldsymbol{\tau}_{p\kappa}-\boldsymbol{\tau}_{p'\kappa'})} e^{-i\mathbf{Q}\cdot\Delta\boldsymbol{\tau}_{p\kappa}} e^{i\mathbf{Q}\cdot\Delta\boldsymbol{\tau}_{p'\kappa'}} \\
&= \frac{m_e^2}{N_p^2\hbar^4}\sum_{\kappa,\kappa'}\sum_{p,p'} f_{e,p}(\mathbf{Q}) f_{e,p'}(\mathbf{Q}) e^{-i\mathbf{Q}\cdot(\boldsymbol{\tau}_{p\kappa}-\boldsymbol{\tau}_{p'\kappa'})} \left\langle e^{-i\mathbf{Q}\cdot\Delta\boldsymbol{\tau}_\kappa} e^{i\mathbf{Q}\cdot\Delta\boldsymbol{\tau}_{\kappa'}} \right\rangle
\end{aligned} \tag{5.1}$$

where we use the fact that, for an infinite crystal, atoms κ and κ' are uncorrelated, so summing over these atoms is equivalent to a thermal average: $\langle\,\rangle = (1/N_p)\sum_\kappa$.

The scope of this section is to derive the primary scattering intensities resulting from elastic and inelastic scattering, equivalent to approximating these thermal averages to zeroth and first orders in the atomic displacements. Later in this work, we will derive a more in depth derivation of infinitely correlated motions of pairs of atoms using complete basis sets of vibrational states $|\chi_{\alpha n}\rangle$, and exactly evaluate these thermal expectations.

Within the harmonic approximation, where phonons can be described by independent harmonic oscillators, we first need to determine the Lagrangian for the system and thus the equation of motion (EOM). In the harmonic picture, the EOM is based solely on the second-order interatomic force constants (c.f. Eq. (3.9a)), yielding an equivalent description of Newton's Second Law for the lattice using the dynamical matrices of

Eq. (3.10):

$$\sum_{\kappa'\alpha'} \left(\mathcal{D}^{\kappa\kappa'}_{\mathbf{q}}\right)_{\alpha\alpha'} \left(\varepsilon_{\mathbf{q}\nu\kappa'}\right)^{\alpha'} = \omega^2_{\mathbf{q}\nu} \left(\varepsilon_{\mathbf{q}\nu\kappa}\right)^{\alpha} \quad . \tag{5.2}$$

In this EOM, the eigenvalues are the vibrational frequencies of the harmonic oscillators, and the eigenvectors $\varepsilon_{\mathbf{q}\nu\kappa}$ are the atomic displacements of atom α at a particular oscillator momentum $\mathbf{q}$ and branch ν[1]. These two parameters completely describe the state of the phonon, and as such allow us to assign a displacement operator for the phonon in a second quanitzation scheme [46, 57]. In such a picture, with bosonic creation and innhilation operators $\hat{a}_{\mathbf{q}\nu}$ and $\hat{a}^\dagger_{\mathbf{q}\nu}$, we write the phonon displacement operator:

$$\hat{\mathbf{u}}_{p\kappa} = \sum_{\mathbf{q}\nu} \sqrt{\frac{\hbar}{2\mu_\kappa N \omega_{\mathbf{q}\nu}}} \left(\hat{a}_{\mathbf{q}\nu} e^{-i\phi_{p\kappa\mathbf{q}\nu}} + \hat{a}^\dagger_{\mathbf{q}\nu} e^{i\phi_{p\kappa\mathbf{q}\nu}}\right) e^{i\mathbf{q}\cdot\boldsymbol{\tau}_{p\kappa}} \boldsymbol{\varepsilon}_{\mathbf{q}\nu\kappa} \tag{5.3}$$

where ϕ is the phase of the lattice wave. Equation (5.3) shows the total combined effect of all phonons at unit cell p on atom κ in the basis.

To proceed, we need to implement what is sometimes referred to as the *geometrization* of physics, by way of Hilbert spaces, where states and observables (like the thermal average in Eq. (5.1)) are viewed as invariant geometric objects (as in groups), while observers themselves (like our phonon operator $\hat{\mathbf{u}}_{p\kappa}$) are coordinate systems (as in algebras). To this aim, to quantify how a composition of observables maps to the original points in coordinate space[2], we state the *Campbell-Baker-Hausdorff theorem* [58]:

Theorem 5.1. *For operators $\hat{X}, \hat{Y} \in \mathfrak{g}(n, \mathbb{C})$, with $\mathfrak{g}(n, \mathbb{C})$ a Lie algebra over $\mathbb{C}^n$ and* exp *the exponential map from the Lie algebra to the Lie group, then* $\exp(\hat{X})\exp(\hat{Y}) = \exp\hat{Z}$ *is an infinite sum of iterated Lie Brackets* $[\,]$*, which are, in this context, the commutation operator.*

$$\exp\hat{Z} = \exp(\hat{X})\exp(\hat{Y}) = \exp\left(\hat{X} + \hat{Y} + \frac{1}{2}\left[\hat{X}, \hat{Y}\right] + \frac{1}{12}\left(\left[\hat{X}, \left[\hat{X}, \hat{Y}\right]\right] + \left[\hat{Y}, \left[\hat{Y}, \hat{X}\right]\right]\right) + \cdots\right) \tag{5.4}$$

[1] From here on out, these will be called simply the phonon frequencies and eigendisplacements to beckon back to their origins in the harmonic approximation.

[2] This is known as the *Lie group-Lie algebra correspondence*.

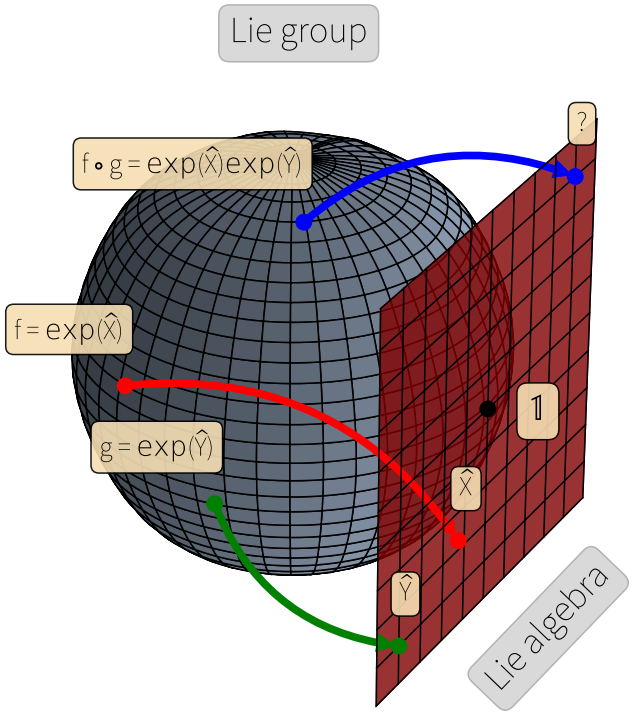

FIGURE 5.1: Visualization of the Campbell-Baker-Hausdorff theorem. Given objects in coordinate space (the Lie algebra), $\hat{X}$ and $\hat{Y}$, that are mapped into observables, f and g, the Campbell-Baker-Hausdorff theorem identifies which point in coordinate space maps to the composition $f \circ g = \exp \hat{X} \exp \hat{Y}$ of the two observables in the Lie group. Here, $\mathbb{1}$ is the identity element of the Lie group which serves as the point of tangency for the Lie algebra.

Corollary 5.1. *For* $\hat{a} \sim \hat{X}$ *and* $\hat{a}^\dagger \sim \hat{Y}$*, since* $[\hat{a}_{\mathbf{q}\nu}, \hat{a}^\dagger_{\mathbf{q}'\nu'}] = \delta_{\mathbf{q}\mathbf{q}'}\delta_{\nu\nu'}$*, we have that* $\left[\hat{X}, [\hat{X}, \hat{Y}]\right] = \left[\hat{Y}, [\hat{X}, \hat{Y}]\right] = 0$*, and so:*

$$\exp \hat{Z} = \exp \hat{X} \exp \hat{Y} = \exp\{X + Y + \frac{1}{2}[X, Y]\} \tag{5.5}$$

We can finally evaluate the thermal average as follows. Utilizing the Bloch identity $\langle e^{\hat{X}} \rangle = e^{\frac{1}{2}\langle \hat{X}^2 \rangle}$ [59], we find:

$$\left\langle e^{-i\mathbf{Q}\cdot\hat{\mathbf{u}}_\kappa} e^{i\mathbf{Q}\cdot\hat{\mathbf{u}}_{\kappa'}} \right\rangle = e^{-\frac{1}{2}\langle(\mathbf{Q}\cdot\hat{\mathbf{u}}_\kappa)^2\rangle} e^{-\frac{1}{2}\langle(\mathbf{Q}\cdot\hat{\mathbf{u}}_{\kappa'})^2\rangle} e^{\left\langle(\mathbf{Q}\cdot\hat{\mathbf{u}}_\kappa)(\mathbf{Q}\cdot\hat{\mathbf{u}}_{\kappa'})\right\rangle} = e^{-W_\kappa} e^{-W_{\kappa'}} e^{\left\langle(\mathbf{Q}\cdot\hat{\mathbf{u}}_\kappa)(\mathbf{Q}\cdot\hat{\mathbf{u}}_{\kappa'})\right\rangle} \tag{5.6}$$

where contributions to the thermal average resulting from autodisplacement are the well-known *Debye-Waller* factors W_κ [60, 61]. Recall that we are interested in determining

the primary contributions to these inelastic terms in the thermal average, corresponding to approximating the exponential with its zeroth and first order terms, given explicitly by $e^{\langle(\mathbf{Q}\cdot\hat{\mathbf{u}}_\kappa)(\mathbf{Q}\cdot\hat{\mathbf{u}}_{\kappa'})\rangle} = 1 + \langle(\mathbf{Q}\cdot\hat{\mathbf{u}}_\kappa)(\mathbf{Q}\cdot\hat{\mathbf{u}}_{\kappa'})\rangle + \mathcal{O}(|\hat{\mathbf{u}}_\kappa|^2|\hat{\mathbf{u}}_{\kappa'}|^2)$. This approximation corresponds to all contributions to the scattering form factor that results from at most single-phonon inelastic diffuse scattering. For simple crystal structures, such as SnSe, MoS_2, and graphite, this approximation is valid, but there are classes of materials where *multi-phonon* diffuse scattering is actually the dominant contribution, such as black phosphorus [62]. We then evaluate:

$$\begin{aligned}
\langle(\mathbf{Q}\cdot\hat{\mathbf{u}}_\kappa)\,(\mathbf{Q}\cdot\hat{\mathbf{u}}_{\kappa'})\rangle &= \frac{\hbar}{2N}\sum_{\kappa,\kappa'}\sum_{\mathbf{q}\mathbf{q}'}\frac{\left(\mathbf{Q}\cdot\boldsymbol{\varepsilon}_{\mathbf{q}\nu\kappa}\right)\left(\mathbf{Q}\cdot\boldsymbol{\varepsilon}_{\mathbf{q}\nu\kappa'}\right)}{\sqrt{\mu_\kappa\mu_{\kappa'}\omega_{\mathbf{q}\nu}\omega_{\mathbf{q}'\nu'}}}e^{i\mathbf{q}\cdot\boldsymbol{\tau}_{p\kappa}}e^{i\mathbf{q}'\cdot\boldsymbol{\tau}_{p'\kappa'}} \\
&\times\left\langle\left[\hat{a}_{\mathbf{q}\nu}e^{-i\phi_{p\kappa\mathbf{q}\nu}}+\hat{a}^\dagger_{\mathbf{q}\nu}e^{i\phi_{p\kappa\mathbf{q}\nu}}\right]\left[\hat{a}_{\mathbf{q}'\nu'}e^{-i\phi_{p'\kappa'\mathbf{q}'\nu'}}+\hat{a}^\dagger_{\mathbf{q}'\nu'}e^{i\phi_{p'\kappa'\mathbf{q}'\nu'}}\right]\right\rangle \\
&= \frac{\hbar}{2N}\sum_{\nu}\sum_{\mathbf{q}}\frac{\left(\mathbf{Q}\cdot\boldsymbol{\varepsilon}_{\mathbf{q}\nu\kappa}\right)\left(\mathbf{Q}\cdot\boldsymbol{\varepsilon}_{\mathbf{q}\nu\kappa'}\right)}{\omega_{\mathbf{q}\nu}\sqrt{\mu_\kappa\mu_{\kappa'}}}e^{i\mathbf{q}\cdot\boldsymbol{\tau}_{p\kappa}}e^{i\mathbf{q}\cdot\boldsymbol{\tau}_{p\kappa'}}\left[2\hat{n}_{\mathbf{q}\nu}+1\right] \\
&= \frac{\hbar}{N}\sum_{\nu}\sum_{\mathbf{q}}\left(\frac{\hat{n}_{\mathbf{q}\nu}+1/2}{\omega_{\mathbf{q}\nu}}\right)\left(\frac{\left(\mathbf{Q}\cdot\boldsymbol{\varepsilon}_{\mathbf{q}\nu\kappa}\right)\left(\mathbf{Q}\cdot\boldsymbol{\varepsilon}_{\mathbf{q}\nu\kappa'}\right)}{\sqrt{\mu_\kappa\mu_{\kappa'}}}\right)e^{i\mathbf{q}\cdot\boldsymbol{\tau}_{p\kappa}}e^{i\mathbf{q}\cdot\boldsymbol{\tau}_{p\kappa'}} \qquad (5.7)
\end{aligned}$$

where we introduced the phonon occupancy operator $\hat{n}_{\mathbf{q}\nu} \triangleq \hat{a}_{\mathbf{q}\nu}\hat{a}^\dagger_{\mathbf{q}\nu} = \hat{a}^\dagger_{\mathbf{q}\nu}\hat{a}_{\mathbf{q}\nu} - 1$, as well as noting that the phases across unit cells are not correlated, cancelling cross terms.

5.1.2 *Scattering amplitude*

We now can finally evaluate the scattering intensity from up to first order inelastic scattering events. In such a framework where we prepare an initial state of the probing electron $|\mathbf{k}_i\rangle$ to scatter to a final state $|\mathbf{k}_f\rangle$, our operators now become observables, and

as such as can reformulate Eq. (5.1) into the following:

$$
\begin{aligned}
|f(\mathbf{Q})|^2 &= \frac{m_e^2}{N_p^2\hbar^4}\sum_{pp'}\sum_{\kappa\kappa'} f_{e,\kappa}(\mathbf{Q}) f_{e,\kappa'} e^{-i\mathbf{Q}\cdot(\boldsymbol{\tau}_{p\kappa}-\boldsymbol{\tau}_{p'\kappa'})} e^{-W_\kappa} e^{-W_{\kappa'}} \left[1 + \langle(\mathbf{Q}\cdot\hat{\mathbf{u}}_\kappa)(\mathbf{Q}\cdot\hat{\mathbf{u}}_{\kappa'})\rangle\right] \\
&= \frac{m_e^2}{N_p^2\hbar^4}\left|\sum_{p\kappa} f_{e,\kappa}(\mathbf{Q}) e^{-W_\kappa} e^{-i\mathbf{Q}\cdot\boldsymbol{\tau}_{p\kappa}}\right|^2 \\
&+ \frac{m_e^2}{NN_p^2\hbar^3}\sum_{\mathbf{q}\nu}\frac{n_{\mathbf{q}\nu}+1/2}{\omega_{\mathbf{q}\nu}}\left|\sum_{p\kappa}\frac{f_{e,\kappa}(\mathbf{Q})e^{-W_\kappa}}{\sqrt{\mu_\kappa}}\left(\mathbf{Q}\cdot\boldsymbol{\varepsilon}_{\mathbf{q}\nu\kappa}\right) e^{-i(\mathbf{Q}-\mathbf{q})\cdot\boldsymbol{\tau}_{p\kappa}}\right|^2 \\
&= \frac{m_e^2}{\hbar^4}\left|\sum_{\mathbf{H}}\sum_{\kappa} f_{e,\kappa}(\mathbf{Q}) e^{-W_\kappa} e^{-i\mathbf{Q}\cdot\mathbf{x}_\kappa}\right|^2 \\
&+ \frac{m_e^2}{NN_p^2\hbar^3}\sum_{\mathbf{q}\nu}\frac{n_{\mathbf{q}\nu}+1/2}{\omega_{\mathbf{q}\nu}}\left|\sum_{p\kappa}\frac{f_{e,\kappa}(\mathbf{Q})e^{-W_\kappa}}{\sqrt{\mu_\kappa}}\left(\mathbf{Q}\cdot\boldsymbol{\varepsilon}_{\mathbf{q}\nu\kappa}\right) e^{-i(\mathbf{Q}-\mathbf{q})\cdot\mathbf{R}_p} e^{-i(\mathbf{Q}-\mathbf{q})\cdot\mathbf{x}_\kappa}\right|^2
\end{aligned}
\tag{5.8}
$$

where Lemma 2.2 simplified the first term in this expression. To simplify the sum over momenta $\mathbf{q}$, we recognize that for a given scattering vector $\mathbf{Q}$, there will be a Bragg peak (reciprocal lattice point) closest to $\mathbf{Q}$ s. t. the scattering vector can be expressed $\mathbf{Q} = \mathbf{H}_\mathbf{Q} + \mathbf{q}_0$, where $\mathbf{q}_0$ is a phonon momentum lying within the first BZ, see Figure 2.1. Noting that eigendisplacements are periodic throughout the reciprocal lattice[3], we can use Lemma 2.3 and Eq. (2.9b) to arrive at expressions for the diffraction intensities. The first term of Eq. (5.8) yields the elastic *Bragg* scattering:

$$
I_0(\mathbf{Q}) = \frac{m_e^2}{r^2\hbar^4}\left|\sum_{\mathbf{H}}\sum_{\kappa} f_{e,\kappa}(\mathbf{Q}) e^{-W_\kappa} e^{-i\mathbf{Q}\cdot\mathbf{x}_\kappa}\delta(\mathbf{Q}-\mathbf{H})\right|^2 \tag{5.9}
$$

We note that this is equivalent to our previous result, except with the addition of the Debye-Waller term taking into account suppression of Bragg peak intensities owing to changes in atomic mean-squared displacement (MSD) resulting from, for example, finite temperature. The second term of Eq. (5.8) yields the inelastic single-phonon *diffuse* scattering:

[3] Namely, $\boldsymbol{\varepsilon}_{\mathbf{q}_0\nu\kappa} e^{-i\mathbf{H}_\mathbf{Q}\cdot\mathbf{x}_\kappa} = \boldsymbol{\varepsilon}_{(\mathbf{q}_0-\mathbf{H}_\mathbf{Q})\nu\kappa} = \boldsymbol{\varepsilon}_{\mathbf{q}_0\nu}$, which effectively removes the phase in Eq. (5.8).

$$I_1(\mathbf{Q}) = \frac{m_e^2}{r^2 N_p \hbar^3} \sum_\nu \frac{n_{\mathbf{q}\nu} + 1/2}{\omega_{\mathbf{q}\nu}} \left| \sum_\kappa \frac{f_{e,\kappa}(\mathbf{Q}) e^{-W_\kappa}}{\sqrt{\mu_\kappa}} \left(\mathbf{Q} \cdot \boldsymbol{\varepsilon}_{\mathbf{q}\nu\kappa}\right) \right|^2 = I_e \sum_\nu \frac{n_{\mathbf{q}\nu} + 1/2}{\omega_{\mathbf{q}\nu}} |\mathfrak{F}_{1\nu}(\mathbf{Q})|^2 \tag{5.10}$$

where $\mathfrak{F}_{1\nu}(\mathbf{Q})$ are known as the *one-phonon structure factor*, named to emphasize the difference between the static structure factor in Eq. (2.9a). The $\mathfrak{F}_{1\nu}$ are geometrical weights that describe the relative strength of scattering from different phonon modes and depend sensitively on the atomic polarization vectors $\{\boldsymbol{\varepsilon}_{\mathbf{q}\nu\kappa}\}$ [63]. Most importantly, $\mathfrak{F}_{1\nu}(\mathbf{Q})$ are relatively large when the phonon mode ν is polarized parallel to the reduced scattering vector $\mathbf{q}$. These phonon scattering selection rules mean that $\mathfrak{F}_{1\nu}$ for the out-of-plane (Z-polarized) modes are very weak in the geometry of these experiments[4]. The amplitude of the diffuse scattering, excluding these geometric weights, indicates that higher occupation of modes results in increased vibrational amplitude as the displacement of atoms is linear in phonon occupancy. Likewise, renormalized vibrational frequency reduces the restoring force of the harmonic oscillator and increases the vibrational amplitude.

The key introductions made by moving to a second quantization scheme have been (i) the Debye-Waller factors, allowing us to now relate transient changes in atomic MSD to Bragg peak intensities, as well as (ii) the first order inelastic scattering that allows for direct observation of increase or suppression of phonon occupancy at arbitrary momentum. Further chapters of this thesis further explore the diffuse scattering in-depth, and discuss avenues through which we can further exploit the one-phonon structure factors, such as extracting energy resolution.

[4] These experiments normally probe layered materials along the stacking axis (in [001] for $\hat{\mathbf{z}}$ the stacking axis).

5.2 EXACT EVALUATION OF ENSEMBLE AVERAGES

The limitation with the previous approach is that it would rely on manual calculation of various commutators and formulae for every order of phonon scattering, which is already untenable by the second order. Many samples will have dominant multi-phonon scattering effects. To this point, now armed with $n_{\mathbf{q}\nu}(\tau)$ from our dynamic theory calculations, we can begin to compute the dynamical structure factor of photoexcited materials using a different approach. Newfound techniques of Zacharias *et al* [64] can be used for inexpensive computation of the diffraction intensity to all orders. The total scattering intensity $I(\mathbf{Q};T)$ for a given lattice temperature T can be evaluated using the Laval-Born-James (LBJ) theory [65, 66, 67]. Iteratively evaluating the LBJ formula for the simulated TDBE phonon occupations at a given time delay yields time-resolved diffuse scattering intensities resulting from all scatterers of the probing electron bunch. These sequential simulations in turn allow direct comparison of the UEDS measurements to first principles results. The critical difference in the following *ab-initio* approach from the previous expression of the diffraction intensity given in Eq. (5.8) is a more robust treatment of the thermal averages $e^{\langle(\mathbf{Q}\cdot\hat{\mathbf{u}}_\kappa)(\mathbf{Q}\cdot\hat{\mathbf{u}}_{\kappa'})\rangle}$ in Eq. (5.6). We have hitherto approximated this expression up to zeroth and first order, but we now develop a formalism to exactly compute these correlations in a way that allows for immediate identification of all order inelastic scattering contributions to the diffraction intensity.

In what is known as the Born-Huang expansion [68], we can determine the intensity of a wave scattered by the crystal [69] as:

$$I_{\alpha n,\beta m}(\mathbf{Q}) = \left| \left\langle \chi_{\alpha n} \left| \sum_{p\kappa} f_\kappa(\mathbf{Q}) e^{i\mathbf{Q}\cdot[\boldsymbol{\tau}_{p\kappa}+\Delta\boldsymbol{\tau}_{p\kappa}]} \right| \chi_{\beta m} \right\rangle \right|^2 \quad . \tag{5.11}$$

Here, $\langle\chi_{\alpha n}|, |\chi_{\beta m}\rangle$ are the initial and final vibrational eigenstates of modes m, n, for a given initial and final electronic states α, β. We now make the Born-Oppenheimer approximation to place electrons in their ground-state for the evaluation of the vibrational modes, i. e. $\alpha = \beta = 0 \implies |\chi_{0n}\rangle \triangleq |\chi_n\rangle$, to obtain the adiabatic scattering intensity in

the electronic ground-state:

$$I_n(\mathbf{Q}) = \left\langle \chi_n \left| I^{\{\tau\}}(\mathbf{Q}) \right| \chi_n \right\rangle \tag{5.12a}$$

$$I^{\{\tau\}}(\mathbf{Q}) = \left| \sum_{p\kappa} f_\kappa(\mathbf{Q}) e^{i\mathbf{Q}\cdot[\boldsymbol{\tau}_{p\kappa}+\Delta\boldsymbol{\tau}_{p\kappa}]} \right|^2 \quad . \tag{5.12b}$$

Here, Eq. (5.12b) is the scattering intensity resulting from an *instantaneous* atomic configuration $\{\boldsymbol{\tau}_{p\kappa}\}$. We can now take the ensemble average over these instantaneous nuclear configurations at finite temperature using the canonical partition function $Z = \sum_n \exp\{-E_n/k_BT\}$, yielding the desired scattering intensity:

$$I(\mathbf{Q}, T) = \frac{1}{Z} \sum_n \exp\{-E_n/k_BT\} I_n(\mathbf{Q}) \quad . \tag{5.13}$$

In order to evaluate this thermal average, we move to the normal mode phonon formalism, where the atomic displacements can be written in terms of the phonon eigendisplacements.

$$\Delta\boldsymbol{\tau}_{p\kappa} = \left(\frac{\mu_0}{N_p \mu_\kappa}\right)^{1/2} \sum_{\mathbf{q}\nu} e^{i\mathbf{q}\cdot\mathbf{R}_p} \boldsymbol{\varepsilon}_{\mathbf{q}\nu\kappa} z_{\mathbf{q}\nu} \tag{5.14}$$

with $z_{\mathbf{q}\nu}$ the complex normal coordinates [70]. We can now express the nuclear wavefunction $|\chi_n\rangle$ as a Hartree product of uncoupled harmonic oscillators and the nuclear energies E_n as a sum on the corresponding quasiparticle energy quanta. It can be shown, via the use of Hermite polynomials and Mehler's sum rule [71, 72, 73], that the LBJ scattering intensity can be written in the following integral formulation

$$I(\mathbf{Q}, T) = \left\langle I^{\{\tau\}}(\mathbf{Q}) \right\rangle = \prod_{\mathbf{q}\nu} \int \frac{dz_{\mathbf{q}\nu}}{\pi u^2_{\mathbf{q}\nu}} e^{-|z_{\mathbf{q}\nu}|^2/u^2_{\mathbf{q}\nu}} I^{\{\tau\}}(\mathbf{Q}) \tag{5.15}$$

with $u^2_{\mathbf{q}\nu} = \frac{\hbar}{2M_0\omega_{\mathbf{q}\nu}}[2n_{\mathbf{q}\nu}(T)+1]$ being the atomic MSD. Using the Bloch identity $\langle e^{i\mathbf{Q}\cdot\Delta\boldsymbol{\tau}_{p\kappa}}\rangle = e^{-\frac{1}{2}\langle(\mathbf{Q}\cdot\Delta\boldsymbol{\tau}_{p\kappa})^2\rangle}$, Eq. (5.14), and the ensemble average of the normal coordinates $\langle z_{\mathbf{q}\nu} z^*_{\mathbf{q}'\nu'}\rangle = u^2_{\mathbf{q}\nu}\delta_{\mathbf{q}\mathbf{q}'}\delta_{\nu\nu'}$, it can be shown [74] that the phonon-induced scattering intensity that results from all phonon scattering processes for a temperature T can be written as:

$$I_{\text{all}}(\mathbf{Q},T) = N_p \sum_{p}^{N_p} \sum_{\kappa\kappa'} f_\kappa(\mathbf{Q}) f^*_{\kappa'}(\mathbf{Q}) e^{i\mathbf{Q}\cdot[\mathbf{R}_p+\mathbf{x}_\kappa-\mathbf{x}_{\kappa'}]} e^{-W_\kappa(\mathbf{Q},T)} e^{-W_{\kappa'}(\mathbf{Q},T)} e^{P_{p,\kappa\kappa'}(\mathbf{Q},T)} \tag{5.16}$$

The exponent of the Debye-Waller factor is defined as:

$$-W_\kappa(\mathbf{Q},T) = -\frac{\mu_0}{N_p \mu_\kappa} \sum_{\mathbf{q}\in\mathcal{B},\nu} |\mathbf{Q}\cdot\boldsymbol{\varepsilon}_{\mathbf{q}\nu\kappa}|^2 u^2_{\mathbf{q}\nu} - \frac{\mu_0}{2N_p \mu_\kappa} \sum_{\mathbf{q}\in\mathcal{A},\nu} |\mathbf{Q}\cdot\boldsymbol{\varepsilon}_{\mathbf{q}\nu\kappa}|^2 u^2_{\mathbf{q}\nu} \tag{5.17}$$

where $\mathcal{A}$ ($\mathcal{B}$) denote the sets of phonons that are (not) related by time-inversion. The exponent of the *phononic* factor is defined as:

$$\begin{aligned} P_{p,\kappa\kappa'}(\mathbf{Q},T) = {} & \frac{2\mu_0 N_P^{-1}}{\sqrt{\mu_\kappa \mu_{\kappa'}}} \sum_{\mathbf{q}\in\mathcal{B},\nu} u^2_{\mathbf{q}\nu} \Re\left\{ (\mathbf{Q}\cdot\boldsymbol{\varepsilon}_{\mathbf{q}\nu\kappa})(\mathbf{Q}\cdot\boldsymbol{\varepsilon}^*_{\mathbf{q}\nu\kappa'}) e^{i\mathbf{q}\cdot\mathbf{R}_p} \right\} \\ & + \frac{\mu_0 N_P^{-1}}{\sqrt{\mu_\kappa \mu_{\kappa'}}} \sum_{\mathbf{q}\in\mathcal{A},\nu} u^2_{\mathbf{q}\nu} (\mathbf{Q}\cdot\boldsymbol{\varepsilon}_{\mathbf{q}\nu\kappa})(\mathbf{Q}\cdot\boldsymbol{\varepsilon}_{\mathbf{q}\nu\kappa'}) \cos(\mathbf{q}\cdot\mathbf{R}_p) \quad . \end{aligned} \tag{5.18}$$

Note that the dynamic phonon occupations of the TDBE appear in both the Debye-Waller and phononic factors via the computed MSD. Formulae for Bragg scattering, one-phonon, and multi-phonon contributions to the scattering intensity correspond to the zeroth-order, first-order, and all higher order terms of the Taylor expansion of the phononic factor, exactly corresponding to our truncation of the thermal average in Eq. (5.6) to order $\mathcal{O}(|\hat{\mathbf{u}}_\kappa|^2|\hat{\mathbf{u}}_{\kappa'}|^2)$, etc. For Bragg and one-phonon terms, noting Lemma 2.2 and that $I_0(\mathbf{H},T) = I_0(-\mathbf{H},T)$, the zeroth and first order terms can be written explicitly.

$$\begin{aligned} I_0(\mathbf{Q},T) = {} & N_p^2 \sum_{\kappa\kappa'} f_\kappa(\mathbf{Q}) f^*_{\kappa'}(\mathbf{Q}) \cos\{\mathbf{Q}\cdot(\mathbf{x}_\kappa - \mathbf{x}_{\kappa'})\} \\ & \times e^{-W_\kappa(\mathbf{Q},T)} e^{-W_{\kappa'}(\mathbf{Q},T)} \delta(\mathbf{Q}-\mathbf{H}) \end{aligned} \tag{5.19}$$

$$\begin{aligned} I_1(\mathbf{Q},T) = {} & N_p \sum_{\kappa\kappa'} f_\kappa(\mathbf{Q}) f^*_{\kappa'}(\mathbf{Q}) \frac{e^{-W_\kappa(\mathbf{Q},T)} e^{-W_{\kappa'}(\mathbf{Q},T)}}{\sqrt{\mu_\kappa \mu_{\kappa'}}} \\ & \times \sum_\nu \Re\{\mathbf{Q}\cdot\boldsymbol{\varepsilon}_{\mathbf{Q}\nu\kappa} \mathbf{Q}\cdot\boldsymbol{\varepsilon}^{\kappa'*}_{\mathbf{Q}\nu} e^{i\mathbf{Q}\cdot[\mathbf{x}_{\kappa'}-\mathbf{x}_\kappa]}\} u^2_{\mathbf{Q}\nu} \end{aligned} \tag{5.20}$$

Note 5.1

The fine grids of these calculations are computationally inexpensive since they do not involve extra *ab-initio* steps, and so these calculations act as a post-processing step. The expense is in computing the interatomic force constants, where the method of generation is not constrained in this framework.

It is clear that Eq. (5.19) agrees with the previous formulation of Bragg scattering of Eq. (5.9) by decomposing the repeated sum into a modulus, with the phase factor not impacting the magnitude of the scattering. For the diffuse scattering, recalling $u^2_{\mathbf{q}\nu} = \frac{\hbar}{2M_0\omega_{\mathbf{q}\nu}}[2n_{\mathbf{q}\nu}(T)+1]$, we can readily rewrite Eq. (5.20) to see that the LBJ theory recreates our previous result for the diffuse scattering in Eq. (5.10). By supplying the time- and momentum-resolved temperatures computed with the TDBE, we can now determine $I(\mathbf{Q},\tau)$, and provide direct comparison with experimental signals.

5.3 SPECIAL DISPLACEMENT METHOD

While exact, the evaluation of the William-Lax thermal average limits the theory to the case of infinite lattices, removing any possibility of scattering from crystal defects, or other localized finite effects such as polarons. A finite lattice theory which allows for the evaluation of William-Lax thermal averages of the functional form in Eq. (5.15) was developed only recently in 2020: the special displacement method (SDM) [71, 75] . The SDM corresponds to determining the collection of scatterers (namely, displacements of which atoms in which unit cells) that best recreate the thermal diffuse scattering in the material. It can be shown [71] that such atomic displacements are of the form:

$$\Delta\boldsymbol{\tau}^{\mathrm{ZG}}_{p\kappa} \triangleq \sqrt{\frac{\mu_0}{N_p\mu_\kappa}}\left[\sum_{\mathbf{q}\in\mathcal{B},\nu} S_{\mathbf{q}\nu}u_{\mathbf{q}\nu}2\Re\{e^{i\mathbf{q}\cdot\mathbf{R}_p}\boldsymbol{\varepsilon}_{\mathbf{q}\nu\kappa}\} + \sum_{\mathbf{q}\in\mathcal{A},\nu} S_{\mathbf{q}\nu}u_{\mathbf{q}\nu}\cos\{\mathbf{q}\cdot\mathbf{R}_p\}\boldsymbol{\varepsilon}_{\mathbf{q}\nu\kappa}\right] \quad . \tag{5.21}$$

Here, we have set $|z_{\mathbf{q}\nu}| = u_{\mathbf{q}\nu}$, and allocated signs $S_{\mathbf{q}\nu}$ of these normal coordinates. To determine these signs, namely the weights of each scatterer, practical calcuations follow

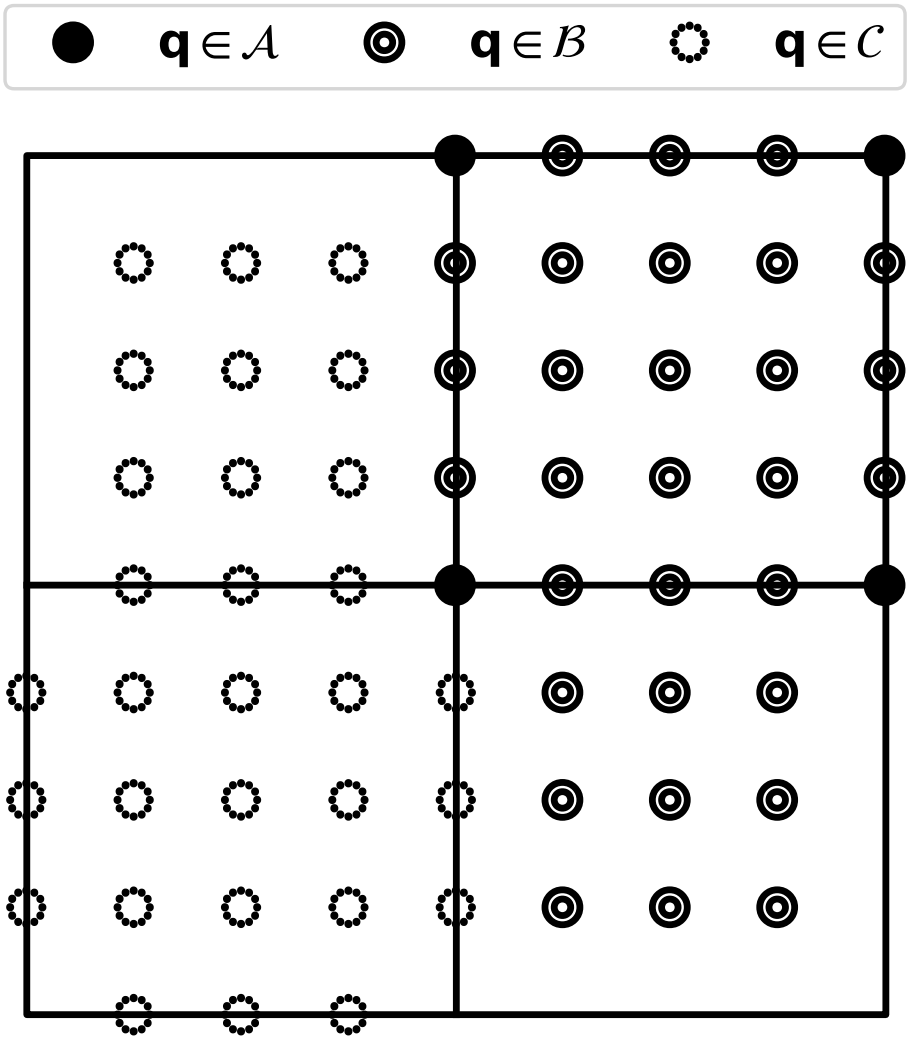

FIGURE 5.2: Illustration of a partitioning of a reducible BZ on an 8×8 Γ-centered grid of a square reciprocal space lattice. Here, $\mathcal{A}$ and $\mathcal{B}$ are as in Eq. (5.17), and $\mathcal{C}$ is the set of momenta of opposite sign as $\mathcal{B}$.

Algorithm 3. To recreate the diffuse scattering intensity, we need only add these ZG displacements to those found in Eq. (5.12b):

$$I_{\mathrm{ZG}}(\mathbf{Q};T) = \left| \sum_{p\kappa} f_\kappa(\mathbf{Q}) e^{i\mathbf{Q}\cdot[\mathbf{R}_p+\boldsymbol{\tau}_\kappa+\Delta\boldsymbol{\tau}^{\mathrm{ZG}}_{p\kappa}]} \right|^2 \tag{5.22}$$

The energy cost associated with only assigning a finite number of scatterers to the lattice

Algorithm 3 Determination of signs of $\Delta\boldsymbol{\tau}^{\mathrm{ZG}}_{p\kappa}$

Precondition:
phonon frequencies $\omega_{\mathbf{q}\nu}$ and eigendisplacements $\boldsymbol{\varepsilon}_{\mathbf{q}\nu\kappa}$,
Postcondition: Signs of ZG scatterers $S_{\mathbf{q}\nu}$

function ZG ENERGY MINIMIZATION($\omega_{\mathbf{q}\nu}$, $\boldsymbol{\varepsilon}^{\kappa}_{\mathbf{q}\nu}$)
  Fourier interpolate phonon properties to same $\mathbf{q}$-grid as the Debye-Waller and phononic factors
  Organize the phonon frequencies and eigendisplacements along simple space-filling curve through all $\mathbf{q}$ points
  Enforce smooth Berry connection between eigendisplacements at adjacent $\mathbf{q}$-points
  Instantiate $2^{\nu_{\max}-1}$ unique combinations of signs to every $2^{\nu_{\max}-1}$ $\mathbf{q}$-point
  for `idt` $\in N_{\mathrm{iter}}$ **do** ▷ Iterate over each atom
    Compute ZG energy of the system
    if $E^{\mathrm{ZG}}_{\mathtt{idt}} - E^{\mathrm{ZG}}_{\mathtt{idt}-1} < \Delta E_{\mathrm{tol}}$ **then return** $\omega_{\mathbf{q}\nu}, \boldsymbol{\varepsilon}_{\mathbf{q}\nu\kappa}$
    else
      Update $S_{\mathbf{q}\nu}$

must be minimized in the choice of signs, given by:

$$E^{\mathrm{ZG}}(\{S_{\mathbf{q}\nu}\}, T) = \sum_{\kappa'\alpha',\kappa\alpha} \Bigg| \sum_{\mathbf{q}\in\mathcal{B},\nu<\nu'} \Re\{(\boldsymbol{\varepsilon}_{\mathbf{q}\nu\kappa})^{\alpha}(\boldsymbol{\varepsilon}_{\mathbf{q}'\nu'\kappa'})^{\alpha'}\} u_{\mathbf{q}\nu} u_{\mathbf{q}\nu'} S_{\mathbf{q}\nu} S_{\mathbf{q}\nu'} + \sum_{\mathbf{q}\in\mathcal{A},\nu<\nu'} (\boldsymbol{\varepsilon}_{\mathbf{q}\nu\kappa})^{\alpha}(\boldsymbol{\varepsilon}_{\mathbf{q}'\nu'\kappa'})^{\alpha'} u_{\mathbf{q}\nu} u_{\mathbf{q}\nu'} S_{\mathbf{q}\nu} S_{\mathbf{q}\nu'} \Bigg|^2 . \tag{5.23}$$

Minimization of this energy ensures that nonperturbative error is eliminated and the anisotropic MSD tensor of Eq. (5.24) is recovered, the diagonal elements from which determine the Debye-Waller factors.

$$U^{\kappa}_{\alpha\alpha'}(T) = \frac{2\mu_0}{N_p \mu_\kappa} \sum_{\mathbf{q}\in\mathcal{B},\nu} \Re\{(\boldsymbol{\varepsilon}_{\mathbf{q}\nu\kappa})(\boldsymbol{\varepsilon}^{*}_{\mathbf{q}\nu\kappa})^{\alpha'}\} u^2_{\mathbf{q}\nu} + \frac{\mu_0}{N_0 \mu_\kappa} \sum_{\mathbf{q}\in\mathcal{A},\nu} (\boldsymbol{\varepsilon}_{\mathbf{q}\nu\kappa})^{\alpha}(\boldsymbol{\varepsilon}_{\mathbf{q}\nu\kappa})^{\alpha'} . \tag{5.24}$$

One can show [75] that the terms involving $\mathbf{q} \in \mathcal{A}$ identically will vanish in the limit of dense Brillouin zone sampling, leaving only contributions from phonon wavevectors not related by inversion (modulo a reciprocal lattice vector). Such partitioning of phonon momenta in the BZ is illustrated in Figure 5.2.

While seemingly tedious to describe various theories of transient ultrafast scattering, it is necessary to illustrate the ideas needed to explain experimental signatures in the

materials considered in this thesis. The next section shows the experimental validation of the exact theory on a 2D material, demonstrating the robustness of the approach even in a system with pronounced quantum effects, such as dielectric and Coulomb screening, excitons, and more. Subsequent chapters expand the theory to incorporate spin- and valley-tronic effects. Finally, scattering from finite (localized) defects, as well as the impact of anharmonicity on diffuse scattering signatures, is integrated into these formalisms.

Part III

TWO-DIMENSIONAL TRANSITION METAL DICHALCOGENIDES

6

The hexagonal miracle

"Hexagons are the bestagons."
—CGP Grey

Obviously existing in three spatial dimensions, most materials and their properties are dependent on each of these dimensions. However, we can create and quantify other systems where the physical size and/or material properties are functions of a reduced number of dimensions. By removing one spatial dimension, we can convert a bulk (3D) material into a two dimensional (2D) material. The first example of an isolated 2D material was graphene, a perfectly hexagonal arrangement of carbon atoms, in 2004 [76]. Since then, many other bulk systems have had nanosheets synthesized from them [77]. We can further reduce the dimensionality and create nanotubes (nanowires) that only have material properties varying along a single spatial dimension (1D). In the most extreme case, we can create nanometer-scale semiconductor particles quantum confined in colloidal suspensions that behave as zero-dimensional (0D) systems called *quantum dots*, first theorized in 1982, and first realised by Louis Brus in 1983 [78], an achievement for which he earned the 2023 Nobel Prize in Chemistry.

While nanotubes and quantum dots have experimentally promising industrial applications, 2D materials have yet to be fully taken advantage of, as the material properties of

strictly two dimensions have been complicated to untangle and thus exploit. Whilst many atomic configurations of bulk materials can yield 2D sheets [79, 80, 81], 2D transition metal dichalcogenides (TMDs) are currently the subject of intense research. These are materials whose atomic configuration is MX_2, where M is a transition metal, and X is a chalcogenide. In bulk, these materials have an indirect band gap transition, but in the monolayer (1L), the transition is direct and in the visible range, yielding exciting electronic and optoelectronic properties.

In general, there are a few key properties of 2D materials that have motivated their exploration.

- VAN DER WAALS INTERACTIONS

Bulk TMDs are known as *van der Waals (vdW)* materials, 2D layers that are weakly bound together by van der Waals interactions. In the bulk, these weak interactions cause low tensile strength owing to the little force required to break these structural bonds. Conversely in the monolayer, only strong covalent bonds are present, making the engineering of 2D Coulomb materials more promising than that of a materials' bulk counterpart. The breaking of vdW forces in graphite means, for example, that graphene has a tensile strength $1000\times$ greater than graphite [82].

- SURFACE AREA-TO-VOLUME RATIO

Owing to the increased surface area of 2D materials, they are much more susceptible to environmental conditions than their bulk counterparts. Thermal transport, electron-lattice coupling, and many other properties are readily influenced by changes in dielectric environment, external electric fields, and others [83, 84].

- IN-PLANE CONFINEMENT

In addition to the creation of a visible-range direct bandgap transition, the transformation from bulk to monolayer in TMDs also creates more strongly-bound excitons, due

to the increased Coulomb interaction from the reduction of electron-hole screening [85]. Both of these properties can be attributed to the lack of spatial inversion symmetry (see Figure 6.1) the monolayer exhibits compared to the bulk [86], and can be tuned depending on the number of layers present in the sample. Furthermore, combinations of monolayers into heterostructures can create exotic optical, electronic, and vibrational properties not found in the constituent materials, such as Moiré excitons [87].

- PHOTOVOLTAICS

  Most TMDs, black phosphorous, and other 2D materials have bandgaps in the visible to near infrared with impressive absorption capabilites such as absorbing as much light in 1 layer of TMD as 100nm of silicon [88]. While insufficient to replace tradition high-efficiency photovoltaics, modifications into heterostructures have allowed monolayer TMDs to achieve as high as 10^8 A/W of optical sensitivity [89, 90]. Furthermore, since the bandgap and work function of these materials can be tuned [85], 2D TMDs find applications as the electron transporting layer (ETL) or hole transporting layer (HTL) for organic and pervoskite solar cells [91]. Whilst promising tunable electronic properties of 2D materials have been put forth, there is much reconsiliation to be done between the 2D materials community and the conventional solar cell community, such as the tradeoff between the increase in conductivity of graphene ETLs/HTLs with the number of layers and the corresponding reduction in transparency that is needed for low series and shunt resistances (and thus efficient solar cells) [92].

- ARTIFICIAL HETEROSTRUCTURES

  With the advent of monolayer materials, we can stack various layers of potentially contrasting materials to create artificially hetero-structured vdW materials that exhibit exotic properties. By stacking two sheets of graphene at specific twist angles (relative to the local hexagonal symmetry), researchers have been able to find "magic angles" s. t. the heterostructure is insulating (blocking all electron flow), or exhibits unconventional

superconductivity [93]. Phononic mechanisms in such systems can also be tunably renormalised by varying the same twist angle [94]. Furthermore, electronic band structures, inter-layer excitons, resulting charge carrier scattering mechanisms, and more can be arbitrarily tuned in such systems [95, 96, 97].

▸ Valley- and spintronics

These (opto)electronic properties arise from the highly correlated nature of TMD's spin [98, 99], valley [100, 101], electronic [102], and vibrational [103] degrees of freedom which can vary dramatically with the number of layers, most notably with the breaking of inversion symmmetry in monolayers. In 1L-MoS_2, strong spin-orbit coupling additionally [104] allows for direct control of the spin and valley degrees of freedom [86, 100] and the possibility of exciting chiral phonons [105, 106]. The coupling of monolayers in heterostructures [107], moiré superlattices [87, 108] or to underlying substrates [109] and modified dielectric environments [110] have opened further avenues for wide tunability in properties and control of these correlated phases.

Many effects in these (and other) 2D materials arise specifically from the interplay between electronic and vibrational degrees of freedom, namely EPC. However, unlike their 3D counterparts where EPC is a fundamental property of the materials, EPC should be uniquely sensitive to the environment of a 2D material where the Coulomb potential is known to be poorly screened within the 2D layer [111]. It is this EPC that drives the unique properties of monolayers, and is the focus of most TMD research. Experiments probing the electronic state of TMD monolayers have been developed most, from time-resolved angle-resolved photoemission spectroscopy (trARPES) of the bandgap renormalization in 1L-MoS_2[85], to magnetophotoluminescence measurements of exciton and trion formation [112], and others. There have been less efforts aimed at probing the vibrational system, as the means to do so reliably have been lacking.

Here we show that UED combined with the recently developed technique of UEDS can provide a momentum-resolved picture of the nonequilibrium phonon dynamics that

follow photocarrier generation in monolayer MoS_2. This electron analog of ultrafast diffuse x-ray scattering [113, 114] has previously provided momentum-resolved information on inelastic electron-phonon scattering [62, 115, 116, 117], soft phonon physics [7], and polaron formation [118] in bulk materials. The extension of this technique to monolayers is possible due to advancements in instrumentation and the large enhancement in atomic scattering cross section for electrons compared to x-rays (see Note 2.1.2). This provides access to novel phenomena, including effects of the local dielectric environment on EPC within the monolayer.

6.1 MATERIAL PROPERTIES

1L-$MoS_2$is a single layer of the bulk van der Waals polytype 2 H$-MoS_2$, in which each molybdenum atom is coordinated by sulphur atoms in a trigonal prism geometry that lacks inversion symmetry (see Figure 6.1). The monolayer has a Hermann-Mauguin spacegroup of P$\bar{6}$m2, or D_{3h} Schöenflies symbol, with hexagonal two-dimensional Brillouin zone, and a real-space lattice parameter of 3.16 Å (determined from relaxed self-consistent calculations). The reciprocal space has the following high-symmetry points (in reduced coordinates): $\Gamma : (0, 0, 0)$, $M : (1/2, 0, 0)$, $K : (1/3, 1/3, 0)$.

In its bulk, MoS_2 is a semiconductor with an indirect bandgap that has mainly found use as dry lubricant, owing to its layered structure and low interlayer coefficients of friction. For this same reason, it is also relatively easy to prepare few-layer samples of MoS_2, as the weak interlayer vdW interactions are easily broken under mechanical exfoliation. The first true characterization of a monolayer TMD was made only in 2010 [119], when advancements in materials synthesis allowed for the repeated removal of a controlled number of layers from the bulk mother crystal. There are other "bottom-up" synthesis approaches to produce monolayer TMDs, such as chemical vapour deposition

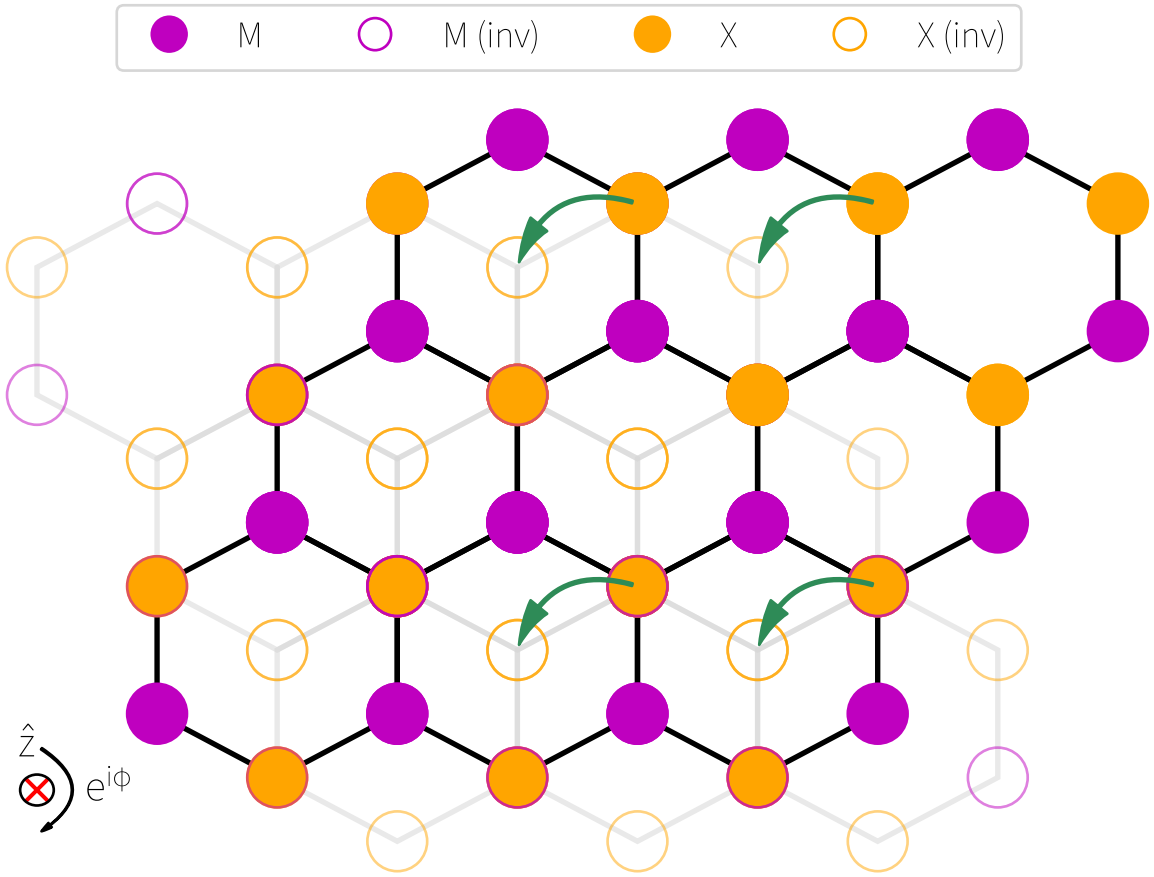

FIGURE 6.1: Illustration of the broken inversion symmetry in the monolayer TMD. The chalcogenide gets mapped to any empty site under inversion about the unit cell center, explitiсly breaking time-inversion symmetry in these materials, affording exotic effects like enhanced spin-orbit coupling, and chiral degrees of freedom in the electronic and vibrational systems.

(CVD)[1] [120, 121], molecular beam epitaxy (MBE)[2] [122, 123, 124], and electrochemical deposition (ED)[3] [125, 126, 127], but the resulting samples feature small in-plane areas, and usually have many compositional and impuriy defects. Further, many parameters will impact the physical qualities of the sample, making this process more complex and expensive than the methods mentioned previously. Its advantage, however, is its large scalability once the recipe for efficient, stable generation of monolayers has been achieved [128]. This is what makes mechanical exfoliation the *de facto* protocol for

[1]This approach relies on the reaction of heated precursor gases (containing the necessary atoms) with the substrate in a furnace, condensing and forming thin layers of the material.
[2]This relies on the epitaxial deposition of crystal by a beam of the target material in UHV.
[3]This relies on covering a plate with cations by means of electric current.

manufacturing of these materials, as it has repeatedly provided many samples with large in-plane areas needed for transmission microscopy.

Note 6.1

The techniques of Liu *et al* were used to generate the 1L-MoS_2sample onto the supporting Si:N substrate [129]. A 150 nm-thick Au film was deposited onto a Si wafer (from Nova Electronic Materials) with e-beam evaporation (0.05 nm/s). Polyvinylpyrrolidone (PVP) solution (from Sigma Aldrich, mw 40000, 10% wt in ethanol/acetonitrile wt 1/1) was spin-coated on the top of the Au film (1500 rpm, acceleration 500 rpm/s, 2 min) and then heated at 150 °C for 5 min. A piece of thermal release tape was used to pick up PVP/Au film and was then gently pressed onto a freshly cleaved bulk MoS_2 single crystal (from HQ graphene). The thermal release tape was gently lifted up and a MoS_2 monolayer is left, attached on the Au. The MoS_2 monolayer was then transferred by pressing the PVP/Au film with MoS_2 monolayer onto a 30 nm thick amorphous silicon nitrite (Si:N) TEM window (Norcada). The thermal release tape was then removed by heating at 130 °C. The PVP layer was removed by dissolving in deionized (DI) water for 2 h. The monolayer covered by Au was rinsed with acetone and cleaned by O_2 plasma for 3 min. After removing the Au cover with a gold etchant solution (2.5g I_2 and 10g KI in 100 mL DI water), the monolayer on substrate was rinsed with DI water and isopropanol, and dried under N_2 flow.

6.2 ELECTRONIC PROPERTIES

There are many rich features to be found in the electronic structure of 1L-MoS_2, informing on the vibrations that can result following photoexcitation in this material. In Figure 6.2 is the in-plane view of the crystal structure, with the corresponding reducible BZ and its high symmetry momenta labelled, followed by the electronic band structure through the

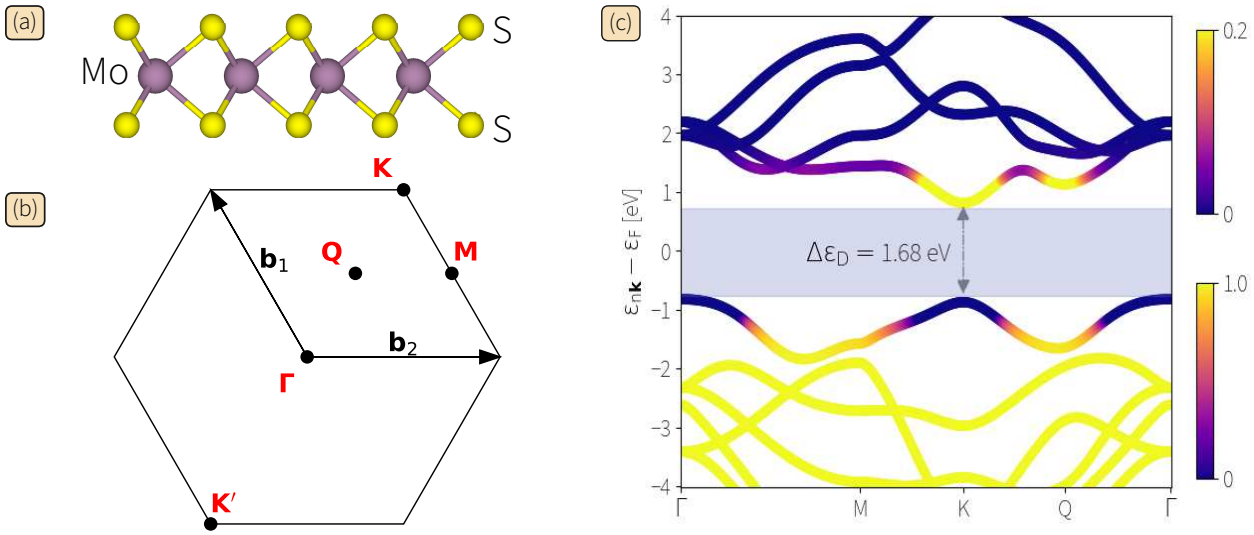

FIGURE 6.2: A synopsis of relevant crystallographic and electronic properties of 1L-MoS_2. (a) The in-plane view of the lattice structure, showing the coordination of chalcogens about the transition metal. (b) The reciprocal lattice structure, with high-symmetry momenta labelled in addition to the reciprocal lattice vectors. (c) Computed electronic band structure, with (distinct) coloration in the valence and conduction manifolds representative of the electron occupation for a chemical potential equivalent to a photo-doped charge carrier density of 10^{14} cm^{-2}.

typical path for hexagonal BZs. The most remarkable property of the material is the transition from an indirect semiconductor to a direct in the monolayer limit, with a direct gap of 1.68 eV. Following ultrafast photoexcitation, this band-gap is renormalized (increase of the valence band maximum) by ~ 100 meV, resulting in the following biexponential behaviour; the inital quick reduction in band-gap results from (i) the poorly screened Coulomb potential and strong many-body interactions within the monolayer, and (ii) the intense Auger recombination in the material [130]. The slow recovery to equilibrium conditions and re-establishment of the band-gap owes to intrinsic (non)radiative decays in the monolayer [131] (although it is worth mentioning how long it takes for radiative carrier recombination [132, 133, 134]).

Note 6.2

The following discussion does not take into consideration spin-orbit coupling (SOC), which is indeed pronounced in this material. The spin-splitting of the bands will be discussed in detail in Chapter 8.

It is clear that the K point contains interesting properties, but it must be noted that there is an additional high symmetry point, namely $Q : (1/6, 1/6, 0)$, that serves as the location in the conduction manifold of the indirect electronic band gap transition, see Figure 6.2c. Electrons (holes) are occupied mainly around K and Q (K and Γ) for an example carrier concentration of $10^{14}\,\mathrm{cm}^{-2}$. It can be shown that the 6-fold degenerate pocket at Q limits electron relaxation and leads to an increase in carriers around this point[52]. This suggests population inversion is possible here, and illustrates pathways through which electrons are excited by the ultrafast laser pulse in a UEDS experiment. With incident photoexcitation at, for example, $400\,\mathrm{nm} \simeq 3.1\,\mathrm{eV}$, electrons are injected into the conduction manifold at Γ from the valence manifold at Γ, from which hot carriers rapidly randomize their momentum to the occupation states given in Figure 6.2c. From here, the high level of symmetry affords many pathways for scattering with the phononic system. A brief qualitative depiction of the available pathways is given in Figure 6.3, where the role of the Q point becomes clear: a satellite valley necessary to completely understand the EPC in this system.

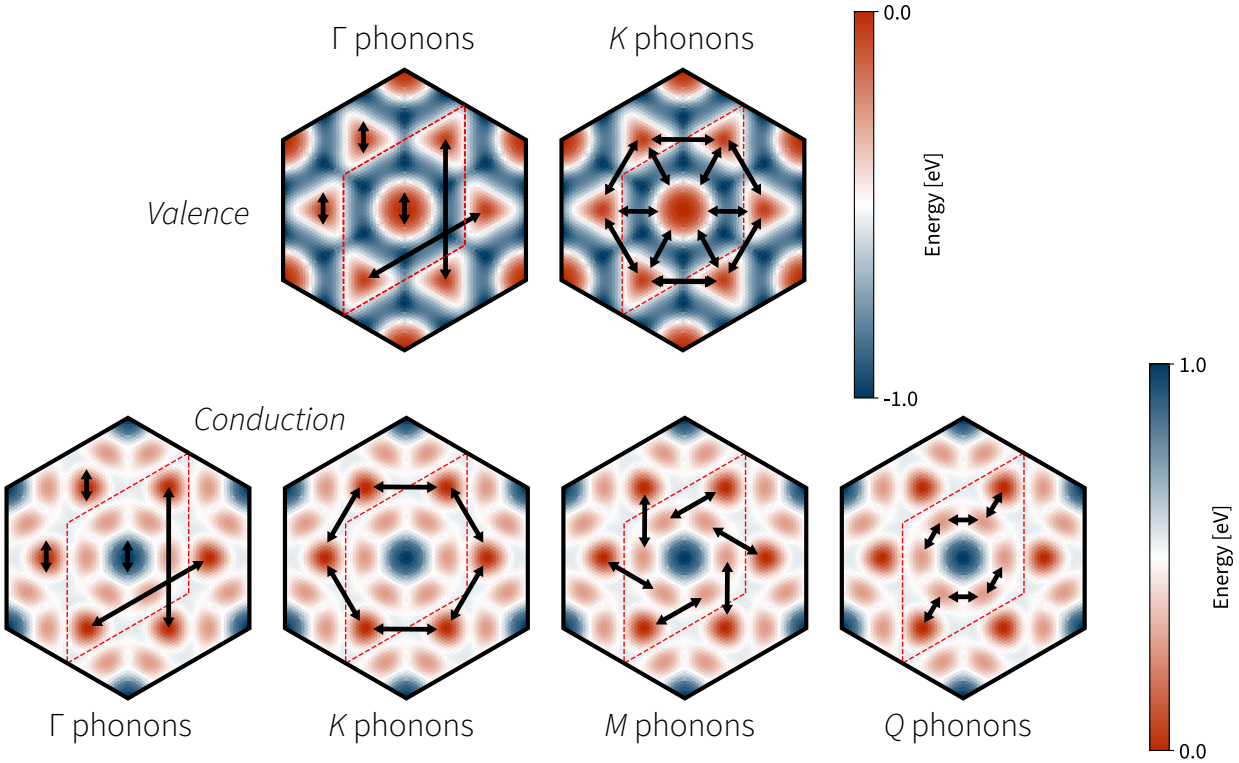

FIGURE 6.3: Available pathways for hot carrier relaxation via phonon scattering, determined by conservation of energy and momenta.

6.3 EXCITONS AND TRIONS

Owing to the poor Coulomb screening at the 2D limit, 1L-MoS_2has (in)direct bright (dark) excitons with some of the largest known binding energies, on the order of $\sim$ 700 meV. The complex structure of these excitons, as well as the many-body extensions of biexcitons and trions, have been mapped extensively before [112], and have illustrated exotic behaviours not found in sibling materials. While the real-space picture of excitons is well established (either in the Wannier or Frenckel pictures), the theory to rigorously decide the impact these quasi-particles have on, for example, the true band-gap of a material, is tedious and detailed. As fully quantum objects, excitons cannot be easily incorporated into the discussed *ab-initio* phonon dynamics simulations of Chapter 4. Such an inclusion would be inconsistent and inaccurate, since the methods used herein, such as the TDBE, are semi-classical, only first order in derivatives with respect to time, and describe only the evolution of statistical distributions. Therefore, to enter into a

regime where the exciton densities subsume the single-body electron (hole) occupations makes the resulting phonon dynamics impossible to determine in the current theoretical framework, a point discussed in more detail in Section 8.3.

To briefly illustrate the complexity of such a description, below in Eq. (6.1) is what is known as the Bethe-Salpeter equation (BSE) [135], giving the four-point reducible polarizability ${}^4\mathcal{L}$ of two-particle interactions (between the hole and the electron), thus containing all the information needed to describe the energy of such a state. We write the Hamiltonian of the corresponding polarizability as:

$$H_{\text{exc}}^{(mn)(m'n')} = \Delta_{\text{GW}}\delta_{mm'}\delta_{nn'} + (f_m - f_n)\langle mn|v - W|m'n'\rangle \rightarrow \{E_\lambda, |A_\lambda\rangle\} \tag{6.1}$$

where Δ_{GW} is the GW band-gap, f_m (f_c) the occupancy of the m^{th} (n^{th}) band, and m (n) the wavefunction of the corresponding state. m (n) is usually taken to be the band that holds the valence manifold maximum (conduction manifold minimum). Its solution produces the eigenenergies E_λ of the resulting excitonic wavefunctions $|A_\lambda\rangle$. The Feynman diagram equivalent of this equation is given in Figure 6.4, illustrating more clearly the role of the v and W interactions found in the BSE.

The inclusion of excitons into a TDBE-like framework is at the cutting-edge of current theory [136], and the complicated exciton-phonon interactions, while calculable [137], are not discussed further here.

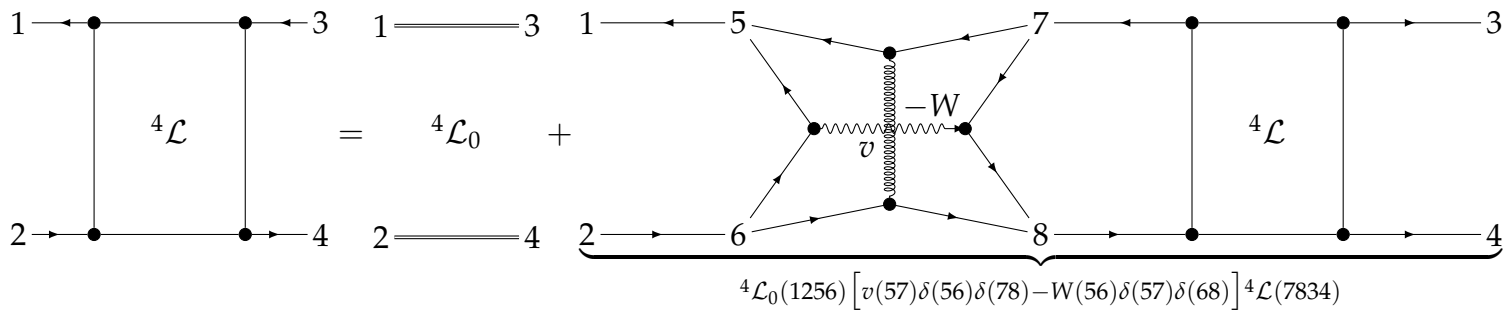

FIGURE 6.4: BSE for excitons. Here, v is the repulsive e-h exchange interaction (dipole-dipole), and $-W$ is the attractive e-h direct interaction (monopole-monopole). For small-gap semiconductions and metals, the excitonic correlation will be screened owing to the reduction in the corresponding v and W interactions. This equation is intrinsically two-particle, and as such, its solution necessitates the determination of the propagation of two particles. The corresponding four-point equation is extremely computationally expensive to solve, although possible [138, 139].

7

Photoexcited MoS_2

"The belief in a single truth is the root cause for all evil in the world."
—Max Born

Owing to the nature of the 2D geometry of a monolayer, the ability to perform transmission electron diffractometry on such a sample is unclear. There are many considerations that can impact the performance of pump-probe spectroscopy that are primarily: (i) the low signal-to-noise ratio (SNR) of diffraction intensities, and (ii) background contributions, either from the installation medium of the sample into the vacuum chamber or from ambient reflected photoexcitation directly illuminating the detector. Both of these affects are more easily dealt with in samples of thicknesses $\gtrsim 30$ nm, owing to the increased probability of electron scattering events in such "thick" samples and increased absorption of the photoexcitation into the total material system.

7.1 BRAGG DYNAMICS

7.1.1 *The use of monolayer in a heterostructure*

Before beginning to examine dynamics of the monolayer following photoexcitation, such sources of noise must be dealt with. Since the electrons scatter off of only ~ 0.7 nm

thick material, the SNR in these monolayer UEDS experiments is the primary limitation and requires that the sample be uniformly illuminated by the full electron beam of the instrument. This requires monolayer samples on the order of 100s μm in width. At these sizes, freestanding monolayer TMD films are unstable, and there are no literature reports to date on freestanding monolayer TMD films of the size (i.e. in-plane area) required. Free-standing TMD or graphene films, however, in the 1-10 μm range have been reported, either on TEM grids [140] or etch holes [141].

This necessitates the use of a supporting silicon nitride (Si_3N_4, abbreviated Si:N) ceramic substrate, a wide-band gap ($\Delta E_g = 5$ eV) ceramic (to avoid absorption of the photoexcitation and thus direct heating) which is largely transparent to the electron beam. Unfortunately, while this substrate is essential to performing these experiments, it contributes $\sim 97\%$ of the diffraction intensity across the image, meaning only $\sim 3\%$ of the electron beam probes the monolayer, which is why SNR optimization is critical.

Fortunately, scattering from the Si:N substrate due to heating shows very weak and diffuse changes. These changes vary smoothly with scattering vector, $\mathbf{Q}$, and do not contribute to observed intensity variations within a single BZ reported here. Clearly, one-photon absorption is not possible with 3.1 eV (400 nm) excitation. Furthermore, the nonlinear absorption coefficient of Si:N under similar excitation conditions is $\gamma_{\text{Si:N}} = 1.75\,\text{m}^{-1}\text{W}^{-1}$, orders of magnitude less than other structures noted for their strong multi-phonon absorption behaviour [142], such as GO-Si structures with $\gamma = 167\,\text{m}^{-1}\,\text{W}^{-1}$. Additionally, the measured two-photon absorption coefficient of Si:N is $\sim 2.9 \cdot 10^{-8}$ cm/GW, which is extremely negligible [143]. We therefore safely ignore two- / multi-phonon absorption in Si:N from our photoexcitation conditions.

Whilst not directly exciting dynamics in the substrate, we may at late times observe changes in the diffuse ring intensity from the Si:N, as heat exchanges from the monolayer to the substrate. The extracted background from the Si:N rings is varying only on the

order of

$$\delta I_{\mathrm{BG}} = \widetilde{I}_{\mathrm{BG}}(\tau = 200\ \mathrm{ps}) - \widetilde{I}_{\mathrm{BG}}(\tau = 10\ \mathrm{ps}) = 0.005\% \tag{7.1}$$

in normalized intensity (integrated over all $|\mathbf{Q}|$), compared to a corresponding $\delta I_{(300)} \simeq 2.5\%$ change in Bragg intensity. Because of $\sim 10^3$ ratio in the difference in heating-induced changes in intensity between the monolayer and the substrate, and the drastically different momentum scales over which this heating of the heterostructure occurs, we approximate the contribution of the substrate to the diffraction pattern as static diffuse rings, namely $I^{\mathrm{sub}}(\mathbf{Q}, \tau) \simeq I^{\mathrm{sub}}(|\mathbf{Q}|)$, see Figure 7.1. This is consistent with our estimation of the change in temperature of the substrate based on the energy of the pump transmitted through the monolayer and the heat capacity of Si:N, about 2.5 °K. Therefore, the substrate contribution to the UEDS pattern can be robustly removed without introducing significant artifacts to the monolayer phonon-diffuse intensity within the individual Brillouin zones that surround each Bragg peak. We have furthermore performed UEDS experiments on Si:N alone under similar photoexcitation conditions and have found no dynamics in the signals reported. This amorphous background subtraction pre-processing step is applied to all diffraction patterns, and allows us to directly determine the dynamics resulting from only changes in the nonequilibrium state of the monolayer. Yet, the presence of the substrate still impacts the behaviour of the monolayer owing to the heterostructure geometry. From the perspective of the monolayer, the substrate is a semi-infinite slab introducing strong dielectric features into the environment, which nontrivially impact our observations.

Note 7.1

The experiments about to be described used a monolayer of MoS_2 mechanically exfoliated onto a 3 mm × 3 mm × 30 nm Si:N substrate with a 200μm×200μm window size. The pump-probe experiment used 400 nm photoexcitation at a fluence of 1.82 mJ·cm^{-2}, with a time resolution of ∼170 fs.

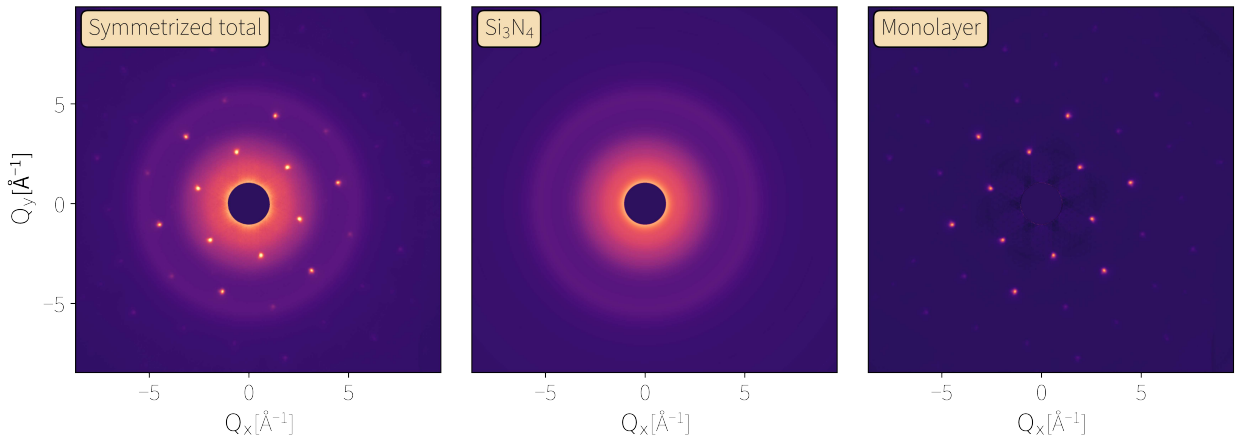

FIGURE 7.1: Comparison of the directly symmetrized data (left), the determined static diffuse background contribution from the Si:N substrate (middle), and the diffraction pattern representative of only monolayer dynamics (right), given by the difference.

7.1.2 *Renormalized Dynamics*

Propagation of the TDBE generates the local phonon occupations that arise from the exchange of energy between the excited hot carriers and the lattice. We emphasize that in these simulations, the influence of screening on the EPC matrix elements is accounted with its full momentum dependence within the MoS_2 monolayer. The approximation introduced in this work, therefore, involves only the substrate-induced screening. In metals, the screening affecting EPC matrix elements is indeed frequency and momentum dependent, and it can be approximated by the Lindhard function as indicated in Eq. (5) of Ref [46]. The situation, however, is different for semiconductors. The dielectric function of large band-gap insulators is a smooth function of momentum, and it therefore is a widely employed approximation to consider the screening of finite-$\mathbf{q}$ perturbation via a momentum and frequency independent dielectric constant. The Si:N substrate is a wide band-gap insulator which, in its crystalline form, has a band gap of $4.6 - 5.2\,\mathrm{eV}$. These considerations are at the basis of the approximation introduced in our work and we do not expect finite-$\mathbf{q}$ coupling to differ significantly from the case examined in our simulations. We can therefore safely approximate the effective dielectric constant of the system as the average permittivities of the semi-infinite slab, and the ambient vacuum

conditions. As the instrument operates in ultra-high vacuum (UHV) conditions ($p < 10^{-8}$ torr), the change in dielectric constant from pure vacuum represents 4 parts in 10,000, and thus yields a negligible contribution to the permittivity used, namely the average of the Si:N permittivity and ambient vacuum permittivity. We readily express this average as:

$$\epsilon_\infty^{\text{sub}} = \frac{1}{2}(\epsilon_\infty + \underbrace{\epsilon^{\text{UHV}}}_{\approx 1}) = \frac{1}{2}(\epsilon_\infty + 1) \tag{7.2}$$

where $\epsilon_\infty = 7.8$ is dielectric constant of bulk Si:N [144, 145]. Depending on the substrate material, the electronic properties of 2D TMDs might be affected significantly. As reported, for example, in Ref. [146], *ab-initio* GW calculations indicate that the quasiparticle band gap and carrier effective masses of 1L-MoS_2can be influenced by the substrate-induced screening. However, as demonstrated in Ref. [147], the electronic structure of MoS_2 remains virtually unchanged when combined with a Si:N substrate. Most importantly, there is no qualitative change in the level alignment of the different valleys involved in phonon-assisted hot-carrier relaxation. Therefore, we do not expect modifications in the electronic band structure of MoS_2 to play an important role in our calculations.

We must consider how the Kohn-Sham potential is affected by changes to the dielectric environment. The first term of the KS potential is the electron-nuclear interaction, which is Coulombic at large distances with nonlinear core corrections applied for small distances, both of which are inversely propertional to the dielectric constant ϵ, and as such are both renormalized by $v \to v/\epsilon_r$. Lastly is the exchange-correlation potential. While this potential is empirical and applied phenomenologically, all XC functionals start in the local density approximation (LDA), where the XC energy is related only to the electron density ρ via $V_{\text{xc}}^{\text{KS}} \propto {}^1/_{\epsilon_0} \int d^3\mathbf{r}\rho^{4/3}(\mathbf{r})$. Higher order approximations include corrections to this, such as the generalized gradient approximation (GGA), including terms $\mathcal{O}(\nabla\rho)$, or metaGGA including $\mathcal{O}\left(\nabla^2\rho\right)$, and so on [148]. All such approximations rely on the electron density renormalized by the dielectric environment, ρ/ϵ. As such, the entire KS potential energy will be renormalized by the relative dielectric constant, made

manifest in a renormalization of the EPC strength via Eq. (3.14) (proven more concretely in Eq. (143) of [46]). We write this normalization explicitly:

$$g^{\nu}_{mn}(\mathbf{k},\mathbf{q}) \to \widetilde{g}^{\nu}_{mn}(\mathbf{k},\mathbf{q}) = g^{\nu}_{mn}(\mathbf{k},\mathbf{q})/\epsilon^{\text{sub}}_{\infty} \tag{7.3}$$

and thus the collision integrals of the TDBE in Eq. (4.16).

▸ ADDITIONAL CONSIDERATIONS

Excitons in 1L-MoS_2 are strongly bound and they are characterized by a binding energy of the order on 1 eV [102]. Owing to the large excitonic energy, any coupling mechanisms simultaneously involving excitons, phonons, and free electrons or holes is forbidden by energy conservation. For example, the energy released by the formation of an exciton can not be transferred to a single phonon, since lattice vibrations in MoS_2 have energies smaller than 60 meV. For these reasons, one can expect the formation or annihilation of excitons to be inconsequential for the non-equilibrium dynamics of the lattice, and so we ignore excitonic interactions in this *ab-initio* scheme. This argument is not in disagreement with the well-known temperature dependence of excitons in 1L-MoS_2 [149], which manifests itself in an increased broadening of the excitonic peak in the absorption spectrum for larger temperatures and suggests a coupling between excitons and phonons. Indeed, in this case, the exciton-phonon interactions is mediated by the electrons, and exciton broadening has been ascribed to the increased broadening of the electronic bands.

7.1.3 *Mean-squared displacements*

We can now begin to examine the dynamics of the monolayer via the UEDS signals. The immediate suppression of the Bragg peak intensities following photoexcitation is mostly always attributed to the transient Debye-Waller effect, where laser light-induced heating increases the effective atomic MSD $\langle u^2 \rangle$. Finite-temperature MSD modulates the

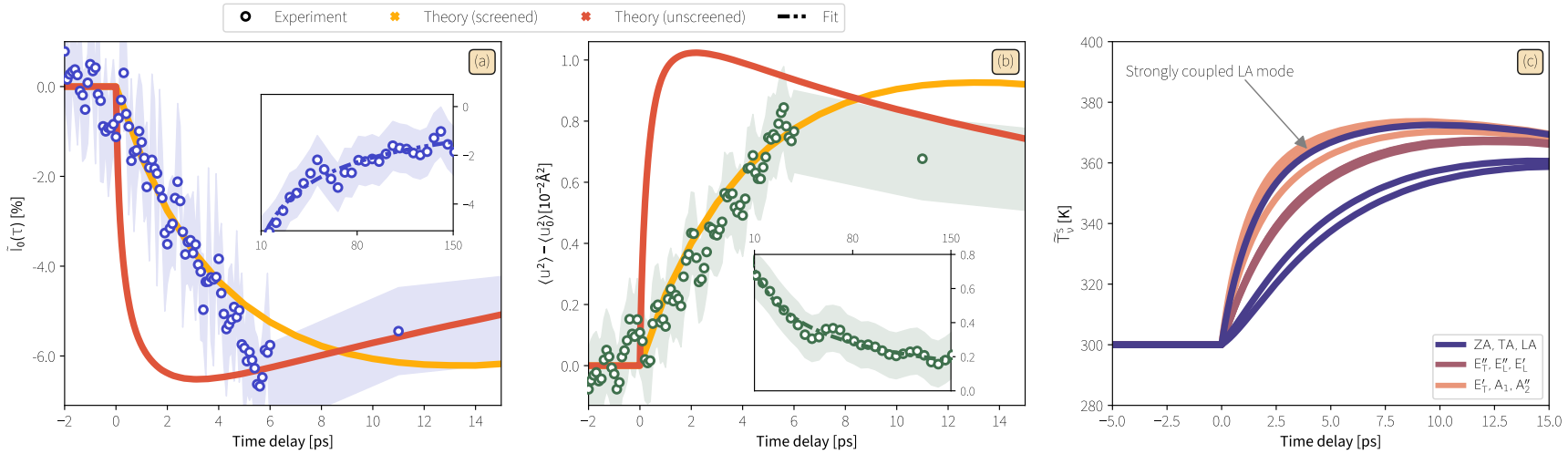

FIGURE 7.2: Photocarrier-phonon equilibration in 1L-MoS_2as measured via Bragg peak Debye-Waller dynamics. (a) Relative change in (300) Bragg peak intensity following photoexcition (blue circles). First-principles calculation of freestanding 1L-MoS2 (red curve) and inclusion of the dielectric environment provided by the Si:N substrate (orange curve). The best fits (dashed lines) are given for long times, described by the 1D heat kernel (see text). The inset highlights the long-term behavior of each signal, and the blue band represents the 1σ uncertainty bound on the data points. (b) Increase in MSD extracted from Bragg intensity by eq 1. Red, orange, and dashed curves are shown as in (a). (c) Average phonon mode temperature (momentum integrated) from ab initio simulations including the Si:N dielectric environment. Reprinted with permission from Ref [84]. Copyright 2022 American Chemical Society.

q	γ_0^{exp}	γ_0^{s}	γ_0^{us}	γ_1^{exp}	γ_1^{s}	γ_1^{us}[ps]
Γ_{300}	3.7 ± 0.1	3.607 ± 0.001	0.61 ± 0.02	52 ± 11	39 ± 2	29 ± 1
K	6.1 ± 0.3	2.472 ± 0.006	0.600 ± 0.001	19.37 ± 0.06	37.6 ± 0.1	29.4 ± 0.4
M	6.1 ± 0.2	4.40 ± 0.04	0.590 ± 0.003	25.20 ± 0.02	37.5 ± 0.1	28.7 ± 0.7
{A}	5.5 ± 0.1	3.567 ± 0.001	0.683 ± 0.004	85.9 ± 0.9	37 ± 1	29 ± 1
{LA}	3.0 ± 0.9	2.92 ± 0.03	0.336 ± 0.007	86.6 ± 0.3	39.8 ± 0.5	28.8 ± 0.3
{TA}	3.83 ± 0.04	3.617 ± 0.004	0.491 ± 0.004	67.6 ± 0.6	40.3 ± 0.7	29.0 ± 0.4

TABLE 7.1: Extracted time constants for all signals described in the main text. The rate of excitation/rise (γ_0) and relaxation/decay (γ_1) are given in ps. Experimental (exp) fits, *ab-initio* results computed both for a free standing film (us) and *ab-initio* results including the Si:N substrate dielectric environment (s).

diffraction intensity from scattering off the ideal lattice according to:

$$I(\mathbf{Q}) = I_0 \exp\left(-\frac{4}{3}\pi^2\langle u^2\rangle \mathbf{Q}^2\right) \quad . \tag{7.4}$$

Inverting this relationship allows for extraction of MSD as:

$$-\frac{3}{4\pi^2}\frac{\ln\left[I(\tau)/I(\tau<\tau_0)\right]}{\mathbf{Q}^2} = \langle u^2\rangle(\tau) - \langle u^2\rangle(\tau<\tau_0) \tag{7.5}$$

where τ_0 is the pump-probe delay time corresponding to exact overlap of pump and probe pulses, and $I(\tau<\tau_0)$ is the average pre-photoexcitation diffraction intensity. We determine an effective relation between the phonon bath in the NLM and MSD [51, 150] as:

$$\langle u^2\rangle(\tau) = \frac{3\hbar}{2M}\int_0^\infty \coth\left(\frac{\hbar\omega}{2k_B T_{\text{eff}}(\tau)}\right)\frac{D_{\text{ph}}(\omega)}{\omega}d\omega \tag{7.6}$$

where $D_{\text{ph}}(\omega)$ is the total phonon DOS. To characterize only the macroscopic behaviour of the lattice, as is needed for the experimental determination of MSD, we require the total DOS, but extensions of Eq. (7.6) into the NLM can easily be made in order to determine phonon mode resolved MSD $\langle u_\nu^2\rangle(\tau)$ corresponding to the specific mode DOS $D_{\text{ph}}^\nu(\omega)$.

The transient rise in MSD provides an average measure of the rate at which photocarrier excitation energy is transferred to phonons in the monolayer, informing on carrier-phonon equilibration through EPC. We compare these measurements directly with the results obtained by combining together *ab-initio* calculations of nonequilibrium

dynamics [52] and scattering intensities [64, 74] in Figure 7.2. The ultrafast dynamics simulations for a free-standing monolayer film are shown in red, predicting a much higher rate of MSD increase than that observed in the experimental data. When the dielectric environment provided by Si:N is included using a semi-infinite slab model with no free parameters, there is quantitative agreement between the rise is MSD measured and that predicted within experimental uncertainties.

The average value of the freestanding matrix elements $g^{\nu}_{mn}(\mathbf{k}, \mathbf{q})$ for the LA and LO (E') phonon modes in free-standing 1L-MoS_2 at K are 19 meV and 23 meV respectively. These are each reduced by a factor of $\epsilon_{\infty}^{\text{sub}} = 4.4$ due to the presence of the Si:N dielectric environment, providing a quantitative explanation for the approximately order-of-magnitude reduction in the rate of photocarrier-phonon energy transfer compared to predictions for a free-standing film (see Table 7.1). The inclusion of the renormalized EPC matrix elements produces quantitative agreement between first-principles and experimental results in both amplitude and rate of change.

The excitation energy has equilibrated between carriers and phonons in 1L-MoS_2 by $\tau \sim 10$ ps, as shown by the peak value of MSD in Figure 7.2b. The roll-over and decay of MSD for $\tau > 10$ ps indicates the reduction in vibrational energy in the monolayer due to phonon transport into the Si:N substrate (Figure 7.2c). The reported rise-time for the MSD following photoexcitation (i.e. the observed Debye-Waller decay of Bragg peak intensities) in the case of 1L-MoS_2 on sapphire is slower than reported here [151, 152], while the opposite is true for 1L-MoS_2 on SiO_2 [153]. This is as expected based on the dielectric constants of these substrate materials, providing additional evidence in support of our conclusions regarding dielectric screening of the electron-phonon interaction in 1L-MoS_2.

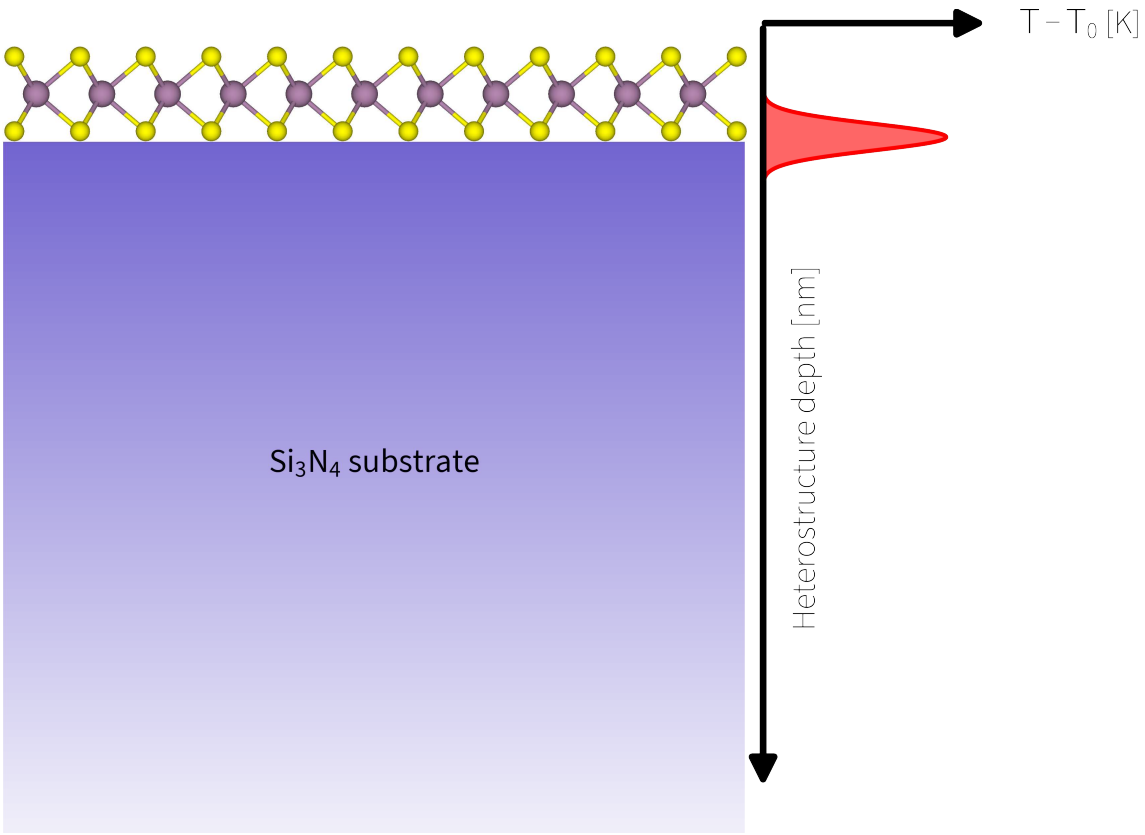

FIGURE 7.3: Schematic of heat transfer model for long times ($\tau > 20$ ps). Instantaneous delivery of heat to the system at $(z, t) = (0, \tau_0)$ induces hot carriers which relax via energy exchange to the lattice. After such time, the rate of heat exchange from the monolayer (lattice at the top) to the substrate (shown in blue below) is modelled by the solution to the 1D heat equation (see text).

7.1.4 *Cooling dynamics*

Since photoexcitation was effectively uniform over the probed 250 μm region ($< 10\%$ variation), thermal transport from the photoexcited monolayer into the Si:N substrate is well described as one-dimensional (1D) on picosecond timescales; a delta-function heat impulse (following photoexcitation of the monolayer) diffuses into the substrate. For later times after the hot carriers have exchanged their free energy to the monolayer lattice, dynamics in the monolayer ι^+ are dominated by the exchange of heat to the substrate, modelled by the 1D heat diffusion equation as follows.

Heat across a bulk system, $u(\mathbf{x}, t)$, can be described in the following partial differential

equation:

$$\partial_t u(\mathbf{x}, t) = D\nabla^2 u(\mathbf{x}, t) \tag{7.7a}$$

$$u(\mathbf{x}, 0) = f(\mathbf{x}) \tag{7.7b}$$

$$\lim_{|\mathbf{x}|\to\infty} u(\mathbf{x}, t) = 0 \; \forall t \tag{7.7c}$$

$$(\mathbf{x}, t) \in \mathbb{R}^n \times [0, \infty) \tag{7.7d}$$

where $f(\mathbf{x})$ is initial heat profile along the bulk, D the diffusion coefficient, and we further assume the ends of the bulk are pinned to a heat sink ($u = 0$). To be able to understand how such a system repsonds to impulse, we define what is known as the two-point[1] *Green's function* $\mathcal{G}(\mathbf{x}, \mathbf{x}'; t, t')$, the definition of which is that the Green's function describes the system response from instantaneous stimulus at one point $(\mathbf{x}, t)$ to another $(\mathbf{x}', t')$.

Definition 8 (Green's Function)**.** For any linear operator $L \triangleq L(\mathbf{x}) : \mathbb{R}^n \to \mathbb{R}^n$, the one-point Green's function $\mathcal{G}(\mathbf{x}, \mathbf{x}')$ is any solution $L\,\mathcal{G}(\mathbf{x}, \mathbf{x}') = \delta(\mathbf{x}' - \mathbf{x})$. This implies directly $\int L\mathcal{G}(\mathbf{x}, \mathbf{x}')f(\mathbf{x}')\,d\mathbf{x}' = \int \delta(\mathbf{x}' - \mathbf{x})f(\mathbf{x}')\,d\mathbf{x}' = f(\mathbf{x})$, and noting that L does not act on the variable of integration, we find $f(\mathbf{x}) = L\big(\int \mathcal{G}(\mathbf{x}, \mathbf{x}')f(\mathbf{x}')\,d\mathbf{x}'\big)$, which means $u(\mathbf{x}) = \int \mathcal{G}(\mathbf{x}, \mathbf{x}')f(\mathbf{x}')\,d\mathbf{x}'$ is a solution to the equation $Lu(\mathbf{x}) = f(\mathbf{x})$.

To determine the Green's function of our model system, we Fourier transform Eq. (7.7) with respect to space:

$$\partial_t \tilde{u}(\mathbf{k}, t) = -D|\mathbf{k}|^2 \tilde{u}(\mathbf{k}, t) \tag{7.8a}$$

$$\tilde{u}(\mathbf{k}, 0) = \tilde{f}(\mathbf{k}) \tag{7.8b}$$

which has the unique solution of $\tilde{u}(\mathbf{k}, t) = \tilde{f}(\mathbf{k})e^{-D|\mathbf{k}|^2 t}$. By the Convolution theorem (a product in Fourier space is a convolution in real-space), we note that:

$$\mathcal{F}^{-1}[e^{-D|\mathbf{k}|^2 t}] = \frac{1}{(4\pi D t)^{3/2}} \exp\left\{-\frac{|\mathbf{x}|^2}{4Dt}\right\} \triangleq S(\mathbf{x}, t) \tag{7.9}$$

[1] This refers only to the fact that we are interested in the stimulated response with respect to two different coordinates, which are, here, space and time.

for $\mathbf{x} \in \mathbb{R}^3$. We can then find the solution to the partial differential equation:

$$u(\mathbf{x},t) = (f * S)(\mathbf{x},t) = \int_{\mathbb{R}^3} f(\mathbf{x}') \underbrace{\frac{1}{(4\pi D t)^{3/2}} \exp\left(-\frac{|\mathbf{x}-\mathbf{x}'|^2}{4Dt}\right)}_{\mathcal{G}(\mathbf{x},\mathbf{x}';t,0)} d^3\mathbf{x}' \tag{7.10}$$

where we have now identified our Green's function $\mathcal{G}(\mathbf{x},\mathbf{x}';t,0)$ for $D \triangleq \kappa/c_p\rho$ the thermal diffusivity, dependent on the thermal conductivity κ, specific heat capacity c_p, and mass density ρ. In the one-dimensional case presented here, this Green's function $\mathcal{G}(z,\tau;0,0) \simeq \mathcal{G}(z,\tau)$ satisfies:

$$\begin{cases} \mathcal{G}_t(z,\tau) - D\mathcal{G}_{zz}(z,\tau) = 0 & \tau \in \mathbb{R} \times (0,\infty) \\ \mathcal{G}(z,0) = \delta(z) & z \in \mathbb{R} \times [0,\infty) \end{cases} \tag{7.11a}$$

$$\mathcal{G}(z,\tau) = \frac{1}{\sqrt{4\pi D\tau}} \exp\left(-\frac{z^2}{4D\tau}\right) \tag{7.11b}$$

Using Neumann boundary conditions and noting that for our ultrafast photoexcitation, $u(z,0) = g(z) \approx \delta(z)$, we find that the dynamics in the monolayer we observe, which lie approximately on the atomic interface at $z = 0$, are given by:

$$\begin{aligned} \iota^+(\tau) &= \int_{\mathbb{R}^+} \mathcal{G}(z-\zeta, \tau-\tau_0^+) g(\zeta)\Big|_{z=0} d\zeta \\ &= \frac{1}{\sqrt{4\pi D(\tau-\tau_0^+)}} \int_0^\infty \left[\exp\left(-\frac{(z-\zeta)^2}{4D(\tau-\tau_0^+)}\right) + \exp\left(-\frac{(z+\zeta)^2}{4D(\tau-\tau_0^+)}\right)\right]\Big|_{z=0} g(\zeta) d\zeta \\ &= \frac{2}{\sqrt{4\pi D(\tau-\tau_0^+)}} \exp\left(-\frac{z^2}{4D(\tau-\tau_0^+)}\right)\Big|_{z=0} \\ &\longrightarrow \left[\frac{A_1}{\sqrt{4\pi\kappa(\tau-\tau_0^+)}} + B_1\right] \end{aligned} \tag{7.12}$$

where τ_0^+ is the time that signifies the "end" of carrier cooling. Fitting to the extracted lattice effective temperature (by inverting Eq. (7.6) for $T_{\text{eff}}(\tau)$), we determine the constants A_1 and B_1. Using the photoexcitation conditions and calculated interlayer spacing (based on the vdW strength of 1L-$MoS_2$and Si:N), we make the necessary unit conversion s. t. the extracted thermal conductivity $\kappa = 313 \pm 4$ W m^{-1}K^{-1} is in standard units. This

model provides an excellent fit of the data for long times in Figure 7.2, far superior than a single exponential decays, yielding a thermal conductivity in reasonable agreement with simulated and experimental values in the c-axis of Si:N [154, 155]. We conclude the thermal boundary resistance between 1L-$MoS_2$and Si:N in the heterostructure is small.

7.2 DIFFUSE DYNAMICS AT HIGH SYMMETRY MOMENTA

The increase in MSD determined from the Debye-Waller suppression of Bragg peak intensities does not uniquely define the microscopic state of the phonon system. In contrast, UEDS measurements together with *ab-initio* simulations yield unprecedented details of mode- and momentum-resolved nonequilibrium phonon population distributions in the monolayer that underlie the changes in MSD observed via the Bragg peak dynamics. The transient UEDS signals from 1L-MoS_2 following photoexcitation show the strongest increases at the K, M, and Q points of the BZ, shown in Figure 7.4. The time- and momentum-resolved phonon excitation dynamics at each of these points in the BZ are in good agreement with our ab initio predictions, provided the effects of Si:N substrate dielectric screening are included (see Figure 7.4b-e).

These combined UEDS and first-principles analyses show that the nonequilibrium state of the phonon system several picoseconds after photoexcitation is profoundly anisotropic in momentum. This anisotropy is primarily determined by the momentum-dependent electron-phonon interaction strength and the available inelastic electron-phonon scattering pathways that are open to the hot carriers. These pathways are constrained by the electronic band structure and carrier distribution (c.f. Figure 6.3) and explain the observed and computed momentum-dependent phonon heating dynamics. Within $5 - 10$ ps, the carrier and phonon systems in 1L-MoS_2 have equilibrated with respect to the partition of excitation energy, but the phonon system remains profoundly out of equilibrium internally.

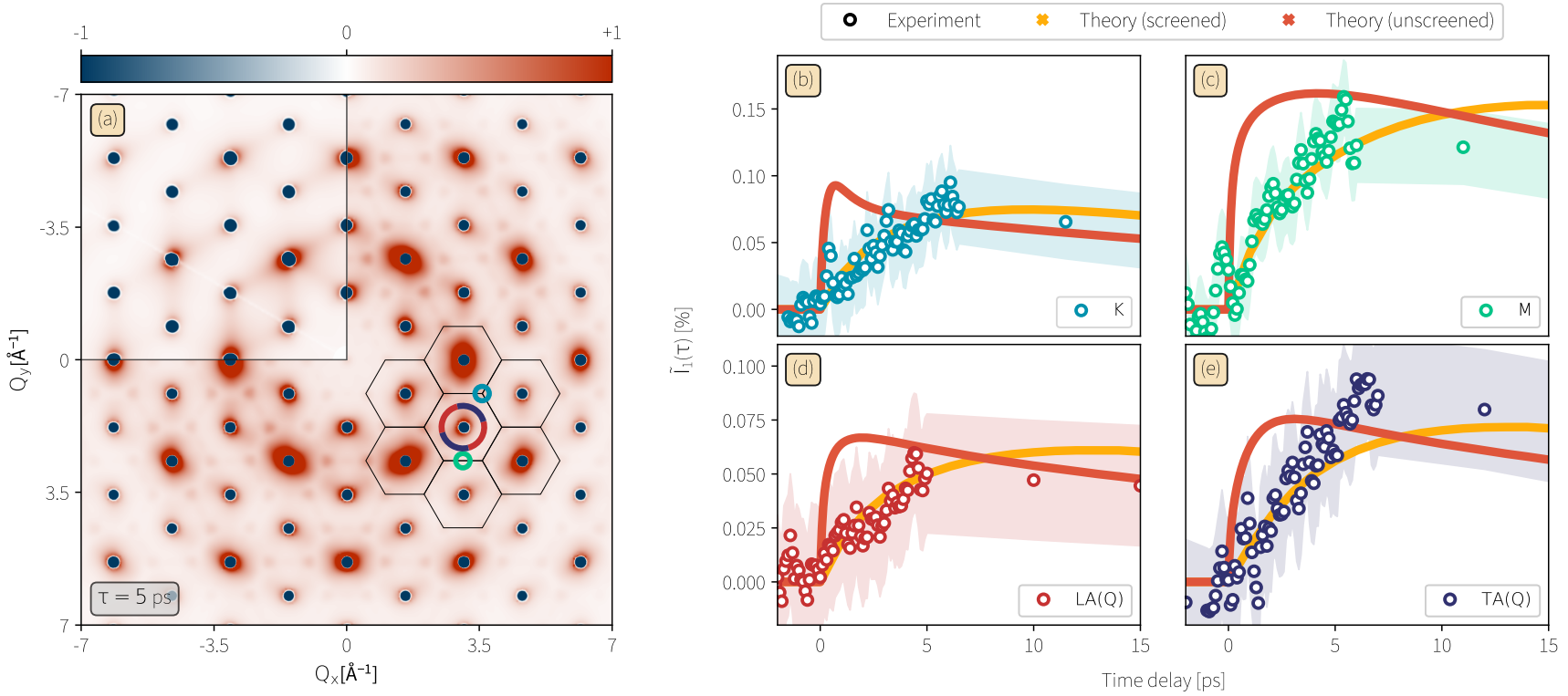

FIGURE 7.4: Momentum-resolved phonon re-equilibration dynamics. (a) All-phonon differential diffuse scattering pattern of 1L-MoS2 calculated from first-principles as $\Delta I = I(\mathbf{Q}, \tau = 5\text{ps}) - I(\mathbf{Q}, T = 300\text{K})$. The inset (upper left) is the thermal differential diffuse scattering pattern calculated as $\Delta I = I(\mathbf{Q}, T = 380\text{K}) - I(\mathbf{Q}, T = 300\text{K})$. The temperature of 380 K corresponds to an effective lattice temperature as extracted from the observed MSD at $\tau = 5$ ps (see text), shown on the same color scale. Black hexagons indicate BZ boundaries. Regions for which data are shown in (b-d) are indicated with the matching color. (b-d) Relative change in diffuse intensity at the reduced scattering vectors (b) K, (c) M, (d) LA phonons at Q and for (e) TA phonons at Q. Signals are obtained by integration over the colored regions in (a), as well as over every visible BZ (see the Supporting Information). Acoustic signals are extracted by integrating over the segmented annuli given in (a), with LA and TA distinction possible due to phonon scattering selection rules. Red and orange curves are shown as in Figure 7.2. Reprinted with permission from Ref [84]. Copyright 2022 American Chemical Society.

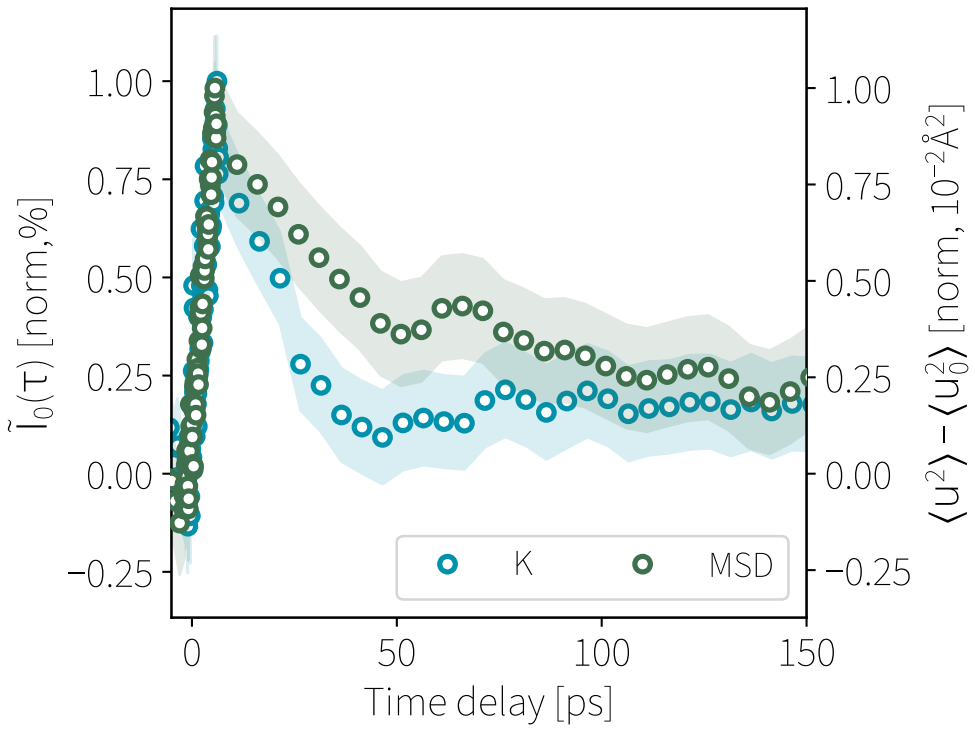

FIGURE 7.5: Comparison of MSD cooling dynamics with phonon anharmonic decay at K up to 150 ps following photoexcitation. Reprinted with permission from Ref [84]. Copyright 2022 American Chemical Society.

Previous work has demonstrated the possibility of defining a time-dependent effective phonon temperature, $T_{\text{eff}}(\tau)$, that corresponds to the observed MSD using the model [51] in Eq. (7.6). However, such a $T_{\text{eff}}(\tau)$ provides a misleading view of the nonequilibrium state of the phonon system during carrier-phonon equilibration. This is illustrated in Figure 7.4a, where the nonequilibrium phonon-diffuse differential scattering intensity at 5 ps is compared with a thermalized phonon-diffuse differential intensity distribution at $T_{\text{eff}}(5\,\text{ps}) = 380$ K (inset), the effective temperature determined by Eq. (7.6) and the measured MSD at 5 ps (c.f. Figure 7.2). The phonon population distribution in 1L-$MoS_2$is still profoundly nonthermal and is not well described by an effective temperature.

Further relaxation of these anisotropic nonequilibrium phonons in 1L-MoS_2involves coupling processes internal to the monolayer and heat transfer between the monolayer and Si:N substrate in the heterostructure. These distinct processes are both resolved by these measurements. In Figure 7.5, the diffuse intensity dynamics at K out to 150 ps are

ν	$\tau^{ph-ph}_{\Gamma,\nu}$ (ps)	$\tau^{ph-ph}_{K,\nu}$ (ps)
1	50.90	52.89
2	97.98	245.99
3	48.67	61.41
4	59.29	17.89
5	33.47	17.74
6	21.95	26.99
7	23.43	29.38
8	18.50	14.69
9	18.45	7.87

TABLE 7.2: Phonon-phonon equilibrium relaxation times at $\mathbf{q} = \Gamma, K$ at room-temperature in 1L-MoS_2.

compared against the MSD dynamics extracted from the Bragg peaks, whose ~ 50 ps decay time (single-exponential fit) indicates the cooling rate of the monolayer to the underlying substrate. The observed decay of diffuse intensity at K is in poor agreement with these MSD dynamics, indicating that a different process is involved. The single-exponential decay time constant determined for the dynamics at K is 25 ps, twice as rapid as the MSD dynamics but in good agreement with the *ab-initio* anharmonic decay rate of the E' optical phonons at K (22 ps), to which UEDS is most sensitive, see Table 7.2. The observed decay of the MSD is, however, in reasonable agreement with the decay in phonon-diffuse scattering measured for both the mid-BZ LA and TA modes, whose heating dynamics are shown in Figure 7.4d,e. For times <30 ps, this subnanoscale phonon transport across the 1L-MoS_2/Si:N heterostructure interface involves a profoundly nonequilibrium population of phonons in the monolayer, including a much higher occupancy of high-wavevector acoustic phonons than would be expected of a thermalized distribution. These conditions are the result of phonon (heat) transport across the monolayer-substrate interface occurring on time scales similar to those for the nonequilibrium phonon relaxation within the monolayer itself. UEDS provides a direct, momentum-resolved window on subnanoscale phonon transport in this far-from-equilibrium regime.

This work has shown the following two key points. Firstly, inelastic scattering experiments are not only possible but sensitive enough to detect the extremely small changes

in intensity at the edges of each BZ even at the 2D limit. Secondly, the developed theory that exactly determines the William-Lax thermal averages is also sensitive enough to take into describe non-standard 3D materials, with the provided modifications. Having shown that an accurate and precise enough theory exists that can be probed by existing instrumentation, we continue by expanding the theory to now incorporate circular dichroism, and explore the effects of chiral phonons in this context.

8

Pseudo-Angular Momentum and Effects of Circular Dichroism

"We mathematicans are all a bit crazy."
—Lev Landau

In 2D systems that feature strong SOC [156, 157, 158] such as 1L-MoS_2 or WSe_2, the coupled spin and momentum-valley physics [104] allow for direct control over valley, spin, and vibrational degrees of freedom [86, 100] using circularly polarized light. Photoexcitation can be used to generate electron hole pairs in either the K or K' region of the BZ, where the carriers have opposite orbital angular momentum. The selective excitation of carriers in terms of both orbital (angular) and valley momentum has been termed carrier valley-polarization.

From the perspective of the phonons, hexagonal lattices also exhibit unusual features not found in other space groups. Typically, phonon normal modes in single crystal systems feature phase mismatched linearly polarized atomic displacements. At the K-points of a 2D hexagonal lattice, however, three-fold symmetry results in the atomic displacements associated with certain optical and acoustic phonon modes executing circular orbits. In bulk (layered) hexagonal materials, these left and right circularly polarized

K-point phonons tend to be degenerate and do not carry net angular momentum since the basis atoms tend to precess in opposite directions. However, in monolayer TMDs the presence of strong SOC and broken inversion symmetry lifts the degeneracy of circular polarized phonons near K and K', and yields phonon modes with non-zero pseudo-angular momentum (PAM). These *chiral phonons* possess finite Berry curvature[1] and can therefore induce a phonon Hall effect, making them prime candidates in unraveling the origins of the thermal Hall effect in many quantum systems, such as Kitaev spin liquids (eg. α-$RuCl_3$ [160]), cuprate superconductors [161], spin ices [162] and frustrated magnets [163].

Taken together, these unusual features of the carriers and phonons near K (K')-points are expected to yield unusual handedness to the EPC in monolayer TMDs. Specifically, during the relaxation of an initially valley-polarized (hot) charge carrier distribution, the equilibration of valley polarized carriers involves intervalley (K - K') transitions that require a change of orbital angular momentum, raising questions about angular momentum conservation. One intervalley relaxation channel that conserves both angular momentum and energy is chiral electron-phonon scattering. Such interactions are thought to be an important factor in the process of valley depolarization. Here, we propose an experimental procedure for direct observation of the nonequilibrium time- and momentum-dependent chiral phonon formation involved in the process of valley depolarization. The approach proposed is based on ultrafast electron or x-ray techniques that measure the time-dependence of phonon-diffuse scattering following optical excitation [113, 115]. While indirect methods have been proposed to observe chiral phonons via their signature in the thermal Hall effect [164], and the observation of chiral phonons have been reported [106] via circular dichroism in the optical transmission of the material, such methods do not directly measure chiral phonon emission. The hallmark of chiral phonon emission during carrier valley depolarization is the generation

[1] Proving so its not relevant here, but can be shown using similar approaches as those found in Ref [159].

IR	Basis Functions	Band
A'	$\Psi^M_{2,-2}, \frac{1}{\sqrt{2}}\left(\Psi^{X_1}_{1,-1} + \Psi^{X_2}_{1,-1}\right)$	VB
A''	$\Psi^M_{2,1}, \frac{1}{\sqrt{2}}\left(\Psi^{X_1}_{1,-1} - \Psi^{X_2}_{1,-1}\right)$	CB + 1
E'_1	$\Psi^M_{2,0}, \frac{1}{\sqrt{2}}\left(\Psi^{X_1}_{1,1} + \Psi^{X_2}_{1,1}\right)$	CB
E'_2	$\Psi^M_{2,2}, \frac{1}{\sqrt{2}}\left(\Psi^{X_1}_{1,0} - \Psi^{X_2}_{1,0}\right)$	VB-3
		CB+2
E_1''	$\Psi^M_{1,0}, \frac{1}{\sqrt{2}}\left(\Psi^{X_1}_{1,1} - \Psi^{X_2}_{1,1}\right)$	VB
E_2''	$\Psi^M_{2,-1}, \frac{1}{\sqrt{2}}\left(\Psi^{X_1}_{1,0} + \Psi^{X_2}_{1,0}\right)$	VB-1

TABLE 8.1: The orbital representations in the C_{3h} point double group (irreducible representations (IRs) at K in 1L-MoS_2), giving the corresponding label of the band relative to the valence (conduction) bands. Time-reversal symmetry relates the K and K' valleys. Here, the basis functions are given in terms of spherical harmonics $\mathcal{Y}$ of quantum numbers (l, m) on the η atom as [166] $\Psi^{\eta}_{l,m}(\mathbf{k}, \mathbf{r}) = \frac{1}{\sqrt{n}} \sum_{\mathbf{R}_n} e^{i\mathbf{k}\cdot(\mathbf{R}_n + \mathbf{t}_\eta)} \mathcal{Y}^m_l(\mathbf{r} - [\mathbf{R}_n + \mathbf{t}_\eta])$.

of a momentum-valley polarized phonon distribution. The direct measurement of such a transient phonon distribution during carrier-valley depolarization in 1L-MoS_2 using ultrafast diffuse scattering is the focus of this chapter. Overall, the goal is to build on our UEDS developements on 1L-MoS_2 [84] and open a window on chiral phonon generation.

8.1 SPIN- AND VALLEYTRONICS

It has been long known [165] that at the K point in TMDs of chemical formulae MX_2, the valence band is dominated by the $|d_{x^2-y^2}\rangle$ and $|d_{xy}\rangle$ (E symmetry) orbitals on M (with small contribution from $|p_x\rangle$ and $|p_y\rangle$ on X) while the conduction band is primarily $|d_{z^2}\rangle$ (A_1 symmetry) on M. The valence hybridization at the valley is given by

$$|\Psi_v\rangle = \frac{1}{\sqrt{2}}\left(|d_{x^2-y^2}\rangle + i\tau|d_{xy}\rangle\right) \tag{8.1}$$

where these combinations are the only allowed owing to the C_{3h} point group symmetry of the hexagonal lattice. We include a summarizing table of the relevant orbitals in Table 8.1. Application of the prime generator of this point group at the valleys, namely threefold

rotation symmetry about the out-of-plane (parallel to the **c** crystal axis) $\mathcal{R}\{2\pi/3, \hat{z}\}$, allows for determination of the azimuthal quantum numbers ℓ in the valence and conduction bands. By defining a valley index $\tau = \pm 1$ that denotes the K (K') valley, we find:

$$\mathcal{R}\{2\pi/3, \hat{z}\}|\Psi_v^\tau\rangle = |\Psi_v^\tau\rangle = e^{i\ell_v 2\pi/3}|\Psi_v^\tau\rangle \implies \ell_v = 0 \tag{8.2a}$$

$$\mathcal{R}\{2\pi/3, \hat{z}\}|\Psi_c^\tau\rangle = e^{i\tau 2\pi/3}|\Psi_c^\tau\rangle = e^{i\ell_c 2\pi/3}|\Psi_c^\tau\rangle \implies \ell_c = \tau \tag{8.2b}$$

showing that intravalley interband transitions are allowed so long as they obey the following selection rules. In the intervalley scattering by phonons, the whole system has threefold rotational symmetry, implying the selection rule of the angular momentum quantum number ℓ:

$$\ell_{c(v)}(K) - \ell_{c(v)}(K') = \pm 1 \tag{8.3}$$

by emitting a circularly-polarized valley phonon ($\ell_{ph} = \pm 1$). Since the minimum of the conduction band valleys in 1L-$MoS_2$are dominated by the $\ell = 0$ d orbitals on the Mo atoms [104], they bear an overall azimuthal quantum number $m_\tau = \tau = \pm 1$ at K (K'). Likewise, the top of the valence bands have no azimuthal quantum number, so $m = 0$. Conservation of the PAM experienced by the system then dictates a selection rule $\Delta m = \pm 1$. By including the incidence of a photon, we can expand the selection rule to determine:

$$\Delta\ell_{\text{el}} = \pm\ell_{\text{ph}} \pm \ell_{\text{photon}} \tag{8.4}$$

where $+$ is emission and $-$ is absorption[2].

To see that it is possible to directly control the valley and spin indices of the charge carrier simultaneously requires ascribing a Hamiltonian to this system. The system Hamiltonian $\hat{\mathcal{H}}$ will have a contribution from a free propagating electron $\hat{\mathcal{H}}_0$, from the SOC $\hat{\mathcal{H}}_{SO}$, and from $\mathbf{k}\cdot\hat{\mathbf{p}}$ theory $\hat{\mathcal{H}}_{\mathbf{k}\cdot\hat{\mathbf{p}}}$. This model will use Lowdin Partitioning [167] to eliminate the degrees of freedom from the proven 7-band model [168] so that we can write

[2] It is worth realizing that these angular momentum quanta obey, in this case, a modular arithmetic owing to the 3-fold symmetry of point group, where the effective quantum ℓ_{eff} for a given ℓ satisfies $\ell \equiv \ell_{\text{eff}}$ mod 3. For example, $\ell = 2 \implies e^{i\ell 2\pi/3} = e^{i4\pi/3} = e^{i(-1)2\pi/3} \implies \ell = -1$, satisfying $2 \equiv -1 \mod 3$.

the Hamiltonian in the new spinful basis. Defining $|s\rangle = \{\uparrow, \downarrow\}$ and $|\Psi_{c(v)}, s\rangle = |\Psi_{c(v)}\rangle \otimes |s\rangle$, we write the free Hamiltonian as $\hat{\mathcal{H}}_0 = (\hbar^2 k^2/2m)(\mathbb{1}_2 \otimes \hat{\sigma}_z)$, where the identity matrix $\mathbb{1}$ operates in electron-hole space, and $\hat{\sigma}_z$ is the Pauli matrix for the 2 basis functions[3]. While the full 7 band model is needed to accurately capture all features of the electronic system [166], such as trigonal warping at the valleys and the spin-splitting of the conduction band, we need only introduce terms linear in the momentum in order to accurately determine the dominant transition mechanisms, given by a simple massive Dirac fermion model. We can write the off diagonal elements of the the Hamiltonian in the $\mathbf{k} \cdot \hat{\mathbf{p}}$ picture as $\hbar/2m_e(k_+\hat{p}_- + k_-\hat{p}_+) \triangleq \hat{\mathcal{H}}^- + \hat{\mathcal{H}}^+$, where $\alpha_\pm = \alpha_x \pm i\alpha_y$. Therefore,

$$
\begin{aligned}
\hat{\mathcal{H}}_{\mathbf{k}\cdot\hat{\mathbf{p}}} &= \begin{bmatrix} \left\langle \Psi_v, s \left| \frac{\hbar^2\hat{p}^2}{2m_e} \right| \Psi_v, s \right\rangle & \left\langle \Psi_v, s \left| \hat{\mathcal{H}}_+ \right| \Psi_c, s \right\rangle \\ \left\langle \Psi_c, s \left| \hat{\mathcal{H}}_- \right| \Psi_v, s \right\rangle & \left\langle \Psi_c, s \left| \frac{\hbar^2\hat{p}^2}{2m_e} \right| \Psi_c, s \right\rangle \end{bmatrix} \\
&= \begin{bmatrix} \varepsilon_{\mathrm{VB}} & at\tau k_- \\ at\tau k_+ & \varepsilon_{\mathrm{CB}} \end{bmatrix} \\
&= at\left(\tau k_x \begin{bmatrix} 0 & 1 \\ 1 & 0 \end{bmatrix} + k_y \begin{bmatrix} 0 & -i \\ i & 0 \end{bmatrix} \right) + \frac{\Delta}{2} \begin{bmatrix} -1 & 0 \\ 0 & 1 \end{bmatrix} \\
&= at(\tau k_x \hat{\sigma}_x + k_y \hat{\sigma}_y) + \frac{\Delta}{2}\hat{\sigma}_z
\end{aligned} \tag{8.5}
$$

where energies are given relative to the Fermi level, Δ is the band-gap, a the lattice constant, and t the effective hopping integral. To determine the contribution of SOC to the Hamiltonian, we note we can write $\hat{\mathbf{L}} \cdot \hat{\mathbf{S}} = \hat{L}_z\sigma_z + \hat{L}_+\sigma_- + \hat{L}_-\sigma_+$, where $\hat{\mathbf{L}}$ is the angular momentum operator and $\hat{\mathbf{S}}$ is the vector of spin Pauli matrices. In this derivation,

[3] From here onward, we omit the technically correct Kronecker product of the local identity operator for simplicity.

we note that $L_\pm$ transforms as the E'' irreducible representation (IR) of C_{3h} (see Table 8.1), and such we can obtain the following relations for the full 7-band model:

$$C_3^+ L_\pm C_3^{+\dagger} = e^{\mp 2\pi i/3} L_\pm \tag{8.6}$$

$$\langle s, \Psi_v | L_- S_+ | \Psi_{v-1}, s \rangle = \Delta_{(v,v-1)} S_+ \tag{8.7}$$

$$\langle s, \Psi_v | L_+ S_- | \Psi_{v-1}, s \rangle = \langle s, \Psi_v | L_z S_z | \Psi_{v-1}, s \rangle = 0 \tag{8.8}$$

With Lowdin partitioning, we assume only nearest neighbor bands couple strongly, and we expect only a diagonal matrix proportional to the spin-splitting in each band of the basis. In our chosen two-band basis (where time-reversal symmetry (TRS) relates the valleys), one can show [166] we can express this as :

$$\hat{\mathcal{H}}_{SO} = \frac{\hbar}{4m_e^2c^2}\frac{1}{r}\frac{\mathrm{d}V(r)}{\mathrm{d}r}\hat{\mathbf{L}}\cdot\hat{\mathbf{S}} = \begin{bmatrix} \tau\Delta_{\mathrm{VB}}s_z & 0 \\ 0 & \underbrace{\tau\Delta_{\mathrm{CB}}s_z}_{\approx 0} \end{bmatrix} = -\tau\Delta_{\mathrm{VB}}\frac{\hat{\sigma}_z - 1}{2}\hat{s}_z \tag{8.9}$$

where $\hat{s}_z$ is the Pauli matrix for spin.

We emphasize spin-splitting is a general consequence of inversion symmetry breaking, and is not dependent on the model Hamiltonian used here. The complete 7-band model correctly predicts coupling between all bands and spin-splittings in the conduction manifold that are not present in the 2-band model. Furthermore, spins are completly decoupled and so the spin quantum number s_z (eigenvalues $s_z = \pm 1$ of the spin Pauli matrix $\hat{s}_z$) remains a good quantum number. This lets us write the entire electron Hamiltonian, first derived by Xiao *et al.* [100, 169], as:

$$\hat{\mathcal{H}} = at(\tau k_x\hat{\sigma}_x + k_y\hat{\sigma}_y) + \frac{\Delta}{2}\hat{\sigma}_z - \tau\Delta_{\mathrm{VB}}\frac{\hat{\sigma}_z - 1}{2}\hat{s}_z \tag{8.10}$$

where we omit the free Hamiltonian as it does not contribute to the physics herein.

From here, we can compute the degree to which circularly polarised photoexcitation couples to electronic transitions via the transition amplitudes of the interband momenta

operators, namely:

$$P_{\pm} = P_x \pm iP_y \tag{8.11a}$$

$$P_{\alpha} \triangleq m_0 \left\langle u_c \left| \frac{1}{\hbar} \frac{\partial \hat{H}}{\partial k_{\alpha}} \right| u_v \right\rangle \tag{8.11b}$$

where u is the periodic part of the Bloch wavefunction [170] in the valence (v) and conduction (c) bands. In terms of the spin-split band gap $\Delta' \triangleq \Delta - \Delta_{\mathrm{VB}} \tau s_z$, the transition amplitudes are:

$$|P_{\pm}(\mathbf{k})|^2 = \frac{m_0^2 a^2 t^2}{\hbar^2} \left(1 \pm \tau \frac{\Delta'}{\sqrt{\Delta'^2 + 4a^2 t^2 k^2}}\right) \overset{\Delta' \gg atk}{=} \frac{m_0^2 a^2 t^2}{\hbar^2} (1 \pm \tau) \tag{8.12}$$

where *ab-initio* calculations predict [156] that for TMDs, $\Delta' \gg atk$. Optical fields couple only to the orbital part of the wave function and spin is conserved in the optical transitions. We therefore obtain the following excitation rule; transitions of electrons to the conduction band (and creation of holes in the valence band) in a definite valley are allowed by photoexcitation of handedness τ (from the perspective of the sender) at energy at least Δ'. The stability of the electronic valley polarization has been verfied experimentally in many different TMDs [100, 171, 172, 173], where the photoexcitation will either generate an exciton (bound electron-hole pair) gas or electron-hole plasma, according to the photoinduced free charge carrier density.

8.2 SCATTERING SELECTION RULES

Note 8.1

The following section discusses the IR at the high-symmetry momentum Q, but in order to distinguish the IR from the scattering vector $\mathbf{Q}$ or high-symmetry momentum Q, the high-symmetry momentum is labelled Λ, and the equivalent IR is $\mathcal{L}$. In the literature, this valley is sometimes also referred to as the Σ or T valley.

	Selection Rule	Process
Intravalley:	$(\mathcal{K}_1 \times \mathcal{K}_1^*)^* = \Gamma_1$	Mainly hole relaxation
	$(\mathcal{L}_1 \times \mathcal{L}_1^*)^* = \Gamma_1$	Electron relaxation
	$(\Gamma_1 \times \Gamma_1^*)^* = \Gamma_1$	
Intervalley:	$(\mathcal{K}_3 \times \mathcal{K}_2^*)^* = \mathcal{K}_3$	Cond. electron scattering
	$(\mathcal{K}_1 \times \mathcal{K}_1^*)^* = \mathcal{K}_1$	Valence hole scattering
	$(\mathcal{L}_1 \times \mathcal{K}_3^*)^* = \mathcal{L}_1$	Hot carrier accumulation
	$(\Gamma_1 \times \mathcal{K}_1^*)^* = \mathcal{K}_1$	Carrier thermalisation

TABLE 8.2: Spin-conserving selection rules of the C_{3h} point group. The nature of the scattering process is given, well as an example of such a process in practice. The rule $(A \times B^*)^* = C$ should be read as a transition from electron momenta A to B requires a mediating phonon of momentum C.

Owing to the hexagonal symmetry of these lattices, we consider the representations of the high symmetry points in the C_{3h} point group[4]. By defining C_3^+ as the anticlockwise threefold rotation, and recognizing the conduction band at K is dominated by $|d_{z^2}\rangle$ on M, we know the corresponding IR ζ must satisfy:

$$\zeta \times C_3^+ = \omega^*, \zeta \times C_3^- = \omega, \zeta \times \sigma_h = +1 \tag{8.13}$$

for $\omega = \exp(i2\pi/3)$ by noting the exponential factor of Eq. (3.5) is determined by the lattice sites, given by the Γ_3 IR (in our notation now $\mathcal{K}_3$ IR). By TRS relating the valleys, we know analgously that the IR of the conduction band at K' (ζ') must satisfy:

$$\zeta' \times C_3^+ = \omega, \zeta \times C_3^- = \omega^*, \zeta \times \sigma_h = +1 \quad . \tag{8.14}$$

Therefore, $\mathcal{K}_2$ is the IR for the primary conduction band at K'.

The local atomic wavefunctions in the valence band obey all symmetries of the C_{3h} double group and thus must transform as unity, obviously $\Gamma_1 \to \mathcal{K}_1$ at K. TRS implies that the IR at K' is $\mathcal{K}_1^* = \mathcal{K}_1$. We can further describe the Λ valleys in the conduction band (along the ΓK axis) by the C_{1h} point double group.

This gives us the following spin-conserving selection rules in Table 8.2. The spin-flipping selection rules can be determined by continuing assignment of the spin-split valence and conduction bands at the high sym points (Γ, Λ, K) to determine allowed processes using the corresponding point double groups.

[4]We consider the C_{3h} point double group for spin-split representations.

As will be important later, we now show that using the C_{3h} point double group, resolving the spin splitting states, we can expand the selection rules as follows[5]. We know that for the valence bands at the K valleys, the IRs of spin-split states (χ and χ') must satisfy:

$$\chi \times \bar{E} = -1 \tag{8.15a}$$

$$\chi \times \bar{C}_3^+ = \omega \tag{8.15b}$$

$$\chi \times \bar{C}_3^- = \omega^* \tag{8.15c}$$

$$\chi' = \chi^* \quad . \tag{8.15d}$$

These are given by $\mathcal{K}_7$ and $\mathcal{K}_8$ IRs at K. To determine the energy ordering of these states, we recognize that at K, the valence band, $|d_{x^2-y^2}\rangle + i|d_{xy}\rangle$, has orbital magnetic moment $m = 2$ which implies that the spin angular momentum of the electron $\ell^s = +1/2$ occupies the higher energy state due to the positive spin-coupling coefficient. This requires the higher energy IR χ satisfy $\chi \times \sigma_h = i$, meaning that at K, the higher energy state is $\mathcal{K}_7$, and lower energy is $\mathcal{K}_8$. TRS shows the opposite is true at K'. We note this implies a new intervalley selection rule between the spin split states $(\mathcal{K}_8 \times \mathcal{K}_7^*)^* = \mathcal{K}_6$. These IRs are superimposed on the spin-split band structure given in Figure 8.1a.

[5]Assignment of the conduction spin-split states is not germane here, and will be skipped.

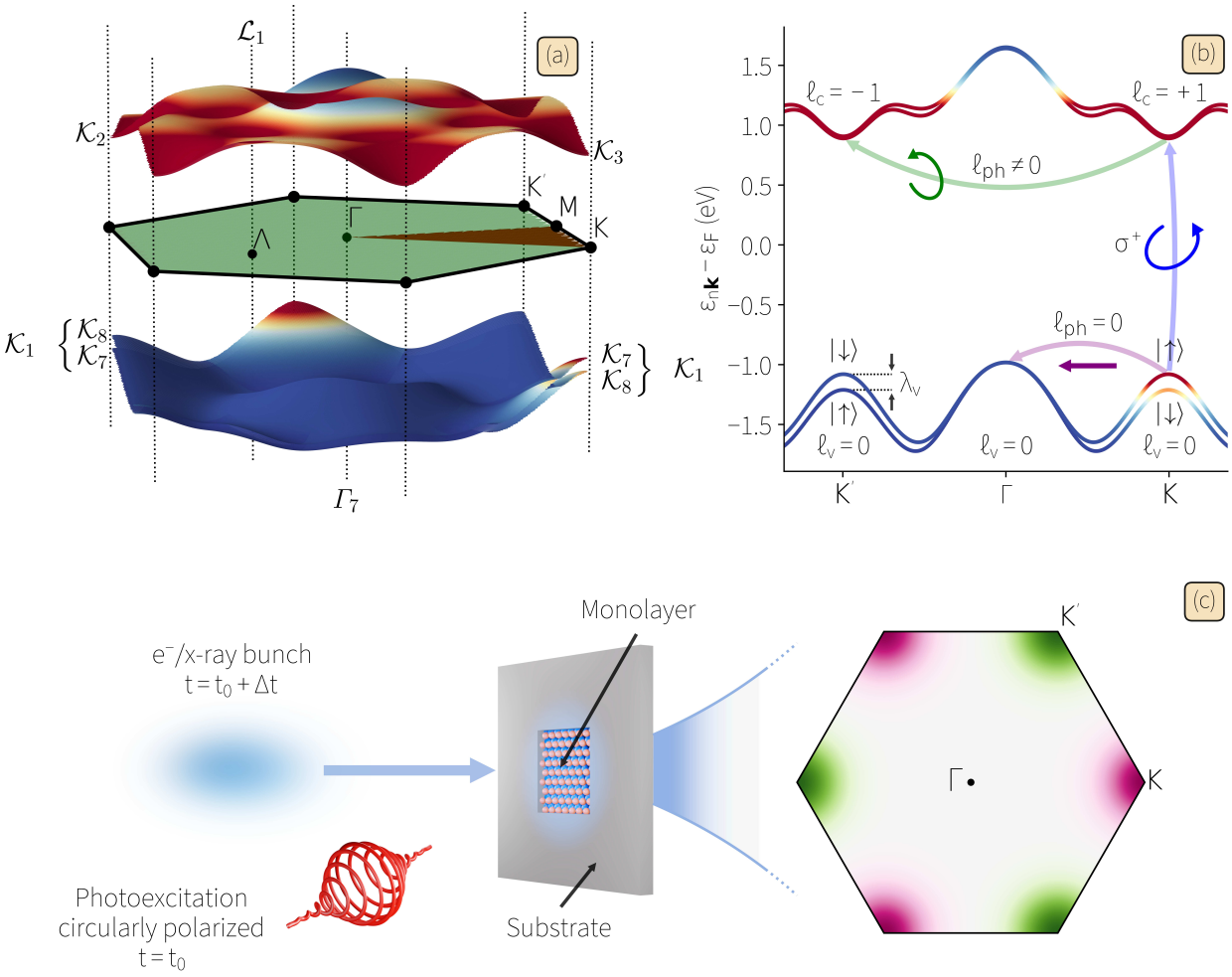

FIGURE 8.1: PAM conserving intervalley carrier scattering and ultrafast phonon diffuse scattering measurements in 1L-MoS_2 (a) Spin-split valence and conduction band structure of 1L-MoS_2. The reducible BZ is shown in green and the irreducible BZ in red, with high symmetry points labeled. Calligraphic annotations denote the irreducible representations of the band structure at the corresponding high symmetry points for a given spin-split band. (b) Bands along the $K'\Gamma K$ direction with coloring identical to (a). Photoexcitation with right-circularly polarized light (blue arrow) leads to a valley-polarized charge carriers distribution around K. Left circularly polarized light drives excitation at K' (not shown). Spin and PAM conserving intervalley scattering processes for conduction (valence) band electrons (holes) to K' (Γ). Electron scattering must involve the emission of a chiral phonon (green arrow) and hole scattering can only involve non-chiral phonons (purple arrow). The valence band shows pronounced energy splitting of the spin states for monolayer TMDs ($\lambda_v \sim$ 100s of meV, much larger than even the highest-energy phonons). The equivalent splitting in the conduction band λ_c is much smaller (< 10s of meV, smaller than all K or K' phonons). (c) Schematic of the ultrafast diffuse scattering experiment. The sample is illuminated with circularly polarized light, after which the system is probed with an electron/x-ray bunch at a pump-probe delay time Δt. Diffuse scattering for a single representative BZ surrounding the Bragg peak at Γ is shown on the right. The colors of the K and K' regions match the arrow colors for the corresponding process illustrated in (b), allowing the separation of chiral electron scattering from non-chiral hole scattering. Reprinted with permission from Ref [174]. Copyright 2023 American Physical Society.

8.3 VALLEY-SELECTIVE EXCITON GENERATION AND DEPOLARIZATION

2D hexagonal lattices fall in the C_{3h} point group (or point double group for spin-split band structure Figure 8.1a), where the symmetry properties of the character table and corresponding allowed intra- and inter-valley and band transitions have been well determined [86]. The valley depolarization of excitons at low density has previously been explained in 1L-MoS_2 [175, 176] with reference to the electron-hole exchange interaction, not carrier-phonon interactions. With regards to impact ionization as a depolarization mechanism, even at n_0 as low as 10^{12} cm^{-2}, this carrier-carrier scattering has been shown to only redistribute excited electrons (holes) in the conduction (valence) band between K and K' after 10 ps (10 s of ns) [177]. More complicated carrier-carrier depolarization mechanisms, as in the Dexter-like transport of momentum-separated excitons [178], become less relevant at large n_0 owing to the increased Coulombic screening of electrons and holes, and thus broken electron-hole correlations. Therefore, at n_0 greater than the exciton Mott threshold to an electron-hole plasma in monolayer TMDs [179, 180, 181], electron-phonon interactions are expected to be the dominant mechanism driving valley depolarization of the charge carrier distribution. Thus, the measurements proposed here can, in principle, be used to monitor the transition from electron-phonon to exchange dominated valley depolarization.

The dominant intervalley (K to K') momentum (and energy) relaxation channels for K-valley polarized conduction band electrons, $(\mathcal{K}_3 \times \mathcal{K}_2^*)^* = \mathcal{K}_3$, are spin conserving, but require a change in the aziumthal quantum number ℓ, as shown in Figure 8.1b. This change in OAM can be provided by the emission or absorption of a chiral phonon at K' as we demonstrate in the next section. The equivalent process for holes requires a spin-flip, $(\mathcal{K}_8 \times \mathcal{K}_7^*)^* = \mathcal{K}_6$, due to the large valence band spin splitting and is expected to be much slower. Spin-flip processes, such as the Bir-Aronov-Pikus mechanism [182] or Dyakonov-Pevel mechanism [183], occur on longer time scales.

The dominant intervalley (K to Γ) momentum (and energy) relaxation channels for K-valley polarized carriers involves valence hole scattering, $(\Gamma_1 \times \mathcal{K}_1^*)^* = \mathcal{K}_1$, and is allowed due to the spin and energy degeneracy at Γ as shown in Figure 8.1b. This channel can only involve scattering from non-chiral K phonons, since there is no associated change in OAM.

These details of hole scattering differ for selenide TMDs, where the valence band maxima at K and Γ are not closely spaced in energy like they are for the sulfide TMDs. In TMDs, it is also possible to exert some control over the relative valence energy at the Γ point by introducing strain.

It is worth mentioning that in these materials, previous computational [52] and experimental [184] work has shown that excited electrons primarily occupy states in the vicinity of the K and Λ valleys. These works further show that there is efficient scattering between them, $(\mathcal{L}_1 \times \mathcal{K}_3^*)^* = \mathcal{L}_1$, especially in the notable exception of WSe_2 where the Λ valley is energetically below K. This would result in an increase of phonon occupation at the six-fold degenerate Λ valleys. These works, however, use excitation energy well above the band-gap s. t. charge carriers are occupied at Λ by the photoexcitation, which enables the efficient scattering to K. We can minimize the occupation of Λ phonons by selective photoexcitation resonant with the A exciton (band-gap excitation). Nonetheless, this scattering is momentum separated from the chiral K/K' scattering in momentum-resolved phonon diffuse scattering, meaning occupancy at Λ can be safely ignored in the discussion of chiral phonons.

8.4 PSEUDO-ANGULAR MOMENTUM

To show that phonons in such a system can have $\ell_{\mathrm{ph}} \neq 0$, we start by evaluating the angular momentum operator for the crystal. For a given atomic motion, we can determine its angular momentum (with respect to $\hat{z}$) as $\mathcal{J}_z = m\mathbf{r} \times \dot{\mathbf{r}}$, where $\dot{(\cdot)} \triangleq \partial_t$.

Defining the atomic displacement vector of the κ^{th} atom in the p^{th} unit cell as $u_{p\kappa} = (u^x_{p1}\, u^y_{p1} \cdots u^x_{pn}\, u^y_{pn})^T$, we can define the total angular momentum of the crystal as:

$$\begin{aligned}
\mathcal{J}_z &= \sum_{p\kappa} m_\kappa \mathbf{u}_{p\kappa} \times \dot{\mathbf{u}}_{p\kappa} = \sum_{p\kappa} m_\kappa \left(u^x_{p\kappa} \dot{u}^y_{p\kappa} - \dot{u}^x_{p\kappa} u^y_{p\kappa}\right) \\
&= \sum_p \begin{pmatrix} u^x_{p1} \\ u^y_{p1} \\ \vdots \\ u^x_{pn} \\ u^y_{pn} \end{pmatrix}^T \begin{pmatrix} 0 & m_1 & & & \\ -m_1 & 0 & & & \\ & & \ddots & & \\ & & & 0 & m_n \\ & & & -m_n & 0 \end{pmatrix} \begin{pmatrix} \dot{u}^x_{p1} \\ \dot{u}^y_{p1} \\ \vdots \\ \dot{u}^x_{pn} \\ \dot{u}^y_{pn} \end{pmatrix} \\
&= \sum_p \mathbf{u}_p^T i M' \dot{\mathbf{u}}_p
\end{aligned} \tag{8.16}$$

where $M' = \left(\begin{smallmatrix} 0 & i \\ i & 0 \end{smallmatrix}\right) \otimes \{m_\kappa\}$, $\{m_\kappa\}$ is the $n \times n$ diagonal matrix of atomic masses, and $\otimes$ is the Kronecker product. By defining $M = \left(\begin{smallmatrix} 0 & i \\ i & 0 \end{smallmatrix}\right) \otimes \mathbb{1}_n$, we can apply second quantization to the atomic displacements in the normal mode coordinate formalism. These displacements can be written as:

$$u^j_{p\kappa} = \sum_{\mathbf{q}\nu} (\boldsymbol{\varepsilon}_{\mathbf{q}\nu\kappa})^j e^{i\cdot(\mathbf{R}_p\cdot\mathbf{q} - \omega_{\mathbf{q}\nu} t)} \sqrt{\frac{\hbar}{2\omega_{\mathbf{q}\nu} N m_\alpha}} a_{\mathbf{q}\nu} + h.c. \tag{8.17}$$

where *h.c.* denotes the Hermitian conjugate, and $(\boldsymbol{\varepsilon}_{\mathbf{q}\nu\kappa})^j$ the j^{th} component of the atomic displacement of the κ^{th} atom at momentum $\mathbf{q}$ in mode ν at energy $\hbar\omega_{\mathbf{q}\nu}$, populated according to the creation operator $a_{\mathbf{q}\nu}$. By ignoring terms like aa and $a^\dagger a^\dagger$ (which vary quickly and have no contribution in equilibrium), we express the total angular momentum in terms of these displacements as:

$$\begin{aligned}
\mathcal{J}_z = \frac{\hbar}{2N} \sum_t \sum_{\mathbf{q}\mathbf{q}'} \sum_{\nu\nu'} & e^{i(\mathbf{q}'-\mathbf{q})\cdot\mathbf{R}_t} e^{i(\omega_{\mathbf{q}\nu} - \omega_{\mathbf{q}'\nu'})t} \\
\times \left\{ \sqrt{\frac{\omega_{\mathbf{q}\nu}}{\omega_{\mathbf{q}'\nu'}}} \epsilon^\dagger_{\mathbf{q}\nu} M \epsilon_{\mathbf{q}'\nu'} a^\dagger_{\mathbf{q}\nu} a_{\mathbf{q}'\nu'} \right. & + \left. \sqrt{\frac{\omega_{\mathbf{q}'\nu'}}{\omega_{\mathbf{q}\nu}}} \epsilon^T_{\mathbf{q}'\nu'} (-M) \epsilon^*_{\mathbf{q}\nu} a_{\mathbf{q}'\nu'} a^\dagger_{\mathbf{q}\nu} \right\}
\end{aligned} \tag{8.18}$$

We note further that $\boldsymbol{\varepsilon}^T_{\mathbf{q}'\nu'}(-M)\boldsymbol{\varepsilon}^*_{\mathbf{q}\nu} = \boldsymbol{\varepsilon}^\dagger_{\mathbf{q}\nu} M \boldsymbol{\varepsilon}_{\mathbf{q}'\nu'}$ and $\frac{1}{N}\sum_p e^{i(\mathbf{q}-\mathbf{q}')\cdot\mathbf{R}_p} = \delta_{\mathbf{q},\mathbf{q}'}$ and that the creation operators satisfy the commutation relation $[a_{\mathbf{q},\nu'}, a^\dagger_{\mathbf{q},\nu}] = \delta_{\nu'\nu}$, we can simplify

this expression to obtain the nonequilibrium phonon angular momenta:

$$\mathcal{J}_z = \frac{\hbar}{2}\sum_{\mathbf{q}\mathbf{q}'}\sum_{\nu\nu'}\boldsymbol{\varepsilon}^{\dagger}_{\mathbf{q}\nu}M\boldsymbol{\varepsilon}_{\mathbf{q}'\nu'}a^{\dagger}_{\mathbf{q}\nu}a_{\mathbf{q}'\nu'}\left\{\sqrt{\frac{\omega_{\mathbf{q}\nu}}{\omega_{\mathbf{q}'\nu'}}}+\sqrt{\frac{\omega_{\mathbf{q}'\nu'}}{\omega_{\mathbf{q}\nu}}}\right\} \times \delta_{\mathbf{q},\mathbf{q}'}e^{i(\omega_{\mathbf{q}\nu}-\omega_{\mathbf{q}'\nu'})t} + \frac{\hbar}{2}\sum_{\mathbf{q}\nu}\boldsymbol{\varepsilon}^{\dagger}_{\mathbf{q}\nu}M\boldsymbol{\varepsilon}_{\mathbf{q}\nu} \tag{8.19}$$

In equilibrium, we know $\langle a^{\dagger}_{\mathbf{q}\nu}a_{\mathbf{q}\nu'}\rangle = n_{\mathbf{q}\nu}\delta_{\nu\nu'}$ (n the phonon occupation, BE at thermal equilibrium), and so we can express the total angular momentum as:

$$\mathcal{J}_z = \sum_{\mathbf{q}\nu}\boldsymbol{\varepsilon}^{\dagger}_{\mathbf{q}\nu}M\boldsymbol{\varepsilon}_{\mathbf{q}\nu}\hbar(n_{\mathbf{q}\nu}+1/2) \triangleq \sum_{\mathbf{q}\nu}\ell^{s}_{\mathbf{q}\nu}(n_{\mathbf{q}\nu}+1/2) \tag{8.20}$$

where the phonon angular momenta at $\mathbf{q}$ is given by $\ell^{s}_{\mathbf{q}\nu}$. We emphasize that there are two contributions to the total phonon angular momentum ℓ^{ph}: (i) the local part yielding spin PAM ℓ^{s}, coming from the eigendisplacements ϵ, and (ii) the nonlocal part determined by $e^{i\mathbf{R}_t\cdot\mathbf{q}}$ yielding orbital PAM ℓ^{0}. The sum of these contributions for each oscillating sublattice yields the total phonon PAM.

Note that this implies at $T = 0$, each mode and momenta, the phononic system has a zero-point spin PAM of $(\hbar/2)\boldsymbol{\varepsilon}^{\dagger}_{\mathbf{q}\nu}M\boldsymbol{\varepsilon}_{\mathbf{q}\nu}$, in addition to the zero-point energy $\hbar\omega_{\mathbf{q}\nu}/2$. Taylor expanding the BE distribution $\{e^{x}-1\}^{-1} \simeq 1/x - 1/2 + x/12 + \cdots$, we find:

$$\mathcal{J}_z(T\to\infty) = \sum_{\mathbf{q}\nu}\left\{\frac{k_BT}{\hbar\omega_{\mathbf{q}\nu}}+\frac{\hbar\omega_{\mathbf{q}\nu}}{12k_BT}\right\}\ell^{s}_{\mathbf{q}\nu} \quad . \tag{8.21}$$

Noting the completeness relation $\sum_{\nu}\boldsymbol{\varepsilon}^{\dagger}_{\mathbf{q}\nu}\otimes\boldsymbol{\varepsilon}_{\mathbf{q}\nu} = \mathbb{1}_{2n\times 2n}$, the closure relation for these orthonormal atomic displacements can be shown [90] to yield

$$\sum_{\nu}\frac{(\boldsymbol{\varepsilon}_{\mathbf{q}\nu})^{i}(\boldsymbol{\varepsilon}^{*}_{\mathbf{q}\nu})^{j}}{\omega_{\mathbf{q}\nu}} = 0 \quad . \tag{8.22}$$

We finally show that at high temperature, there cannot be spin angular momentum in the system. This is consistent with the notion that at high temperature, atoms are equally likely to be displaced in all directions, yielding cancelling contributions to the spin PAM:

$$\lim_{T\to\infty}\mathcal{J}_z(T)=\sum_{\mathbf{q}\nu}\ell^s_{\mathbf{q}\nu}\frac{k_BT}{\hbar\omega_{\mathbf{q}\nu}}+\ell^s_{\mathbf{q}\nu}\frac{\hbar\omega_{\mathbf{q}\nu}}{k_BT}=\sum_{\substack{\mathbf{q}\\ j,i}}M_{ji}\cancelto{0}{\sum_{\nu}\frac{(\boldsymbol{\varepsilon}_{\mathbf{q}\nu})^i(\boldsymbol{\varepsilon}^*_{\mathbf{q}\nu})^j}{\omega_{\mathbf{q}\nu}}T}+\frac{1}{k_BT}\ell^s_{\mathbf{q}\nu}\hbar\omega_{\mathbf{q}\nu}=0 \tag{8.23}$$

There are additional constraints on this PAM that restrict the present of chiral phonons in standard systems. Firstly, conservation of angular momentum dictates that the spin angular momentum of the phonon modes must cancel, namely:

$$\sum_{\nu}\ell^s_{\mathbf{q}\nu}=\sum_{\nu}\boldsymbol{\varepsilon}^\dagger_{\mathbf{q}\nu}M\boldsymbol{\varepsilon}_{\mathbf{q}\nu}\hbar=i\hbar\sum_{\nu}\sum_{\kappa}\left[(\boldsymbol{\varepsilon}^*_{\mathbf{q}\nu\kappa})^y(\boldsymbol{\varepsilon}_{\mathbf{q}\nu\kappa})^x-(\boldsymbol{\varepsilon}^*_{\mathbf{q}\nu\kappa})^x(\boldsymbol{\varepsilon}_{\mathbf{q}\nu\kappa})^y\right]=0\quad . \tag{8.24}$$

Furthermore, there cannot be phonon PAM in systems with no spin-phonon interaction. In such systems, we completely describe the trivial phonon system by solving the dynamical matrix equation $\hat{D}(\mathbf{q})\boldsymbol{\varepsilon}_{\mathbf{q}\nu}=\omega^2_{\mathbf{q}\nu}\boldsymbol{\varepsilon}_{\mathbf{q}\nu}$. In such a system, the eigenvalues and eigenvectors satisfy $\omega_{-\mathbf{q}\nu}=\omega_{\mathbf{q}\nu}$ and $\boldsymbol{\varepsilon}_{-\mathbf{q}\nu}=\boldsymbol{\varepsilon}_{\mathbf{q}\nu}$ respectively. Noting $M^T=-M$, one can show $\ell^s_{-\mathbf{q}\nu}=-\ell^s_{\mathbf{q}\nu}$, and using the fact the $n_{-\mathbf{q}\nu}=n_{\mathbf{q}\nu}$ we find $\mathcal{J}_z\equiv 0$. In systems with spin-phonon interaction, the dynamical matrix equation will be of the form $[(-i\omega+A)^2+D]\boldsymbol{\varepsilon}=0$, and TRS will be explicitly broken, allowing $\mathcal{J}_z\neq 0$.

In practice, stating that phonons can have PAM does not inherently bridge these theoretical predictions with an experimentally accessible phenomenon. To determine how these chiral phonons manifest themselves in the lattice, we perform a basis transformation on the atomic displacements $\boldsymbol{\varepsilon}$ as follows. Let the new basis be:

$$\begin{aligned}|R_1\rangle&\triangleq\frac{1}{\sqrt{2}}(1\ i\ 0\ \cdots\ 0)^T\qquad |L_1\rangle\triangleq\frac{1}{\sqrt{2}}(1\ -i\ 0\ \cdots\ 0)^T\\ |R_n\rangle&\triangleq\frac{1}{\sqrt{2}}(0\ \cdots\ 0\ 1\ i)^T\qquad |L_n\rangle\triangleq\frac{1}{\sqrt{2}}(0\ \cdots\ 0\ 1\ -i)^T\quad .\end{aligned} \tag{8.25}$$

We can define the coefficients of the basis transformation $\boldsymbol{\varepsilon}_{R_\alpha}=\langle R_\alpha|\boldsymbol{\varepsilon}\rangle=(x_\alpha-iy_\alpha)/\sqrt{2}$ and $\boldsymbol{\varepsilon}_{L_\alpha}=\langle L_\alpha|\boldsymbol{\varepsilon}\rangle=(x_\alpha+iy_\alpha)/\sqrt{2}$ s. t. [6] $\boldsymbol{\varepsilon}=\sum_\alpha \boldsymbol{\varepsilon}_{R_\alpha}|R_\alpha\rangle+\boldsymbol{\varepsilon}_{L_\alpha}|L_\alpha\rangle$. We note that we can

[6] We note that this basis transformation is unitary and as such maintains the completeness and closure relations of the eigendisplacements.

define the phonon circular polarization operator

$$\hat{S}_z^{\mathrm{ph}} \triangleq \sum_\alpha \left(|R_\alpha\rangle\langle R_\alpha| - |L_\alpha\rangle\langle L_\alpha| \right) = \begin{pmatrix} 0 & -i \\ i & 0 \end{pmatrix} \otimes \mathbb{1}_{n\times n} \tag{8.26}$$

which is identically equal to the M matrix from before. We can therefore compute the phonon polarisation s_z^{ph} as:

$$s_z^{\mathrm{ph}} = \sum_\alpha \left(|\boldsymbol{\varepsilon}_{R_\alpha}|^2 - |\boldsymbol{\varepsilon}_{L_\alpha}|^2 \right)\hbar = \boldsymbol{\varepsilon}^\dagger \hat{S}_z \boldsymbol{\varepsilon}\hbar = \boldsymbol{\varepsilon}^\dagger M \boldsymbol{\varepsilon}\hbar \triangleq \ell_z^s \quad . \tag{8.27}$$

This shows that phonon circular polarisation and phonon spin angular momenta are entirely equivalent in this formalism, namely that phonons with nonzero PAM must inherently induce circular atomic orbits, see Figure 8.2. By characterizing those modes with nonzero PAM, we can then exactly determine the corresponding real space motion of the atoms in the 2D material.

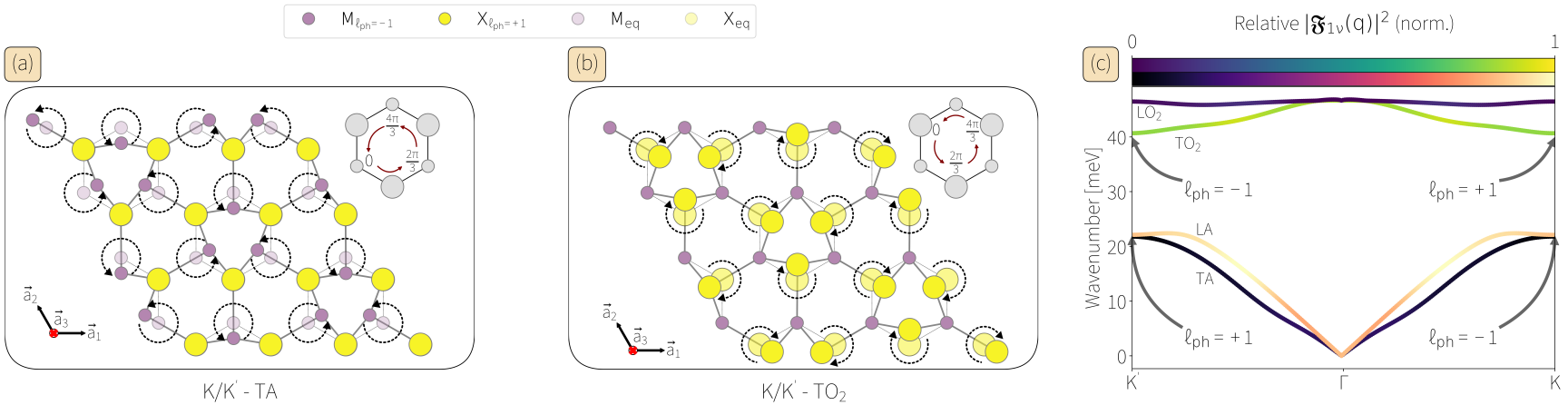

FIGURE 8.2: Chiral phonon in 1L-MX_2 materials. (a) The TA chiral phonon at the K-point ($\ell_{ph} = -1$). The transition metal precesses in a circular orbit about its average position in thermal equilibrium, while the chalcogen atoms are static. (b) The TO_2 chiral phonon at the K-point ($\ell_{ph} = +1$). The chalcogens orbit clockwise and the transition metal remains static for the. Inset on the top right of each panel is the phase correlation of the atomic motions. (c) Phonon normal mode dispersion of chiral (acoustic and E' optical) phonon branches in 1L- MX_2 materials. The relative strength of the one-phonon structure factor for these modes is given by the coloration for the acoustic and optical branches respectively. Note that these modes are the brightest in the proposed UEDS experiment, and are responsible for (non)chiral charge carrrier scattering. The Z-polarized modes are not visible in the geometry proposed and the single phonon structure factor of the E//optical modes are much smaller than for the E' modes shown. The chirality at K of the TA and TO_2 modes are labelled, with the chiralities flipping sign at K' owing to the TRS. Reprinted with permission from Ref [174]. Copyright 2023 American Physical Society.

8.5 GENERATION OF CHIRAL PHONONS

By using ultrashort pulses of circularly polarized light, spin-conserving interband electronic transitions can be driven that impulsively photodope carriers into either the K (σ^+) or K' (σ^-) valley of monolayer TMDs. This nonequilibrium distribution of valley-polarized carriers will depolarize as the carrier distribution thermalizes to the band edges through allowed momentum and energy relaxation channels.

Equation (8.12) shows that linearly-polarized photoexcitation (polarization state $\left(|L\rangle + |R\rangle\right)/\sqrt{2}$) induces interband electronic transitions at the band edges with equal amplitude at TRS related K and K' valleys. The subsequent relaxation of the (hot) charge carriers back to the band edges occurs through interactions with phonons and is determined by the magnitude of the EPC matrix elements $|g^{\nu}_{mn}(\mathbf{k}, \mathbf{q})|^2$, where m, n (ν) index electronic bands (phonon dispersion modes) at electronic (phononic) momentum $\mathbf{k}$ ($\mathbf{q}$). This coupling may be screened by ambient conditions, such as the dielectric environment to which 2D materials are more susceptible, leading to a renormalization of the EPC strength.

Only the ultrafast lattice and charge carrier dynamics following linearly-polarized above band-gap photoexcitation have been previously studied, either with *ab initio* methods [52] or ultrafast electron diffuse scattering techniques in 1L-MoS_2 [84]. Here, the ultrafast relaxation results in a phonon population distribution that is profoundly anisotropic in momentum, but has no momentum-valley polarization. Circularly polarized light and the associated (initial) valley polarized carrier distribtuion change the resulting dynamics profoundly compared to linear polarized excitation. Intervalley momentum and energy relaxation of electrons in the conduction band at K (or K') can only occur via scattering with a chiral phonon of momentum K' (or K) that connects the K-valleys (Figure 8.1b). Intervalley momentum and energy relaxation of holes in the valence band at K (or K') can only occur via scattering with non-chiral phonons of momentum K (or K') that connects

ν	Label	D_{3h}	ω_K^a	s^z_{Mo}	s^z_{S}	$\ell^{s\ b}_{\mathrm{Mo}}$	$\ell^{s\ b}_{\mathrm{S}}$	ℓ^b_{ph}	M_s^c
1	ZA	A_2	21.791	0	−0.325	0	−1	1	−1
2	TA		22.096	0.552	0	1	0	−1	1
3	LA		28.219	−0.301	0.348	−1	1	0	1
4	TO_1	E''	40.959	0	0	0	0	0	−1
5	LO_1	E''	40.064	0	0.500	0	1	0	1
6	TO_2	E'	40.664	0	−0.500	0	−1	1	1
7	LO_2	E'	46.458	−0.206	0.397	−1	1	0	1
8	ZO_2	A_1	48.886	0.083	0	1	0	−1	1
9	ZO_1	A_2''	45.803	0	−0.412	0	−1	1	−1

[a] in units of meV
[b] in units of $\hbar$
[c] mirror symmetry is with respect to the $x-y$ plane

TABLE 8.3: Chirality of phonons in 1L-MoS_2. The symmetries of each oscillation are given by the label and C_{3h} point group representation where applicable. Circular polarizations and spin pseudo-angular momentum of Mo (S) are given by s^z_{Mo} (s^z_{S}) and ℓ^s_{Mo} (ℓ^s_{S}) respectively. Phonon angular momentum is given by ℓ_{ph} and the parity of the mirror symmetry of each mode is given by M_s.

the K (or K') and Γ valleys (Figure 8.1b). Thus, on the picosecond timescale associated with rapid EPC processes, a profoundly momentum-valley polarized phonon distribution is expected. Namely, chiral phonons are expected in the K valley opposite to the initially prepared valley, while non-chiral phonons are expected in the K valley into which carriers were pumped. It is worth noting that in W-based monolayer TMDs, the hole relaxation channel is not present due to the large Γ - K valley energy splitting in the valence band, resulting in a "pure" momentum-valley polarized chiral phonon distribution.

8.6 VALLEY-SELECTIVE DIFFUSE DYNAMICS

As a prototypical spin- and valleytronic 2D hexagonal material, here we examine UEDS as a probe of chiral phonons in 1L-MoS_2 through the lenses of the *ab-initio* scattering theory developed thusfar. Standard density functional perturbation theory (DFPT) allows for computation of the atomic polarization vectors for each phonon mode, computed using the code suites of `QuantumESPRESSO`[185, 186]. We can compute the phonon PAM of each mode by the sum of orbital and spin components for each sublattice that is oscillating

for the valley phonons. Doing so, we obtain the chart in Table 8.3.

The modes with nonzero PAM must jointly satisfy $\{\nu|\ell_{\rm ph} \neq 0 \cup M_s \equiv 1\}$, where even parity of the in-plane mirror symmetry is needed to not get cancelling contributions to the PAM from different locations in the supercell. This allows for the identification of three chiral modes in this system. For chirality $+1$ (in units of $\hbar$), there is only the transverse optical mode of E' symmetry (TO_2), corresponding to the sulfur sublattice oscillating clockwise. For chirality -1, we identify both the transverse acoustic (TA) mode and Z-polarised optical mode of A_1 symmetry (ZO_2). Both these modes involve the oscillation of the moldybdenum sublattice in an anticlockwise direction, but the ZO_2 mode has a much lower degree of polarization (by an order of magnitude) and will not be as readily excited in the generation schemes proposed here.

For the case of monolayer TMDs, the phonon scattering selection rules mean that $\mathfrak{F}_{1\nu}$ for the out-of-plane (Z-polarized) modes and the optical modes of E'' symmetry are very weak in the geometry of these experiments (along the [001] direction). These experiments primarily probe the $\mathbf{q}$-dependent population dynamics of the E' optical and LA/TA modes, which are exactly the modes that are characterized by $\ell_{\rm ph} \neq 0$.

Note 8.2

In the first Born approximation, namely that single phonon scattering dominates the diffuse intensity, we compute the scattering intensities for phonons of chirality ± 1 within the Laval-Born-James theory [65, 66, 67] using modified versions of the codes in the `EPW/ZG` suite of `QuantumESPRESSO`. Band-structure calculations used fully-relativistic norm-conserving Troullier-Martins pseudopotentials [187] and the Perdew-Burke-Ernzerhof (PBE) GGA for the exchange-correlation functional [188]. We employed a planewave energy cutoff of 120 Ry, and a $20 \times 20 \times 1$ Monkhorst-Pack $\mathbf{k}$-grid for the monolayer, and $20 \times 20 \times 20$ for the bulk. In order to avoid spurious interactions among periodic replicas of the monolayers in the out-of-

plane direction, an interlayer vacuum spacing of 18 Å and truncated coulomb interaction were employed [189]. For all calculations, we used the primitive cell of MoS_2, with relaxed lattice parameter of 3.16 Å. Second-order interatomic force constants were computed using DFPT on an $8 \times 8 \times 1$ $\mathbf{q}$-grid for 1L-MoS_2, and a $4 \times 4 \times 4$ $\mathbf{q}$-grid for bulk MoS_2 and Fourier interpolated onto a $256 \times 256 \times 1$ $\mathbf{q}$-grid to compute phonon normal mode dispersions and thus the diffuse scattering patterns.

In this work, we make no attempt to perform a full simulation of the nonequilibrium chiral carrier-phonon interactions that following circularly polarized excitation in 1L-MoS_2. Instead, we present a simplified, but qualitatively accurate model for the nonequilibrium phonon populations that result transiently from valley depolarization driven by inelastic chiral carrier-phonon scattering in order to determine the observable impact on UEDS patterns. To model the effect of the momentum-valley polarized phonon occupations following carrier valley depolarization, we take the nonchiral modes to be occupied according to the BE distribution at room temperature and the chiral modes involved in valley depolarization at an elevated "effective temperature" of 380 K within a Gaussian window of full-width half-max (FWHM) 0.1 reduced lattice units[7] around K (K'). The qualitative features in the diffuse scattering pattern are not sensitive to the precise values of these temperatures. Using the framework described above, we compute UEDS patterns under the nonthermal occupation of phonons.

The signature of chiral phonon emission is the relative diffuse intensities at the K (K') valleys. We can define the phonon momentum-valley anisotropy as:

$$\eta(\tau) \triangleq \frac{I_1(\mathbf{q} = K', \tau) - I_1(\mathbf{q} = K, \tau)}{I_1(\mathbf{q} = K', \tau) + I_1(\mathbf{q} = K, \tau)} \quad . \tag{8.28}$$

[7] This value is the average FWHM of the s^z distribution for the respective orbiting sublattices of the chiral modes. The results herein do not depend sensitively on the exact value chosen.

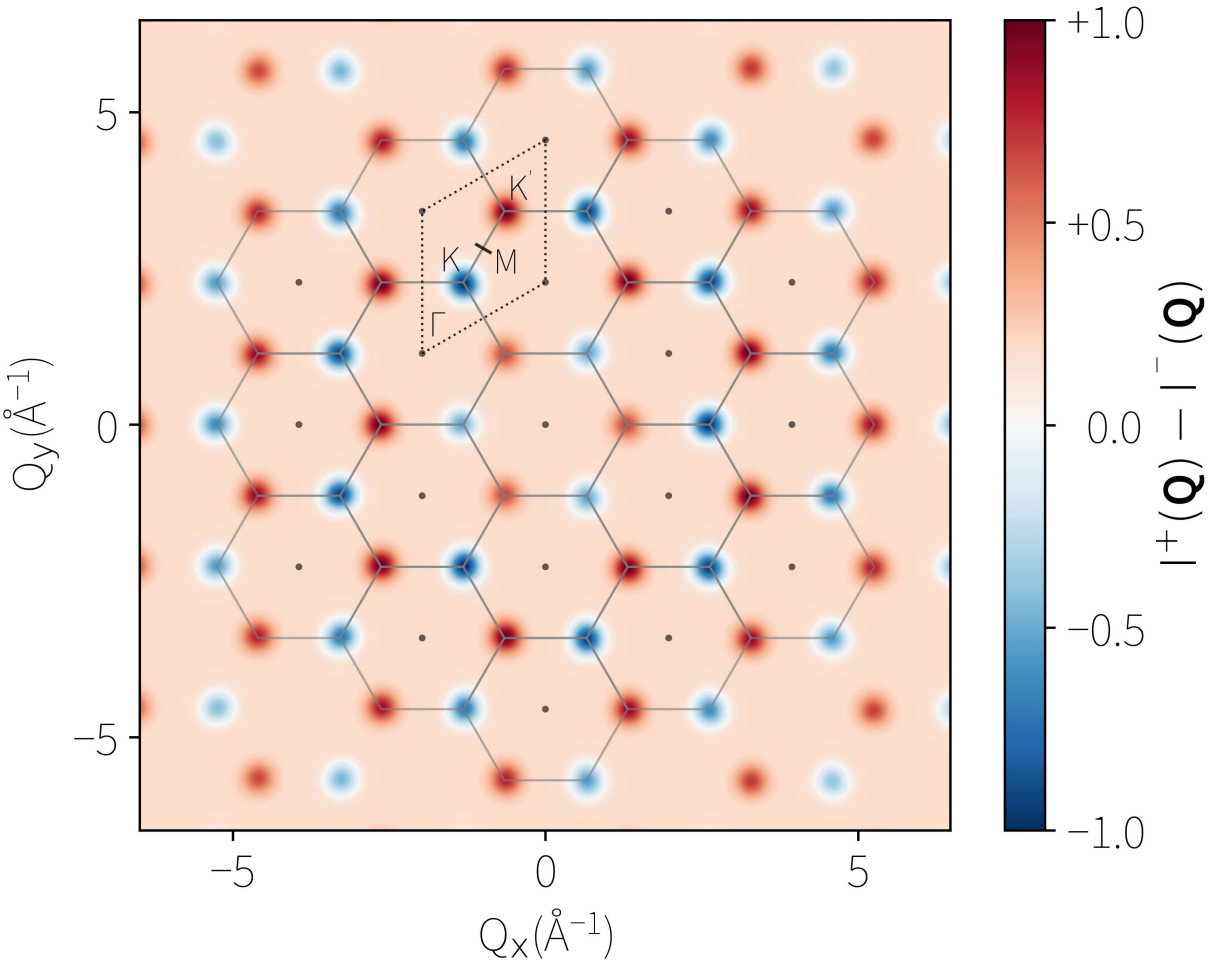

FIGURE 8.3: The diffuse scattering intensity dichroism induced by charge carrier depolarization following circularly-polarized photoexcitation, taken as $I^+ - I^-$. A selection of BZs are outlined, with the dots representing the Γ points, emphasizing the locality of the features around the K valleys. Reprinted with permission from Ref [174]. Copyright 2023 American Physical Society.

For initial carrier polarization at K, pump-probe delay times where $\eta > 0$ are indicative of dynamics dominated by a K' chiral phonon assisted conduction electron K-K' scattering, as opposed to $\eta < 0$ where nonchiral assisted valence hole K-Γ scattering is dominant. The differential diffuse scattering intensity predicted for photoexcitation of handedness σ^+ (thus $\ell_{\text{ph}} = -1$, the TA mode with occupancy centered at K') minus σ^- (thus $\ell_{\text{ph}} = +1$, the TO_2 mode with occupancy centered at K) is shown in Figure 8.3. The differential pattern shows clear features at the K points associated with nonequilibrium populations of chiral phonons that should be measurable in circularly polarized pump-probe experi-

ments. The time-constants associated with the red (K') and blue (K) intensity features in Figure 8.3 provides a measure of the strength of chiral carrier-phonon coupling to the TA and TO_2 chiral modes respectively. Further, the intensity contrast visible in Figure 8.3 is reduced (or disappears entirely) if carrier valley-depolarization occurs by means unrelated to inelastic phonon scattering on a timescale shorter than that associated with EPC, e.g. via the exchange interaction. Thus, these observable features in the differential phonon-diffuse intensity provide a sensitive test of phonon-assisted valley depolarization in monolayer TMDs, allowing for the identification of regimes in time and values of n_0 where chiral phonon emission, electron-hole exchange, or carrier-carrier scattering become dominant with regards to the charge carrier depolarization. The profound impact of the nonequilibrium momentum-valley polarized chiral phonon populations on diffuse scattering contrast in K and K' regions that emerges transiently during valley-depolarization of the carrier system due to EPC (Figure 8.3) can be contrasted with the expected differences in phonon diffuse scattering between monolayer and bulk samples at thermal equilibrium. Chiral phonons manifest in monolayer TMDs, with distinct phonon-diffuse signatures in momentum space, even at thermal equilibrium. However, the momentum anisotropy due to chiral phonons is not evident in the differential diffuse scattering intensity comparing bulk and monolayer MoS_2 at thermal equilibrium shown in Figure 8.4. There are intensity contrasts visible in this difference pattern, but none at momentum positions associated with the K-point chiral modes, thus necessitating nonequilibrium measurements to observe chiral phonon emission.

While we did not compute fully the TDBE for this system, taking into account the angular momentum conservation, it has recently been performed by collaborators [190], where the theoretical predictions of this work have been exactly validated.

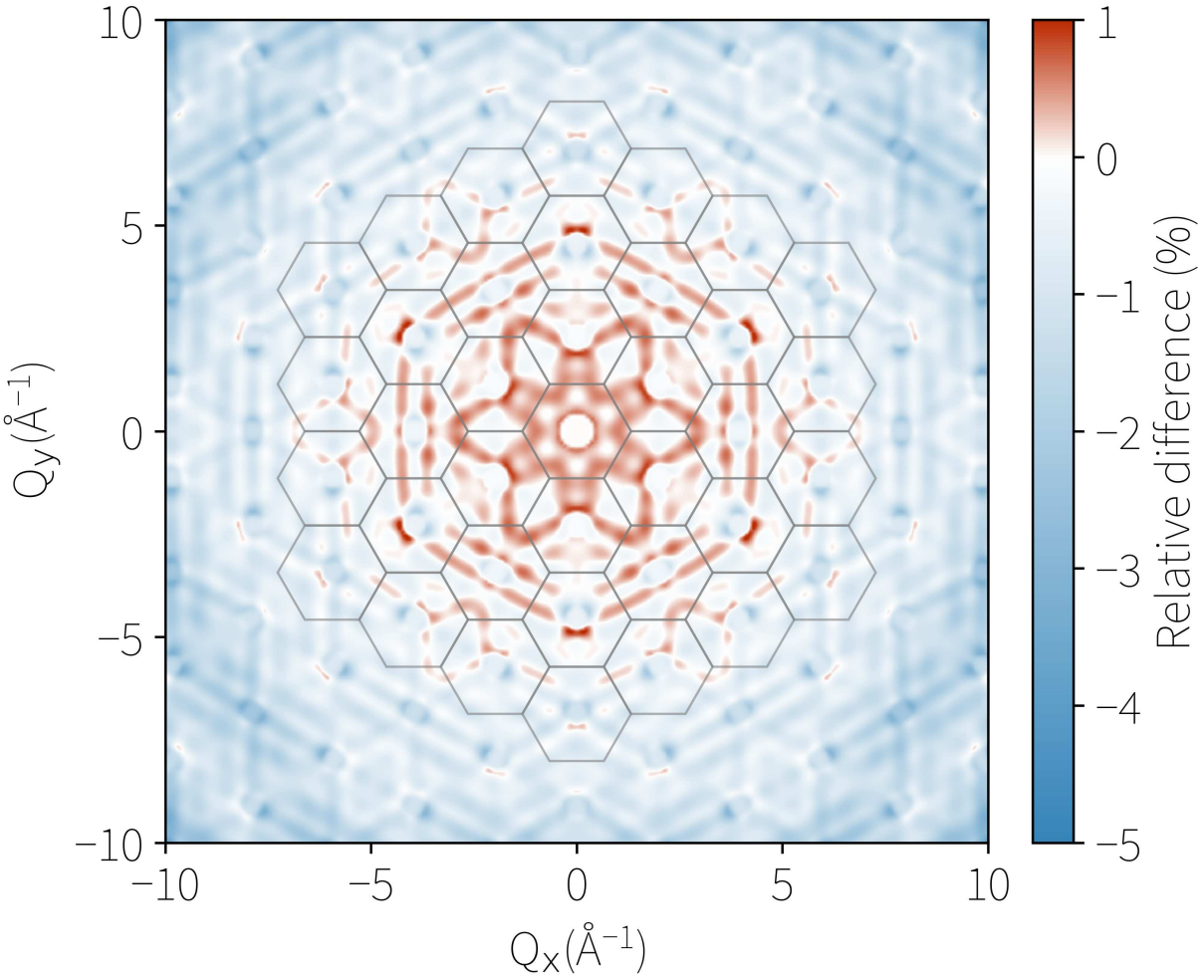

FIGURE 8.4: Relative percent difference of bulk diffuse scattering versus monolayer scattering $(I^1_{\text{bulk}} - I^1_{\text{ml}})/I^1_{\text{bulk}}$. There is clear structure across the image showing significant changes in diffuse scattering between multi-layer and monolayer, but there are no features around the K valleys, indicating that the observation of chiral phonons cannot be done in an equilibrium measurement. Reprinted with permission from Ref [174]. Copyright 2023 American Physical Society.

8.7 OUTLOOK

The properties of monolayer hexagonal lattices have been shown to yield chiral electron-phonon interactions that can be a key feature of carrier valley depolarization processes following photoexcitation with circularly polarized light. The allowed momentum and energy relaxation processes involved populate valley-polarized, nonequilibrium distributions of chiral phonons whose circular atomic oribts and angular momentum are required to conserve total angular momentum of the coupled electron-lattice system dur-

ing valley depolarization. Further, these chiral carrier-phonons interactions are uniquely hallmarked by increases in chiral phonon occupancy at either K or K' points in the BZ. As a state-of-the-art technique for the direct measurement of nonequilibrium phonon occupancy with full momentum resolution, UEDS can directly identify the resulting valley polarized chiral phonon distributions in a pump-probe experiment. Further, the technique will also be able to distinguish between chiral and non-chiral dominated scattering regimes occurring on the picosecond timescale provided data of sufficient signal-to-noise ratio and sample quality.

Part IV

POLARONIC MATERIALS

9

To the harmonic approximation and beyond

"Theory and practice sometimes clash.
And when that happens, theory loses.
Every single time."
—Linus Torvalds

Tin selenide (SnSe) is a unique material in that it pretty completely violates the typical assumptions of condensed-matter analysis, namely that the material is "harmonic". Here, harmonic refers to the notion that pair-wise interactions between atoms, and the resulting forces between them, are sufficient to describe the equilibrium vibronic state of the lattice. This assumptions crops up in many places, including crucially the calculation of phonon dispersion in typical DFT codes (for example Eq. (5.2)). A layered material, SnSe is what is known as a *thermoelectric*, with an outstandingly high figure-of-merit (FOM) zT [191, 192, 193]. This class of materials is extremely desirable for applications where heat sources are abundant, while sources of electricities are not (namely, Mars), for the recuperation of energy lost to heat (internal combustion engines, power processing plants, etc), and others. The very nature of this class of materials is complicated to understand, as it relies on a highly convoluted interaction between the electronic system of the material and its lattice, in ways not yet entirely understood, especially with respect to EPC. This combination of attractive industrial applications and low-level scientific

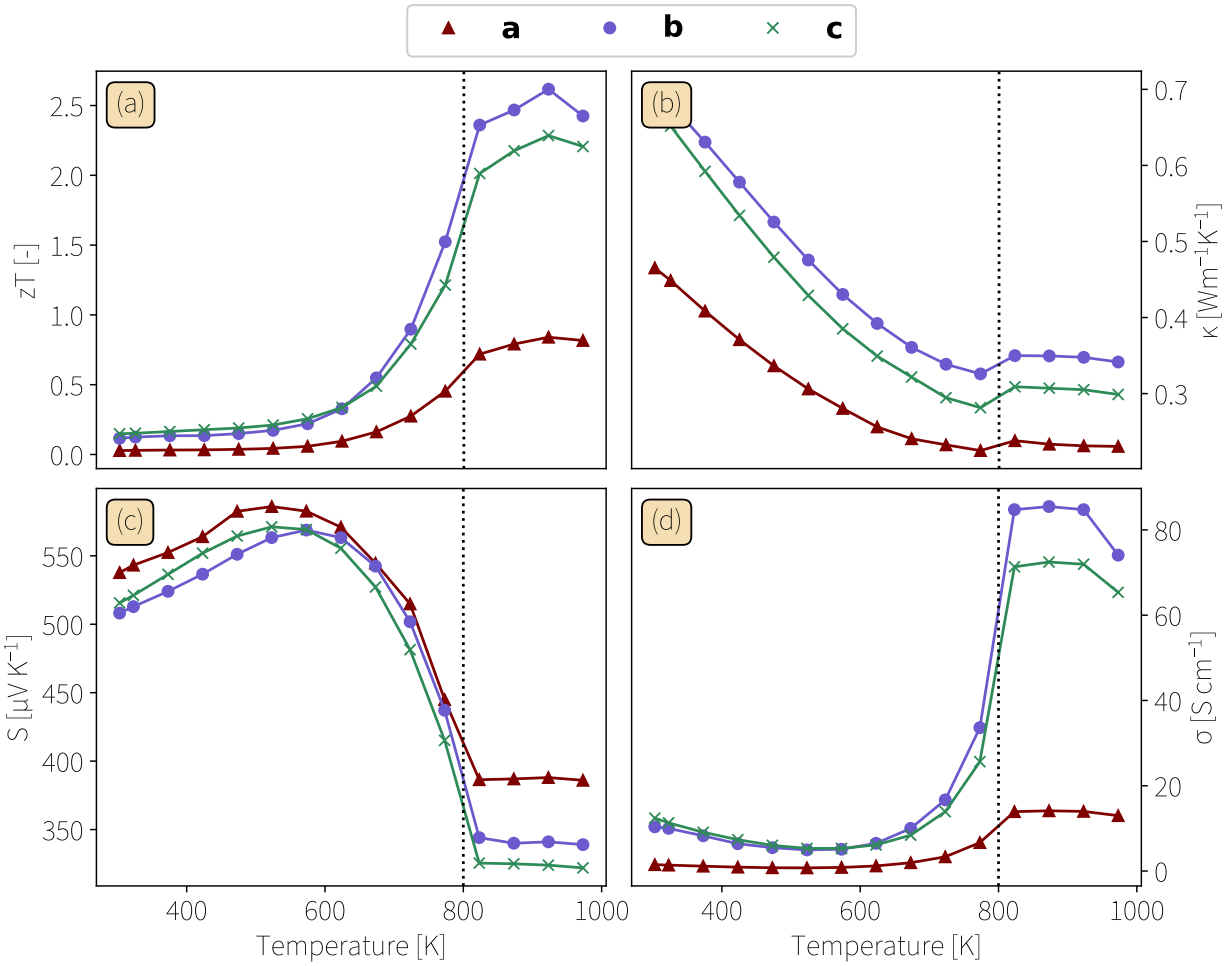

FIGURE 9.1: zT of SnSe versus temperature, data taken from [191]. (a) The thermoelectric FOM zT across the phase transition from the *Pnma* to the *Cmcm* phase, where the FOM increasing massively for the reasons outlined in the main text. (b) The lattice thermal conductivity, showing the needed decrease to afford such a large increase in zT. (c) The Seebeck coefficient S, which reflects the increase in carrier mobility in the *Cmcm* phase. (d) The specific electrical conductivity, which increases in the *Cmcm* phase by almost $\times 5$ compared to the *Pnma* phase. The unit cells have been rendered using the VESTA visualization software.

intrigue has spawned much research on this material in recent years.

Definition 9 (Thermoelectric effect)**.** Process through which a temperature gradient induces an electric potential inside a material or an electric current produces a temperature gradient. This can be compartmentalized into the *Seebeck* effect [194] (creating a voltage drop from a temperature gradient), the *Peltier* effect [195] (creating a heat flux from electric current), and the *Thompson* effect [196] (heating or cooling in the presence of both an electric current and temperature gradient).

The FOM for these materials will depend on a few material properties that we address in turn.

- THE SEEBECK COEFFICIENT

  Known as the thermopower of a material, the Seebeck coefficient $S = -\Delta V/\Delta T$ is a simple measure of the amount of electric potential induced (ΔV) for a given gradient in temperature ΔT, and therefore has units $\mu V/K$. A nice physical picture of S comes by a re-arrangement of the units:

$$\frac{V}{K} = \frac{J}{K-e} = \frac{[S]}{[Q]} \tag{9.1}$$

  where the new interpretation is that the Seebeck coefficient gives the entropy per unit charge carried by the moving charge carriers in the material (negative for electrons, positive for holes). It is clear that any thermoelectric FOM should be at least linearly proportional to this coefficient: if the material has no induced potential drop for an applied thermal gradient, then by definition it is not a thermoelectric!

- SPECIFIC ELECTRICAL CONDUCTIVITY

  The intrinsic measure of a materials ability to resist electric current, the specific electrical conductivity σ relates the ability of electrons in the material to freely move, to the effective resistance to current the material provides. In metals, because many of the electrons reside in energy near the Fermi level, the electrical conductivity will be high. Again, it is clear that the thermoelectric FOM should be related to this: if a material cannot move charges freely, then even for high S, it will be impossible to realize a practical device using this material as a thermoelectric, since the total electric power it provides would be low.

- THERMAL CONDUCTIVITY

  A direct measure of the materials ability to propagate heat, the thermal conductivity κ implies that materials with extremely rigid atomic bonds would propagate heat less easily

than other materials. The rate of heat transport is directly related to the magnitude of κ, necessitating its inclusion in the thermoelectric FOM.

We can now combine all these ingredients into the FOM [197]:

$$zT = \frac{\sigma S^2 T}{\kappa} \tag{9.2}$$

where the FOM is by convention defined for a temperature T, which should be interpreted as "for the given thermal energy at temperature T, how well does this material induce the thermoelectric effect?".

A materials engineer might see this figure of merit and be excited by the prospect that there are clear components that can serve as "tuning knobs", fine tuning the FOM one degree of freedom at a time. Unfortunately, owing to EPC and other effects, the ingredients in zT are all intertwined, and cannot be easily separated. For example, the total effective thermal conductivity in a material is given as a sum of the electron contribution and the phonon contribution $\kappa = \kappa_e + \kappa_{ph}$, where the Widermann-Franz law shows:

$$\kappa_e = \frac{\pi^2}{3}\left(\frac{k_B}{e}\right)^2 \sigma T = \sigma L T \tag{9.3}$$

where $L \simeq 2.44 \times 10^{-8}\,\mathrm{V^2K^{-2}}$ is the *Lorenz number*, suggesting that increasing σ yields increasing κ_e, dropping zT. The electron (phonon) component will dominate in metals (semiconductors), so the material of interest should keep the ratio κ_{ph}/κ_e low, minimizing κ_{ph} and maximizing σ, implying a highly doped semiconductor. It is for this very reason that the good thermoelectric materials should satisfy the following:

- Phonons, which directly control κ, must scatter as much as possible, like in a glass, thus lowering κ
- Electrons, which directly control σ, must scatter as little as possible, like in a crystal, thus maintaining σ

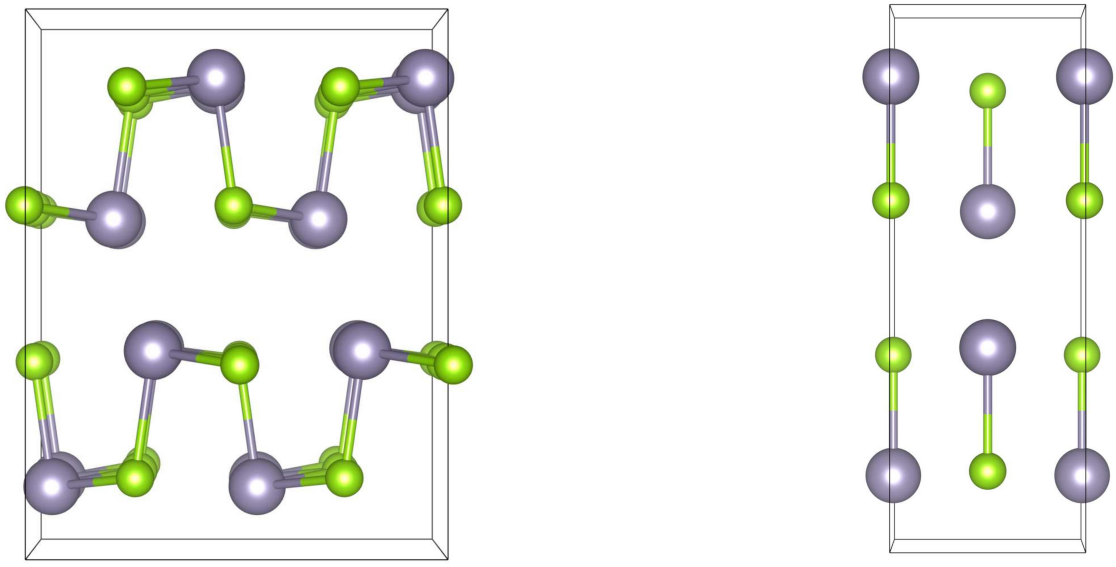

FIGURE 9.2: Atomic configurations of SnSe, with the *Pnma* configuration of SnSe, for example at room temperature, on the left and the *Cmcm* configuration of SnSe, for example at high temperatures, on the right.

The combination of these effects leads to the sobriquet *phonon-glass electron-crystal* for thermoelectrics. How does one achieve this phonon-glass electron-crystal condition in a material? Material scientists have historically used the following tactics:

- ALLOYS can induce spatial variation in the composition density of a material, introduce site vacancies, or dope materials with atoms that have large vibrational amplitudes s. t. phonons will scatter often [198].

- COMPLEX CRYSTALS take inspiration from superconductors, where distortions are contained by the phonon glass that does not interupt the electron crystal [199]

- NANOSTRUCTURES utilizes the direct manipulation of the crystal configuration on the nanoscale such as to induces atomic configurations that direclty result in low κ, but leave the intrinsic electronic conductivity untouched, either through laser ablation techniques, 3D printing, etc [200].

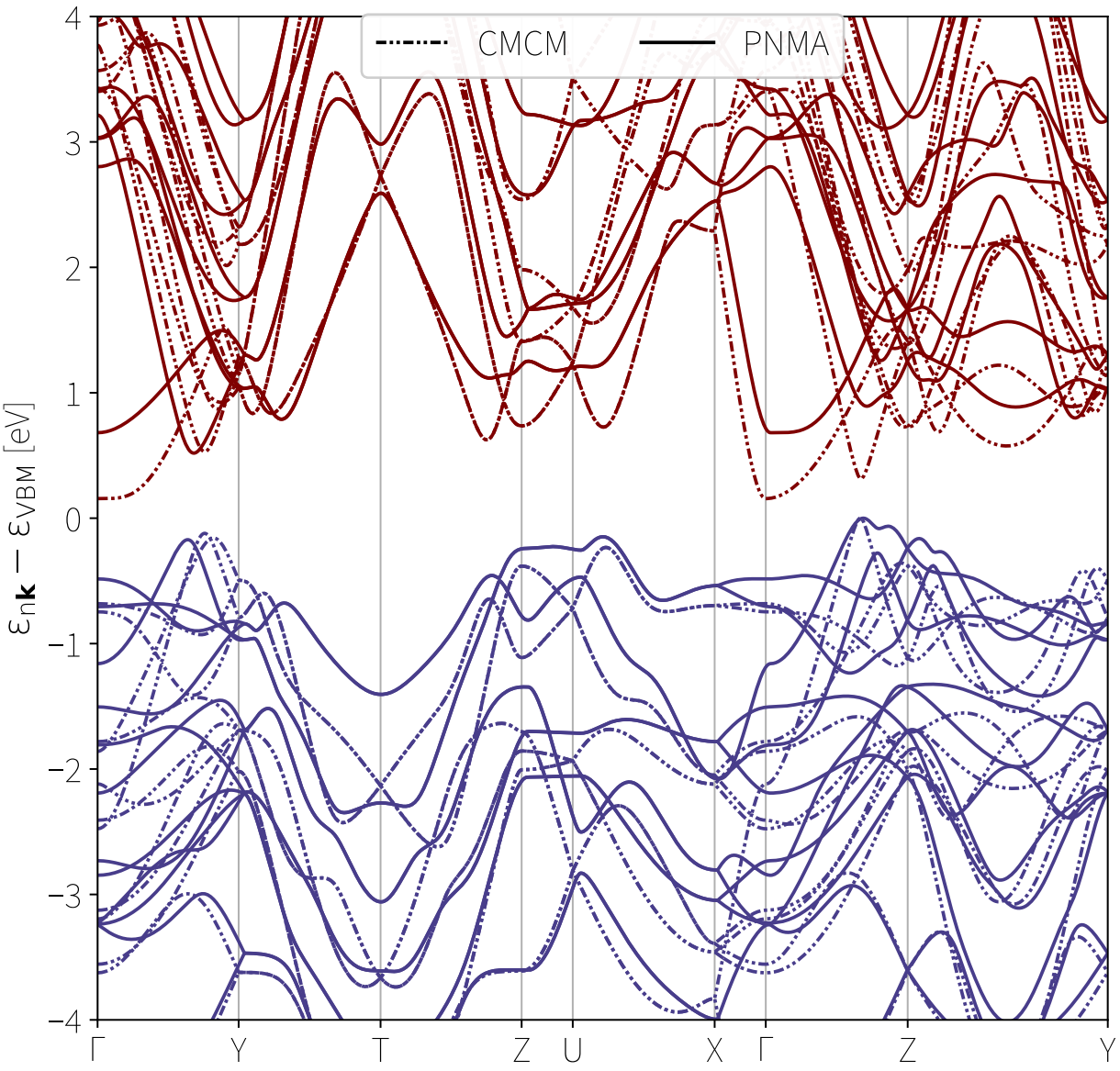

FIGURE 9.3: Electronic band structures of SnSe in the *Pnma* and *Cmcm* phases. In the *Pnma* phase, SnSe is an indirect band semiconductor of bandgap 51.9 meV, where the conduction band minimum at $\frac{2}{3}Y$. In *Cmcm*, it is direct bandgap at 15.6 meV with the conduction band minimum now at Γ.

9.1 ELECTRONIC PROPERTIES

SnSe in both phases has a *complicated* electronic band structure, consisting of mostly Se-4p orbitals in the valence band and Sn-5p orbitals in the conduction band [201, 202]. Indirect in the *Pnma* phase, and direct in the *Cmcm* phase, this p-type semiconductor has its electronic band structures shown in Figure 9.3.

9.1.1 *Crystallographic properties*

The mission is clear: to understand why SnSe has such a good zT at room temperature equates to understanding why it has such a low κ. The room temperature phase is the orthorhombic phase (Hermann-Maugin spacegroup *Pnma*, Schönflies symbol D_{2h}^{16}, corresponding to a zigzag-armchair configuration within each layer), where the room temperature $\kappa \simeq 1\,\mathrm{Wm^{-1}K^{-1}}$ in the plane of the layer is particular low. As with the monolayer TMDs, the 2D nature of an individual layer of SnSe confines charge carriers and provides additional phonon scattering channels [200].

Going to high temperatures, at around $T \sim 800\,\mathrm{K}$, there is a structural phase transition that straightens the zigzag and armchair directions of the layers (Hermann-Maugin spacegroup *Cmcm*, Schönflies symbol D_{2h}^{17}) that not only reduces the bandgap of the material (putting more electrons close to the Fermi level), but increases the carrier mobility [191], both increasing σ and thus zT. The conventional 8-atom unit cells for both of these phases are rendered in Figure 9.2, and the atomic positions (in terms of the lattice vectors) are:

$$\begin{pmatrix} \mathrm{Se}_1 & \mathrm{Se}_2 & \mathrm{Se}_3 & \mathrm{Se}_4 & \mathrm{Sn}_1 & \mathrm{Sn}_2 & \mathrm{Sn}_3 & \mathrm{Sn}_4 \end{pmatrix} = \begin{pmatrix} \mathbf{a} & \mathbf{b} & \mathbf{c} \end{pmatrix} \times \left\{ \begin{array}{ll} \begin{pmatrix} 0.14 & 0.36 & 0.64 & 0.86 & 0.12 & 0.38 & 0.62 & 0.88 \\ 3/4 & 1/4 & 3/4 & 1/4 & 1/4 & 3/4 & 1/4 & 3/4 \\ 0.52 & 0.02 & 0.98 & 0.48 & 0.09 & 0.59 & 0.41 & 0.91 \end{pmatrix} & \textit{Pnma} \\ \\ \begin{pmatrix} 0.14 & 0.36 & 0.64 & 0.86 & 0.12 & 0.38 & 0.62 & 0.88 \\ 1/2 & 0.00 & 0.00 & 1/2 & 0.00 & 1/2 & 1/2 & 0.00 \\ 3/4 & 1/4 & 3/4 & 1/4 & 1/4 & 3/4 & 1/4 & 3/4 \end{pmatrix} & \textit{Cmcm} \end{array} \right. \tag{9.4}$$

The relaxed lattice parameters for the *Pnma* phase are a =11.55 Å, b =4.172 Å, and

c =4.483 Å, with **a** being the stacking direction. For the *Cmcm* phase in the conventional unit cell, the lattice parameters are a =11.76 Å, b =4.26 Å, and c =4.24 Å.

9.2 PREVIOUS RESEARCH TO DATE

Experimental studies have often probed individual aspects of the material, such as exploring the anharmonic dampening of the low energy modes [203], by disecting the polar phonon modes via their polaronic signatures in angle-resolved photoemission spectroscopy (ARPES) spectra [204], which independently do not provide a complete picture. To tackle this, studies have relied on ultrafast x-ray or electron (in)elastic scattering to unravel the interplay between the electronic system and the (potentially anharmonic) lattice, as such approaches can even be sensitive to spin- and valley-tronic effects like chiral phonons in 2D materials [174].

Unfortunately, these scattering experiments to date have offered competing interpretations of the resulting behaviour. Following photoexcitation, ultrafast elastic x-ray scattering have posited that the material prefers a metastable atomic configuration commensurate with the orthorhombic distortion of the rocksalt *Immm* structure [205], which they determined by computing the atomic mean-squared displacements via the elastic Bragg peak transient intensity. However, other work used momentum-resolved UEDS, which failed to show such behaviour in the elastic scattering, as well as offered unique features in the resulting phonon occupancy following photoexcitation [118]. This momentum-resolved data showed extreme anisotropy in the resulting dynamics for scattering vectors **Q** parallel or perpendicular to the **c** crystal axis, which cannot be explained by a simple deformation of the lattice into the proposed metastable *Immm* phase. The unusual anisotropy in the data was interpreted as evidence of polaron formation. This interpretation was supported by a simple point defect model for polaron diffuse scattering that showed excellent agreement with the momentum-dependence of

the diffuse scattering for *a-priori* reasonable polaron sizes. The extremely polar lattice of SnSe seemed to provide further qualitative support (Born effective charges of -3.8 on Se and +3.8 on Sn).

In the following chapters, we first explore from first-principles the properties of polarons and their diffuse scattering signatures. After validating the approach in a verified polaronic material, we proceed to determine the properties of polarons in SnSe, at a level of detail far beyond the point defect model, in the room temperature phase. We continue by disecting the behaviour of the EPC in SnSe, then quantifying the anharmonicity of the lattice, thus determining how such strong anharmonic effects are made manifest in scattering experiments. This work aims to offer a fresh interpretation of previous ultrafast scattering data in light of our new findings. Namely, neither electron nor hole polarons are found to exist in the room temperature phase of SnSe, and that the momentum anisotropy found in these experiments matches identically to behaviours in the EPC of the material and anharmonic phonon lifetimes.

10

Polaron-Diffuse Scattering

The first successful *ab-initio* theory of polarons was the Landau-Pekar model [206, 207], where the underlying assumption was that the electron wave function extends over many unit cells, allowing for the neglect of any details of the lattice in order to use continuum electrostatics. By adding a single electron to system with wavefunction ψ extending spatially over many unit cells, we can readily identify the change in system energy from simple sums of kinetic and potential energies associated with the new wavefunction [208]:

$$E_{LP} = \underbrace{\frac{\hbar^2}{2m^*}\int d\mathbf{r}|\nabla\psi|^2}_{\text{band energy of extra } e^-} + \underbrace{\frac{1}{2}\int d\mathbf{r}\,\mathbf{E}\cdot\mathbf{D}}_{\text{electrostatic energy of dielectric}} \quad . \tag{10.1}$$

The displacement field will be related to the density of free carriers (ergo to the wavefunction) via Gauss's law:

$$\begin{aligned} \nabla\cdot\mathbf{D} = -e|\psi(\mathbf{r})|^2 \Leftrightarrow \mathbf{D} &= \frac{e}{4\pi}\nabla\int d\mathbf{r}'\frac{|\psi(\mathbf{r})'|^2}{|\mathbf{r}-\mathbf{r}'|} \\ \overset{\mathbf{D}=\epsilon_0\epsilon^0\mathbf{E}}{\Longrightarrow}\quad \frac{1}{2}\int d\mathbf{r}\,\mathbf{E}\cdot\mathbf{D} &= \frac{1}{2}\frac{e^2}{4\pi\epsilon_0}\frac{1}{\epsilon^0}\int d\mathbf{r}d\mathbf{r}'\frac{|\psi(\mathbf{r})|^2|\psi(\mathbf{r}')|^2}{|\mathbf{r}-\mathbf{r}'|} \quad . \end{aligned} \tag{10.2}$$

Yet, since the electronic contribution to the dielectric screening is already accounted for by the band structure in the first term of Eq. (10.1), we subtract the portion corresponding to ionic screening turned off ($\epsilon^0 \to \epsilon^\infty$, the high-frequency permittivity). Defining the

reicprocal effective permittivity $1/\kappa = 1/\epsilon^{\infty} - 1/\epsilon^{0}$, we now find a complete expression for the ground-state energy of the LP polaron:

$$E'_{LP}[\psi] = \frac{\hbar^2}{2m^*}\int d\mathbf{r}|\nabla\psi(\mathbf{r})|^2 - \frac{1}{2}\frac{e^2}{4\pi\epsilon_0}\frac{1}{\kappa}\int d\mathbf{r}\,d\mathbf{r}'\frac{|\psi(\mathbf{r})|^2|\psi(\mathbf{r}')|^2}{|\mathbf{r}-\mathbf{r}'|} - \underbrace{\varpi\left(\int d\mathbf{r}|\psi(\mathbf{r})|^2 - 1\right)}_{\text{Lagrange multiplier } \varpi} \tag{10.3}$$

where we have added a Lagrange multiplier ϖ to enforce the constraint that the resulting new wavefunction should still be normalised $\int d\mathbf{r}|\psi(\mathbf{r})|^2 = 1$. Taking functional derivatives with respect to ϖ and ψ^* yield Schrödinger problem for the wavefunction:

$$\frac{\delta E'_{LP}}{\delta\varpi} : \int d\mathbf{r}|\psi(\mathbf{r})|^2 = 1 \tag{10.4a}$$

$$\frac{\delta E'_{LP}}{\delta\psi^*} : -\frac{\hbar^2}{2m^*}\nabla^2\psi(\mathbf{r}) - \frac{e^2}{4\pi\epsilon_0}\frac{1}{\kappa}\int d\mathbf{r}'\frac{|\psi(\mathbf{r}')|^2}{|\mathbf{r}-\mathbf{r}'|}\psi(\mathbf{r}) = \varpi\psi(\mathbf{r}) \quad . \tag{10.4b}$$

Projection onto ψ^* then yields the energy of the LP polaron:

$$E_{LP}[\psi] = \varpi + \frac{1}{2}\frac{e^2}{4\pi\epsilon}\frac{1}{\kappa}\int d\mathbf{r}d\mathbf{r}'\frac{|\psi(\mathbf{r})|^2|\psi(\mathbf{r}')|^2}{|\mathbf{r}-\mathbf{r}'|} \tag{10.5}$$

It can be shown ground state energy ($\min E_{LP}[\psi]$) is physical only for $1/\kappa > 0 \Leftrightarrow \epsilon^0 > \epsilon^{\infty}$ *i.e.* polar crystals (ruling out all polarons in non-polar semiconductors) [209, 210]. Further, since EPC has contributions from short- and long-range lattice distortions and is therefore related to the ionic dielectric constribution [211], this model rules out (piezo)acoustic polarons. What's more, it assumes isotropic dielectric behaviour throughout the crystal (making polarons in layered materials not possible for instance), as well as ignoring all knowledge of the nature of the lattice. Unfortunately, this model is essentially never valid since it assumes large polarons to therefore use continuum electrostatics, but is valid mainly for strong coupling and therefore small polarons [212]. To combat this limitation and create a theoretical view of polarons that further allowed for polarons in nonpolar crystals, as well as acoustic polarons, Sio *et al* began from density functional theory (DFT) to include EPC from the premise [213].

10.1 A DFT APPROACH TO POLARONS

Denoting the equilibrium electronic wavefunctions $\psi^0_{\nu\mathbf{k}}$ with atoms at equilibrium positions plus displacements, $\boldsymbol{\tau} = \boldsymbol{\tau}^0 + \Delta\boldsymbol{\tau}$, we expand the DFT energy in terms of second-order force constants $C^0_{\kappa\alpha p,\kappa'\alpha' p'}$, nonequilibrium atomic displacements for a single electron (hole) in the conduction (valence) band with wavefunction ψ and change in charge density $\Delta n = |\psi|^2$ up to $\mathcal{O}(\Delta\boldsymbol{\tau}^3) + \mathcal{O}(\Delta n^2)$:

$$\begin{aligned} E^{\mathrm{DFT}}[\{\psi_\nu\mathbf{k}\},\{\boldsymbol{\tau}_{\kappa\alpha}\}] = E^{\mathrm{DFT}}[\{\psi^0_\nu\mathbf{k}\},\{\boldsymbol{\tau}^0_{\kappa\alpha}\}] + \frac{1}{2}\sum_{\substack{\kappa\alpha p\\ \kappa'\alpha' p}} C^0_{\kappa\alpha p,\kappa'\alpha' p'}\Delta\tau_{\kappa\alpha p}\Delta\tau_{\kappa'\alpha' p'} + \mathcal{O}(\Delta\boldsymbol{\tau}^3) \\ + E^{\mathrm{Ha}}\int d\mathbf{r}\psi^*(\mathbf{r})\hat{\mathcal{H}}^{\mathrm{KS}}[n(\mathbf{r}),\{\boldsymbol{\tau}_{\kappa p}\}]\psi(\mathbf{r}) \\ + \frac{1}{2}E^{\mathrm{Ha}}\Bigg[\int d\mathbf{r}d\mathbf{r}'\frac{1}{E^{\mathrm{Ha}}}\frac{\delta^2 E^{\mathrm{xc}}}{(\delta n^\uparrow)^2}\Delta n(\mathbf{r})\Delta n(\mathbf{r}') \\ + \sum_{\mathbf{T}}\int d\mathbf{r}d\mathbf{r}'\frac{[\Delta n(\mathbf{r}) - 1/N_p\Omega][\Delta n(\mathbf{r}') - 1/N_p\Omega]}{|\mathbf{r}-\mathbf{r}'-\mathbf{T}|/a_0}\Bigg] \quad . \end{aligned} \tag{10.6}$$

$\mathcal{O}(\Delta n^2)$

$\mathcal{O}(\Delta n^2)$

After expanding the KS Hamiltonian into a perturbation picture with respect to the atomic displacements, namely $\hat{\mathcal{H}}^{\mathrm{KS}}[n(\mathbf{r}),\{\boldsymbol{\tau}_{\kappa p}\}] = \hat{\mathcal{H}}^{\mathrm{KS}}[n^0(\mathbf{r}),\{\boldsymbol{\tau}^0_{\kappa p}\}] + \sum_{\kappa\alpha p}\frac{\partial V^{\mathrm{KS}}_0}{\partial\tau_{\kappa\alpha p}}\Delta\tau_{\kappa\alpha p} + \mathcal{O}(\Delta\tau^2)$, we find now our polaron energy functional:

$$\begin{aligned} E_P[\psi,\{\Delta\tau_{\kappa\alpha p}\}] = E_P[\psi^0,\{\Delta\boldsymbol{\tau}^0_{\kappa p}\}] + \frac{1}{2}\sum_{\substack{\kappa\alpha p\\ \kappa'\alpha' p}} C^0_{\kappa\alpha p,\kappa'\alpha' p'}\Delta\tau_{\kappa\alpha p}\Delta\tau_{\kappa'\alpha' p'} \\ + \int d\mathbf{r}\psi^*(\mathbf{r})\left[\hat{\mathcal{H}}^{\mathrm{KS}}_0 + \sum_{\kappa\alpha p}\frac{\partial V^{\mathrm{KS}}_0}{\partial\tau_{\kappa\alpha p}}\Delta\tau_{\kappa\alpha p}\right]\psi(\mathbf{r}) \end{aligned} \tag{10.7}$$

Again adding Lagrange multipliers (same procedure as before), minimising functional derivatives with respect to $\Delta\tau_{\kappa\alpha p}$ and ψ^* yield coupled system

$$\hat{\mathcal{H}}^{\mathrm{KS}}_0\psi(\mathbf{r}) - \int d\mathbf{r}'\mathcal{G}(\mathbf{r},\mathbf{r}')|\psi(\mathbf{r}')|^2\psi(\mathbf{r}) = \varpi\psi(\mathbf{r}) \tag{10.8a}$$

$$\Delta\tau_{\kappa\alpha p} = -\sum_{\kappa'\alpha' p'} (C^0)^{-1}_{\kappa\alpha p,\kappa'\alpha' p'} \int d\mathbf{r} \frac{\partial V_0^{\mathrm{KS}}}{\partial \tau_{\kappa'\alpha' p'}} |\psi(\mathbf{r})|^2 \tag{10.8b}$$

where we have now identified the Green's function of the polaron response:

$$\mathcal{G}(\mathbf{r},\mathbf{r}') = \sum_{\kappa\alpha p}\sum_{\kappa'\alpha' p'} \frac{\partial V_0^{\mathrm{KS}}(\mathbf{r})}{\partial \tau_{\kappa\alpha p}} (C^0)^{-1}_{\kappa\alpha p,\kappa'\alpha' p'} \frac{\partial V_0^{\mathrm{KS}}(\mathbf{r}')}{\partial \tau_{\kappa'\alpha' p'}} \tag{10.9}$$

This is the core idea. We can write all desired quantities in the basis of KS states and phonon normal modes! For example,recasting Eqs. (3.9a) and (3.14) into the following forms:

$$g^{\nu}_{mn}(\mathbf{k},\mathbf{q}) = \sum_{\kappa\alpha p} \left(\frac{\hbar}{2M_\kappa \omega_{\mathbf{q}\nu}}\right)^{1/2} (e_{\mathbf{q}\nu\kappa})^{\alpha} e^{i\mathbf{q}\cdot\mathbf{R}_p} \int d\mathbf{r} \psi^*_{m\mathbf{k}+\mathbf{q}} \frac{\partial V_0^{\mathrm{KS}}}{\partial \tau_{\kappa'\alpha' p'}} \psi_{n\mathbf{k}}(\mathbf{r}) \tag{10.10a}$$

$$(C^0)^{-1}_{\kappa\alpha p,\kappa'\alpha' p'} = \frac{1}{N_p} \sum_{\mathbf{q}\nu} \frac{(e_{\mathbf{q}\nu\kappa})^{\alpha} (e^*_{\mathbf{q}\nu\kappa'})^{\alpha'}}{\sqrt{M_\kappa M_{\kappa'}}\omega^2_{\mathbf{q}\nu}} e^{i\mathbf{q}\cdot(\mathbf{R}_p - \mathbf{R}_{p'})} \tag{10.10b}$$

we can describe the polaron by its momentum-resolved contributions from both electronic and phononic systems:

$$\begin{aligned} \frac{2}{N_p}\sum_{\mathbf{q}m\nu} B_{\mathbf{q}\nu} \left(g^{\nu}_{mn}(\mathbf{k},\mathbf{q})\right)^* A_{m\mathbf{k}+\mathbf{q}} &= (\varepsilon_{n\mathbf{k}} - \omega) A_{n\mathbf{k}} \\ \frac{1}{N_p}\sum_{mn\mathbf{k}} A^*_{m\mathbf{k}+\mathbf{q}} \frac{g^{\nu}_{mn}(\mathbf{k},\mathbf{q})}{\hbar\omega_{\mathbf{q}\nu}} A_{n\mathbf{k}} &= B_{\mathbf{q}\nu} \end{aligned} \tag{10.11}$$

Practically, these equations are solved by instantiating the electronic weights with Gaussian-distributed values about the valence band maximum (conduction band minimum) for the hole (electron) polaron with a full-max half-width matching reasonable *a priori* sizes for the polaron. The solution is solved self-consistently and is said to be converged when the maximum difference in atomic displacements across the supercell between successive iterations is below a set tolerance ($\max_{pk} \Re\{\Delta\tau^{n+1}_{pk} - \Delta\tau^{n}_{pk}\} < \delta\tau$). Further, the starting location in the BZ is iterated to ensure global convergence. The full workflow is given in Figure 10.1. Remarkably, we can rewrite all desired quantities in

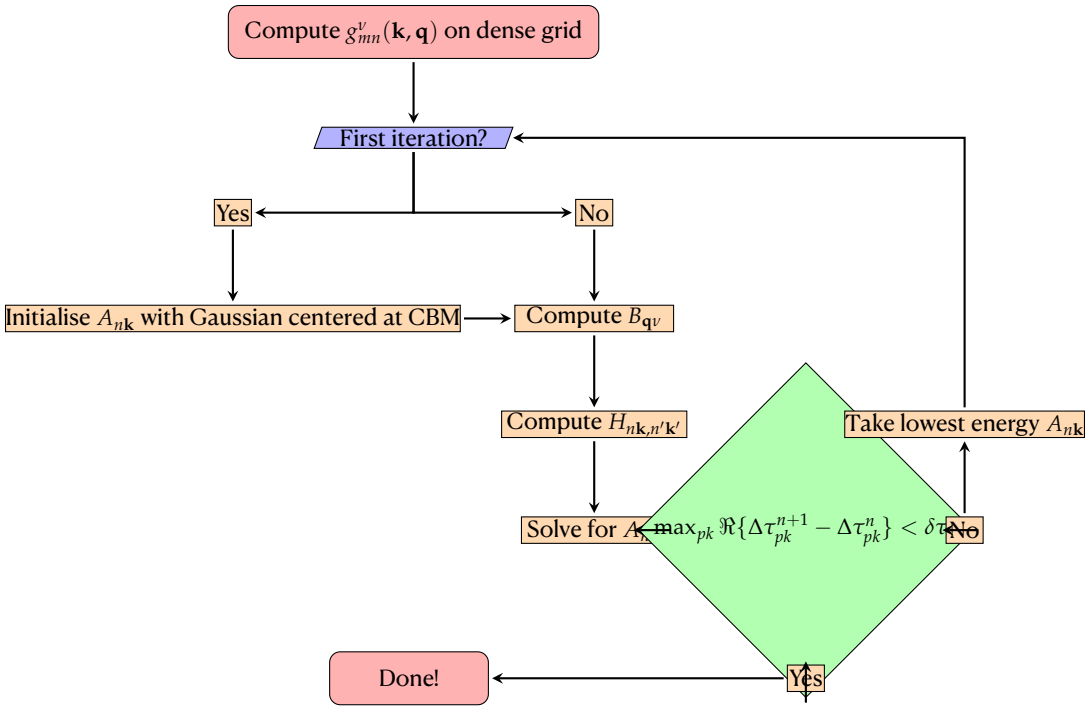

FIGURE 10.1: Workflow for the practical calculation of the numerical solution to the self-consistent polaron equations in Eq. (10.11). After initialising electronic weights at the momentum closest to the manifold extrema (valence band maximum for the hole polaron, conduction band minimum for the electron polaron), the equations are evaluated iteratively to determine eigenenergies ϖ and eigenstates $A_{n\mathbf{k}}$. Should the iterative change in formation energy be above a set tolerance, the lowest energy eigenstate is used to initialize the solution to the self-consistent equations. Iteration occurs until changes in formation energy are below a tolerance.

terms of electron and phonon contributions, $A_{n\mathbf{k}}$ and $B_{\mathbf{q}\nu}$ respectively

$$\Delta\tau^{\text{pol}}_{\kappa\alpha p} = -\frac{2}{N_p}\sum_{\mathbf{q}\nu} B^{*}_{\mathbf{q}\nu}\left(\frac{\hbar}{2M_\kappa\omega_{\mathbf{q}\nu}}\right)^{1/2}\varepsilon^{\alpha}_{\mathbf{q}\nu\kappa}(\mathbf{q})e^{i\mathbf{q}\cdot\mathbf{R}_p} \tag{10.12a}$$

$$\Delta E_f = \varpi - \varepsilon_{\text{CBM}} + \frac{1}{N_p}\sum_{\mathbf{q}\nu}|B_{\mathbf{q}\nu}|^2\hbar\omega_{\mathbf{q}\nu} \tag{10.12b}$$

where $\Delta\tau^{\text{pol}}_{\kappa\alpha p}$ are the atomic displacements of the atoms in the supercell caused by the presence (absence) of charge wavefunction density in the system, and ΔE_f the formation energy of the polaron in terms of the conduction band minimum (CBM) energy for the electron polaron (the valence band maximum energy for the hole polaron) and the polaron eigenvalue ϖ. Due to the periodic boundary conditions of the supercell simulation, in this case the formation energy is expected to decay as $1/L$. Therefore, determining the linear regression of $\frac{1}{N_k V^{1/3}}$ versus the formation energy and extrapolating

to $1/L \to 0 \implies L \to \infty$ yields the reported formation energies [214], a process known as Makov-Payne extrapolation [215].

In so much as the polaron vibrational weights $B_{\mathbf{q}\nu}$ correspond to a real-space atomic displacements as in Eq. (10.12a), we can analagously determine the real-space polaron wavefunction in terms of the electronic weights $A_{n\mathbf{k}}$ as:

$$\Psi_{\text{pol}}(\mathbf{r}) = \frac{1}{N_p} \sum_{mp} \sum_{n\mathbf{k}} e^{i\mathbf{k}\cdot\mathbf{R}_p} U^{\dagger}_{mn\mathbf{k}} A_{n\mathbf{k}} w_m(\mathbf{r} - \mathbf{R}_p) \tag{10.13}$$

where $w_m(\mathbf{r})$ is a Wannier function in the unit cell (normalized in the supercell), and $U^{\dagger}_{mn\mathbf{k}}$ is the unitary matrix ensuring a smooth Bloch gauge in the Wannerization process.

10.2 DIFFUSE-SCATTERING SIGNATURES OF POLARONS

From a theoretical point of view, one could use the phononic amplitudes of the polaron $B_{\mathbf{q}\nu}$ as simple weights of the phonon strengths in the diffuse scattering pattern, for example in Eq. (5.10) taking:

$$n_{\mathbf{q}\nu} \to \frac{B_{\mathbf{q}\nu} n_{\mathbf{q}\nu}}{\sum_{\nu'} \int_{\text{BZ}} \frac{d\mathbf{q}'}{\Omega_{\text{BZ}}} B_{\mathbf{q}'\nu'}} \tag{10.14}$$

which would seem a reasonable approach to compute the diffuse scattering of the polaron. Unfortunately, the evaluation of the William-Lax thermal average in Eq. (5.15) assumes dense partitioning of the BZ (therefore large supercells). In the limit that $B_{\mathbf{q}\nu}$ were computed for an "infinite" supercell, this approach would be fruitful. Computationally, however, $B_{\mathbf{q}\nu}$ must be solved on finite supercells, which would seem to introduce artifacts in the diffuse scattering pattern with periodicity on the order of the supercell size.

As we have shown, the intensity of a wave scattered by the atoms in a crystalline lattice can be expressed within the Laval-Born-James theory [65, 66, 67] as:

$$I(\mathbf{Q}) = \left| \sum_{p\kappa} f_{\kappa}(\mathbf{Q}) e^{i\mathbf{Q}\cdot\left[\mathbf{R}_p + \boldsymbol{\tau}_{\kappa} + \Delta\boldsymbol{\tau}_{p\kappa}\right]} \right|^2 \tag{10.15}$$

At zero temperature and in absence of polarons, the atomic coordinates coincide with the equilibrium ones ($\Delta\boldsymbol{\tau}_{p\kappa} = 0$). To account for the influence of a static polaronic distortion on the diffuse scattering intensity at zero temperature, we identify the nuclear displacement $\Delta\boldsymbol{\tau}_{p\kappa}$ in Eq. (10.15) with the structural changes induced by the polaron formation $\Delta\boldsymbol{\tau}^{\mathrm{pol}}_{p\kappa}$ in Eq. (10.12a), with envelop functions $B_{\mathbf{q}\nu}$ obtained from the solution of the self-consistent polaron equations [Eq. (10.11)]. Correspondingly, we express the changes of scattering intensity as:

$$I_{\mathrm{pol}}(\mathbf{Q}) = \left| \sum_{p\kappa} f_\kappa(\mathbf{Q}) e^{i\mathbf{Q}\cdot\left[\mathbf{R}_p + \boldsymbol{\tau}_\kappa + \Delta\boldsymbol{\tau}^{\mathrm{pol}}_{p\kappa}\right]} \right|^2 . \tag{10.16}$$

This definition enables us to promptly integrate polaronic effects in *ab-initio* simulations of inelastic scattering experiments.

The extension to finite temperature is conducted via the formalism of the ZG displacements in Eq. (5.22), where the ZG displacements of Eq. (5.21) represent the collection of scatterers in a finite supercell that best approximate thermal diffuse scattering, enabling us to sample thermal effects with a single atomic configuration. To this aim, we can distort the lattice according to the ZG displacements, then distort the lattice again by the polaron to directly view the impact of the defect on the resulting pattern:

$$I_{\mathrm{ZG+pol}}(\mathbf{Q}; T) = \left| \sum_{p\kappa} f_\kappa(\mathbf{Q}) e^{i\mathbf{Q}\cdot\left[\mathbf{R}_p + \boldsymbol{\tau}_\kappa + \Delta\boldsymbol{\tau}^{\mathrm{ZG}}_{p\kappa} + \Delta\boldsymbol{\tau}^{\mathrm{pol}}_{p\kappa}\right]} \right|^2 \tag{10.17}$$

In this approach, finite temperature effects of the renormalization of polaron envelop functions are neglected.

10.2.1 *Relation to the polaron envelop function*

In the following, we demonstrate that the change of diffuse scattering intensity introduced by the formation of polarons admits a simple representation in terms of the polaron envelop function $B_{\mathbf{q}\nu}$. A direct consequence of this result is that inelastic scat-

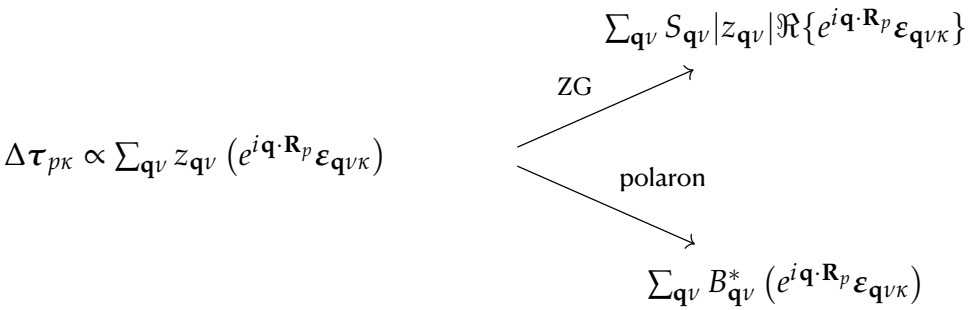

FIGURE 10.2: Schematic of atomic displacements for nonequilibrium configurations of a finite supercell, illustrating clearly the nature of the ZG displacements (weighting phonon normal mode coordinates by the correct combination of signs $S_{\mathbf{q}\nu}$ to approximate thermal scattering), and of the polaron displacements (using the polaron vibrational weights $B_{\mathbf{q}\nu}$ to introduce the needed real-space distortion from the polaron).

tering constitutes a direct route to directly probe polarons in crystals and it should in principles be capable of providing information on the degree of localization of polaronic distortions (polaron radius).

To illustrate these points, we focus for simplicity on the low-temperature limit ($T = 0$) and we begin by rewriting the scattering intensity in presence of a polaron by a Tailor expansion of the exponential up to second order:

$$I_{\mathrm{pol}}(\mathbf{Q}) = \sum_{pp'\kappa\kappa'} f_\kappa(\mathbf{Q}) f^*_{\kappa'}(\mathbf{Q}) e^{i\mathbf{Q}[(\mathbf{R}_p - \mathbf{R}_{p'}) + (\boldsymbol{\tau}_\kappa - \boldsymbol{\tau}_{\kappa'})]} \times [1 + i\mathbf{Q}(\Delta\boldsymbol{\tau}^{\mathrm{pol}}_{p\kappa} - \Delta\boldsymbol{\tau}^{\mathrm{pol}}_{p'\kappa'}) + [\mathbf{Q}\cdot(\Delta\boldsymbol{\tau}^{\mathrm{pol}}_{p\kappa} - \Delta\boldsymbol{\tau}^{\mathrm{pol}}_{p'\kappa'})]^2] \quad . \tag{10.18}$$

The lowest-order term in the expansion coincides with $I_0(\mathbf{Q})$, the contribution of a static lattice to the scattering intensity in the absence of polarons. It can be easily verified, that the first-order term in the expansion only contribute to elastic scattering processes, and it can thus only lead to a renormalization of the Debye-Waller factor. The second-order term, conversely, is the lowest-order contribution to the diffuse scattering intensity.

As we are primarily interested in diffuse scattering, we omit the first-order term henceforth, and retain only second-order terms in the following discussion. Correspondingly, the change of diffuse scattering intensity due to the formation of polaron can be

expressed as:

$$\begin{aligned}\Delta I_{\mathrm{pol}}(\mathbf{Q}) &\equiv I_{\mathrm{pol}}(\mathbf{Q}) - I_0(\mathbf{Q}) \\ &= \sum_{pp'\kappa\kappa'} f_\kappa(\mathbf{Q}) f^*_{\kappa'}(\mathbf{Q}) e^{i\mathbf{Q}[(\mathbf{R}_p-\mathbf{R}_{p'})+(\boldsymbol{\tau}_\kappa-\boldsymbol{\tau}_{\kappa'})]} [\mathbf{Q}\cdot(\Delta\boldsymbol{\tau}^{\mathrm{pol}}_{\kappa p} - \Delta\boldsymbol{\tau}^{\mathrm{pol}}_{\kappa' p'})]^2 \quad . \end{aligned} \tag{10.19}$$

After a few algebraic manipulation, we deduce an explicit expression of $\Delta I_{\mathrm{pol}}(\mathbf{Q})$ in terms of the polaron envelop function:

$$\Delta I_{\mathrm{pol}}(\mathbf{Q}) = 2\hbar\Re \sum_{\nu\nu'} \frac{B_{\mathbf{q}\nu} B^*_{\mathbf{q}\nu'}}{\sqrt{\omega_{\mathbf{q}\nu}\omega_{\mathbf{q}\nu'}}} \sum_{\kappa\kappa'} f_\kappa(\mathbf{Q}) f^*_{\kappa'}(\mathbf{Q}) e^{i\mathbf{Q}[(\tau_\kappa-\tau_{\kappa'})]} \frac{(\mathbf{Q}\cdot\boldsymbol{\varepsilon}_{\mathbf{q}\nu'\kappa'})(\mathbf{Q}\cdot\boldsymbol{\varepsilon}^*_{\mathbf{q}\nu\kappa})}{\sqrt{M_\kappa M_{\kappa'}}} \quad . \tag{10.20}$$

This result has been obtained by combining Eqs. (10.11) and (10.19) with the Born-von-Kármán sum rule ($\sum_p e^{i\mathbf{q}\mathbf{R}_p} = N_p \delta^G_{\mathbf{q},0}$), and making use of the conditions $B_{-\mathbf{q}\nu} = [B_{\mathbf{q}\nu}]^*$ and $\boldsymbol{\varepsilon}_{-\mathbf{q}\nu\kappa} = [\boldsymbol{\varepsilon}_{\mathbf{q}\nu\kappa}]^*$.

For materials in which polarons are associated with structural distortions along a single polar phonon – as, e.g., in the case of LiF – this expression simplifies further and we can express the change of diffuse scattering intensity induced by the polaron formation as:

$$\Delta I_{\mathrm{pol}}(\mathbf{Q}) = \frac{|B_{\mathbf{q}}|^2}{\omega_{\mathbf{q}}} F^2(\mathbf{Q}) \tag{10.21}$$

where we introduced the function:

$$F^2(\mathbf{Q}) = 2\hbar \left| \sum_\kappa e^{i\mathbf{Q}\cdot\boldsymbol{\tau}_\kappa} \frac{f_\kappa(\mathbf{Q})}{\sqrt{M_\kappa}} (\mathbf{Q}\cdot\mathbf{e}_{\mathbf{q}\kappa}) \right|^2 \tag{10.22}$$

analogously to the single-phonon structure factor. Overall, Eq. (10.21) indicates the changes of diffuse scattering intensity induced by the formation of a polaron are directly proportional to the polaron envelop function. This simple result establishes a direct link between polaronic distortion in crystals and their fingerprints in diffuse scattering experiments.

We start by determining the diffuse scattering signatures of polarons in a system where they have been independently verified to exist, and compare those diffuse scattering signatures to those reported in the alleged polaronic material SnSe. As such, in addition

to SnSe, we also perform all polaron calculations on the prototypical ionic wide-gap insulator lithium floride (LiF), which is known to host both electron and hole polarons in equilbrium [214, 216, 217, 218, 219, 220, 221, 222, 223].

10.3 POLARONS IN LITHIUM FLORIDE

Note 10.1

The calculations used in this work relied on the computational suite `QuantumESPRESSO` [185, 186], using norm-conserving Troullier Martins pseudopotentials [187] and the Perdew-Burke-Ernzerhof generalized gradient approximation for the exchange-correlation functional [188]. We used an energy cutoff of 150 Ry, and an $12 \times 12 \times 12$ Monkhorst-Pack $\mathbf{k}$-grid for the electronic structure calculations. Second order force constants were computed using DFPT on an $12 \times 12 \times 12$ $\mathbf{q}$-grid.

The determination of the polaron weights, as well as the EPC calculations and the polaron diffuse scattering patterns, were computed using developer versions of the `EPW` suite [224, 225, 226] using the maximally-localized Wannier functions computed by `wannier90` [227] and the self-consistent polaron equations of Sio *et al* [213]. Polar corrections to the MLWF interpolation of the EPC matrix elements were explicitly implemented to account for short- and long-range interactions [211]. The EPC matrix elements were exactly computed on the origin $12 \times 12 \times 12$ $\mathbf{k}$- and $\mathbf{q}$-grids, and interpolated onto the supercell for the calculation of the polaron weights (largest size of supercell is $24 \times 24 \times 24$). All diffuse scattering calculations utilized a developer version of the `disca.x` and `ZG.x` codes in the `EPW` suite [74]. The exact diffuse scattering calculations utilized the same sampling density of the BZ as their were supercells in the polaron calculation ($24 \times 24 \times 24$), and the ZG displacements were computed on this same supercell size.

Energy (eV)	Hole	Electron
Eigenvalue	4.44	−0.61
Phonon contrib	−2.62	−0.49
Electron contrib	0.80	0.37
Formation energy	−1.82	−0.12

TABLE 10.1: The associated energies of each polaron determined by Eq. (10.12b) in LiF for a $24 \times 24 \times 24$ supercell.

We solve the self-consistent Eq. (10.11) and render the sets of weights $\{A_{n\mathbf{k}}\}$ and $\{B_{\mathbf{q}\nu}\}$ in Figure 10.3, and tabulate the formation energies in Table 10.1 for a finite supercell of LiF. Both such polarons are found to exist with formation energies and real-space extents matching those reported [213]. Namely, the momentum-resolved weights of the hole polaron are dispersed throughout the BZ, consistent with a small real-space polaron with extracted real-space spread of $2r_{\text{pol}}^{\text{hole}} = 0.93$ Å, and using Makov-Payne extrapolation [215], we find a formation energy of -1.978 eV. Conversely, the electron polaron has weights highly localized in the BZ, consistent with a large real-space polaron with an extracted real-space spread of $2r_{\text{pol}}^{\text{elec}} = 8.59$ Å, and an extrapolated formation energy of -268 meV. The visualization of the Makov-Payne extrapolation is shown in Figure 10.4. The sizes of the polarons are determined via the full-width half-maxima of $|\Psi_{\text{pol}}(\mathbf{r})|^2$ along a representative dimension of the polaron, in this case the [111] direction as shown in Figure 10.5, and yield formation energies of -1.978 eV and -268 meV for the hole and electron polarons respectively.

10.3.1 *Polaron-Diffuse Scattering in LiF*

We thus proceed to determine the expected polaron-diffuse scattering signatures as measurable by UED and UEDS. Computing the hole-polaron-diffuse scattering pattern via Eq. (10.17), as in Figure 10.7c and e, shows a small anisotropic change compared to equilibrium scattering, shown in Figure 10.7b. The low intensity of the differential scattering in Figure 10.7g owes to the small spatial extent of the polaron, and the anisotropy

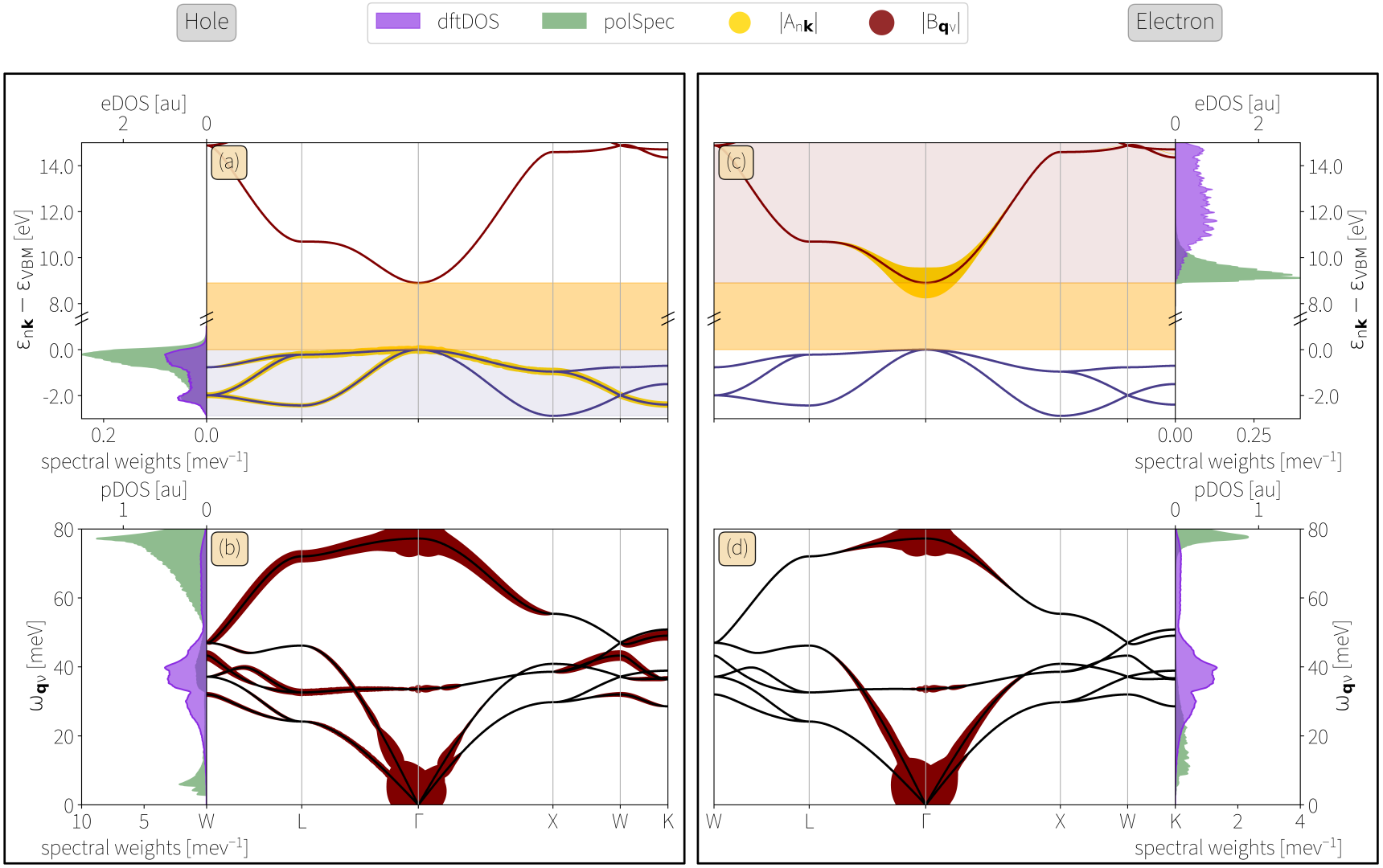

FIGURE 10.3: Electronic and vibrational momentum-resolved weights needed for polaron formation according to Eq. (10.11) in the insulator LiF. The electronic band structure and phonon dispersions are shown. The thickness of the bands at that particular point in the band is directionally proportional to the magnitude of the weights. The electronic weights, $A_{n\mathbf{k}}$, are given by the yellow coloration on the bands, and the vibrational weights, $B_{\mathbf{q}\nu}$, are given by the dark red coloration on the phonon dispersions. The weights are given for the electron system and phonon system for the hole polaron in (a) and (b), and for the electron polaron in (c) and (d). For the electronic weights, the bands included in the self-consistent calculation are those encompassed within the appropriate shaded region (dark blue for valence states in the hole polaron, maroon for conduction states in the electron polaron). The electronic bands have the band-gap region shaded in orange. Next to each primary axis is the DFT density of states (purple, arbitrary units) with the polaron spectral weight for the electronic and phononic system (green, meV^{-1}).

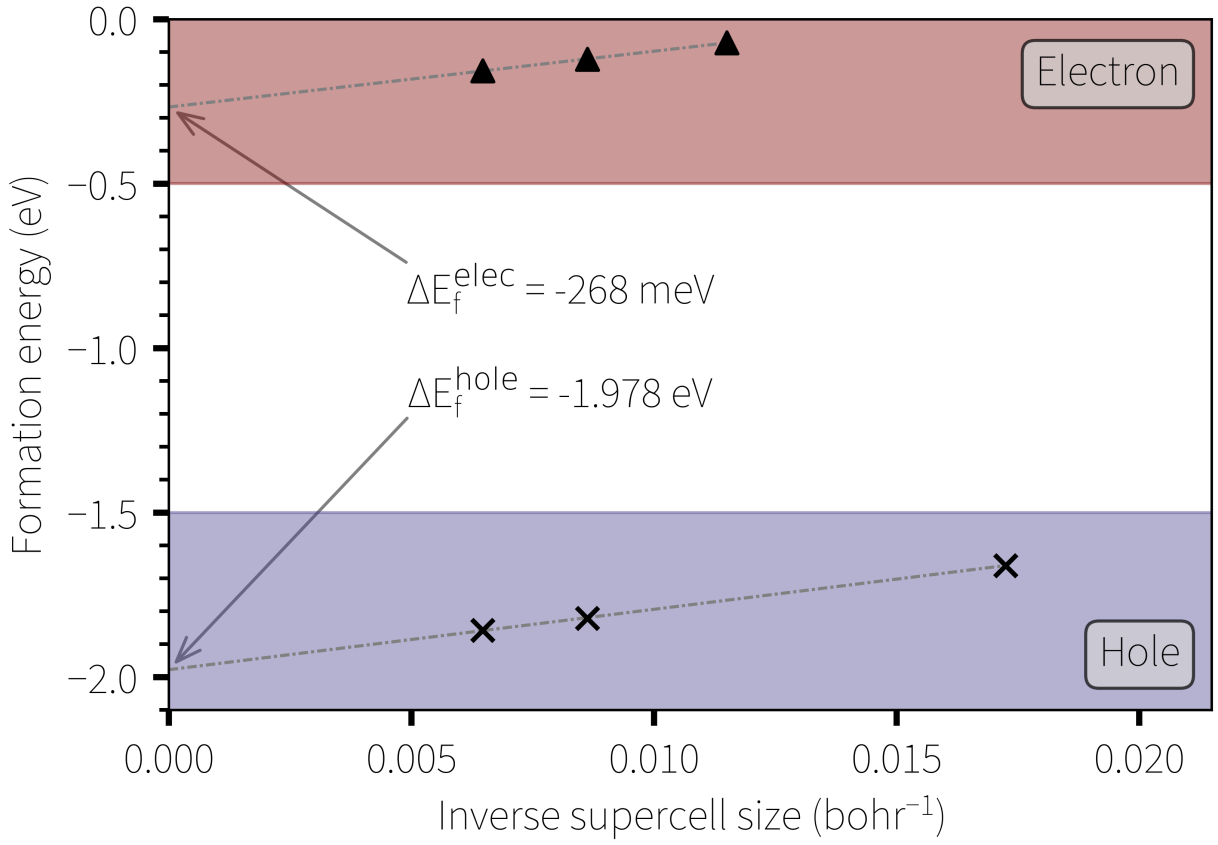

FIGURE 10.4: Makov-Payne extrapolation of polaron formation energies in LiF as a function of inverse supercell dimension, with the extrapolation to $L \to \infty$ indicated. The hole polaron was calculated on $12 \times 12 \times 12$, $24 \times 24 \times 24$, and $32 \times 32 \times 32$ grids. The electron polaron was calculated on $18 \times 18 \times 18$, $24 \times 24 \times 24$, and $32 \times 32 \times 32$ grids.

with respect to phonon momentum results from the anisotropic p-like orbital character of the hole polaron atomic displacements and the corresponding wavefunction (see Figures 10.5 and 10.6) that extend along the diagonal of the projected [111] scattering. However, the electron polaron (shown in Figure 10.7d and f), extending over many unit cells, shows a differntial increase in diffuse intensity in a ring about the Bragg peaks (Figure 10.7h). The point defect model of René de Cotret *et al* [118] shows that an atomic displacement field with Gaussian distributed values about some charge trapping center ($\mathbf{u}(\mathbf{r}) \propto e^{|\mathbf{r}|/r_{\text{pol}}^2}\hat{\mathbf{u}}$) would result in an annular momentum dependence to the diffuse scattering about a Bragg peak. Namely:

$$\frac{I(\Delta\boldsymbol{\tau}_{p\kappa}^{\text{pol}}) - I(\Delta\boldsymbol{\tau}_{p\kappa} = 0)}{I(\Delta\boldsymbol{\tau}_{p\kappa} = 0)} \propto |\mathbf{q}| r_{\text{pol}}^2 e^{-|\mathbf{q}|^2 r_{\text{pol}}^2/2} \quad . \tag{10.23}$$

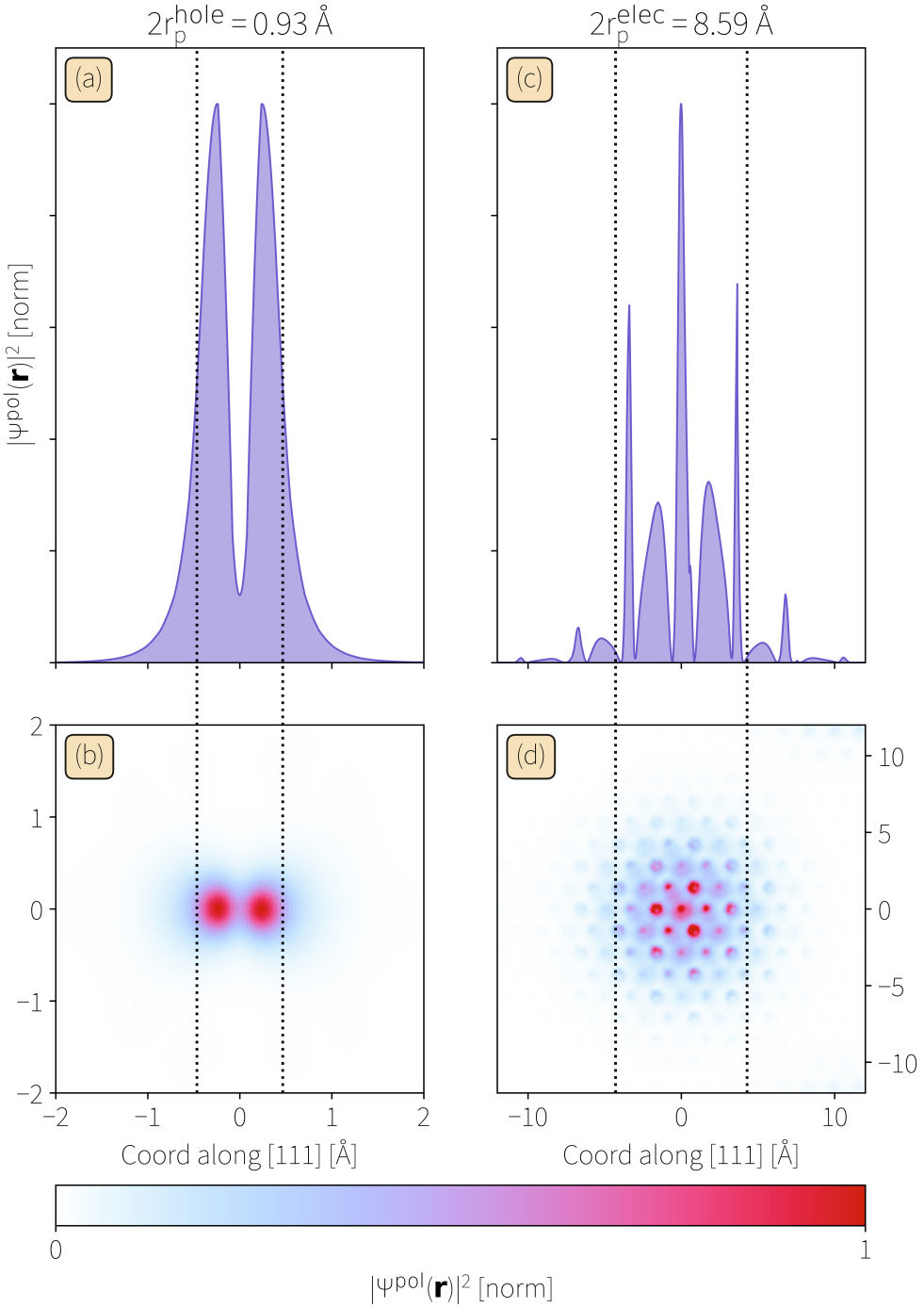

FIGURE 10.5: The polaronic wavefunctions of the hole and electron polarons in LiF. A linecut of the wavefunctions are given for the hole (a) and electron (c) polarons with the sizes of each polaron given in the title of the panel. The sizes of the polarons are determined via the full-width half-maxima of $|\Psi_{\text{pol}}(\mathbf{r})|^2$ along a representative dimension of the polaron, in this case the [111] direction. The 2D cuts of the wavefunctions are given in panels (b) and (d) for the hole and electron polarons respectively. The wavefunctions in (b) and (d) are generated by projecting the wavefunction along the [111] plane, with the points spanning the plane generated by the $[1-10]$ and $[-101]$ directions.

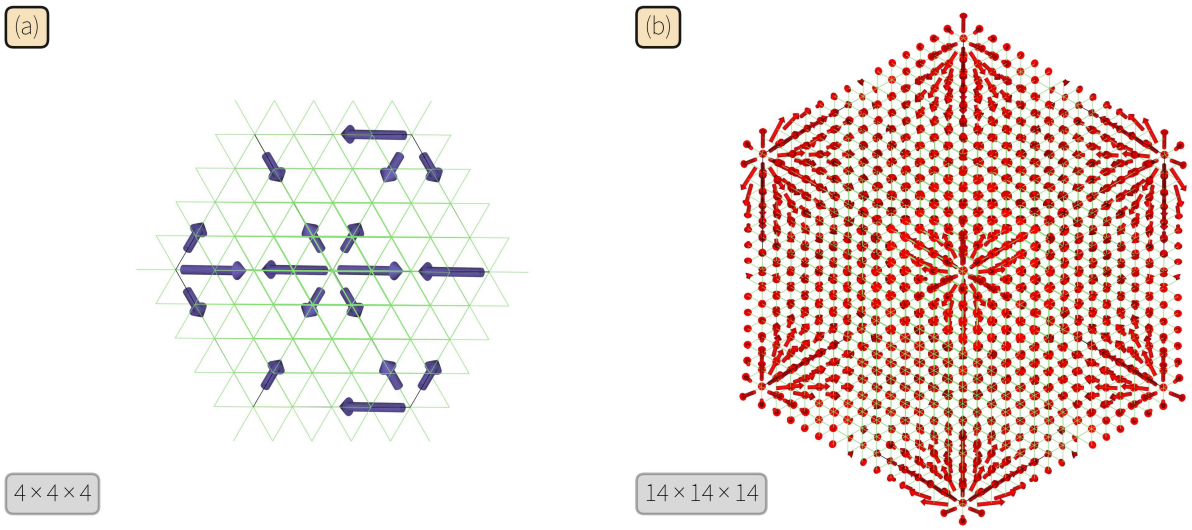

FIGURE 10.6: Atomic displacements of the hole (a) and electron (b) polarons in LiF. Displacements less than 10^{-3} Å are not rendered for clarity. The displacements of the hole polaron are magnified $3\times$, and are computed for a $4 \times 4 \times 4$ supercell, while the displacements of the electron polaron, computed on a $14 \times 14 \times 14$ supercell, are rendered to scale. Both supercells are viewed from the [111] direction.

In this instance, the electron-polaron-diffuse scattering qualitatively matches the point defect model indicated by the Gaussian-like distribution of atomic displacements (see Figure 10.6) about the charge trapping center. We show the linecuts along the $|\Gamma W|$ path for the electron polaron in both $I_{\mathrm{ZG+pol}}$ and I_{pol} in Figure 10.7g, where the fit to the point defect model extracts values of $12 - 14$ Å, matching closely the true value of 8.56 Å. We conclude that a polaron, which extends over many unit cells so as to scatter strongly, may have a diffuse-scattering signature of an increase in intensity in a ring about the Bragg peak. We will show, however, that there are other linear combinations of atomic displacments (occupation distribution functions of phonons) that can also provide such an annular momentum dependence to diffuse scattering images, concluding that polarons may yield rings in diffuse scattering images, but not all rings in diffuse scattering images result from polarons.

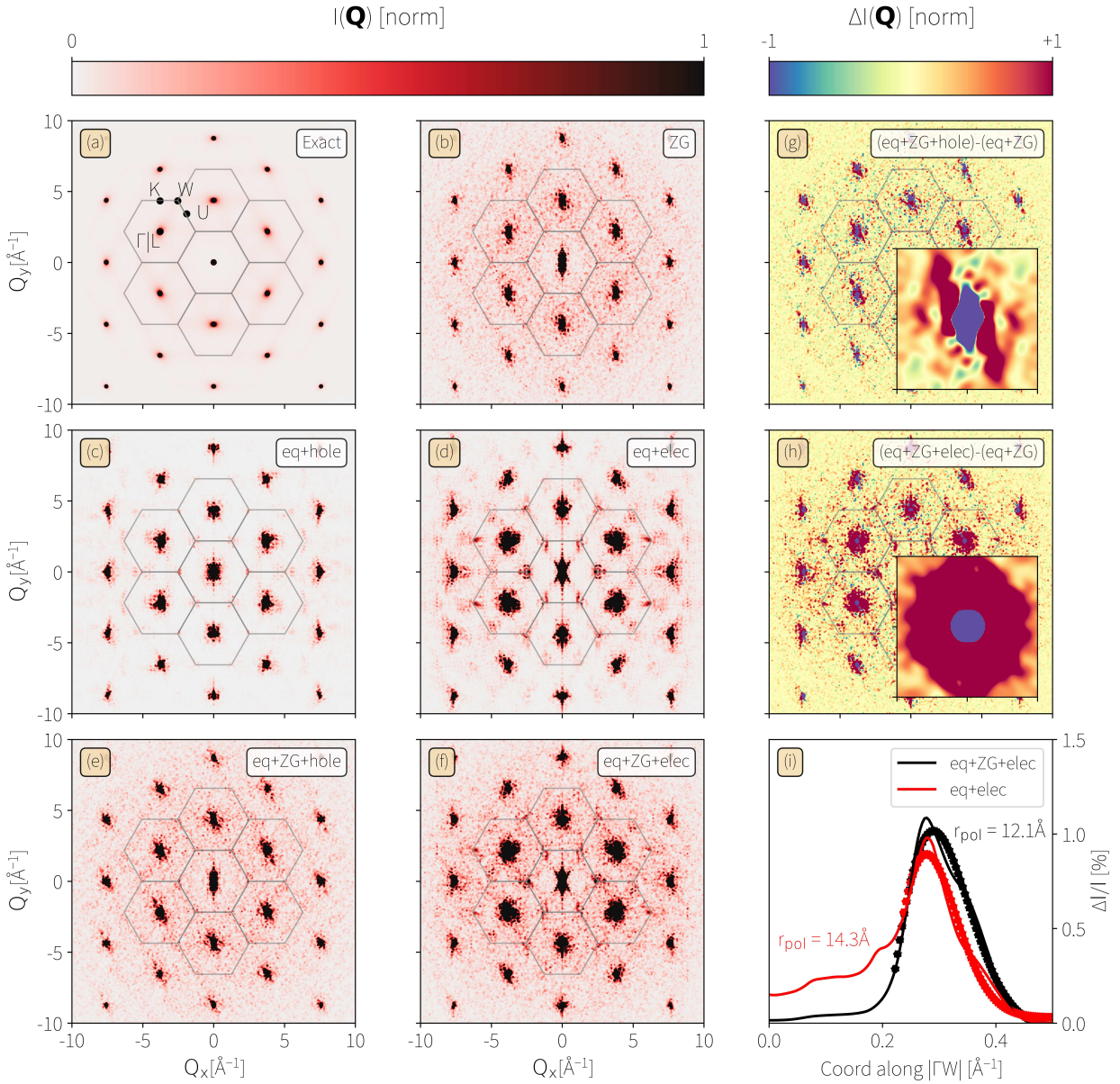

FIGURE 10.7: Polaron-diffuse scattering in LiF. All diffuse scattering patterns are for scattering in the [111] direction of the FCC lattice, thus yielding six-fold symmetry. The exact diffuse scattering intensity from Eq. (5.16) is given in panel (a) with the high symmetry points of the BZ from the [111] projection labelled, and the ZG scattering intensity is in panel (b). The static polaron scattering intensity from Eq. (10.16) is given for the hole polaron in panel (c) and for the electron polaron in panel (d), with the inclusion of thermal effects via the ZG displacements in Eq. (10.17) in panels (e) and (f) respectively. The differential diffuse intensity, given by $\Delta I = I_{\text{ZG+pol}} - I_{\text{ZG}}$, for the hole and electron polarons are given in panels (g) and (f) respectively. Inset in these panels are the average of the first-order reflections across the entire BZ. Panel (g) gives the linecut of relative differential intensity for the electron polaron, with the radius of the polaron determined via the point defect model shown.

10.4 INVESTIGATION OF POLARONS IN *Pnma* SNSE

Note 10.2

Calculations on SnSe used the same computational setup as previously, again using norm-conserving Troullier Martins pseudopotentials [187] and the Perdew-Burke-Ernzerhof generalized gradient approximation for the exchange-correlation functional [188]. We used an energy cutoff of 60 Ry, and an $8 \times 16 \times 16$ Monkhorst-Pack $\mathbf{k}$-grid for the electronic structure calculations. Second-order force constants were computed using density functional perturbation theory on a $4 \times 8 \times 8$ $\mathbf{q}$-grid. A vdW dispersion correction was applied to account for interlayer coupling using the D3 approach of Grimme [228], including three-body terms for the electronic calculations, and using Becke-Johnson damping for the lattice calculations to ensure the dispersion correction does not diverge at small distances [229, 230]. To account for the divergence of the EPC matrix elements at $\mathbf{q} \to \Gamma$, the EPC matrix elements were truncated at 10$^{\text{th}}$ nearest neighbor interactions (real-space cutoff of 4.69 Å, momentum-space cutoff of 1.34 Å^{-1}) by setting the value of the EPC-prepared hot phonon distribution $g_{\mathbf{q}\nu}$ to the average value of the corresponding nearest neighbors at the momentum cutoff for $|\mathbf{q}| < |\mathbf{q}_{\text{min}}|$. Image renders of $g_{\mathbf{q}\nu}$ were obtained via Wannier-interpolation from the original $4 \times 8 \times 8$ $\mathbf{q}$-grid onto a $1 \times 16 \times 16$ $\mathbf{q}$-grid, with subsequent linear nearest-neighbor interpolation onto 128×128 $\mathbf{q}$-grid. Likewise, the polaron weights $A_{n\mathbf{k}}$ and $B_{\mathbf{q}\nu}$ as well as the ZG displacements were explicitly solved on an $8 \times 16 \times 16$ $\mathbf{k}$- and $\mathbf{q}$-grids.

We obtain the electron and phonon weights given in Figure 10.8, and find that neither the electronic system nor the vibronic system contribute strongly to either the hole or electron polarons. The formation energies are extremely small, given by $-0.640\,\mu$eV and $-2.453\,\mu$eV for the hole and electron polarons respectively. The energies given (tabulated in Table 10.2) suggest that there is no energy to be gained by deforming the

Energy (μeV)	Hole	Electron
Eigenvalue	1.280	−4.907
Phonon contrib	−0.640	−2.453
Electron contrib	0.000	0.000
Formation energy	−0.640	−2.453

TABLE 10.2: The associated energies of each polaron determined by Eq. (10.12b) in SnSe for an $8 \times 16 \times 16$ supercell. Note that the units are in μeV unlike Table 10.1.

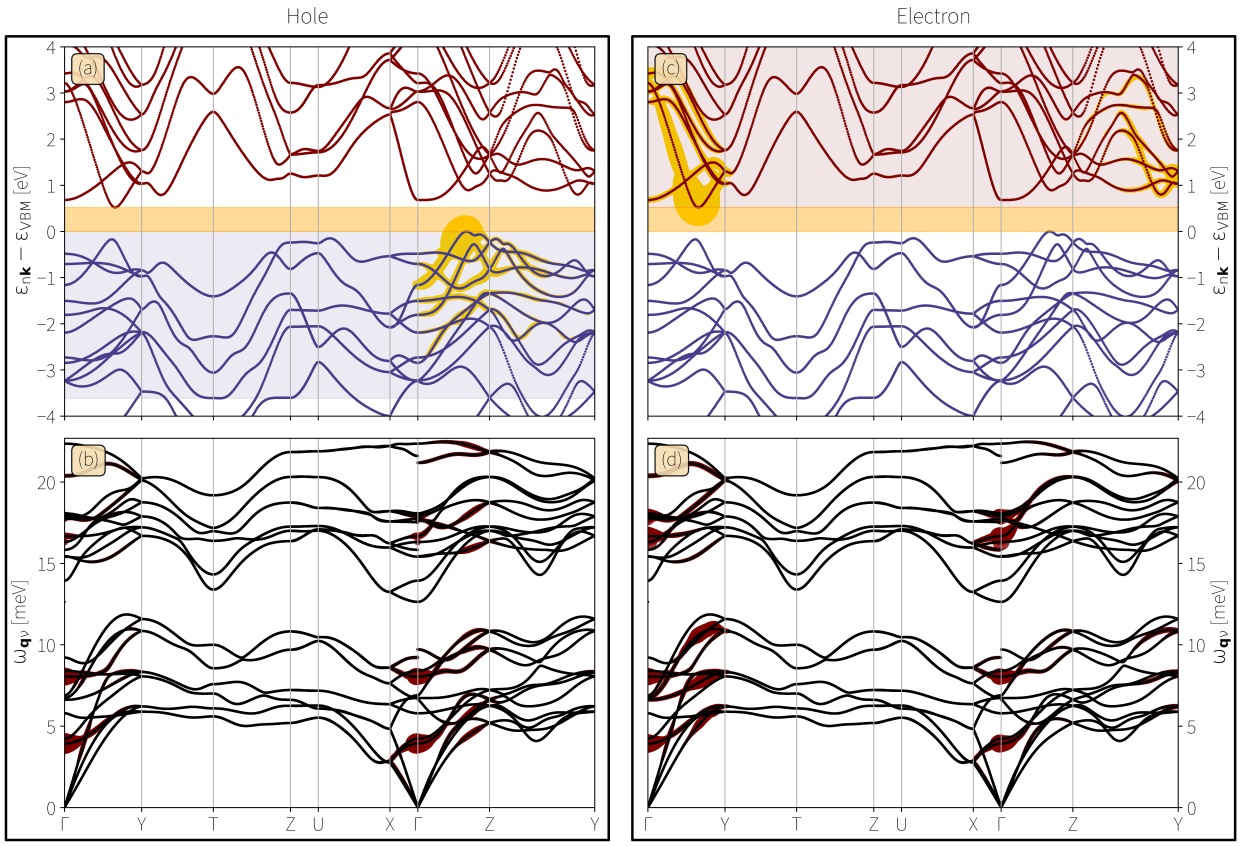

FIGURE 10.8: Polaron electronic and vibrational weights given in Eq. (10.11). The electronic band structure and phonon dispersions are shown. The thickness of the bands at that particular point in the band is directionally proportional to the magnitude of the weights. Due to the extremely delocalised polarons found in SnSe, the electronic weights $A_{n\mathbf{k}}$, given by the yellow coloration on the bands, are magnified by 50, and the vibrational weights $B_{\mathbf{q}\nu}$, given by the dark red coloration on the phonon dispersions, are magnified by 100. The weights are given for the electron system and phonon system for the hole polaron in (a) and (b), and for the electron polaron in (c) and (d). For the electronic weights, the bands included in the self-consistent calculation are those encompassed within the appropriate shaded region (dark blue for valence states in the hole polaron, maroon for conduction states in the electron polaron). The electronic bands have the band-gap region shaded in orange.

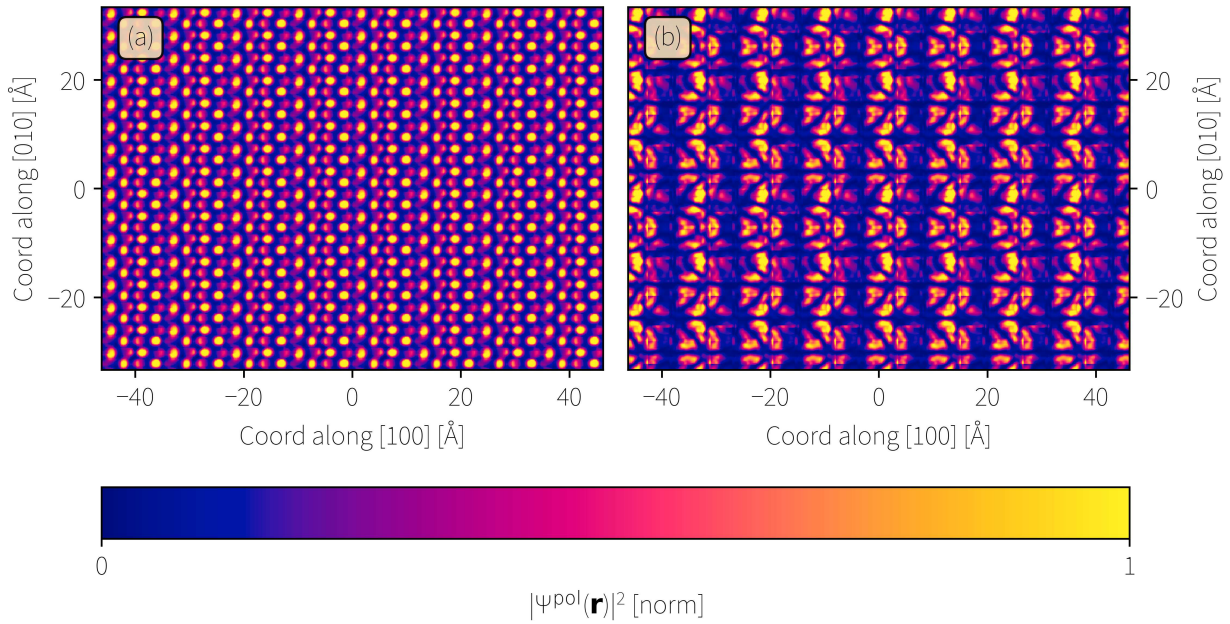

FIGURE 10.9: Real-space wavefunctions of the hole (a) and electron (b) wavefunctions in SnSe projected along the [001] axis and rendered along the stacking and zigzag directions. The severe delocalisation of the polaron is clear from the extent of these wavefunctions over the entirety of the supercell with uniform intensity (periodic between unit cells) along any given linecut across the computed region.

lattice around an additional or missing charge (charge trapping) in the material, resulting in a spatially delocalised polaron. This is consistent with a recent theoretical study that determined only the electron polaron is suspected to exist, but with a spatial extent in each direction on the order of $10^2 - 10^3$Å [231]. The lack of a spatially confined polaron in such a polar material we ascribe to the immense dielectric screening of the charges (large delocalisation length), seen by the computed dielectric constant $\epsilon^{\infty} = 19.6$. Yet, despite the apparent delocalisation of the polaron and low binding energy, it is unlikely to completely exclude a possible influence of the polarons in UEDS with recently reported sensitivity [84]. We therefore proceed to validate their effects based on *ab-initio* methods.

Not only did previous experimental work see an annular momentum dependence to the diffuse scattering, but it saw intensity anisotropy with respect to the crystal axes which the authors attributed to various polaronic-like distortions in each direction following photoexcitation. We have rigorously shown that polarons are likely to not

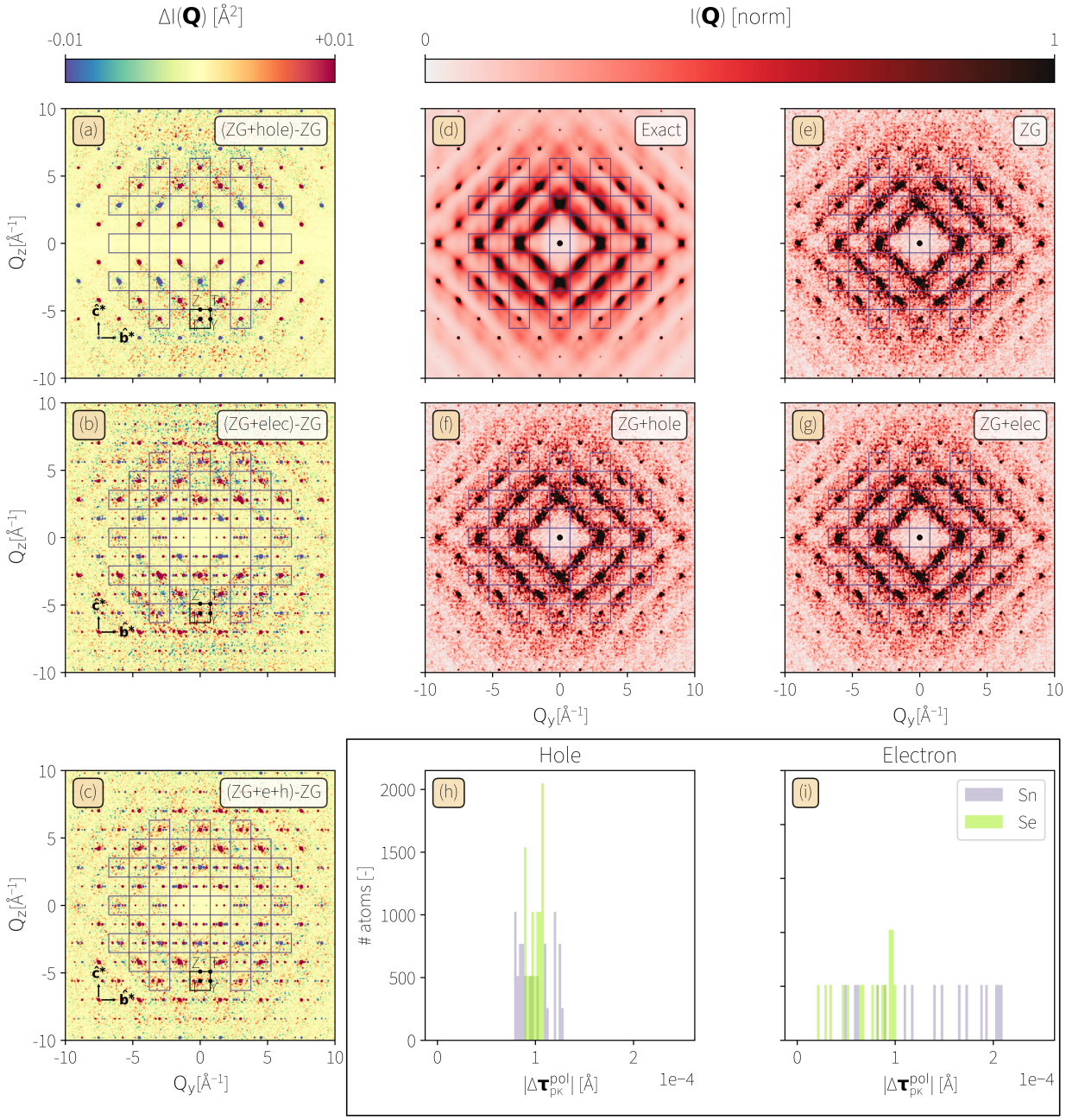

FIGURE 10.10: Polaron scattering in the room temperature phase of SnSe. Figures (a) - (c) show the differential diffuse scattering patterns resulting from the differences of Eq. (10.17) and Eq. (5.22) for the hole polaron (a), the electron polaron (b), and the linear superposition of electron and hole polarons (c). Panels (d) - (g) show the absolute intensity using the formalisms in Eqs. (5.16), (5.22) and (10.17) respectively for thermal equilbrium (d)-(e) and for the polaron scattering of the hole and electron polarons (f)-(g). Panels (h)-(i) give the histograms of the atomic displacements resulting from the polarons. The hole polaron corresponds to a compression of the accordion axis, reducing the Sn-Se-Sn bond angle, while the electron polaron tries to increase this angle, as well as twist the accordion into the zigzag direction.

exist in this material, so how do we explain this intensity anisotropy? The exact [100] diffuse scattering pattern of *Pnma*-SnSe is given in Figure 10.10a. Equation (5.16) already solves one outstanding question among previous studies in SnSe to date: the origin of the intensity anisotropy in BZs with respect to the different crystal axes. In short, the exponent of the DW factor, directly related to the anisotropic atomic displacements tensor [232] from Eq. (5.24), is different for each of these directions (see Table 10.3). As the displacements tensor is greater for $\mathbf{Q} \parallel \mathbf{c}$ than $\mathbf{Q} \perp \mathbf{c}$, and since both elastic and inelastic scattering are directly proportional to the exponential of the DW factor, the diffuse scattering has higher amplitude for $\mathbf{Q} \perp \mathbf{c}$ than $\mathbf{Q} \parallel \mathbf{c}$.

The resulting patterns are the polaron diffuse scattering are shown in Figure 10.10. We find there is only a simple modulation of the crystal structure factor resulting from the severe delocalisation of the polaron. The atomic displacements are therefore distributed more or less uniformly throughout the supercell. The features are contained to the Bragg peaks, with little extent into the diffuse regime, indicating that the small displacements from the polaron modulate only the geometric structure factor of the crystal. The resulting atomic displacements of the hole polaron (the scattering of which is given in Figure 10.10b) try to compress the Sn-Se bonds and elongate the Se-Sn bonds at the top and bottom of the accordion, trying to straighten the accordion direction as in the high temperature *Cmcm* phase, see Figure 10.11. The electron polarons (the scattering of which is given in Figure 10.10c) do the opposite motion, with the addition of also twisting the accordion about its central axis. While the determination of polaron weights relied on a BE distribution of phonons, the inability of the material to form a polaron in equilibrium casts doubts on the ability of mechanisms, like EPC, to create the specific distribution of phonons required to form a polaron quasiparticle in the nonequilibrium regime.

Given that neither electron nor hole polarons are found to exist in SnSe, and that *Pnma*-SnSe has only very weakly bound excitons [233], we can exclude the possibility that electron-hole pairs will induce polaronic signatures in UEDS. We determine the effect of

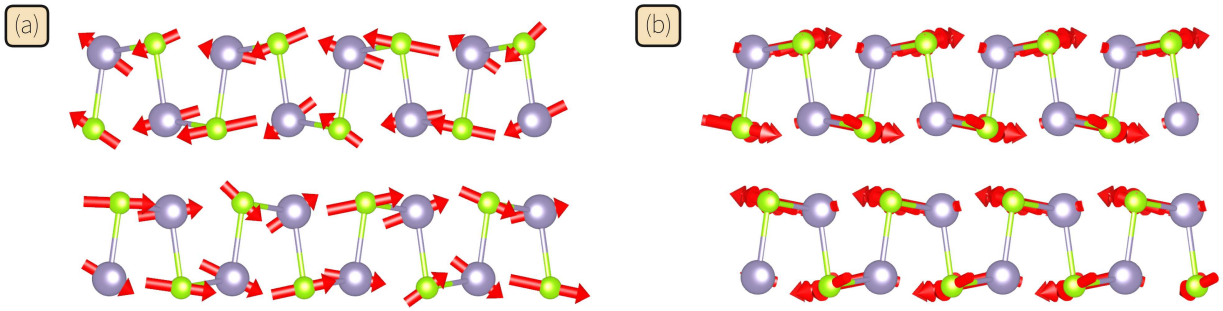

FIGURE 10.11: Representative polaron displacements in SnSe in the room temperature phase. The atomic displacements for the hole (a) and electron (b) polarons, viewed along the **b**-crystal axis. The arrows indicate the direction of displacement, and are not drawn to scale. The hole polaron results in an only a straightening of the layer in the armchair direction, while the electron polaron twists the atoms as well.

this "exciton-polaron" as a linear superposition of the atomic displacements resulting from the electron and hole polarons. While this approach overestimates in intensity the diffuse scattering, it does indeed fail to replicate the experimental diffuse scattering pattern, see Figure 10.10. We safely conclude that there are no polaron signatures in SnSe.

The absolute scattering intensities of the thermal equilibrium, hole polaron, and electron polaron conditions are given in Figure 10.10d-g, with histograms of the polaronic displacements in Figure 10.10h-i. A representative unit cell showing the calculated polaron displacements is shown in Figure 10.11.

Sn atomic index	$U_{\mathrm{Sn}_k,\alpha\alpha'}$	Se atomic index	$U_{\mathrm{Se}_k,\alpha\alpha'}$
1	$\begin{pmatrix} 0.01539113 & 0.00000000 & 0.00038529 \\ 0.00000000 & 0.01285731 & -0.00000000 \\ 0.00038529 & -0.00000000 & 0.01464373 \end{pmatrix}$	**1**	$\begin{pmatrix} 0.01824479 & 0.00000000 & -0.00387067 \\ 0.00000000 & 0.01575535 & -0.00000000 \\ -0.00387067 & -0.00000000 & 0.01938273 \end{pmatrix}$
2	$\begin{pmatrix} 0.01539113 & 0.00000000 & -0.00038530 \\ 0.00000000 & 0.01285731 & -0.00000000 \\ -0.00038530 & -0.00000000 & 0.01464373 \end{pmatrix}$	**2**	$\begin{pmatrix} 0.01824479 & 0.00000000 & 0.00387067 \\ 0.00000000 & 0.01575535 & -0.00000000 \\ 0.00387067 & -0.00000000 & 0.01938273 \end{pmatrix}$
3	$\begin{pmatrix} 0.01539113 & 0.00000000 & -0.00038530 \\ 0.00000000 & 0.01285731 & -0.00000000 \\ -0.00038530 & -0.00000000 & 0.01464373 \end{pmatrix}$	3	$\begin{pmatrix} 0.01824479 & 0.00000000 & 0.00387067 \\ 0.00000000 & 0.01575535 & -0.00000000 \\ 0.00387067 & -0.00000000 & 0.01938273 \end{pmatrix}$
4	$\begin{pmatrix} 0.01539113 & 0.00000000 & 0.00038529 \\ 0.00000000 & 0.01285731 & -0.00000000 \\ 0.00038529 & -0.00000000 & 0.01464373 \end{pmatrix}$	4	$\begin{pmatrix} 0.01824479 & 0.00000000 & -0.00387067 \\ 0.00000000 & 0.01575535 & -0.00000000 \\ -0.00387067 & -0.00000000 & 0.01938273 \end{pmatrix}$

TABLE 10.3: The values of the anisotropic displacement tensor for each atom in the unit cell, given by Eq. (5.24) of the main text in units of Å^2. We note that for all atoms the **b**-axis row is smaller in magnitude than the **c**-axis row, which implies scattering for $\mathbf{Q} \parallel \mathbf{b}$ is larger than $\mathbf{Q} \parallel \mathbf{c}$ as in Section 10.4.

10.5 DISSECTING EPC IN *Pnma*

To further unravel the role of EPC in SnSe via UEDS, we aim to envisage the EPC strength as a function of phonon momentum $\mathbf{q}$. While in general describing the coupling of a particular interband transition to the phonon system, we focus here on a specific coupling: intraband hole scattering in the upper most valence band. By isolating this particular transition (valence to valence (val), given by the band indexing $m = \text{val} = n$) and integrating over electronic degrees of freedom, we can identify a unique coupling of hole scattering to the entirety of a given phonon mode:

$$g_{\mathbf{q}\nu} \triangleq \int_{\text{BZ}} \frac{d^3\mathbf{k}}{(2\pi)^3} g^{\nu}_{\text{val-val}}(\mathbf{k}, \mathbf{q}) \tag{10.24}$$

which can now serve as a relative contribution of a particular phonon mode to the diffuse scattering pattern following this intraband transition. We focus on the intravalence hole scattering process, although the intraconduction electron scattering process yields qualitatively similar results, see Figure 10.12.

We can now determine the amount each mode (via Eq. (5.10)) will be occupied and thus diffract due to hole scattering by weighting the modes with Eq. (10.24):

$$I_1(\mathbf{Q}) = \sum_{\nu} I_1^{\nu}(\mathbf{Q}) \longrightarrow \frac{\sum_{\nu} g^{\nu}(\mathbf{Q}) I_1^{\nu}(\mathbf{Q})}{\sum_{\nu} g^{\nu}(\mathbf{Q})} \tag{10.25}$$

where the extension of the weights $g_{\mathbf{q}\nu}$ to the entire range of scattering vectors $g^{\nu}(\mathbf{Q})$ is done by tiling $\mathbf{q} \to \mathbf{Q} = \mathbf{q} + \mathbf{G}$ for $\mathbf{G}$ a reciprocal lattice vector. The unweighted scattering patterns of Eq. (5.10) show how a thermal equilibrium (BE) distribution of phonons scatters, while the weighted patterns of Eq. (10.25) show how the distribution of hot phonons, as prepared by the phonon-momentum dependence of the EPC, will scatter. Equation (10.26) shows the differences in scattering between these two distributions, where the differential diffuse scattering in Figure 10.13 that results from the EPC weighting

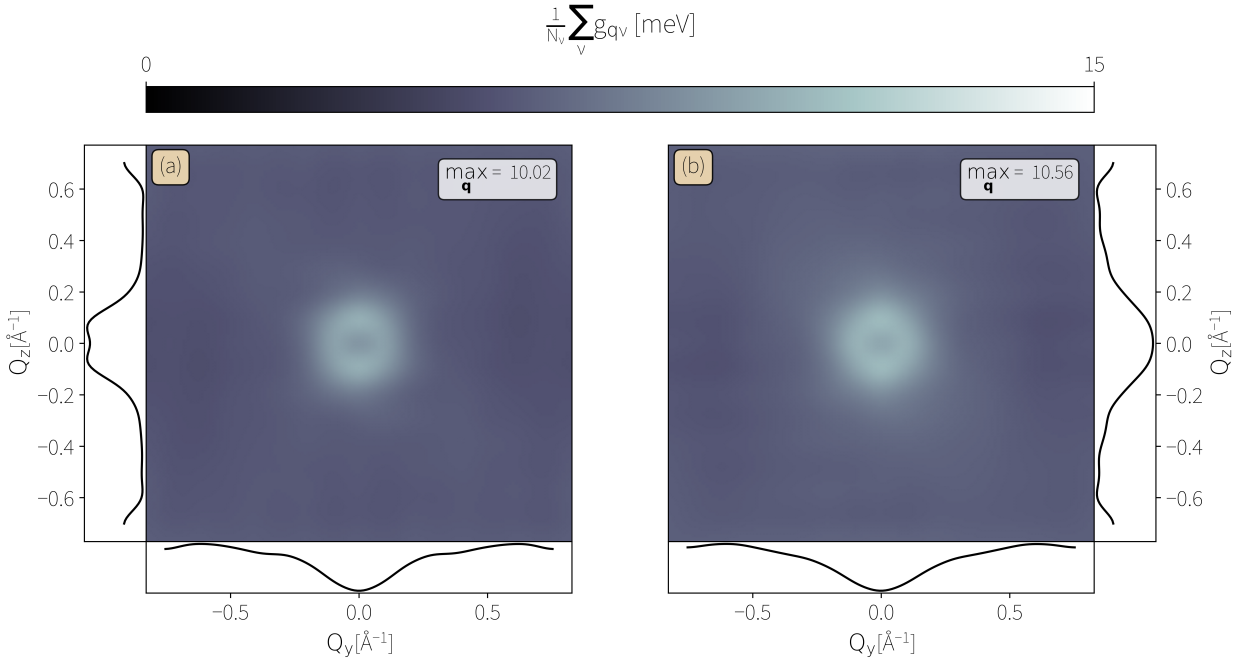

FIGURE 10.12: Average EPC weighting for the intravalence hole scattering process (a) and for the intraconduction electron scattering process (b). Both show qualitatively the same features, namely annular pattern around zone center as expected for a highly polar lattice. The linecuts in each dimension are given along each of the primary axes. While nearly identical, the hole weights are much more annular than the electron weights around Γ, more consistent with experimental diffuse scattering results, while the electron weights are more Gaussian distributed.

is the experimental observable reported by UEDS *immediately* following photoexcitation.

$$\Delta I^{\mathrm{EPC}} = \underbrace{\left(\frac{\sum_\nu g^\nu(\mathbf{Q}) I_1^\nu(\mathbf{Q})}{\sum_\nu g^\nu(\mathbf{Q})}\right)}_{\substack{\text{EPC-prepared}\\ \text{hot distribution}}} - \underbrace{\left(\sum_\nu I_1^\nu(\mathbf{Q})\right)}_{\substack{\text{BE equilibrium}\\ \text{distribution}}} \quad . \tag{10.26}$$

Remarkably, the resulting differential pattern shows excellent agreement with experimental diffuse scattering images in its momentum dependence around Γ [118, 143]. Namely, the modes that dually scattering strongly and are coupled well to the intraband hole transitions result in an annular momentum dependence, centered at zone center. Both Refs [118, 143] interpret the resulting data as being indiciative of a large scale real-space dislocation of the atomic positions, which we dismiss from the previous polaron calculations. These studies discredited EPC as the cause of the momentum dependence of the diffuse scattering. However, this analysis suggests that the underlying cause of each interpretation, polaron formation or domain fracture respectivey, is the expected

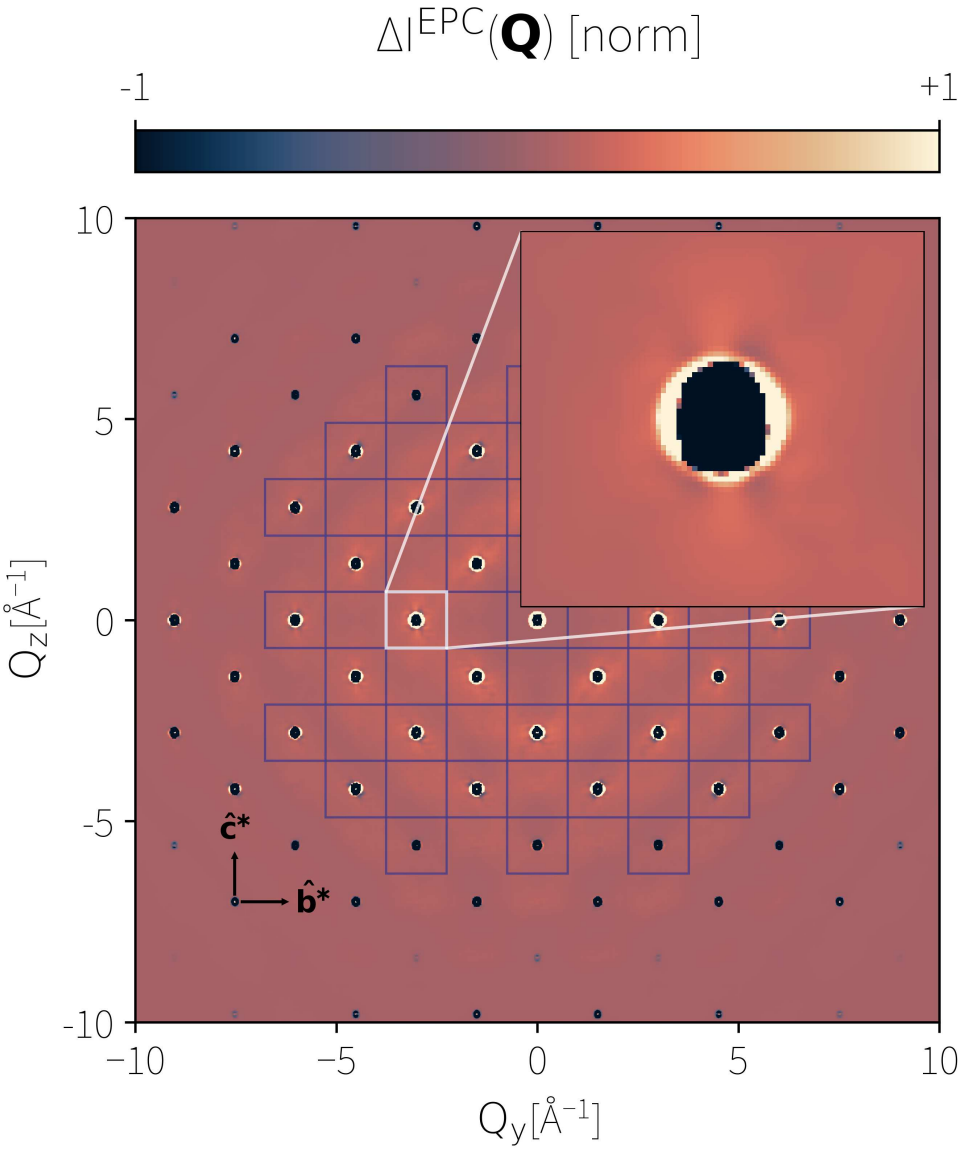

FIGURE 10.13: EPC-weighted differential diffuse scattering pattern resulting from the intraband hole scattering within the valence manifold compared to equilibrium diffuse scattering. The patterns show a clear annular momentum dependence consistent with previous experimental ultrafast scattering data [118].

scattering from a hot distribution of phonons as prepared by the calculated EPC.

10.6 ANHARMONIC COUPLING

One of the most interesting features about SnSe is the stability of the lattice with respect to the interatomic forces. As a specific example, the lowest energy mode of A_g symmetry (in-plane polarized) freezes at the phase transition, and decomposes into an optical mode at Γ and an acoustic mode at Y in the $Cmcm$ phase. The coupling between these two modes is entirely anharmonic, and in fact each of the atomic configurations of SnSe are extremely anharmonic. Here, *anharmonic* means that second-order force constants become entirely insufficient to completely describe the state of the lattice; without higher order interactions, the material would not be stable! Fourth order and higher processes are mainly relevant at higher temperatures or for phase transition and thermal expansion studies [234]. Calculation has been done before of the quartic terms, but remains a cumbersome and expensive calculation [235].

Note 10.3

The fourth-order force constants $\Phi_{ijkl}^{\alpha\beta\gamma\theta}$ will necessitate 100s of explicit supercell calculations (corresponding to dense Monkhorst-Pack grids in $\mathbf{q}$-space) to achieve reasonable accuracy, providing an extreme rate limiting step that makes these calculations tedious and expensive.

The higher-order force constants were computed using the finite-displacement method on a $2 \times 4 \times 4$ supercell including up to 10^{th} nearest neighbor interactions, resulting in 58 triplet equivalence classes for a total of 448 DFT runs for third-order force constants, and 154 quartet equivalence classes for a total of 7816 total DFT runs for the fourth-order force constants. The anharmonic scattering rates were computed on a $4 \times 8 \times 8$ $\mathbf{q}$-grid, using the complete iterative solution of the Boltzmann transport equation for the 3ph processes [55] while the 4ph processes were evaluated in the relaxation time approximation. The anharmonic calculations,

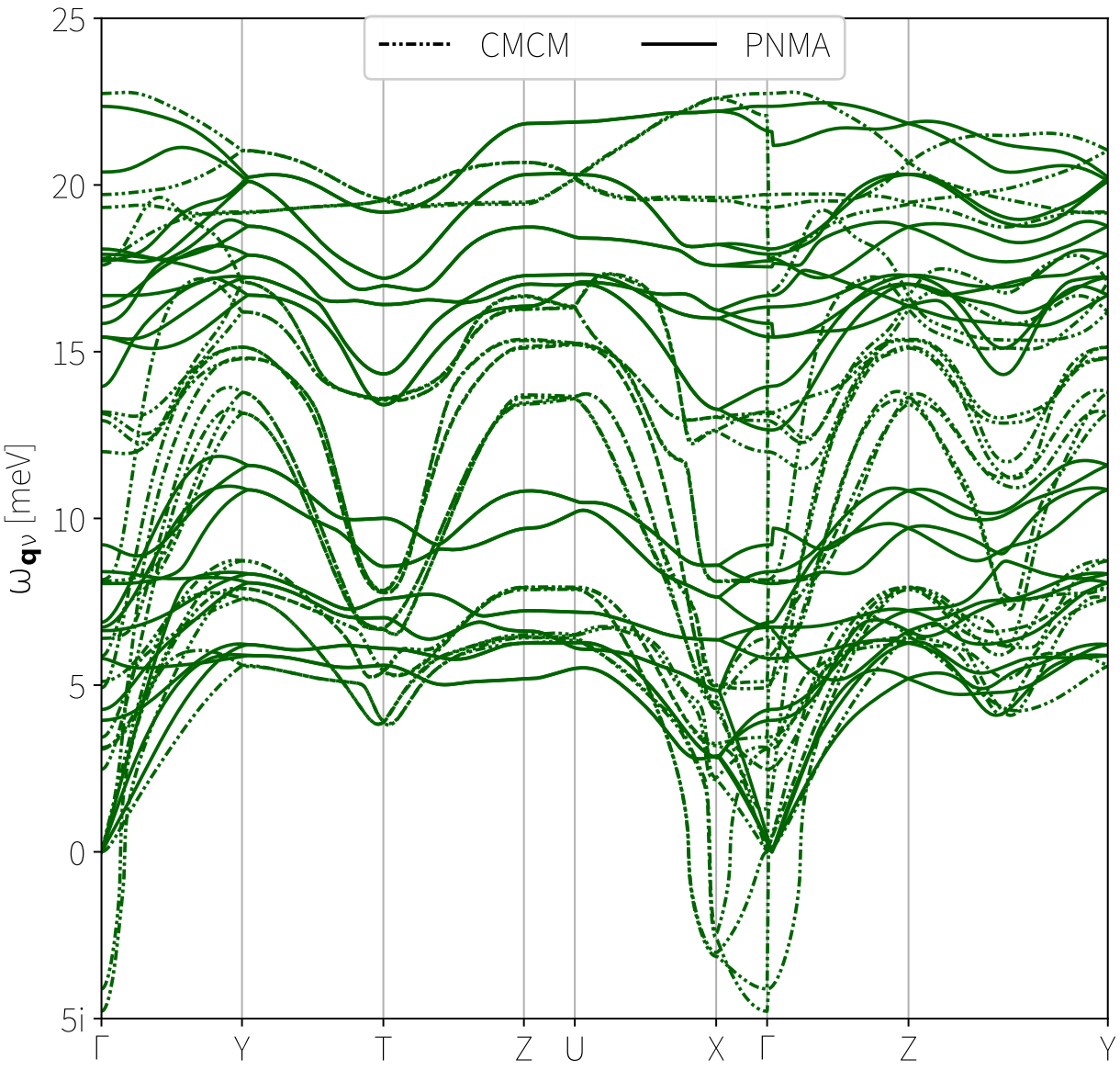

FIGURE 10.14: Phonon dispersions of SnSe in both the *Pnma* and *Cmcm* phases. The imaginary frequencies of the *Cmcm* indicate that these phonons are not stable, and thus require anharmonic couplings to stabilize the lattice at equilibrium.

including the higher-order force constant calcualtions, utilized modified versions of the `FourPhonon` package [235]. Divergences at Γ (where applicable) were treated in the same way as the EPC weights, and image renders used the same interpolation scheme and density for the anharmonic **q**-grid.

10.6.1 *Expanding anharmonicity to the fourth order*

In these fourth-order calculations, in a completely analagous description to that of the third-order phase space in Eq. (4.20), we can write the transition probability matrices as the Fourier transform of the fourth-order force constants:

$$\left(\Psi^{\nu\nu'\nu''\nu'''}_{\mathbf{q}\mathbf{q}'\mathbf{q}''\mathbf{q}'''}\right)^{\pm\pm} = \sum_{ijkl}\sum_{\alpha\beta\gamma\theta} \Phi^{\alpha\beta\gamma\theta}_{ijkl} \frac{(\boldsymbol{\varepsilon}^{i}_{\mathbf{q}\nu})^{\alpha}(\boldsymbol{\varepsilon}^{j}_{\pm\mathbf{q}'\nu'})^{\beta}(\boldsymbol{\varepsilon}^{k}_{\pm\mathbf{q}''\nu''})^{\gamma}(\boldsymbol{\varepsilon}^{l}_{-\mathbf{q}'''\nu'''})^{\theta}}{\sqrt{\mu_i\mu_j\mu_k\mu_l}} e^{\pm i\mathbf{q}'\cdot\mathbf{R}_j} e^{\pm\mathbf{q}''\cdot\mathbf{R}_k} e^{-\mathbf{q}'''\cdot\mathbf{R}_l} \tag{10.27}$$

where the fourth-order force constants $\Phi^{\alpha\beta\gamma\theta}_{ijkl}$ contribute the latest term in the expansion of the crystal potential energy:

$$E^{\mathrm{DFT}} = E^{\mathrm{DFT}}_0 + \frac{1}{2}\sum_{\substack{ij\\\alpha\beta}} \Phi^{\alpha\beta}_{ij} r^{\alpha}_i r^{\beta}_j + \frac{1}{3!}\sum_{\substack{ijk\\\alpha\beta\gamma}} r^{\alpha}_i r^{\beta}_j r^{\gamma}_k + \frac{1}{4!}\sum_{\substack{ijkl\\\alpha\beta\gamma\theta}} \Phi^{\alpha\beta\gamma\theta}_{ijkl} r^{\alpha}_i r^{\beta}_j r^{\gamma}_k r^{\theta}_l + \cdots \tag{10.28}$$

We can determine these fourth order force constants from finite-difference again:

$$\Phi^{\alpha\beta\gamma\theta}_{ijkl} = \frac{\partial^4 E^{\mathrm{DFT}}}{\partial r^{\alpha}_i \partial r^{\beta}_j \partial r^{\gamma}_k \partial r^{\theta}_l} \approx \frac{1}{2h}\left[\frac{\partial^3 E^{\mathrm{DFT}}}{\partial r^{\beta}_j \partial r^{\gamma}_k \partial r^{\theta}_l}(r^{\alpha}_i = h) - \frac{\partial^3 E^{\mathrm{DFT}}}{\partial r^{\beta}_j r^{\gamma}_k r^{\theta}_l}(r^{\alpha}_i = -h)\right] \tag{10.29}$$

where the 3rd order terms can be expanded according to Eq. (4.20c). Symmetry arguments can be made to reduce the computational cost of these force constants by recognizing that $\Phi^{\alpha\beta\gamma\theta}_{ijkl} = \Phi^{\alpha\beta\theta\gamma}_{ijlk} = \cdots$ (providing 24 equality constraints). Further, to take advantage of crystal symmetries, the following can be shown [235] to hold:

$$\Phi^{\alpha'\beta'\gamma'\theta'}_{\mathbf{T}_{b(i)}\mathbf{T}_{b(j)}\mathbf{T}_{b(k)}\mathbf{T}_{b(l)}} = \sum_{\alpha\beta\gamma\theta} \mathbf{T}^{\alpha'\alpha}\mathbf{T}^{\beta'\beta}\mathbf{T}^{\gamma'\gamma}\mathbf{T}^{\theta'\theta}\Phi^{\alpha\beta\gamma\theta}_{ijkl} \tag{10.30}$$

where, for point-group and translation operators $\mathbf{T}$ and $\mathbf{b}$, $\mathbf{T}_{b(i)}$ represents the the mapping of atom i under the given operation. The symmetry operators further must satisfy $\sum_{\alpha}\mathbf{T}^{\alpha'\alpha}\mathbf{R}^{\alpha}_i + \mathbf{b}^{\alpha'} = \mathbf{R}^{\alpha'}_{\mathbf{T}_{b(i)}}$.

10.6.2 *Anharmonicity in SnSe*

While EPC might readily explain the scattering intensity as a function of phonon momentum, the resulting dynamics following photoexcitation will be strongly dependent on

anharmonic effects, required by the fact that the lattice must thermalize in the long-time limit. To this aim, given that SnSe is a strongly anharmonic material, we strive to explore the influence of anharmonicities on UEDS via three-phonon (3ph) and four-phonon (4ph) scattering processes.

We start by determining expressions for the scattering rates associated with 3ph and 4ph scattering processes, where we allow for absorption (+) and emission (-) processes in the 3ph picture, and for total absorption (++), partial transfer (+-), and total emission (--) processes in the 4ph picture. We can derive expressions for the scattering rate in the RTA from 3ph processes [52] and from 4ph processes [235] as:

$$\frac{1}{\tau^{3\mathrm{ph}}_{\mathbf{q}\nu}} = \frac{\hbar\pi}{4}\sum_{\nu'\nu''}\int\frac{d\mathbf{q}'}{\Omega_{\mathrm{BZ}}}\Big\{\left|\Psi^{\nu\nu'\nu''}_{\mathbf{q}\mathbf{q}'\mathbf{q}''}\right|^2_{+}(n_{\mathbf{q}'\nu'}-n_{\mathbf{q}''\nu''})\delta(\omega_{\mathbf{q}\nu}+\omega_{\mathbf{q}'\nu'}-\omega_{\mathbf{q}''\nu''})\delta^{\mathbf{G}}_{\mathbf{q}+\mathbf{q}'-\mathbf{q}''} + \left|\Psi^{\nu\nu'\nu''}_{\mathbf{q}\mathbf{q}'\mathbf{q}''}\right|^2_{-}\frac{1}{2}(n_{\mathbf{q}'\nu'}+n_{\mathbf{q}''\nu''}+1)\delta(\omega_{\mathbf{q}\nu}-\omega_{\mathbf{q}'\nu'}-\omega_{\mathbf{q}''\nu''})\delta^{\mathbf{G}}_{\mathbf{q}-\mathbf{q}'-\mathbf{q}''}\Big\} \tag{10.31}$$

$$\begin{aligned}\frac{1}{\tau^{4\mathrm{ph}}_{\mathbf{q}\nu}} = \frac{\hbar^2\pi}{8}\sum_{\nu'\nu''\nu'''}\int\frac{d\mathbf{q}'\,d\mathbf{q}''}{\Omega^2_{\mathrm{BZ}}}\Big\{ &\left|\Psi^{\nu\nu'\nu''\nu'''}_{\mathbf{q}\mathbf{q}'\mathbf{q}''\mathbf{q}'''}\right|^2_{++}\frac{1}{2}(1+n_{\mathbf{q}'\nu'})(1+n_{\mathbf{q}''\nu''})n_{\mathbf{q}'''\nu'''}\delta(\omega_{\mathbf{q}\nu}+\omega_{\mathbf{q}'\nu'}+\omega_{\mathbf{q}''\nu''}-\omega_{\mathbf{q}'''\nu'''})\delta^{\mathbf{G}}_{\mathbf{q}+\mathbf{q}'+\mathbf{q}''-\mathbf{q}'''}\\ &\left|\Psi^{\nu\nu'\nu''\nu'''}_{\mathbf{q}\mathbf{q}'\mathbf{q}''\mathbf{q}'''}\right|^2_{+-}\frac{1}{2}(1+n_{\mathbf{q}'\nu'})n_{\mathbf{q}''\nu''}n_{\mathbf{q}'''\nu'''}\delta(\omega_{\mathbf{q}\nu}+\omega_{\mathbf{q}'\nu'}-\omega_{\mathbf{q}''\nu''}-\omega_{\mathbf{q}'''\nu'''})\delta^{\mathbf{G}}_{\mathbf{q}+\mathbf{q}'-\mathbf{q}''-\mathbf{q}'''}\\ &\left|\Psi^{\nu\nu'\nu''\nu'''}_{\mathbf{q}\mathbf{q}'\mathbf{q}''\mathbf{q}'''}\right|^2_{--}\frac{1}{6}n_{\mathbf{q}'\nu'}n_{\mathbf{q}''\nu''}n_{\mathbf{q}'''\nu'''}\delta(\omega_{\mathbf{q}\nu}-\omega_{\mathbf{q}'\nu'}-\omega_{\mathbf{q}''\nu''}-\omega_{\mathbf{q}'''\nu'''})\delta^{\mathbf{G}}_{\mathbf{q}-\mathbf{q}'-\mathbf{q}''-\mathbf{q}'''}\Big\}\quad .\end{aligned} \tag{10.32}$$

The previous hypothesis of polaron / domain formation in this material was based on the premise that anharmonic decay, in the limit of momentum-conserving scattering, could not explain the momentum anisotropy in the transient UEDS signals. To quantify the validity of this assumption, we enumerate, at the evaluation of each of the integrands in Eqs. (10.31) and (10.32), whether that process describes normal or Umklapp scattering by using the first BZ image of each $\mathbf{q}$ point, $\widehat{\mathbf{q}}$. For 3ph processes (and analagously for 4ph processes), a $\pm$ process is considered to be normal if $\widehat{\mathbf{q}} \pm \widehat{\mathbf{q}}' = \widehat{\mathbf{q}}''$, and Umklapp otherwise.

By using the average number of processes for each type of scattering across the BZ for each mode, we determine that the Umklapp processes (averaging over the modes) actually account for 65% of the anharmonic scattering in this material, invalidating the assumption of solely momentum-conserving decay channels in previous studies. This necessitates a closer look at the behaviour of anharmonic effects in this material as a possible explanation for its behaviour following photoexcitation.

Weighting the diffuse scattering by the EPC strengths as in Eq. (10.26) was an effective measure of early time diffuse scattering immediately following photoexcitation and at the onset of hot carrier relaxation and scattering. The long-time behaviour of the lattice, however, will be dominated by anharmonic decay channels so that the lattice self-thermalizes. In order to quantify the effects of anharmonicity, we define the momentum-resolved anharmonic scattering rates $\Gamma^{\text{anh}}_{\mathbf{q}\nu}$ as the weights through which anharmonic effects will manifest themselves in the mode-resolved diffuse scattering patterns $I^{\nu}_{1}(\mathbf{Q})$. This scattering rate results from all anharmonicities of the lattice to fourth order; yet as Sn (Se) has 10 (5) stable isotopes in nontrivial natural abundances, we also include the effects of isotope scattering in the anharmonic weights [236]:

$$\Gamma^{\text{iso}}_{\mathbf{q}\nu} = \frac{\pi\omega_{\mathbf{q}\nu}}{2}\sum_{\nu'}\int\frac{d\mathbf{q}'}{\Omega_{\text{BZ}}}\sum_{\kappa}\left\{\underbrace{\left[\sum_{s}a^{s}_{\kappa}\left[1-M^{s}_{\kappa}/\langle M^{s}_{\kappa}\rangle\right]^{2}\right]}_{g_{\kappa}}\times\left|\boldsymbol{\varepsilon}^{*}_{\mathbf{q}\nu\kappa}\cdot\boldsymbol{\varepsilon}_{\mathbf{q}'\nu'\kappa}\right|^{2}\delta(\omega_{\mathbf{q}\nu}-\omega_{\mathbf{q}'\nu'})\right\} \tag{10.33}$$

where g_{κ} is the Pearson coefficient of the variations in isotope mass M^{s}_{κ} of the κ^{th} atom and its s^{th} isotope, with $\langle M^{s}_{\kappa}\rangle$ the average isotope mass given relative abundances a^{s}_{κ}. We then can determine the total anharmonic lifetime of the phonons via Matthiessen's rule [237], as these scattering events are independent:

$$\Gamma^{\text{anh}}_{\mathbf{q}\nu} \triangleq \frac{1}{\tau^{\text{anh}}_{\mathbf{q}\nu}} = \frac{1}{\tau^{\text{3ph}}_{\mathbf{q}\nu}} + \frac{1}{\tau^{\text{4ph}}_{\mathbf{q}\nu}} + \frac{1}{\tau^{\text{anh}}_{\mathbf{q}\nu}} = \Gamma^{\text{3ph}}_{\mathbf{q}\nu} + \Gamma^{\text{4ph}}_{\mathbf{q}\nu} + \Gamma^{\text{iso}}_{\mathbf{q}\nu} \quad . \tag{10.34}$$

Following photoexcitation, experimental work showed in increase in phonon occupancy at wavevectors $\mathbf{q} \sim \Gamma$, as we have explained in Section 10.5, with a rise time of ~ 300 fs.

Simultaneously, phonon occupancy rose, slowly but consistently, for wavevectors $\mathbf{q} \approx \Gamma$. To this point, we inspect the anharmonic scattering rates in an annulus about zone center, specifically those modes $0.1\,\text{Å}^{-1} < |\mathbf{q}| < 0.2\,\text{Å}^{-1}$ which is the same range of wavevectors used for "zone-center" modes in Ref [118]. Inspecting the value of the anharmonic lifetimes within this region across the phonon modes yields an anharmonic decay rate of zone-center modes to be 6.43 ps, very closely matching the experimental decay rate of ~ 5 ps. We visualize the mode-resolved phase spaces and anharmonic lifetimes in Appendix B. Previous scattering studies posited that the $\mathbf{Q}$-dependence of the diffuse intensity at long times was indicative of the formation of a small polaron or local domain. Yet, given the previous analysis of EPC in the material, we explain the long-time behaviour by the constant anharmonic decay of zone-center modes into multiple phonons at higher wavevector in such a way that energy and momentum are conserved. This arises from the strong degree of anharmonicity in this material, where the immense available phase space for 3ph processes dominates for phonon energies where the phonon DOS is minimal, namely for $\mathbf{q} \sim \Gamma$, while nearly every phonon across the BZ has allowed 4ph scattering processes, aligning the 4ph phase space as a function of phonon energy with the pDOS (c.f. Figure 10.15). Taken together with the EPC analysis, we conclude there are no polaron diffuse scattering signatures in SnSe.

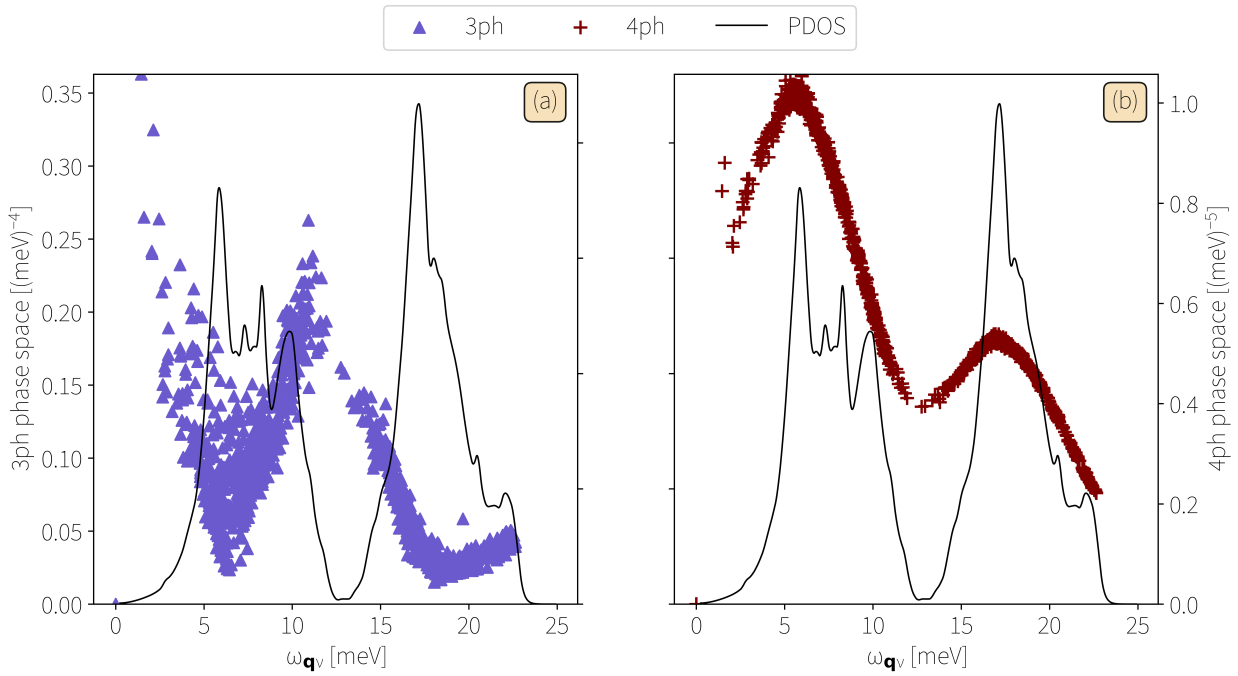

FIGURE 10.15: Anharmonic phase spaces in SnSe for three-phonon (left) and four-phonon (right) processes. The phonon DOS is rendered on both panels to illustrate the dominant regions of the phonon dispersion for each type of process.

10.7 OUTLOOK

We start by describing polaron formation within the basis of Kohn-Sham orbitals, and phonon normal modes. Such a description allows for the rapid identification of diffuse scattering signatures of polarons within Laval-Born-James theory, as well as relates experimentally accessible diffuse scattering images directly to the underlying envelope of the polaron wavefunction. We extend the formalism to include finite-temperature phonon-assisted scattering, and validate the approach on a prototypical ionic insulator LiF. Here, we discover that the electron polaron, with large spatial extent, can be reasonably described as a point defect in the material, and admits an annular momentum dependence to the resulting scattering about zone center. We then apply these analyses on the alleged polaronic material SnSe, where we find polaron formation is unlikely due to both the extreme delocalization of the polaron wavefunctions and the trivial polaron formation energies. We reconcile previous ultrafast scattering data on SnSe with more

conventional explanations. Namely, the intensity anisotropy with respect to Brillouin zones aligned with various crystal axes is explained by anisotropy in the Debye-Waller factors along each crystal axis. Further, the annular diffuse scattering signatures from experimental data are captured by the expected phonon momentum dependence of the electron-phonon coupling matrix elements. We show that the experimentally measured decay of zone-center phonon occupation is explained by the expected anharmonic lifetimes in the material resulting from 3ph and 4ph processes. The *ab-initio* insights of this work allow for a new experimental probe of polarons in systems where they exist, and have allowed for the reconciliation of previous conflicting reports in the thermoelectric SnSe.

Part V

EPILOGUE

11

Conclusion

While advances in recent years with respect to ultrafast laser light generation, electron beamline manipulation, RF compression techiques, and electron imaging detectors have progressed TEM far, there are still systems at the frontier of condensed matter science that leave much to discover. The progression of UED and UEDS theory to explore novel systems, such as monolayers and thermoelectrics, would not have been possible without these many advances in various technologies and theories.

Having started with the creation of monolayer samples with large in-plane area, we showed that currently existing instrumentation is able to detect, with extreme sensitivity, changes in phonon occupancy and atomic MSD in even 2D samples, where SNR could not be more limited. The development of Laval-Born-James (LBJ) theory to exactly describe transients in diffuse scattering signatures further opened up avenues for continued exploration of other exotic systems, without the attention to detail required to operate such an electron microscope column.

To continue pushing the bounds of what electron microscopy can do, we showed that distinct patterns in the inelastic phonon diffuse scattering of a material can even be sensitive enough to describe various mechanisms of charge carrier valley depolarization, as well as observe chiral phonons by their direct hallmark of increase in phonon

occupancy at the K valley of monolayer TMDs.

Finally, we illustrated that the combination of EPC calculations and the determination of anharmonic scattering processes can, without a full numerical solution of the TDBE, completely describe diffuse scattering data in an exotic system, SnSe. Further, the unique signatures of polaron formation on the diffuse scattering pattern were shown. While the polaron was found to unfortunately not exist in SnSe, the technique will hopefully be applied to other systems such as lead-halide perovskites or LiF to continue to probe their unique properties. The *ab-initio* insight from these results will, hopefully, inspire further works to continue to explore the range of possiblities afforded by UED and UEDS.

A

Appendix - Multiple Scattering Cross Section

The scattering form factor for secondary scattering $f^{(2)}(\mathbf{Q})$ given in Lemma 2.1 is:

$$\begin{aligned} f^{(2)}(\mathbf{k}_f, \mathbf{k}_i) &= -\frac{m_e L^3}{2\pi\hbar^2}\langle \mathbf{k}_f|\hat{V}\frac{1}{E_i - \hat{H}_0 + i\epsilon}\hat{V}|\mathbf{k}_i\rangle \\ &= -\frac{m_e L^3}{2\pi\hbar^2}\int d\mathbf{x}'\int d\mathbf{x}''\langle \mathbf{k}_f|\mathbf{x}'\rangle V(\mathbf{x}')\langle \mathbf{x}'\frac{1}{E_i - \hat{H}_0 + i\epsilon}\mathbf{x}''\rangle V(\mathbf{x}'')\langle \mathbf{x}''|\mathbf{k}_i\rangle \\ &= \left(\frac{m_e}{2\pi\hbar^2}\right)^2\int d\mathbf{x}'\int d\mathbf{x}'' e^{-i\mathbf{k}_f\cdot\mathbf{x}'}V(\mathbf{x}')\left(\frac{e^{i|\mathbf{k}_i||\mathbf{x}'-\mathbf{x}''|}}{|\mathbf{x}'-\mathbf{x}''|}\right)e^{i\mathbf{k}_i\cdot\mathbf{x}''}V(\mathbf{x}'') \end{aligned} \tag{A.1}$$

Note 1.1

In the derivation of Eq. (A.1) we've transformed the propagator into a representation with two complete basis sets, as well as utilised the result from the derivation of the Lippmann-Schwinger Equation, namely that

$$\langle \mathbf{x}'|\frac{1}{E_i - \hat{H}_0 + i\epsilon}|\mathbf{x}''\rangle = -\frac{m_e}{2\pi\hbar^2}\frac{e^{i|\mathbf{k}_i||\mathbf{x}'-\mathbf{x}''|}}{|\mathbf{x}'-\mathbf{x}''|}$$

We can directly compare the corresponding scattering cross section by computing an upper bound to determine the relative liklihood that such scattering occurs. To this aim, we make the approximation that transmission electron scattering experiments require thin (∼10s of nm thick) samples, so multiple electron scattering from the *same*

atom is very unlikely, and so the integrals approach zero as $|\mathbf{x}' - \mathbf{x}''| \to 0$. As such, the integral is effectively split into $\int d\mathbf{x}' \int d\mathbf{x}'' \to \int d\mathbf{x}' \left[\int_{|\mathbf{x}'-\mathbf{x}''|\leq a} d\mathbf{x}'' + \int_{|\mathbf{x}'-\mathbf{x}''|>a} d\mathbf{x}'' \right]$, with a the interatomic lattice spacing. We then write the scattering cross section as:

$$\begin{aligned}
\frac{d\sigma_2}{d\Omega} &< \frac{1}{a} \left| \left(\frac{m_e}{2\pi\hbar^2} \right)^2 \int d\mathbf{x}' \int d\mathbf{x}'' e^{-i\mathbf{k}_f \cdot \mathbf{x}'} V(\mathbf{x}') e^{i\mathbf{k}_i \cdot \mathbf{x}''} V(\mathbf{x}'') \right|^2 \\
&< \frac{1}{a} \left| \left(\frac{m_e}{2\pi\hbar^2} \right)^2 \int d\mathbf{x}' e^{-i\mathbf{k}_f \cdot \mathbf{x}'} V(\mathbf{x}') \int d\mathbf{x}'' e^{i\mathbf{k}_i \cdot \mathbf{x}''} V(\mathbf{x}'') \right|^2 \\
&< \frac{1}{a} \left| \frac{m_e}{2\pi\hbar^2} \int d\mathbf{x}' e^{-i\mathbf{k}_f \cdot \mathbf{x}'} V(\mathbf{x}') \right|^2 \left| \frac{m_e}{2\pi\hbar^2} \int d\mathbf{x}'' e^{i\mathbf{k}_i \cdot \mathbf{x}''} V(\mathbf{x}'') \right|^2 < \frac{1}{a} \left(\frac{d\sigma_1}{d\Omega} \right)^2
\end{aligned} \tag{A.2}$$

As most materials have lattice constants $[a] \sim$ Å, the relative liklihood of multiple scattering is therefore low.

B

Appendix - EPC and anharmonic weights in SnSe

The EPC weights used to produce the diffuse scattering pattern in Figure 10.13 is given in Figure B.1, while the anharmonic weights are given in Figures B.2 to B.5. The anharmonic 3- and 4- phonon phase spaces are given in Figures B.6 and B.7.

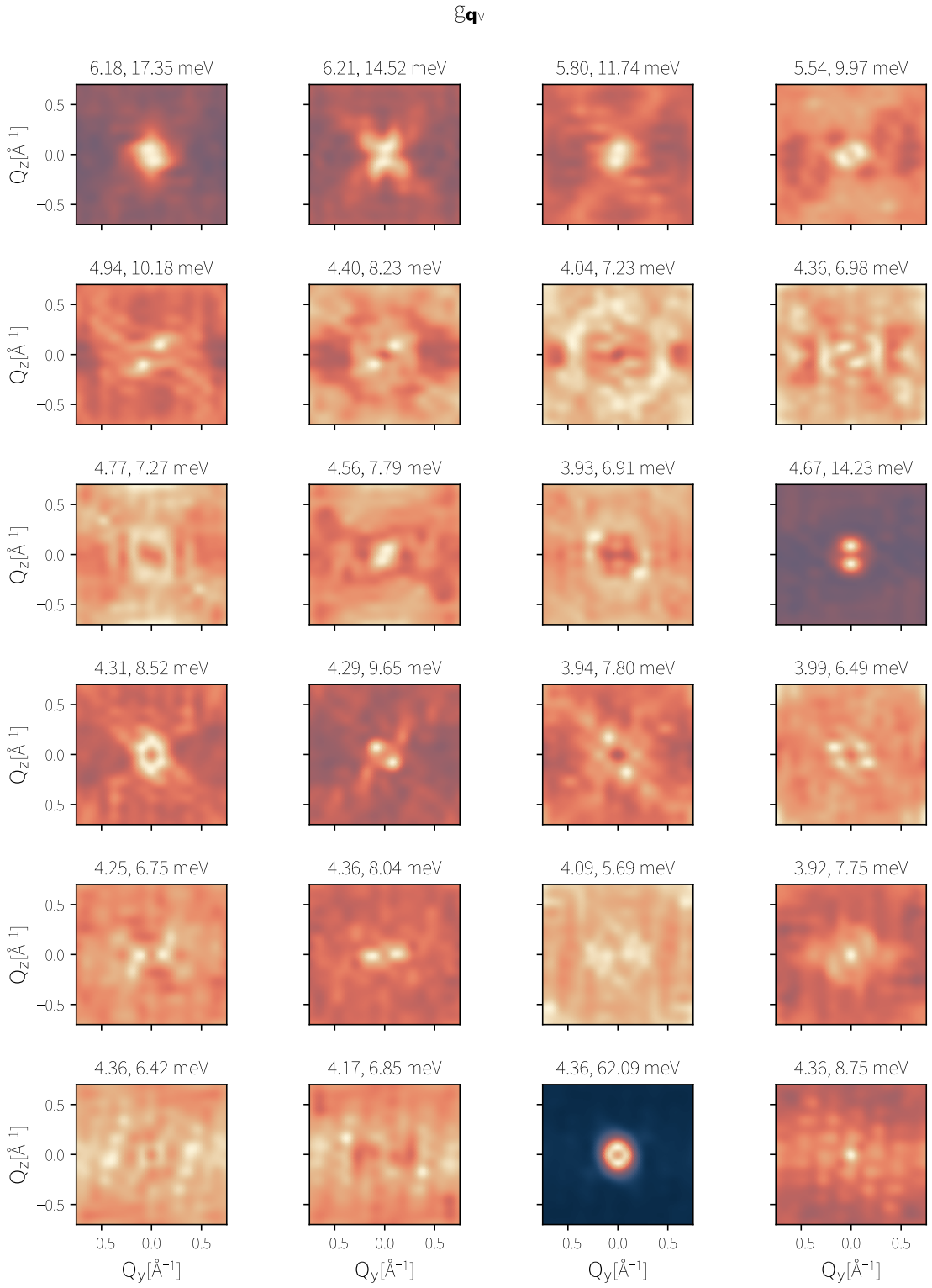

FIGURE B.1: Intravalence hole scattering coupling to each phonon mode as a function of phonon momenta $g_{\mathbf{q}\nu}$. Each panel title gives the minimum and maximum coupling energy across the BZ for the given branch. Phonon modes are sorted by increasing energy at Γ, and are indexed left to right, then top to bottom.

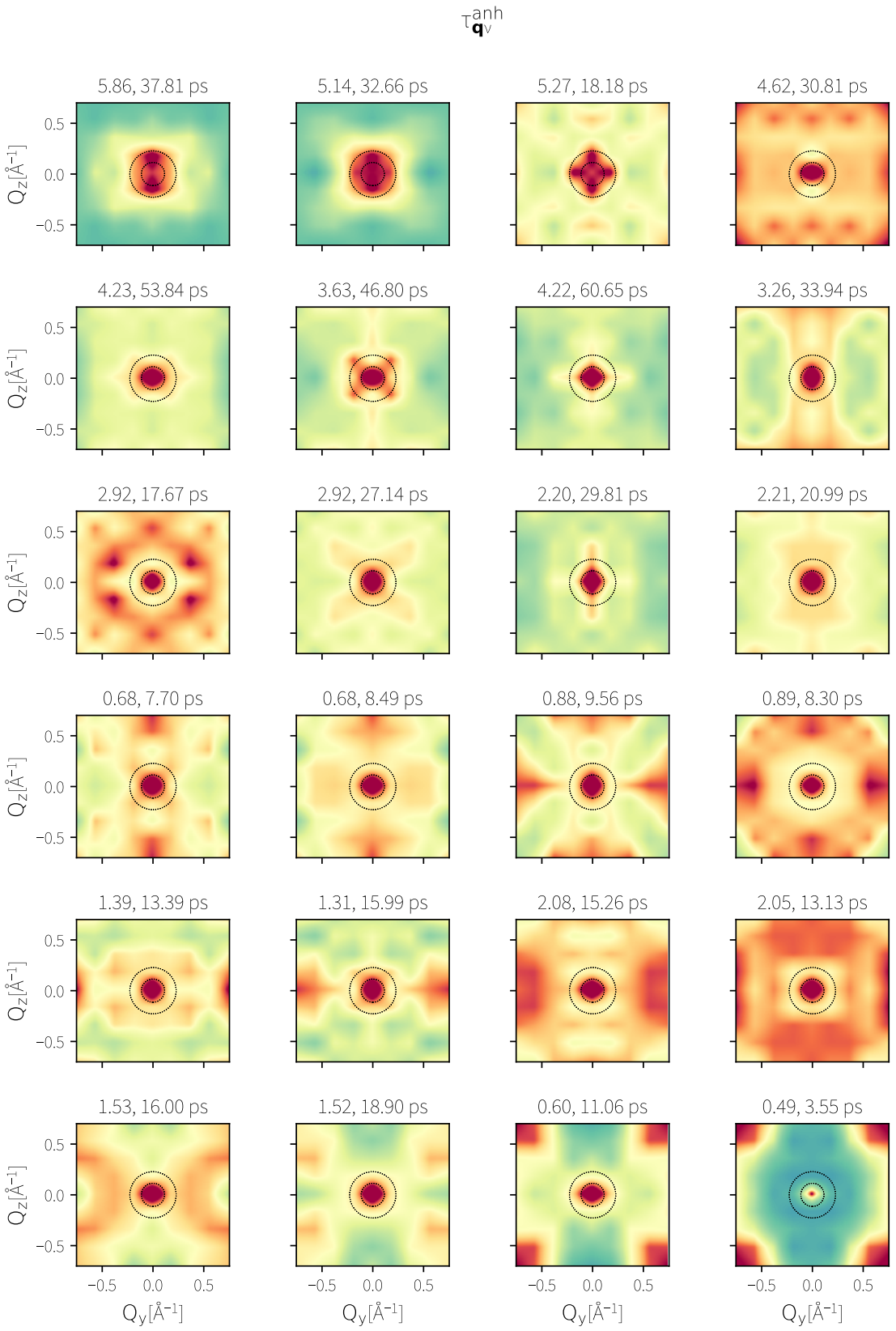

FIGURE B.2: Anharmonic phonon lifetimes taken as a reciprocal sum of lifetimes from 3ph scattering, 4ph scattering, and isotope scattering. Each panel title gives the minimum and maximum phonon lifetime across the BZ for the given branch. Phonon modes are sorted by increasing energy at Γ, and are indexed left to right, then top to bottom. Inset is the annular region defined to be "zone-center".

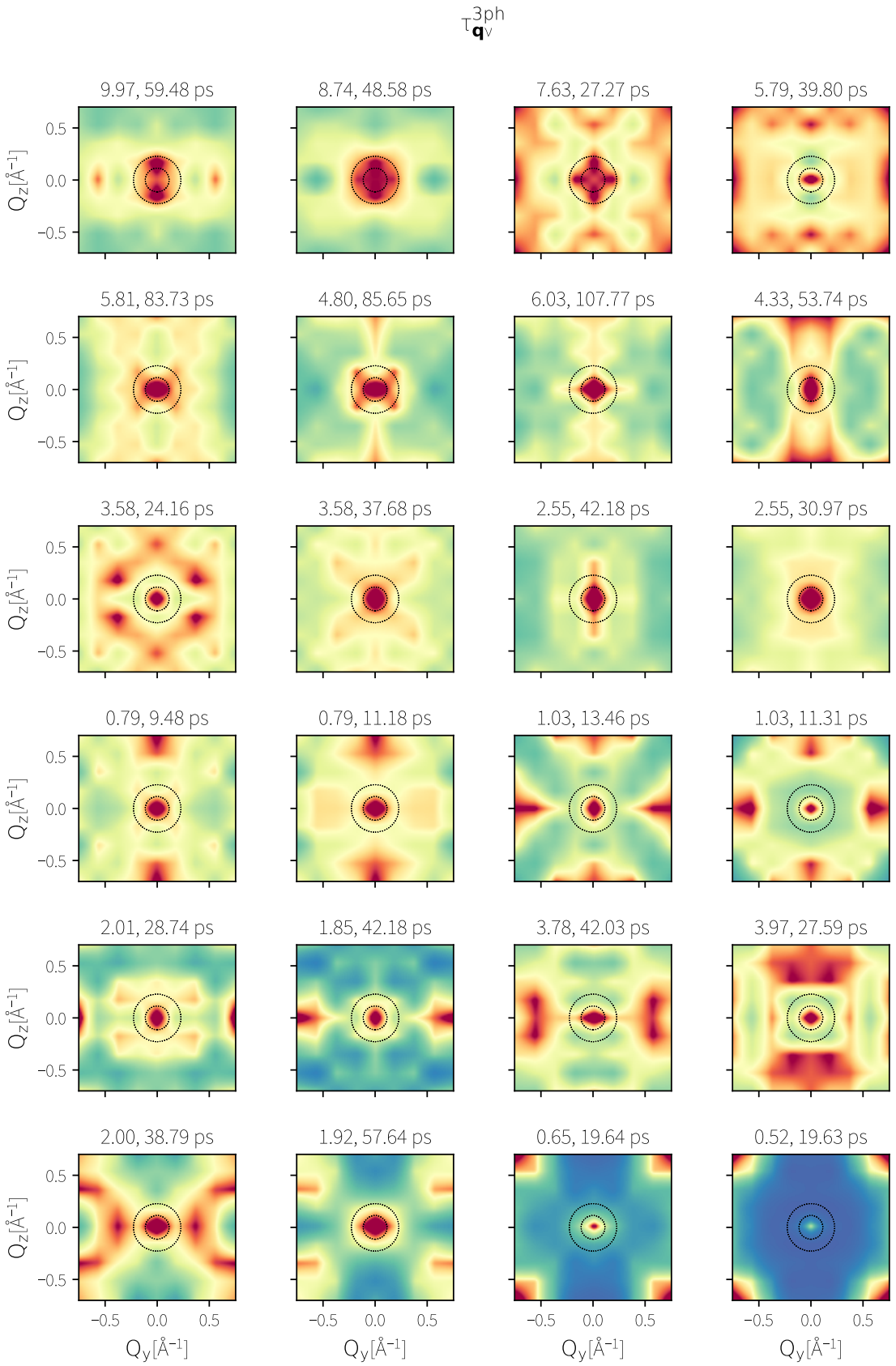

FIGURE B.3: Anharmonic phonon lifetime contribution from 3ph processes. Each panel title gives the minimum and maximum phonon lifetime across the BZ for the given branch. Phonon modes are sorted by increasing energy at Γ, and are indexed left to right, then top to bottom. Inset is the annular region defined to be "zone-center".

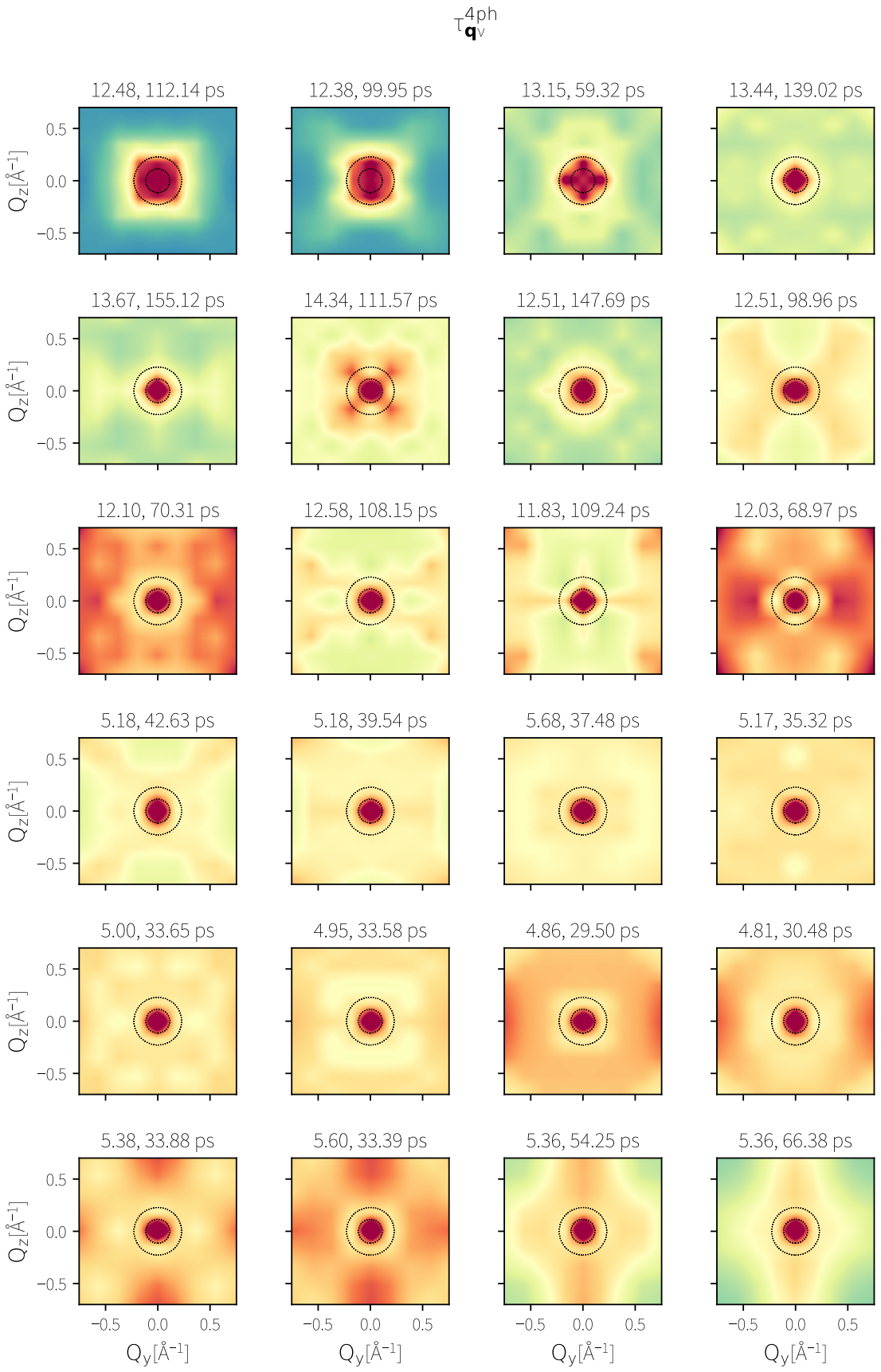

FIGURE B.4: Anharmonic phonon lifetime contribution from 4ph processes. Each panel title gives the minimum and maximum phonon lifetime across the BZ for the given branch. Phonon modes are sorted by increasing energy at Γ, and are indexed left to right, then top to bottom. Inset is the annular region defined to be "zone-center".

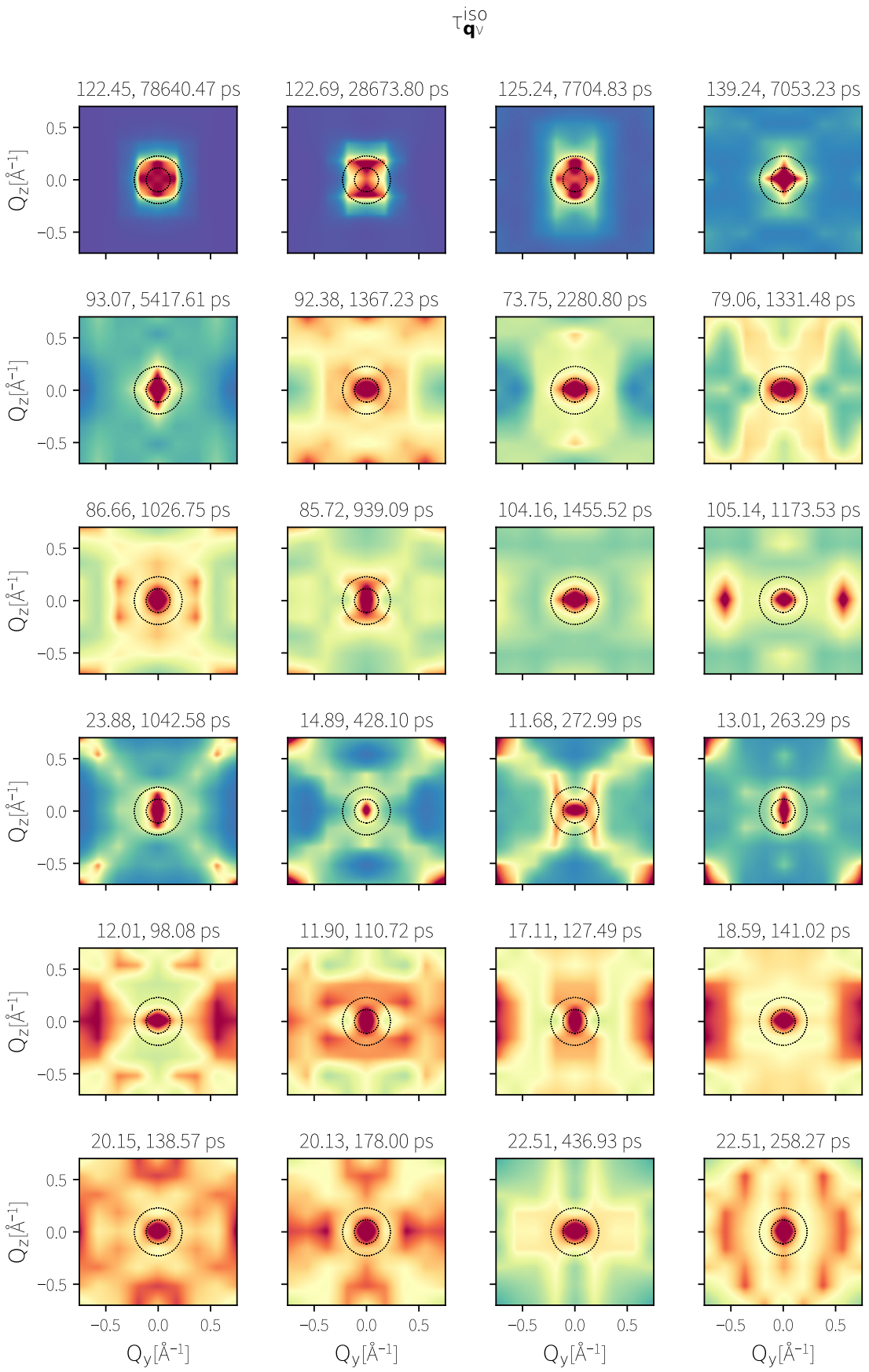

FIGURE B.5: Anharmonic phonon lifetime contribution from isotope scattering. Each panel title gives the minimum and maximum phonon lifetime across the BZ for the given branch. Phonon modes are sorted by increasing energy at Γ, and are indexed left to right, then top to bottom. Inset is the annular region defined to be "zone-center".

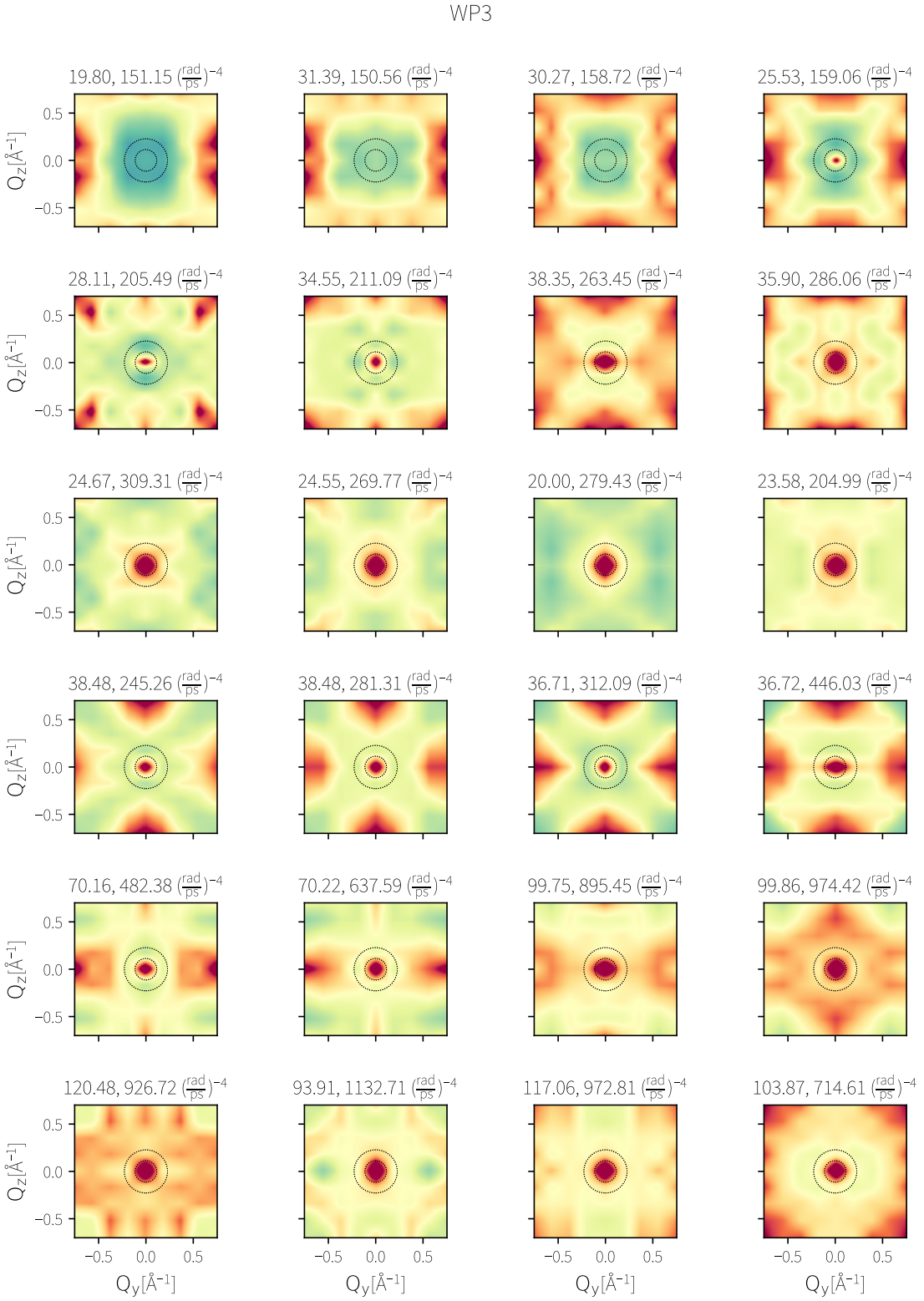

FIGURE B.6: Weighted three-phonon phase space in SnSe. Each panel title gives the minimum and maximum phase space magnitude across the BZ for the given branch. Inset is the annular region defined to be "zone-center".

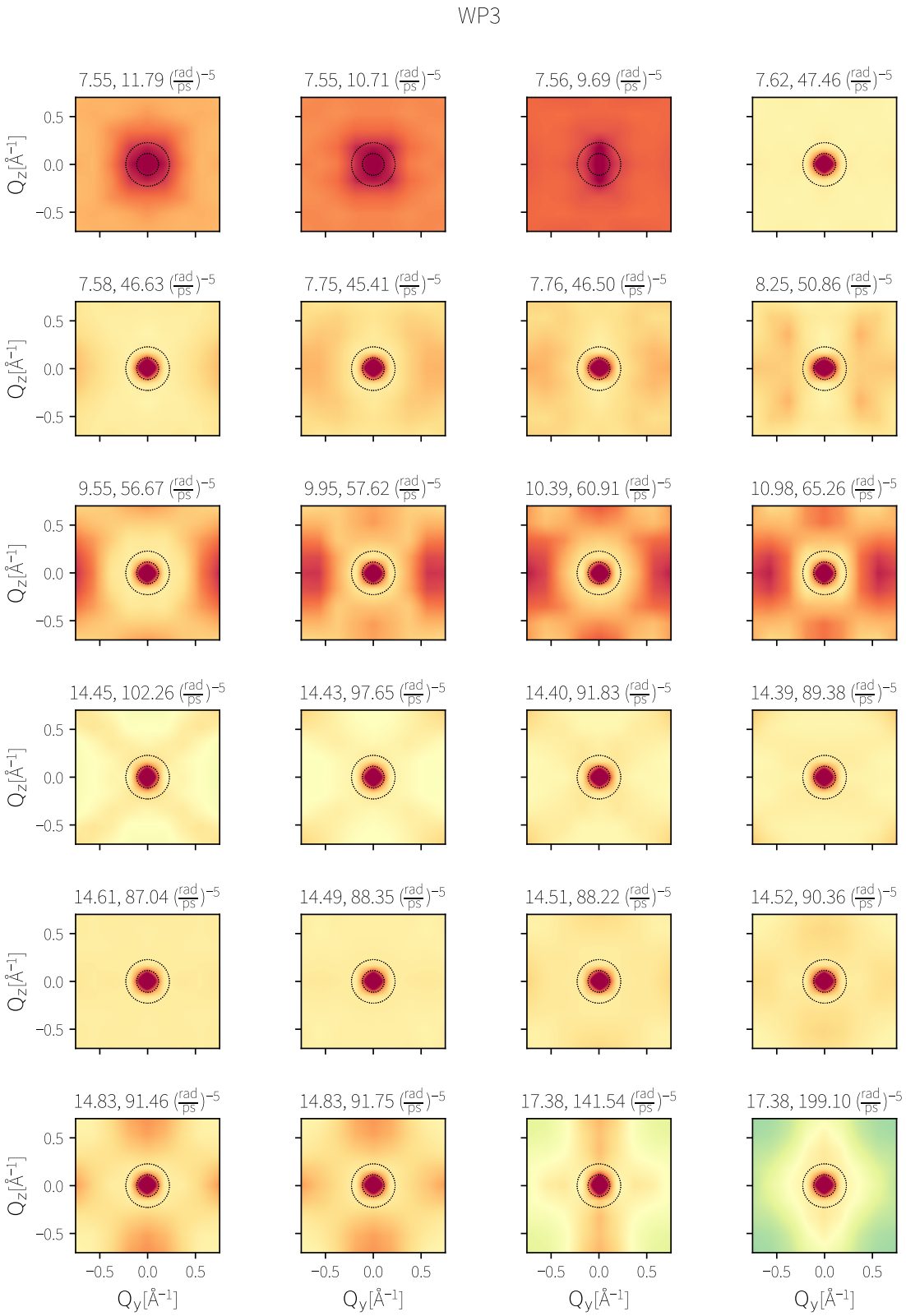

FIGURE B.7: Weighted four-phonon phase space in SnSe. Each panel title gives the minimum and maximum phase space magnitude across the BZ for the given branch. Inset is the annular region defined to be "zone-center".

Bibliography

[1] Anton L. van Helden, S. Dupré, Robert H. van Gent, and Huib J. Zuidervaart. "The origins of the telescope". In: 2010. URL: https://api.semanticscholar.org/CorpusID:129053124 (cit. on p. 4).

[2] H. Hertz. "Ueber einen Einfluss des ultravioletten Lichtes auf die electrische Entladung". In: *Annalen der Physik* 267.8 (1887), pp. 983–1000. DOI: https://doi.org/10.1002/andp.18872670827. eprint: https://onlinelibrary.wiley.com/doi/pdf/10.1002/andp.18872670827. URL: https://onlinelibrary.wiley.com/doi/abs/10.1002/andp.18872670827 (cit. on p. 4).

[3] A. Einstein. "Über einen die Erzeugung und Verwandlung des Lichtes betreffenden heuristischen Gesichtspunkt". In: *Annalen der Physik* 322.6 (1905), pp. 132–148. DOI: https://doi.org/10.1002/andp.19053220607. eprint: https://onlinelibrary.wiley.com/doi/pdf/10.1002/andp.19053220607. URL: https://onlinelibrary.wiley.com/doi/abs/10.1002/andp.19053220607 (cit. on p. 4).

[4] Martin M. Freundlich. "Origin of the Electron Microscope". In: *Science* 142.3589 (1963), pp. 185–188. DOI: 10.1126/science.142.3589.185. eprint: https://www.science.org/doi/pdf/10.1126/science.142.3589.185. URL: https://www.science.org/doi/abs/10.1126/science.142.3589.185 (cit. on p. 4).

[5] Henry V. Hopwood. *Living pictures : their history, photo-production and practical working : with a digest of British patents and annotated bibliography, 1899*. eng. London, 1899 (cit. on p. 5).

[6] A. Sauer, D. A. Zocco, A. H. Said, R. Heid, A. Böhmer, and F. Weber. "Electron-phonon coupling and superconductivity-induced distortion of the phonon lineshape in V_3Si". In: *Phys. Rev. B* 99 (13 2019), p. 134511. DOI: 10.1103/PhysRevB.99.134511. URL: https://link.aps.org/doi/10.1103/PhysRevB.99.134511 (cit. on p. 6).

[7] Martin R. Otto, Jan-Hendrik Pöhls, Laurent P. René de Cotret, Mark J. Stern, Mark Sutton, and Bradley J. Siwick. "Mechanisms of electron-phonon coupling unraveled in momentum and time: The case of soft phonons in TiSe2". In: *Science Advances* 7.20 (2021). DOI: 10.1126/sciadv.abf2810. URL: https://advances.sciencemag.org/content/7/20/eabf2810 (cit. on pp. 6, 83).

[8] Jin-Jian Zhou, Olle Hellman, and Marco Bernardi. "Electron-Phonon Scattering in the Presence of Soft Modes and Electron Mobility in $SrTiO_3$ Perovskite from First Principles". In: *Phys. Rev. Lett.* 121 (22 2018), p. 226603. DOI: 10.1103/PhysRevLett.121.226603. URL: https://link.aps.org/doi/10.1103/PhysRevLett.121.226603 (cit. on p. 6).

[9] Eberhard Zeidler. "Rigorous Finite-Dimensional Magic Formulas of Quantum Field Theory". In: *Quantum Field Theory I: Basics in Mathematics and Physics: A Bridge between Mathematicians and Physicists*. Berlin, Heidelberg: Springer Berlin Heidelberg, 2006, pp. 327–498. ISBN: 978-3-540-34764-4. DOI: 10.1007/978-3-540-34764-4_8. URL: https://doi.org/10.1007/978-3-540-34764-4_8 (cit. on p. 7).

[10] D. Filippetto, P. Musumeci, R. K. Li, B. J. Siwick, M. R. Otto, M. Centurion, and J. P. F. Nunes. "Ultrafast electron diffraction: Visualizing dynamic states of matter". In: *Rev. Mod. Phys.* 94 (4 2022), p. 045004. DOI: 10.1103/RevModPhys.94.045004. URL: https://link.aps.org/doi/10.1103/RevModPhys.94.045004 (cit. on p. 9).

[11] Robert Schoenlein, Thomas Elsaesser, Karsten Holldack, Zhirong Huang, Henry Kapteyn, Margaret Murnane, and Michael Woerner. "Recent advances in ultrafast X-ray sources". In: *Philosophical Transactions of the Royal Society A: Mathematical, Physical and Engineering Sciences* 377.2145 (Apr. 2019), p. 20180384. DOI: 10.1098/rsta.2018.0384. URL: https://doi.org/10.1098/rsta.2018.0384 (cit. on p. 10).

[12] Laurent René de Cotret. "From carrier cooling to polaron formation: ultrafast phonon dynamics across the Brillouin zone". Available at https://escholarship.mcgill.ca/concern/theses/8049g981d. PhD thesis. Montréal, QC: McGill University, 2023 (cit. on pp. 12, 18).

[13] F. J. Grüner, C. B. Schroeder, A. R. Maier, S. Becker, and J. M. Mikhailova. "Space-charge effects in ultrahigh current electron bunches generated by laser-plasma accelerators". In: *Phys. Rev. ST Accel. Beams* 12 (2 2009), p. 020701. DOI: 10.1103/PhysRevSTAB.12.020701. URL: https://link.aps.org/doi/10.1103/PhysRevSTAB.12.020701 (cit. on p. 13).

[14] Martin Reiser. "Linear Beam Optics with Space Charge: Sections 4.1 - 4.4". In: *Theory and Design of Charged Particle Beams*. John Wiley & Sons, Ltd, 2008. Chap. 4, pp. 163–232. ISBN: 9783527622047. DOI: https://doi.org/10.1002/9783527622047.ch4a. eprint: https://onlinelibrary.wiley.com/doi/pdf/10.1002/9783527622047.ch4a. URL: https://onlinelibrary.wiley.com/doi/abs/10.1002/9783527622047.ch4a (cit. on p. 13).

[15] Krzysztof P. Grzelakowski and Rudolf M. Tromp. "Temporal and lateral electron pulse compression by a compact spherical electrostatic capacitor". In: *Ultramicroscopy* 130 (2013). Eighth International Workshop on LEEM/PEEM, pp. 36–43. ISSN: 0304-3991. DOI: https://doi.org/10.1016/j.ultramic.2013.03.022. URL: https://www.sciencedirect.com/science/article/pii/S0304399113000922 (cit. on p. 14).

[16] Hyun Woo Kim, Nikolay A. Vinokurov, In Hyung Baek, Key Young Oang, Mi Hye Kim, Young Chan Kim, Kyu-Ha Jang, Kitae Lee, Seong Hee Park, Sunjeong Park, Junho Shin, Jungwon Kim, Fabian Rotermund, Sunglae Cho, Thomas Feurer, and Young Uk Jeong. "Towards jitter-free ultrafast electron diffraction technology". In: *Nature Photonics* 14.4 (2020), pp. 245–249. ISSN: 1749-4893. DOI: 10.1038/s41566-019-0566-4. URL: https://doi.org/10.1038/s41566-019-0566-4 (cit. on p. 14).

[17] Bradley J. Siwick, Jason R. Dwyer, Robert E. Jordan, and R. J. Dwayne Miller. "Ultrafast electron optics: Propagation dynamics of femtosecond electron packets". In: *Journal of Applied Physics* 92.3 (July 2002), pp. 1643–1648. ISSN: 0021-8979. DOI: 10.1063/1.1487437. eprint: https://pubs.aip.org/aip/jap/article-pdf/92/3/1643/10620971/1643_1_online.pdf. URL: https://doi.org/10.1063/1.1487437 (cit. on p. 15).

[18] Ursula Keller. "Nonlinear Pulse Propagation". In: *Ultrafast Lasers: A Comprehensive Introduction to Fundamental Principles with Practical Applications*. Cham: Springer International Publishing, 2021, pp. 131–183. ISBN: 978-3-030-82532-4. DOI: 10.1007/978-3-030-82532-4_4. URL: https://doi.org/10.1007/978-3-030-82532-4_4 (cit. on p. 19).

[19] H. J. Qian, C. Li, Y. C. Du, L. X. Yan, J. F. Hua, W. H. Huang, and C. X. Tang. "Experimental investigation of thermal emittance components of copper photocathode". In: *Phys. Rev. ST Accel. Beams* 15 (4 2012), p. 040102. DOI: 10.1103/PhysRevSTAB.15.040102. URL: https://link.aps.org/doi/10.1103/PhysRevSTAB.15.040102 (cit. on p. 21).

[20] Toshiaki Munakata, Takeharu Sugiyama, Takuya Masuda, and Nobuo Ueno. "Photoemission microspectroscopy of occupied and unoccupied surface states of crystalline facets formed on polycrystalline copper". In: *Phys. Rev. B* 68 (16 2003), p. 165404. DOI: 10.1103/PhysRevB.68.165404. URL: https://link.aps.org/doi/10.1103/PhysRevB.68.165404 (cit. on p. 21).

[21] Martin Otto. "Advancements in electron pulse compression technology applied to ultrafast electron scattering". PhD thesis. McGill University, 2020. URL: https://escholarship.mcgill.ca/concern/theses/s4655m80w (cit. on p. 23).

[22] J. J. Sakurai and Jim Napolitano. *Modern Quantum Mechanics*. 2nd ed. Cambridge University Press, 2017. DOI: 10.1017/9781108499996 (cit. on p. 28).

[23] D. R. Hartree. "The Wave Mechanics of an Atom with a Non-Coulomb Central Field. Part II. Some Results and Discussion". In: *Mathematical Proceedings of the Cambridge Philosophical Society* 24.1 (1928), pp. 111–132. DOI: 10.1017/S0305004100011920 (cit. on pp. 30, 41).

[24] V. Fock. "Näherungsmethode zur Lösung des quantenmechanischen Mehrkörperproblems". In: *Zeitschrift für Physik* 61.1 (1930), pp. 126–148. ISSN: 0044-3328. DOI: 10.1007/BF01340294. URL: https://doi.org/10.1007/BF01340294 (cit. on pp. 30, 41).

[25] C F Fischer. "Hartree–Fock method for atoms. A numerical approach". In: (1977). URL: https://www.osti.gov/biblio/5156729 (cit. on p. 30).

[26] James C. Phillips. "Energy-Band Interpolation Scheme Based on a Pseudopotential". In: *Phys. Rev.* 112 (3 1958), pp. 685–695. DOI: 10.1103/PhysRev.112.685. URL: https://link.aps.org/doi/10.1103/PhysRev.112.685 (cit. on p. 30).

[27] Steven G. Louie, Sverre Froyen, and Marvin L. Cohen. "Nonlinear ionic pseudopotentials in spin-density-functional calculations". In: *Phys. Rev. B* 26 (4 1982), pp. 1738–1742. DOI: 10.1103/PhysRevB.26.1738. URL: https://link.aps.org/doi/10.1103/PhysRevB.26.1738 (cit. on p. 30).

[28] D. R. Hamann, M. Schlüter, and C. Chiang. "Norm-Conserving Pseudopotentials". In: *Phys. Rev. Lett.* 43 (20 1979), pp. 1494–1497. DOI: 10.1103/PhysRevLett.43.1494. URL: https://link.aps.org/doi/10.1103/PhysRevLett.43.1494 (cit. on p. 30).

[29] David Vanderbilt. "Soft self-consistent pseudopotentials in a generalized eigenvalue formalism". In: *Phys. Rev. B* 41 (11 1990), pp. 7892–7895. DOI: 10.1103/PhysRevB.41.7892. URL: https://link.aps.org/doi/10.1103/PhysRevB.41.7892 (cit. on p. 30).

[30] L.M. Peng, S.L. Dudarev, and M.J. Whelan. *High Energy Electron Diffraction and Microscopy*. Monographs on the Physics and Chemistry of Materials. OUP Oxford, 2011. ISBN: 9780199602247. URL: https://books.google.ca/books?id=ee43OKuP8ZUC (cit. on p. 30).

[31] Nevill Francis Mott. "The scattering of electrons by atoms". In: *Proceedings of the Royal Society of London. Series A, Containing Papers of a Mathematical and Physical Character* 127.806 (June 1930), pp. 658–665. DOI: 10.1098/rspa.1930.0082. URL: https://doi.org/10.1098/rspa.1930.0082 (cit. on p. 31).

[32] H. Bethe. "Zur Theorie des Durchgangs schneller Korpuskularstrahlen durch Materie". In: *Annalen der Physik* 397.3 (1930), pp. 325–400. DOI: https://doi.org/10.1002/andp.19303970303. URL: https://onlinelibrary.wiley.com/doi/abs/10.1002/andp.19303970303 (cit. on p. 31).

[33] Michèle Audin. "Euclidean Geometry in the Plane". In: *Geometry*. Berlin, Heidelberg: Springer Berlin Heidelberg, 2003, pp. 65–111. ISBN: 978-3-642-56127-6. DOI: 10.1007/978-3-642-56127-6_4. URL: https://doi.org/10.1007/978-3-642-56127-6_4 (cit. on p. 31).

[34] 1945 or 1946 Hubbard John H. (John Hamal) and Barbara Burke 1948 Hubbard. *Vector calculus, linear algebra, and differential forms : a unified approach*. English. 4th ed. Ithaca, NY: Matrix Editions, 2009 (cit. on p. 31).

[35] W. H. Miller. "A treatise on crystallography". In: *The London, Edinburgh, and Dublin Philosophical Magazine and Journal of Science* 16.100 (1840), pp. 65–67. DOI: 10.1080/14786444008649974. eprint: https://doi.org/10.1080/14786444008649974. URL: https://doi.org/10.1080/14786444008649974 (cit. on p. 32).

[36] E.L. Robinson. *Data Analysis for Scientists and Engineers*. Princeton University Press, 2016. ISBN: 9781400883066. URL: https://books.google.ca/books?id=FclIDAAAQBAJ (cit. on p. 33).

[37] Christian Reiher Henry Cohn Abhinav Kumar and Achill Schürmann. "Formal duality and generalizations of the Poisson summation formula". In: *Discrete Geometry and Algebraic Combinatorics*. Ed. by Alexander Barg and Oleg Musin. Providence, Rhode Island: American Mathematical Society, 2014, pp. 123–140. DOI: 10.1090/conm/625. URL: https://doi.org/10.1090/conm/625 (cit. on p. 33).

[38] P. Hohenberg and W. Kohn. "Inhomogeneous Electron Gas". In: *Phys. Rev.* 136 (3B 1964), B864–B871. DOI: 10.1103/PhysRev.136.B864. URL: https://link.aps.org/doi/10.1103/PhysRev.136.B864 (cit. on p. 41).

[39] W. Kohn and L. J. Sham. "Self-Consistent Equations Including Exchange and Correlation Effects". In: *Phys. Rev.* 140 (4A 1965), A1133–A1138. DOI: 10.1103/PhysRev.140.A1133. URL: https://link.aps.org/doi/10.1103/PhysRev.140.A1133 (cit. on p. 42).

[40] Richard M. Martin. *Electronic Structure: Basic Theory and Practical Methods*. Cambridge University Press, 2004. DOI: 10.1017/CBO9780511805769 (cit. on p. 43).

[41] David Sholl and Janice Steckel. *Density Functional Theory: A Practical Introduction*. John Wiley & Sons, Ltd, 2009, pp. 49–81. ISBN: 9780470447710. DOI: https://doi.org/10.1002/9780470447710.ch3. eprint: https://onlinelibrary.wiley.com/doi/pdf/10.1002/9780470447710.ch3. URL: https://onlinelibrary.wiley.com/doi/abs/10.1002/9780470447710.ch3 (cit. on p. 44).

[42] Gregory H. Wannier. "The Structure of Electronic Excitation Levels in Insulating Crystals". In: *Phys. Rev.* 52 (3 1937), pp. 191–197. DOI: 10.1103/PhysRev.52.191. URL: https://link.aps.org/doi/10.1103/PhysRev.52.191 (cit. on p. 45).

[43] Nicola Marzari, Arash A. Mostofi, Jonathan R. Yates, Ivo Souza, and David Vanderbilt. "Maximally localized Wannier functions: Theory and applications". In: *Rev. Mod. Phys.* 84 (4 2012), pp. 1419–1475. DOI: 10.1103/RevModPhys.84.1419. URL: https://link.aps.org/doi/10.1103/RevModPhys.84.1419 (cit. on p. 45).

[44] Xavier Gonze and Changyol Lee. "Dynamical matrices, Born effective charges, dielectric permittivity tensors, and interatomic force constants from density-functional perturbation theory". In: *Phys. Rev. B* 55 (16 1997), pp. 10355–10368. DOI: 10.1103/PhysRevB.55.10355. URL: https://link.aps.org/doi/10.1103/PhysRevB.55.10355 (cit. on p. 47).

[45] A. A. Maradudin and S. H. Vosko. "Symmetry Properties of the Normal Vibrations of a Crystal". In: *Rev. Mod. Phys.* 40 (1 1968), pp. 1–37. DOI: 10.1103/RevModPhys.40.1. URL: https://link.aps.org/doi/10.1103/RevModPhys.40.1 (cit. on p. 47).

[46] Feliciano Giustino. "Electron-phonon interactions from first principles". In: *Rev. Mod. Phys.* 89 (1 2017), p. 015003. DOI: 10.1103/RevModPhys.89.015003. URL: https://link.aps.org/doi/10.1103/RevModPhys.89.015003 (cit. on pp. 49, 50, 60, 65, 94, 96).

[47] Fabio Caruso and Dino Novko. "Ultrafast dynamics of electrons and phonons: from the two-temperature model to the time-dependent Boltzmann equation". In: *Advances in Physics: X* 7.1 (2022), p. 2095925. DOI: 10.1080/23746149.2022.2095925. URL: https://doi.org/10.1080/23746149.2022.2095925 (cit. on p. 51).

[48] Goran Grimvall. *Electron/Phonon Interaction in Metals*. en. Selected Topics in Solid State Physics. London, England: Elsevier Science, 1981 (cit. on p. 53).

[49] Zhibin Lin, Leonid V. Zhigilei, and Vittorio Celli. "Electron-phonon coupling and electron heat capacity of metals under conditions of strong electron-phonon nonequilibrium". In: *Phys. Rev. B* 77 (7 2008), p. 075133. DOI: 10.1103/PhysRevB.77.075133. URL: https://link.aps.org/doi/10.1103/PhysRevB.77.075133 (cit. on p. 54).

[50] Pablo Maldonado, Karel Carva, Martina Flammer, and Peter M. Oppeneer. "Theory of out-of-equilibrium ultrafast relaxation dynamics in metals". In: *Phys. Rev. B* 96 (17 2017), p. 174439. DOI: 10.1103/PhysRevB.96.174439. URL: https://link.aps.org/doi/10.1103/PhysRevB.96.174439 (cit. on p. 55).

[51] Lutz Waldecker, Roman Bertoni, Ralph Ernstorfer, and Jan Vorberger. "Electron-Phonon Coupling and Energy Flow in a Simple Metal beyond the Two-Temperature Approximation". In: *Phys. Rev. X* 6 (2 2016), p. 021003. DOI: 10.1103/PhysRevX.6.021003. URL: https://link.aps.org/doi/10.1103/PhysRevX.6.021003 (cit. on pp. 55, 98, 105).

[52] Fabio Caruso. "Nonequilibrium Lattice Dynamics in Monolayer MoS_2". In: *The Journal of Physical Chemistry Letters* 12.6 (2021). PMID: 33569950, pp. 1734–1740. DOI: 10.1021/acs.jpclett.0c03616. URL: https://doi.org/10.1021/acs.jpclett.0c03616 (cit. on pp. 55–57, 87, 99, 120, 126, 176).

[53] Marco Bernardi. "First-principles dynamics of electrons and phonons". In: *The European Physical Journal B* 89.11 (2016), p. 239. ISSN: 1434-6036. DOI: 10.1140/epjb/e2016-70399-4. URL: https://doi.org/10.1140/epjb/e2016-70399-4 (cit. on p. 56).

[54] J.M. Ziman. *Electrons and Phonons: The Theory of Transport Phenomena in Solids*. International series of monographs on physics. Clarendon Press, 1960. URL: https://books.google.ca/books?id=2SMIAQAAIAAJ (cit. on p. 58).

[55] Wu Li, Jesús Carrete, Nebil A. Katcho, and Natalio Mingo. "ShengBTE: A solver of the Boltzmann transport equation for phonons". In: *Computer Physics Communications* 185.6 (2014), pp. 1747–1758. ISSN: 0010-4655. DOI: https://doi.org/10.1016/j.cpc.2014.02.015. URL: https://www.sciencedirect.com/science/article/pii/S0010465514000484 (cit. on pp. 59, 173).

[56] Brent Fultz and James M. Howe. "Inelastic Electron Scattering and Spectroscopy". In: *Transmission Electron Microscopy and Diffractometry of Materials*. Berlin, Heidelberg: Springer Berlin Heidelberg, 2008, pp. 163–221. ISBN: 978-3-540-73886-2. DOI: 10.1007/978-3-540-73886-2_4. URL: https://doi.org/10.1007/978-3-540-73886-2_4 (cit. on p. 64).

[57] Alexander Altland and Ben D. Simons. *Condensed Matter Field Theory*. 2nd ed. Cambridge University Press, 2010. DOI: 10.1017/CBO9780511789984 (cit. on p. 65).

[58] John Stillwell. *Naive Lie Theory*. Springer New York, 2008. DOI: 10.1007/978-0-387-78214-0. URL: https://doi.org/10.1007%2F978-0-387-78214-0 (cit. on p. 65).

[59] Max Born and Kathleen Sarginson. "The effect of thermal vibrations on the scattering of X -rays". In: *Proceedings of the Royal Society of London. Series A. Mathematical and Physical Sciences* 179.976 (1941), pp. 69–93. DOI: 10.1098/rspa.1941.0080. URL: https://doi.org/10.1098%2Frspa.1941.0080 (cit. on p. 66).

[60] P. Debye. "Interferenz von Röntgenstrahlen und Wärmebewegung". In: *Annalen der Physik* 348.1 (1913), pp. 49–92. DOI: https://doi.org/10.1002/andp.19133480105. eprint: https://onlinelibrary.wiley.com/doi/pdf/10.1002/andp.19133480105. URL: https://onlinelibrary.wiley.com/doi/abs/10.1002/andp.19133480105 (cit. on p. 66).

[61] Ivar Waller. "Zur Frage der Einwirkung der Wärmebewegung auf die Interferenz von Röntgenstrahlen". In: *Zeitschrift für Physik* 17.1 (1923), pp. 398–408. ISSN: 0044-3328. DOI: 10.1007/BF01328696. URL: https://doi.org/10.1007/BF01328696 (cit. on p. 66).

[62] Hélène Seiler, Daniela Zahn, Marios Zacharias, Patrick-Nigel Hildebrandt, Thomas Vasileiadis, Yoav William Windsor, Yingpeng Qi, Christian Carbogno, Claudia Draxl, Ralph Ernstorfer, and Fabio Caruso. "Accessing the Anisotropic Nonthermal Phonon Populations in Black Phosphorus". In: *Nano Letters* 21.14 (2021). PMID: 34279103, pp. 6171–6178. DOI: 10.1021/acs.nanolett.1c01786. eprint: https://doi.org/10.1021/acs.nanolett.1c01786. URL: https://doi.org/10.1021/acs.nanolett.1c01786 (cit. on pp. 67, 83).

[63] Laurent P. René de Cotret, Jan-Hendrik Pöhls, Mark J. Stern, Martin R. Otto, Mark Sutton, and Bradley J. Siwick. "Time- and momentum-resolved phonon population dynamics with ultrafast electron diffuse scattering". In: *Phys. Rev. B* 100 (21 2019), p. 214115. DOI: 10.1103/PhysRevB.100.214115. URL: https://link.aps.org/doi/10.1103/PhysRevB.100.214115 (cit. on p. 69).

[64] Marios Zacharias, Hélène Seiler, Fabio Caruso, Daniela Zahn, Feliciano Giustino, Pantelis C Kelires, and Ralph Ernstorfer. "Efficient first-principles methodology for the calculation of the all-phonon inelastic scattering in solids". In: *Physical review letters* 127.20 (2021), p. 207401 (cit. on pp. 70, 99).

[65] Jean Laval. "Étude expérimentale de la diffusion des rayons X par les cristaux". In: *Bulletin de Minéralogie* 62.4 (1939), pp. 137–253. DOI: 10.3406/bulmi.1939.4465. URL: https://www.persee.fr/doc/bulmi_0366-3248_1939_num_62_4_4465 (cit. on pp. 70, 128, 152).

[66] Max Born. "Theoretical investigations on the relation between crystal dynamics and x-ray scattering". In: *Reports on Progress in Physics* 9.1 (1942), pp. 294–333. DOI: 10.1088/0034-4885/9/1/319. URL: https://doi.org/10.1088/0034-4885/9/1/319 (cit. on pp. 70, 128, 152).

[67] R W James. *The optical principles of the diffraction of x-rays*. London: G. Bell and Sons, 1948 (cit. on pp. 70, 128, 152).

[68] Max Born and Kun Huang. "Dynamical Theory of Crystal Lattices". In: *American Journal of Physics* 23.7 (1955), pp. 474–474. DOI: 10.1119/1.1934059. eprint: https://doi.org/10.1119/1.1934059. URL: https://doi.org/10.1119/1.1934059 (cit. on p. 70).

[69] A.A. Maradudin, E.W. Montroll, and G.H. Weiss. *Theory of Lattice Dynamics in the Harmonic Approximation*. Solid state physics : advances in research and applications. Academic Press, 1963. ISBN: 9780126077834. URL: https://books.google.ca/books?id=4SspAQAAMAAJ (cit. on p. 70).

[70] Peter Brüesch. *Phonons: Theory and Experiments I - Lattice Dynamics and Models of Interatomic Forces*. Springer Berlin Heidelberg, 1982. DOI: 10.1007/978-3-642-81781-6. URL: https://doi.org/10.1007%2F978-3-642-81781-6 (cit. on p. 71).

[71] Marios Zacharias and Feliciano Giustino. "Theory of the special displacement method for electronic structure calculations at finite temperature". In: *Phys. Rev. Research* 2 (1 2020), p. 013357. DOI: 10.1103/PhysRevResearch.2.013357. URL: https://link.aps.org/doi/10.1103/PhysRevResearch.2.013357 (cit. on pp. 71, 73).

[72] G. N. Watson. "Notes on Generating Functions of Polynomials: (2) Hermite Polynomials". In: *Journal of the London Mathematical Society* s1-8.3 (1933), pp. 194–199. DOI: https://doi.org/10.1112/jlms/s1-8.3.194. eprint: https://londmathsoc.onlinelibrary.wiley.com/doi/pdf/10.1112/jlms/s1-8.3.194. URL: https://londmathsoc.onlinelibrary.wiley.com/doi/abs/10.1112/jlms/s1-8.3.194 (cit. on p. 71).

[73] Christopher E Patrick and Feliciano Giustino. "Unified theory of electron–phonon renormalization and phonon-assisted optical absorption". In: *Journal of Physics: Condensed Matter* 26.36 (2014), p. 365503. DOI: 10.1088/0953-8984/26/36/365503. URL: https://doi.org/10.1088/0953-8984/26/36/365503 (cit. on p. 71).

[74] Marios Zacharias, Hélène Seiler, Fabio Caruso, Daniela Zahn, Feliciano Giustino, Pantelis C. Kelires, and Ralph Ernstorfer. "Multiphonon diffuse scattering in solids from first principles: Application to layered crystals and two-dimensional materials". In: *Phys. Rev. B* 104 (20 2021), p. 205109. DOI: 10.1103/PhysRevB.104.205109. URL: https://link.aps.org/doi/10.1103/PhysRevB.104.205109 (cit. on pp. 71, 99, 156).

[75] Marios Zacharias and Feliciano Giustino. "One-shot calculation of temperature-dependent optical spectra and phonon-induced band-gap renormalization". In: *Phys. Rev. B* 94 (7 2016), p. 075125. DOI: 10.1103/PhysRevB.94.075125. URL: https://link.aps.org/doi/10.1103/PhysRevB.94.075125 (cit. on pp. 73, 75).

[76] K. S. Novoselov, A. K. Geim, S. V. Morozov, D. Jiang, Y. Zhang, S. V. Dubonos, I. V. Grigorieva, and A. A. Firsov. "Electric Field Effect in Atomically Thin Carbon Films". In: *Science* 306.5696 (2004), pp. 666–669. DOI: 10.1126/science.1102896. eprint: https://www.science.org/doi/pdf/10.1126/science.1102896. URL: https://www.science.org/doi/abs/10.1126/science.1102896 (cit. on p. 79).

[77] Nicolas Mounet, Marco Gibertini, Philippe Schwaller, Davide Campi, Andrius Merkys, Antimo Marrazzo, Thibault Sohier, Ivano Eligio Castelli, Andrea Cepellotti, Giovanni Pizzi, and Nicola Marzari. "Two-dimensional materials from high-throughput computational exfoliation of experimentally known compounds". In: *Nature Nanotechnology* 13.3 (2018), pp. 246–252. ISSN: 1748-3395. DOI: 10.1038/s41565-017-0035-5. URL: https://doi.org/10.1038/s41565-017-0035-5 (cit. on p. 79).

[78] R. Rossetti, S. Nakahara, and L. E. Brus. "Quantum size effects in the redox potentials, resonance Raman spectra, and electronic spectra of CdS crystallites in aqueous solution". In: *The Journal of Chemical Physics* 79.2 (1983), pp. 1086–1088. DOI: 10.1063/1.445834. eprint: https://doi.org/10.1063/1.445834. URL: https://doi.org/10.1063/1.445834 (cit. on p. 79).

[79] J.O. Island and A. Castellanos-Gomez. "Chapter Seven - Black Phosphorus-Based Nanodevices". In: *2D Materials*. Ed. by Francesca Iacopi, John J. Boeckl, and Chennupati Jagadish. Vol. 95. Semiconductors and Semimetals. Elsevier, 2016, pp. 279–303. DOI: https://doi.org/10.1016/bs.semsem.2016.03.002. URL: https://www.sciencedirect.com/science/article/pii/S0080878416300023 (cit. on p. 80).

[80] F. Reis, G. Li, L. Dudy, M. Bauernfeind, S. Glass, W. Hanke, R. Thomale, J. Schäfer, and R. Claessen. "Bismuthene on a SiC substrate: A candidate for a high-temperature quantum spin Hall material". In: *Science* 357.6348 (2017), pp. 287–290. DOI: 10.1126/science.aai8142. eprint: https://www.science.org/doi/pdf/10.1126/science.aai8142. URL: https://www.science.org/doi/abs/10.1126/science.aai8142 (cit. on p. 80).

[81] Xu Wu, Yan Shao, Hang Liu, Zili Feng, Ye-Liang Wang, Jia-Tao Sun, Chen Liu, Jia-Ou Wang, Zhong-Liu Liu, Shi-Yu Zhu, Yu-Qi Wang, Shi-Xuan Du, You-Guo Shi, Kurash Ibrahim, and Hong-Jun Gao. "Epitaxial Growth and Air-Stability of Monolayer Antimonene on PdTe2". In: *Advanced Materials* 29.11 (2017), p. 1605407. DOI: https://doi.org/10.1002/adma.201605407. eprint: https://onlinelibrary.wiley.com/doi/pdf/10.1002/adma.201605407. URL: https://onlinelibrary.wiley.com/doi/abs/10.1002/adma.201605407 (cit. on p. 80).

[82] Changgu Lee, Xiaoding Wei, Jeffrey W. Kysar, and James Hone. "Measurement of the Elastic Properties and Intrinsic Strength of Monolayer Graphene". In: *Science* 321.5887 (2008), pp. 385–388. DOI: 10.1126/science.1157996. eprint: https://www.science.org/doi/pdf/10.1126/science.1157996. URL: https://www.science.org/doi/abs/10.1126/science.1157996 (cit. on p. 80).

[83] Archana Raja, Andrey Chaves, Jaeeun Yu, Ghidewon Arefe, Heather M. Hill, Albert F. Rigosi, Timothy C. Berkelbach, Philipp Nagler, Christian Schüller, Tobias Korn, Colin Nuckolls, James Hone, Louis E. Brus, Tony F. Heinz, David R. Reichman, and Alexey Chernikov. "Coulomb engineering of the bandgap and excitons in two-dimensional materials". In: *Nature Communications* 8.1 (2017), p. 15251. ISSN: 2041-1723. DOI: 10.1038/ncomms15251. URL: https://doi.org/10.1038/ncomms15251 (cit. on p. 80).

[84] Tristan L. Britt, Qiuyang Li, Laurent P. René de Cotret, Nicholas Olsen, Martin Otto, Syed Ali Hassan, Marios Zacharias, Fabio Caruso, Xiaoyang Zhu, and Bradley J. Siwick. "Direct View of Phonon Dynamics in Atomically Thin MoS2". In: *Nano Letters* 22.12 (2022). PMID: 35671172, pp. 4718–4724. DOI: 10.1021/acs.nanolett.2c00850. eprint: https://doi.org/10.1021/acs.nanolett.2c00850. URL: https://doi.org/10.1021/acs.nanolett.2c00850 (cit. on pp. 80, 97, 104, 105, 111, 126, 165).

[85] Fang Liu, Mark E. Ziffer, Kameron R. Hansen, Jue Wang, and Xiaoyang Zhu. "Direct Determination of Band-Gap Renormalization in the Photoexcited Monolayer MoS_2". In: *Phys. Rev. Lett.* 122 (24 2019), p. 246803. DOI: 10.1103/PhysRevLett.122.246803. URL: https://link.aps.org/doi/10.1103/PhysRevLett.122.246803 (cit. on pp. 81, 82).

[86] Yang Song and Hanan Dery. "Transport Theory of Monolayer Transition-Metal Dichalcogenides through Symmetry". In: *Phys. Rev. Lett.* 111 (2 2013), p. 026601. DOI: 10.1103/PhysRevLett.111.026601. URL: https://link.aps.org/doi/10.1103/PhysRevLett.111.026601 (cit. on pp. 81, 82, 109, 119).

[87] Nan Zhang, Alessandro Surrente, Michał Baranowski, Duncan K Maude, Patricia Gant, Andres Castellanos-Gomez, and Paulina Plochocka. "Moiré intralayer excitons in a MoSe2/MoS2 heterostructure". In: *Nano letters* 18.12 (2018), pp. 7651–7657. DOI: https://doi.org/10.1021/acs.nanolett.8b03266. URL: https://pubs.acs.org/doi/10.1021/acs.nanolett.8b03266 (cit. on pp. 81, 82).

[88] Marco Bernardi, Maurizia Palummo, and Jeffrey C. Grossman. "Extraordinary Sunlight Absorption and One Nanometer Thick Photovoltaics Using Two-Dimensional Monolayer Materials". In: *Nano Letters* 13.8 (2013). PMID: 23750910, pp. 3664–3670. DOI: 10.1021/nl401544y. eprint: https://doi.org/10.1021/nl401544y. URL: https://doi.org/10.1021/nl401544y (cit. on p. 81).

[89] Oriol Lopez-Sanchez, Dominik Lembke, Metin Kayci, Aleksandra Radenovic, and Andras Kis. "Ultrasensitive photodetectors based on monolayer MoS2". In: *Nature Nanotechnology* 8.7 (2013), pp. 497–501. ISSN: 1748-3395. DOI: 10.1038/nnano.2013.100. URL: https://doi.org/10.1038/nnano.2013.100 (cit. on p. 81).

[90] Lifa Zhang and Qian Niu. "Angular Momentum of Phonons and the Einstein–de Haas Effect". In: *Phys. Rev. Lett.* 112 (8 2014), p. 085503. DOI: 10.1103/PhysRevLett.112.085503. URL: https://link.aps.org/doi/10.1103/PhysRevLett.112.085503 (cit. on pp. 81, 122).

[91] Sonali Das, Deepak Pandey, Jayan Thomas, and Tania Roy. "The Role of Graphene and Other 2D Materials in Solar Photovoltaics". In: *Advanced Materials* 31.1 (2019), p. 1802722. DOI: https://doi.org/10.1002/adma.201802722. eprint: https://onlinelibrary.wiley.com/doi/pdf/10.1002/adma.201802722. URL: https://onlinelibrary.wiley.com/doi/abs/10.1002/adma.201802722 (cit. on p. 81).

[92] Stephen J. Fonash. "Chapter Two - Material Properties and Device Physics Basic to Photovoltaics". In: *Solar Cell Device Physics (Second Edition)*. Ed. by Stephen J. Fonash. Second Edition. Boston: Academic Press, 2010, pp. 9–65. ISBN: 978-0-12-374774-7. DOI: https://doi.org/10.1016/B978-0-12-374774-7.00002-9. URL: https://www.sciencedirect.com/science/article/pii/B9780123747747000029 (cit. on p. 81).

[93] Yuan Cao, Valla Fatemi, Shiang Fang, Kenji Watanabe, Takashi Taniguchi, Efthimios Kaxiras, and Pablo Jarillo-Herrero. "Unconventional superconductivity in magic-angle graphene superlattices". In: *Nature* 556.7699 (2018), pp. 43–50. ISSN: 1476-4687. DOI: 10.1038/nature26160. URL: https://doi.org/10.1038/nature26160 (cit. on p. 82).

[94] Jiamin Quan, Lukas Linhart, Miao-Ling Lin, Daehun Lee, Jihang Zhu, Chun-Yuan Wang, Wei-Ting Hsu, Junho Choi, Jacob Embley, Carter Young, et al. "Phonon renormalization in reconstructed MoS 2 moiré superlattices". In: *Nature materials* (2021), pp. 1–6. DOI: https://doi.org/10.1038/s41563-021-00960-1. URL: https://www.nature.com/articles/s41563-021-00960-1 (cit. on p. 82).

[95] Simone Latini, Kirsten T. Winther, Thomas Olsen, and Kristian S. Thygesen. "Interlayer Excitons and Band Alignment in MoS2/hBN/WSe2 van der Waals Heterostructures". In: *Nano Letters* 17.2 (2017). PMID: 28026961, pp. 938–945. DOI: 10.1021/acs.nanolett.6b04275. eprint: https://doi.org/10.1021/acs.nanolett.6b04275. URL: https://doi.org/10.1021/acs.nanolett.6b04275 (cit. on p. 82).

[96] Ioannis Paradisanos, Shivangi Shree, Antony George, Nadine Leisgang, Cedric Robert, Kenji Watanabe, Takashi Taniguchi, Richard J. Warburton, Andrey Turchanin, Xavier Marie, Iann C. Gerber, and Bernhard Urbaszek. "Controlling interlayer excitons in MoS2 layers grown by chemical vapor deposition". In: *Nature Communications* 11.1 (2020), p. 2391. ISSN: 2041-1723. DOI: 10.1038/s41467-020-16023-z. URL: https://doi.org/10.1038/s41467-020-16023-z (cit. on p. 82).

[97] Di Huang, Junho Choi, Chih-Kang Shih, and Xiaoqin Li. "Excitons in semiconductor moiré superlattices". In: *Nature Nanotechnology* 17.3 (2022), pp. 227–238. ISSN: 1748-3395. DOI: 10.1038/s41565-021-01068-y. URL: https://doi.org/10.1038/s41565-021-01068-y (cit. on p. 82).

[98] Benjamin T. Zhou, Katsuhisa Taguchi, Yuki Kawaguchi, Yukio Tanaka, and K. T. Law. "Spin-orbit coupling induced valley Hall effects in transition-metal dichalcogenides". In: *Communications Physics* 2.1 (2019), p. 26. ISSN: 2399-3650. DOI: 10.1038/s42005-019-0127-7. URL: https://doi.org/10.1038/s42005-019-0127-7 (cit. on p. 82).

[99] Alejandro Molina-Sánchez, Davide Sangalli, Kerstin Hummer, Andrea Marini, and Ludger Wirtz. "Effect of spin-orbit interaction on the optical spectra of single-layer, double-layer, and bulk MoS_2". In: *Phys. Rev. B* 88 (4 2013), p. 045412. DOI: 10.1103/PhysRevB.88.045412. URL: https://link.aps.org/doi/10.1103/PhysRevB.88.045412 (cit. on p. 82).

[100] Di Xiao, Gui-Bin Liu, Wanxiang Feng, Xiaodong Xu, and Wang Yao. "Coupled Spin and Valley Physics in Monolayers of MoS_2 and Other Group-VI Dichalcogenides". In: *Phys. Rev. Lett.* 108 (19 2012), p. 196802. DOI: 10.1103/PhysRevLett.108.196802. URL: https://link.aps.org/doi/10.1103/PhysRevLett.108.196802 (cit. on pp. 82, 109, 114, 115).

[101] H. Beyer, G. Rohdeabo, familyi=v., given=A., giveni=A., „ A. Stange, T. Jacobsen, L. Bignardi, D. Lizzit, P. Lacovig, C. E. Sanders, S. Lizzit, K. Rossnagel, P. Hofmann, and M. Bauer. "80% Valley Polarization of Free Carriers in Singly Oriented Single-Layer WS_2 on Au(111)". In: *Phys. Rev. Lett.* 123 (23 2019), p. 236802. DOI: 10.1103/PhysRevLett.123.236802. URL: https://link.aps.org/doi/10.1103/PhysRevLett.123.236802 (cit. on p. 82).

[102] Diana Y. Qiu, Felipe H. da Jornada, and Steven G. Louie. "Optical Spectrum of MoS_2: Many-Body Effects and Diversity of Exciton States". In: *Phys. Rev. Lett.* 111 (21 2013), p. 216805. DOI: 10.1103/PhysRevLett.111.216805. URL: https://link.aps.org/doi/10.1103/PhysRevLett.111.216805 (cit. on pp. 82, 96).

[103] Wang Yao, Di Xiao, and Qian Niu. "Valley-dependent optoelectronics from inversion symmetry breaking". In: *Phys. Rev. B* 77 (23 2008), p. 235406. DOI: 10.1103/PhysRevB.77.235406. URL: https://link.aps.org/doi/10.1103/PhysRevB.77.235406 (cit. on p. 82).

[104] Eugene S. Kadantsev and Pawel Hawrylak. "Electronic structure of a single MoS_2 monolayer". In: *Solid State Communications* 152.10 (2012), pp. 909–913. ISSN: 0038-1098. DOI: https://doi.org/10.1016/j.ssc.2012.02.005. URL: https://www.sciencedirect.com/science/Article/pii/S0038109812000889 (cit. on pp. 82, 109, 112).

[105] Lifa Zhang and Qian Niu. "Chiral phonons at high-symmetry points in monolayer hexagonal lattices". In: *Physical review letters* 115.11 (2015), p. 115502. DOI: http://dx.doi.org/10.1103/PhysRevLett.115.115502. URL: https://journals.aps.org/prl/abstract/10.1103/PhysRevLett.115.115502 (cit. on p. 82).

[106] Hanyu Zhu, Jun Yi, Ming-Yang Li, Jun Xiao, Lifa Zhang, Chih-Wen Yang, Robert A. Kaindl, Lain-Jong Li, Yuan Wang, and Xiang Zhang. "Observation of chiral phonons". In: *Science* 359.6375 (2018), pp. 579–582. DOI: 10.1126/science.aar2711. eprint: https://www.science.org/doi/pdf/10.1126/science.aar2711. URL: https://www.science.org/doi/abs/10.1126/science.aar2711 (cit. on pp. 82, 110).

[107] Halleh B Balch, Austin M Evans, Raghunath R Dasari, Hong Li, Ruofan Li, Simil Thomas, Danqing Wang, Ryan P Bisbey, Kaitlin Slicker, Ioannina Castano, et al. "Electronically Coupled 2D Polymer/-MoS2 Heterostructures". In: *Journal of the American Chemical Society* 142.50 (2020), pp. 21131–21139. DOI: https://doi.org/10.1021/jacs.0c10151. URL: https://pubs.acs.org/doi/10.1021/jacs.0c10151 (cit. on p. 82).

[108] Indrajit Maity, Arash A Mostofi, and Johannes Lischner. "Chiral valley phonons and flat phonon bands in moire materials". In: *Physical Review B* 105.4 (2022), p. L041408. DOI: https://doi.org/10.1103/PhysRevB.105.L041408. URL: https://journals.aps.org/prb/abstract/10.1103/PhysRevB.105.L041408 (cit. on p. 82).

[109] Daniel J Trainer, BaoKai Wang, Fabrizio Bobba, Noah Samuelson, Xiaoxing Xi, John Zasadzinski, Jouko Nieminen, Arun Bansil, and Maria Iavarone. "Proximity-induced superconductivity in monolayer MoS2". In: *ACS nano* 14.3 (2020), pp. 2718–2728. DOI: https://doi.org/10.1021/acsnano.9b07475. URL: https://pubs.acs.org/doi/10.1021/acsnano.9b07475 (cit. on p. 82).

[110] Sven Borghardt, Jhih-Sian Tu, Florian Winkler, Jürgen Schubert, Willi Zander, Kristjan Leosson, and Beata E Kardynał. "Engineering of optical and electronic band gaps in transition metal dichalcogenide monolayers through external dielectric screening". In: *Physical review materials* 1.5 (2017), p. 054001. DOI: https://doi.org/10.1103/PhysRevMaterials.1.054001. URL: https://journals.aps.org/prmaterials/abstract/10.1103/PhysRevMaterials.1.054001 (cit. on p. 82).

[111] Xiaoyang Zhu, Nicholas R. Monahan, Zizhou Gong, Haiming Zhu, Kristopher W. Williams, and Cory A. Nelson. "Charge Transfer Excitons at van der Waals Interfaces". In: *Journal of the American Chemical Society* 137.26 (2015). PMID: 26001297, pp. 8313–8320. DOI: 10.1021/jacs.5b03141. eprint: https://doi.org/10.1021/jacs.5b03141. URL: https://doi.org/10.1021/jacs.5b03141 (cit. on p. 82).

[112] Minhao He, Pasqual Rivera, Dinh Van Tuan, et al. "Valley phonons and exciton complexes in a monolayer semiconductor". In: *Nature Communications* 11.1 (2020), p. 618. ISSN: 2041-1723. DOI: 10.1038/s41467-020-14472-0. URL: https://doi.org/10.1038/s41467-020-14472-0 (cit. on pp. 82, 88).

[113] Mariano Trigo, Matthias Fuchs, Jian Chen, MP Jiang, Marco Cammarata, Stephen Fahy, David M Fritz, Kelly Gaffney, Shambhu Ghimire, Andrew Higginbotham, et al. "Fourier-transform inelastic X-ray scattering from time-and momentum-dependent phonon–phonon correlations". In: *Nature Physics* 9.12 (2013), pp. 790–794 (cit. on pp. 83, 110).

[114] Samuel W Teitelbaum, Thomas C Henighan, Hanzhe Liu, Mason P Jiang, Diling Zhu, Matthieu Chollet, Takahiro Sato, Éamonn D Murray, Stephen Fahy, Shane O'Mahony, et al. "Measurements of nonequilibrium interatomic forces using time-domain x-ray scattering". In: *Physical Review B* 103.18 (2021), p. L180101 (cit. on p. 83).

[115] Mark J. Stern, Laurent P. René de Cotret, Martin R. Otto, Robert P. Chatelain, Jean-Philippe Boisvert, Mark Sutton, and Bradley J. Siwick. "Mapping momentum-dependent electron-phonon coupling and nonequilibrium phonon dynamics with ultrafast electron diffuse scattering". In: *Phys. Rev. B* 97 (16 2018), p. 165416. DOI: 10.1103/PhysRevB.97.165416. URL: https://link.aps.org/doi/10.1103/PhysRevB.97.165416 (cit. on pp. 83, 110).

[116] L. Waldecker, R. Bertoni, H. Hübener, T. Brumme, T. Vasileiadis, D. Zahn, A. Rubio, and R. Ernstorfer. "Momentum-Resolved View of Electron-Phonon Coupling in Multilayer WSe_2". In: *Phys. Rev. Lett.* 119 (3 2017), p. 036803. DOI: 10.1103/PhysRevLett.119.036803. URL: https://link.aps.org/doi/10.1103/PhysRevLett.119.036803 (cit. on p. 83).

[117] T. Chase, M. Trigo, A. H. Reid, R. Li, T. Vecchione, X. Shen, S. Weathersby, R. Coffee, N. Hartmann, D. A. Reis, X. J. Wang, and H. A. Dürr. "Ultrafast electron diffraction from non-equilibrium phonons in femtosecond laser heated Au films". In: *Applied Physics Letters* 108.4 (2016), p. 041909. DOI: 10.1063/1.4940981. eprint: https://doi.org/10.1063/1.4940981. URL: https://doi.org/10.1063/1.4940981 (cit. on p. 83).

[118] Laurent P. René de Cotret, Martin R. Otto, Jan-Hendrik Pöhls, Zhongzhen Luo, Mercouri G. Kanatzidis, and Bradley J. Siwick. "Direct visualization of polaron formation in the thermoelectric SnSe". In: *Proceedings of the National Academy of Sciences* 119.3 (2022). ISSN: 0027-8424. DOI: 10.1073/pnas.2113967119. eprint: https://www.pnas.org/content/119/3/e2113967119.full.pdf. URL: https://www.pnas.org/content/119/3/e2113967119 (cit. on pp. 83, 144, 159, 171, 172, 178).

[119] Kin Fai Mak, Changgu Lee, James Hone, Jie Shan, and Tony F. Heinz. "Atomically Thin MoS_2: A New Direct-Gap Semiconductor". In: *Phys. Rev. Lett.* 105 (13 2010), p. 136805. DOI: 10.1103/PhysRevLett.105.136805. URL: https://link.aps.org/doi/10.1103/PhysRevLett.105.136805 (cit. on p. 83).

[120] Jiadong Zhou et al. "A library of atomically thin metal chalcogenides". In: *Nature* 556.7701 (2018), pp. 355–359. ISSN: 1476-4687. DOI: 10.1038/s41586-018-0008-3. URL: https://doi.org/10.1038/s41586-018-0008-3 (cit. on p. 84).

[121] Se-Yang Kim, Jinsung Kwak, Cristian V. Ciobanu, and Soon-Yong Kwon. "Recent Developments in Controlled Vapor-Phase Growth of 2D Group 6 Transition Metal Dichalcogenides". In: *Advanced Materials* 31.20 (2019), p. 1804939. DOI: https://doi.org/10.1002/adma.201804939. eprint: https://onlinelibrary.wiley.com/doi/pdf/10.1002/adma.201804939. URL: https://onlinelibrary.wiley.com/doi/abs/10.1002/adma.201804939 (cit. on p. 84).

[122] Yaxu Wei, Chunguang Hu, Yanning Li, Xiaotang Hu, Kaihao Yu, Litao Sun, Michael Hohage, and Lidong Sun. "Initial stage of MBE growth of MoSe2 monolayer". In: *Nanotechnology* 31.31 (2020), p. 315710. DOI: 10.1088/1361-6528/ab884b. URL: https://dx.doi.org/10.1088/1361-6528/ab884b (cit. on p. 84).

[123] Kinga Lasek, Paula Mariel Coelho, Krzysztof Zberecki, Yan Xin, Sadhu K. Kolekar, Jingfeng Li, and Matthias Batzill. "Molecular Beam Epitaxy of Transition Metal (Ti-, V-, and Cr-) Tellurides: From Monolayer Ditellurides to Multilayer Self-Intercalation Compounds". In: *ACS Nano* 14.7 (2020). PMID: 32584543, pp. 8473–8484. DOI: 10.1021/acsnano.0c02712. eprint: https://doi.org/10.1021/acsnano.0c02712. URL: https://doi.org/10.1021/acsnano.0c02712 (cit. on p. 84).

[124] Masaki Nakano, Yue Wang, Yuta Kashiwabara, Hideki Matsuoka, and Yoshihiro Iwasa. "Layer-by-Layer Epitaxial Growth of Scalable WSe2 on Sapphire by Molecular Beam Epitaxy". In: *Nano Letters* 17.9 (2017). PMID: 28849935, pp. 5595–5599. DOI: 10.1021/acs.nanolett.7b02420. eprint: https://doi.org/10.1021/acs.nanolett.7b02420. URL: https://doi.org/10.1021/acs.nanolett.7b02420 (cit. on p. 84).

[125] Yasir J. Noori, Shibin Thomas, Sami Ramadan, Danielle E. Smith, Vicki K. Greenacre, Nema Abdelazim, Yisong Han, Richard Beanland, Andrew L. Hector, Norbert Klein, Gillian Reid, Philip N. Bartlett, and C. H. Kees de Groot. "Large-Area Electrodeposition of Few-Layer MoS2 on Graphene for 2D Material Heterostructures". In: *ACS Applied Materials & Interfaces* 12.44 (2020). PMID: 33079533, pp. 49786–49794. DOI: 10.1021/acsami.0c14777. eprint: https://doi.org/10.1021/acsami.0c14777. URL: https://doi.org/10.1021/acsami.0c14777 (cit. on p. 84).

[126] Y J Noori, S Thomas, S Ramadan, V K Greenacre, N M Abdelazim, Y Han, J Zhang, R Beanland, A L Hector, N Klein, G Reid, P N Bartlett, and C H de Groot. "Electrodeposited WS2 monolayers on patterned graphene". In: *2D Materials* 9.1 (2021), p. 015025. DOI: 10.1088/2053-1583/ac3dd6. URL: https://dx.doi.org/10.1088/2053-1583/ac3dd6 (cit. on p. 84).

[127] Xi Wan, Kun Chen, Zefeng Chen, Fangyan Xie, Xiaoliang Zeng, Weiguang Xie, Jian Chen, and Jianbin Xu. "Controlled Electrochemical Deposition of Large-Area MoS2 on Graphene for High-Responsivity Photodetectors". In: *Advanced Functional Materials* 27.19 (2017), p. 1603998. DOI: https://doi.org/10.1002/adfm.201603998. eprint: https://onlinelibrary.wiley.com/doi/pdf/10.1002/adfm.201603998. URL: https://onlinelibrary.wiley.com/doi/abs/10.1002/adfm.201603998 (cit. on p. 84).

[128] Yung-Huang Chang, Wenjing Zhang, Yihan Zhu, Yu Han, Jiang Pu, Jan-Kai Chang, Wei-Ting Hsu, Jing-Kai Huang, Chang-Lung Hsu, Ming-Hui Chiu, Taishi Takenobu, Henan Li, Chih-I Wu, Wen-Hao Chang, Andrew Thye Shen Wee, and Lain-Jong Li. "Monolayer MoSe2 Grown by Chemical Vapor Deposition for Fast Photodetection". In: *ACS Nano* 8.8 (2014). PMID: 25094022, pp. 8582–8590. DOI: 10.1021/nn503287m. eprint: https://doi.org/10.1021/nn503287m. URL: https://doi.org/10.1021/nn503287m (cit. on p. 84).

[129] Fang Liu, Wenjing Wu, Yusong Bai, Sang Hoon Chae, Qiuyang Li, Jue Wang, James Hone, and X.-Y. Zhu. "Disassembling 2D van der Waals crystals into macroscopic monolayers and reassembling into artificial lattices". In: *Science* 367.6480 (2020), pp. 903–906. DOI: 10.1126/science.aba1416. eprint: https://www.science.org/doi/pdf/10.1126/science.aba1416. URL: https://www.science.org/doi/abs/10.1126/science.aba1416 (cit. on p. 85).

[130] Paul D. Cunningham, Kathleen M. McCreary, and Berend T. Jonker. "Auger Recombination in Chemical Vapor Deposition-Grown Monolayer WS2". In: *The Journal of Physical Chemistry Letters* 7.24 (2016). PMID: 27973899, pp. 5242–5246. DOI: 10.1021/acs.jpclett.6b02413. eprint: https://doi.org/10.1021/acs.jpclett.6b02413. URL: https://doi.org/10.1021/acs.jpclett.6b02413 (cit. on p. 86).

[131] Maurizia Palummo, Marco Bernardi, and Jeffrey C. Grossman. "Exciton Radiative Lifetimes in Two-Dimensional Transition Metal Dichalcogenides". In: *Nano Letters* 15.5 (2015). PMID: 25798735, pp. 2794–2800. DOI: 10.1021/nl503799t. eprint: https://doi.org/10.1021/nl503799t. URL: https://doi.org/10.1021/nl503799t (cit. on p. 86).

[132] Matin Amani, Der-Hsien Lien, Daisuke Kiriya, Jun Xiao, Angelica Azcatl, Jiyoung Noh, Surabhi R. Madhvapathy, Rafik Addou, Santosh KC, Madan Dubey, Kyeongjae Cho, Robert M. Wallace, Si-Chen Lee, Jr-Hau He, Joel W. Ager, Xiang Zhang, Eli Yablonovitch, and Ali Javey. "Near-unity photoluminescence quantum yield in MoS_2". In: *Science* 350.6264 (2015), pp. 1065–1068. DOI: 10.1126/science.aad2114. eprint: https://www.science.org/doi/pdf/10.1126/science.aad2114. URL: https://www.science.org/doi/abs/10.1126/science.aad2114 (cit. on p. 86).

[133] Yiling Yu, Yifei Yu, Chao Xu, Andy Barrette, Kenan Gundogdu, and Linyou Cao. "Fundamental limits of exciton-exciton annihilation for light emission in transition metal dichalcogenide monolayers". In: *Phys. Rev. B* 93 (20 2016), p. 201111. DOI: 10.1103/PhysRevB.93.201111. URL: https://link.aps.org/doi/10.1103/PhysRevB.93.201111 (cit. on p. 86).

[134] Alexander W. Bataller, Robert A. Younts, Avinash Rustagi, Yiling Yu, Hossein Ardekani, Alexander Kemper, Linyou Cao, and Kenan Gundogdu. "Dense Electron-Hole Plasma Formation and Ultralong Charge Lifetime in Monolayer MoS2 via Material Tuning". In: *Nano Letters* 19.2 (2019), pp. 1104–1111. DOI: 10.1021/acs.nanolett.8b04408. eprint: https://doi.org/10.1021/acs.nanolett.8b04408. URL: https://doi.org/10.1021/acs.nanolett.8b04408 (cit. on p. 86).

[135] E. E. Salpeter and H. A. Bethe. "A Relativistic Equation for Bound-State Problems". In: *Phys. Rev.* 84 (6 1951), pp. 1232–1242. DOI: 10.1103/PhysRev.84.1232. URL: https://link.aps.org/doi/10.1103/PhysRev.84.1232 (cit. on p. 89).

[136] Diana Y. Qiu, Galit Cohen, Dana Novichkova, and Sivan Refaely-Abramson. "Signatures of Dimensionality and Symmetry in Exciton Band Structure: Consequences for Exciton Dynamics and Transport". In: *Nano Letters* 21.18 (2021), pp. 7644–7650. DOI: 10.1021/acs.nanolett.1c02352. URL: https://doi.org/10.1021/acs.nanolett.1c02352 (cit. on p. 89).

[137] Galit Cohen, Jonah B. Haber, Jeffrey B. Neaton, Diana Y. Qiu, and Sivan Refaely-Abramson. *Phonon-driven femtosecond dynamics of excitons in crystalline pentacene from first principles*. 2023. arXiv: 2305.04223 [cond-mat.mtrl-sci] (cit. on p. 89).

[138] Jack Deslippe, Georgy Samsonidze, David A. Strubbe, Manish Jain, Marvin L. Cohen, and Steven G. Louie. "BerkeleyGW: A massively parallel computer package for the calculation of the quasiparticle and optical properties of materials and nanostructures". In: *Computer Physics Communications* 183.6 (2012), pp. 1269–1289. ISSN: 0010-4655. DOI: https://doi.org/10.1016/j.cpc.2011.12.006. URL: https://www.sciencedirect.com/science/article/pii/S0010465511003912 (cit. on p. 90).

[139] D Sangalli, A Ferretti, H Miranda, C Attaccalite, I Marri, E Cannuccia, P Melo, M Marsili, F Paleari, A Marrazzo, G Prandini, P Bonfà, M O Atambo, F Affinito, M Palummo, A Molina-Sánchez, C Hogan, M Grüning, D Varsano, and A Marini. "Many-body perturbation theory calculations using the yambo code". In: *Journal of Physics: Condensed Matter* 31.32 (2019), p. 325902. DOI: 10.1088/1361-648X/ab15d0. URL: https://dx.doi.org/10.1088/1361-648X/ab15d0 (cit. on p. 90).

[140] Jinhua Hong, Ryosuke Senga, Thomas Pichler, and Kazu Suenaga. "Probing Exciton Dispersions of Freestanding Monolayer WSe_2 by Momentum-Resolved Electron Energy-Loss Spectroscopy". In: *Phys. Rev. Lett.* 124 (8 2020), p. 087401. DOI: 10.1103/PhysRevLett.124.087401. URL: https://link.aps.org/doi/10.1103/PhysRevLett.124.087401 (cit. on p. 92).

[141] Ryan J. T. Nicholl, Nickolay V. Lavrik, Ivan Vlassiouk, Bernadeta R. Srijanto, and Kirill I. Bolotin. "Hidden Area and Mechanical Nonlinearities in Freestanding Graphene". In: *Phys. Rev. Lett.* 118 (26 2017), p. 266101. DOI: 10.1103/PhysRevLett.118.266101. URL: https://link.aps.org/doi/10.1103/PhysRevLett.118.266101 (cit. on p. 92).

[142] Yunyi Yang, Jiayang Wu, Xingyuan Xu, Yao Liang, Sai T. Chu, Brent E. Little, Roberto Morandotti, Baohua Jia, and David J. Moss. "Enhanced four-wave mixing in waveguides integrated with graphene oxide". In: *APL Photonics* 3.12 (2018), p. 120803. DOI: 10.1063/1.5045509. eprint: https://doi.org/10.1063/1.5045509. URL: https://doi.org/10.1063/1.5045509 (cit. on p. 92).

[143] Yuchen Wang, Vincent Pelgrin, Samuel Gyger, Gius Md Uddin, Xueyin Bai, Christian Lafforgue, Laurent Vivien, Klaus D. Jöns, Eric Cassan, and Zhipei Sun. "Enhancing Si3N4 Waveguide Nonlinearity with Heterogeneous Integration of Few-Layer WS2". In: *ACS Photonics* 8.9 (2021), pp. 2713–2721. DOI: 10.1021/acsphotonics.1c00767. eprint: https://doi.org/10.1021/acsphotonics.1c00767. URL: https://doi.org/10.1021/acsphotonics.1c00767 (cit. on pp. 92, 171).

[144] Hans Warlimont. "Ceramics". In: *Springer Handbook of Condensed Matter and Materials Data*. Ed. by Werner Martienssen and Hans Warlimont. Berlin, Heidelberg: Springer Berlin Heidelberg, 2005, pp. 431–476. ISBN: 978-3-540-30437-1. DOI: 10.1007/3-540-30437-1_6. URL: https://doi.org/10.1007/3-540-30437-1_6 (cit. on p. 95).

[145] B. Balland and A. Glachant. "Chapter 1 Silica, silicon nitride and oxynitride thin films: An overview of fabrication techniques, properties and applications". In: *New Insulators, Devices and Radiation Effects*. Ed. by Gérard Barbottin and André Vapaille. Vol. 3. Instabilities in Silicon Devices. North-Holland, 1999, pp. 3–144. DOI: https://doi.org/10.1016/S1874-5903(99)80007-X. URL: https://www.sciencedirect.com/science/article/pii/S187459039980007X (cit. on p. 95).

[146] Nourdine Zibouche, Martin Schlipf, and Feliciano Giustino. "GW band structure of monolayer MoS_2 using the SternheimerGW method and effect of dielectric environment". In: *Phys. Rev. B* 103 (12 2021), p. 125401. DOI: 10.1103/PhysRevB.103.125401. URL: https://link.aps.org/doi/10.1103/PhysRevB.103.125401 (cit. on p. 95).

[147] Yulin Yang, Tong Yang, Tingting Song, Jun Zhou, Jianwei Chai, Lai Mun Wong, Hongyi Zhang, Wenzhang Zhu, Shijie Wang, and Ming Yang. "Selective hydrogenation improves interface properties of high-k dielectrics on 2D semiconductors". In: *Nano Research* (2022). ISSN: 1998-0000. DOI: 10.1007/s12274-021-4025-4. URL: https://doi.org/10.1007/s12274-021-4025-4 (cit. on p. 95).

[148] Takao Tsuneda. "Exchange-Correlation Functionals". In: *Density Functional Theory in Quantum Chemistry*. Tokyo: Springer Japan, 2014, pp. 101–124. ISBN: 978-4-431-54825-6. DOI: 10.1007/978-4-431-54825-6_5. URL: https://doi.org/10.1007/978-4-431-54825-6_5 (cit. on p. 95).

[149] Alejandro Molina-Sánchez, Maurizia Palummo, Andrea Marini, and Ludger Wirtz. "Temperature-dependent excitonic effects in the optical properties of single-layer MoS_2". In: *Phys. Rev. B* 93 (15 2016), p. 155435. DOI: 10.1103/PhysRevB.93.155435. URL: https://link.aps.org/doi/10.1103/PhysRevB.93.155435 (cit. on p. 96).

[150] V. F. Sears and S. A. Shelley. "Debye-Waller Factor for Elemental Crystals". In: *Acta Crystallographica Section A Foundations of Crystallography* 47.4 (1991), pp. 441–446. DOI: doi:10.1107/s0108767391002970. URL: https://sci-hub.se/10.1107/s0108767391002970 (cit. on p. 98).

[151] Ehren M. Mannebach, Renkai Li, et al. "Dynamic Structural Response and Deformations of Monolayer MoS_2 Visualized by Femtosecond Electron Diffraction". In: *Nano Letters* 15.10 (2015). PMID: 26322659, pp. 6889–6895. DOI: 10.1021/acs.nanolett.5b02805. URL: https://doi.org/10.1021/acs.nanolett.5b02805 (cit. on p. 99).

[152] Xing He, Mazhar Chebl, and Ding-Shyue Yang. "Cross-Examination of Ultrafast Structural, Interfacial, and Carrier Dynamics of Supported Monolayer MoS2". In: *Nano Letters* 20.3 (2020). PMID: 32031381, pp. 2026–2033. DOI: 10.1021/acs.nanolett.9b05344. eprint: https://doi.org/10.1021/acs.nanolett.9b05344. URL: https://doi.org/10.1021/acs.nanolett.9b05344 (cit. on p. 99).

[153] Duan Luo, Jian Tang, Xiaozhe Shen, Fuhao Ji, Jie Yang, Stephen Weathersby, Michael E Kozina, Zhijiang Chen, Jun Xiao, Yusen Ye, et al. "Twist-Angle-Dependent Ultrafast Charge Transfer in MoS2-Graphene van der Waals Heterostructures". In: *Nano Letters* 21.19 (2021), pp. 8051–8057. DOI: https://doi.org/10.1021/acs.nanolett.1c02356. URL: https://pubs.acs.org/doi/10.1021/acs.nanolett.1c02356 (cit. on p. 99).

[154] Feng Hu, Zhi-Peng Xie, Jian Zhang, Zun-Lan Hu, and Di An. "Promising high-thermal-conductivity substrate material for high-power electronic device: silicon nitride ceramics". In: *Rare Metals* 39.5 (2020), pp. 463–478. ISSN: 1867-7185. DOI: 10.1007/s12598-020-01376-7. URL: https://doi.org/10.1007/s12598-020-01376-7 (cit. on p. 103).

[155] Naoto Hirosaki, Shigenobu Ogata, Cenk Kocer, Hiroshi Kitagawa, and Yasuhiro Nakamura. "Molecular dynamics calculation of the ideal thermal conductivity of single-crystal α- and $\beta - Si_3N_4$". In: *Phys. Rev. B* 65 (13 2002), p. 134110. DOI: 10.1103/PhysRevB.65.134110. URL: https://link.aps.org/doi/10.1103/PhysRevB.65.134110 (cit. on p. 103).

[156] Z. Y. Zhu, Y. C. Cheng, and U. Schwingenschlögl. "Giant spin-orbit-induced spin splitting in two-dimensional transition-metal dichalcogenide semiconductors". In: *Phys. Rev. B* 84 (15 2011), p. 153402. DOI: 10.1103/PhysRevB.84.153402. URL: https://link.aps.org/doi/10.1103/PhysRevB.84.153402 (cit. on pp. 109, 115).

[157] mider, familyi=s., given=K., giveni=K., „ J. W. González, and J. Fernández-Rossier. "Large spin splitting in the conduction band of transition metal dichalcogenide monolayers". In: *Phys. Rev. B* 88 (24 2013), p. 245436. DOI: 10.1103/PhysRevB.88.245436. URL: https://link.aps.org/doi/10.1103/PhysRevB.88.245436 (cit. on p. 109).

[158] Andor Kormányos, Viktor Zólyomi, Neil D. Drummond, and Guido Burkard. "Spin-Orbit Coupling, Quantum Dots, and Qubits in Monolayer Transition Metal Dichalcogenides". In: *Phys. Rev. X* 4 (1 2014), p. 011034. DOI: 10.1103/PhysRevX.4.011034. URL: https://link.aps.org/doi/10.1103/PhysRevX.4.011034 (cit. on p. 109).

[159] Lifa Zhang, Jie Ren, Jian-Sheng Wang, and Baowen Li. "Topological Nature of the Phonon Hall Effect". In: *Phys. Rev. Lett.* 105 (22 2010), p. 225901. DOI: 10.1103/PhysRevLett.105.225901. URL: https://link.aps.org/doi/10.1103/PhysRevLett.105.225901 (cit. on p. 110).

[160] ois, familyi=c., given=É., giveni=E., „ G. Grissonnanche, J. Baglo, P. Lampen-Kelley, J.-Q. Yan, C. Balz, D. Mandrus, S. E. Nagler, S. Kim, Young-June Kim, N. Doiron-Leyraud, and Louis Taillefer. "Evidence of a Phonon Hall Effect in the Kitaev Spin Liquid Candidate $\alpha-RuCl_3$". In: *Phys. Rev. X* 12 (2 2022), p. 021025. DOI: 10.1103/PhysRevX.12.021025. URL: https://link.aps.org/doi/10.1103/PhysRevX.12.021025 (cit. on p. 110).

[161] G. Grissonnanche, A. Legros, S. Badoux, E. Lefrançois, V. Zatko, M. Lizaire, F. Laliberté, A. Gourgout, J.-S. Zhou, S. Pyon, T. Takayama, H. Takagi, S. Ono, N. Doiron-Leyraud, and L. Taillefer. "Giant thermal Hall conductivity in the pseudogap phase of cuprate superconductors". In: *Nature* 571.7765 (2019), pp. 376–380. ISSN: 1476-4687. DOI: 10.1038/s41586-019-1375-0. URL: https://doi.org/10.1038/s41586-019-1375-0 (cit. on p. 110).

[162] Taiki Uehara, Takumi Ohtsuki, Masafumi Udagawa, Satoru Nakatsuji, and Yo Machida. "Phonon thermal Hall effect in a metallic spin ice". In: *Nature Communications* 13.1 (2022), p. 4604. ISSN: 2041-1723. DOI: 10.1038/s41467-022-32375-0. URL: https://doi.org/10.1038/s41467-022-32375-0 (cit. on p. 110).

[163] Yuji Hirokane, Yoichi Nii, Yasuhide Tomioka, and Yoshinori Onose. "Phononic thermal Hall effect in diluted terbium oxides". In: *Phys. Rev. B* 99 (13 2019), p. 134419. DOI: 10.1103/PhysRevB.99.134419. URL: https://link.aps.org/doi/10.1103/PhysRevB.99.134419 (cit. on p. 110).

[164] Hao Chen, Weikang Wu, Jiaojiao Zhu, Shengyuan A. Yang, and Lifa Zhang. "Propagating Chiral Phonons in Three-Dimensional Materials". In: *Nano Letters* 21.7 (2021). PMID: 33764075, pp. 3060–3065. DOI: 10.1021/acs.nanolett.1c00236. eprint: https://doi.org/10.1021/acs.nanolett.1c00236. URL: https://doi.org/10.1021/acs.nanolett.1c00236 (cit. on p. 110).

[165] J.A. Wilson and A.D. Yoffe. "The transition metal dichalcogenides discussion and interpretation of the observed optical, electrical and structural properties". In: *Advances in Physics* 18.73 (1969), pp. 193–335. DOI: 10.1080/00018736900101307. eprint: https://doi.org/10.1080/00018736900101307. URL: https://doi.org/10.1080/00018736900101307 (cit. on p. 111).

[166] Andor Kormányos, Guido Burkard, Martin Gmitra, Jaroslav Fabian, Viktor Zólyomi, Neil D Drummond, and Vladimir Fal'ko. "$\mathbf{k}\cdot\mathbf{p}$ theory for two-dimensional transition metal dichalcogenide semiconductors". In: *2D Materials* 2.2 (2015), p. 022001. DOI: 10.1088/2053-1583/2/2/022001. URL: https://doi.org/10.1088/2053-1583/2/2/022001 (cit. on pp. 111, 113, 114).

[167] Roland Winkler. *Spin-orbit Coupling Effects in Two-Dimensional Electron and Hole Systems*. Berlin: Springer, 2003 (cit. on p. 112).

[168] Andor Kormányos, Viktor Zólyomi, Neil D. Drummond, Péter Rakyta, Guido Burkard, and Vladimir I. Fal'ko. "Monolayer MoS_2: Trigonal warping, the Γ valley, and spin-orbit coupling effects". In: *Phys. Rev. B* 88 (4 2013), p. 045416. DOI: 10.1103/PhysRevB.88.045416. URL: https://link.aps.org/doi/10.1103/PhysRevB.88.045416 (cit. on p. 112).

[169] Di Xiao, Ming-Che Chang, and Qian Niu. "Berry phase effects on electronic properties". In: *Rev. Mod. Phys.* 82 (3 2010), pp. 1959–2007. DOI: 10.1103/RevModPhys.82.1959. URL: https://link.aps.org/doi/10.1103/RevModPhys.82.1959 (cit. on p. 114).

[170] Ming-Che Chang and Qian Niu. "Berry phase, hyperorbits, and the Hofstadter spectrum: Semiclassical dynamics in magnetic Bloch bands". In: *Phys. Rev. B* 53 (11 1996), pp. 7010–7023. DOI: 10.1103/PhysRevB.53.7010. URL: https://link.aps.org/doi/10.1103/PhysRevB.53.7010 (cit. on p. 115).

[171] Hualing Zeng, Junfeng Dai, Wang Yao, Di Xiao, and Xiaodong Cui. "Valley polarization in MoS2 monolayers by optical pumping". In: *Nature Nanotechnology* 7.8 (2012), pp. 490–493. ISSN: 1748-3395. DOI: 10.1038/nnano.2012.95. URL: https://doi.org/10.1038/nnano.2012.95 (cit. on p. 115).

[172] Aaron M. Jones, Hongyi Yu, Nirmal J. Ghimire, Sanfeng Wu, Grant Aivazian, Jason S. Ross, Bo Zhao, Jiaqiang Yan, David G. Mandrus, Di Xiao, Wang Yao, and Xiaodong Xu. "Optical generation of excitonic valley coherence in monolayer WSe2". In: *Nature Nanotechnology* 8.9 (Aug. 2013), pp. 634–638. DOI: 10.1038/nnano.2013.151. URL: https://doi.org/10.1038/nnano.2013.151 (cit. on p. 115).

[173] Xiaodong Xu, Wang Yao, Di Xiao, and Tony F. Heinz. "Spin and pseudospins in layered transition metal dichalcogenides". In: *Nature Physics* 10.5 (Apr. 2014), pp. 343–350. DOI: 10.1038/nphys2942. URL: https://doi.org/10.1038/nphys2942 (cit. on p. 115).

[174] Tristan L. Britt and Bradley J. Siwick. "Ultrafast phonon diffuse scattering as a tool for observing chiral phonons in monolayer hexagonal lattices". In: *Phys. Rev. B* 107 (21 2023), p. 214306. DOI: 10.1103/PhysRevB.107.214306 (cit. on pp. 118, 125, 130, 132, 144).

[175] Søren Ulstrupabo, familyi=v., given=Antonija Grubiši ć, giveni=A. G. c. v. a. c., „ Deepnarayan Biswas, Jonathon M. Riley, Maciej Dendzik, Charlotte E. Sanders, Marco Bianchi, Cephise Cacho, Dan Matselyukh, Richard T. Chapman, Emma Springate, Phil D. C. King, Jill A. Miwa, and Philip Hofmann. "Spin and valley control of free carriers in single-layer WS_2". In: *Phys. Rev. B* 95 (4 2017), p. 041405. DOI: 10.1103/PhysRevB.95.041405. URL: https://link.aps.org/doi/10.1103/PhysRevB.95.041405 (cit. on p. 119).

[176] Lawson T. Lloyd, Ryan E. Wood, Fauzia Mujid, Siddhartha Sohoni, Karen L. Ji, Po-Chieh Ting, Jacob S. Higgins, Jiwoong Park, and Gregory S. Engel. "Sub-10 fs Intervalley Exciton Coupling in Monolayer MoS2 Revealed by Helicity-Resolved Two-Dimensional Electronic Spectroscopy". In: *ACS Nano* 15.6 (2021), pp. 10253–10263. DOI: 10.1021/acsnano.1c02381. eprint: https://doi.org/10.1021/acsnano.1c02381. URL: https://doi.org/10.1021/acsnano.1c02381 (cit. on p. 119).

[177] A Steinhoff, M Florian, M Rösner, M Lorke, T O Wehling, C Gies, and F Jahnke. "Nonequilibrium carrier dynamics in transition metal dichalcogenide semiconductors". In: *2D Materials* 3.3 (2016), p. 031006. DOI: 10.1088/2053-1583/3/3/031006. URL: https://dx.doi.org/10.1088/2053-1583/3/3/031006 (cit. on p. 119).

[178] Malte Selig, Florian Katsch, Robert Schmidt, Steffen Michaelis de Vasconcellos, Rudolf Bratschitsch, Ermin Malic, and Andreas Knorr. "Ultrafast dynamics in monolayer transition metal dichalcogenides: Interplay of dark excitons, phonons, and intervalley exchange". In: *Phys. Rev. Res.* 1 (2 2019), p. 022007. DOI: 10.1103/PhysRevResearch.1.022007. URL: https://link.aps.org/doi/10.1103/PhysRevResearch.1.022007 (cit. on p. 119).

[179] R. L. Wilmington, H. Ardekani, A. Rustagi, A. Bataller, A. F. Kemper, R. A. Younts, and K. Gundogdu. "Fermi liquid theory sheds light on hot electron-hole liquid in $1L - MoS_2$". In: *Phys. Rev. B* 103 (7 2021), p. 075416. DOI: 10.1103/PhysRevB.103.075416. URL: https://link.aps.org/doi/10.1103/PhysRevB.103.075416 (cit. on p. 119).

[180] Alexey Chernikov, Claudia Ruppert, Heather M. Hill, Albert F. Rigosi, and Tony F. Heinz. "Population inversion and giant bandgap renormalization in atomically thin WS2 layers". In: *Nature Photonics* 9.7 (2015), pp. 466–470. ISSN: 1749-4893. DOI: 10.1038/nphoton.2015.104. URL: https://doi.org/10.1038/nphoton.2015.104 (cit. on p. 119).

[181] A. Steinhoff, M. Florian, M. Rösner, G. Schönhoff, T. O. Wehling, and F. Jahnke. "Exciton fission in monolayer transition metal dichalcogenide semiconductors". In: *Nature Communications* 8.1 (2017), p. 1166. ISSN: 2041-1723. DOI: 10.1038/s41467-017-01298-6. URL: https://doi.org/10.1038/s41467-017-01298-6 (cit. on p. 119).

[182] G. L. Bir, A. G. Aronov, and G. E. Pikus. "Spin relaxation of electrons due to scattering by holes". In: *Zh. Eksp. Teor. Fiz* 69 (1975), pp. 1382–1397. URL: http://jetp.ras.ru/cgi-bin/dn/e_042_04_0705.pdf (cit. on p. 119).

[183] A. I. Prazdnichnykh, M. M. Glazov, L. Ren, C. Robert, B. Urbaszek, and X. Marie. "Control of the exciton valley dynamics in atomically thin semiconductors by tailoring the environment". In: *Phys. Rev. B* 103 (8 2021), p. 085302. DOI: 10.1103/PhysRevB.103.085302. URL: https://link.aps.org/doi/10.1103/PhysRevB.103.085302 (cit. on p. 119).

[184] R. Bertoni, C. W. Nicholson, L. Waldecker, H. Hübener, C. Monney, U. De Giovannini, M. Puppin, M. Hoesch, E. Springate, R. T. Chapman, C. Cacho, M. Wolf, A. Rubio, and R. Ernstorfer. "Generation and Evolution of Spin-, Valley-, and Layer-Polarized Excited Carriers in Inversion-Symmetric WSe_2". In: *Phys. Rev. Lett.* 117 (27 2016), p. 277201. DOI: 10.1103/PhysRevLett.117.277201. URL: https://link.aps.org/doi/10.1103/PhysRevLett.117.277201 (cit. on p. 120).

[185] Paolo Giannozzi et al. "QUANTUM ESPRESSO: a modular and open-source software project for quantum simulations of materials". In: *Journal of Physics: Condensed Matter* 21.39 (2009), p. 395502. DOI: 10.1088/0953-8984/21/39/395502. URL: https://doi.org/10.1088/0953-8984/21/39/395502 (cit. on pp. 127, 156).

[186] P Giannozzi et al. "Advanced capabilities for materials modelling with Quantum ESPRESSO". In: *Journal of Physics: Condensed Matter* 29.46 (2017), p. 465901. DOI: 10.1088/1361-648x/aa8f79. URL: https://doi.org/10.1088/1361-648x/aa8f79 (cit. on pp. 127, 156).

[187] N. Troullier and José Luís Martins. "Efficient pseudopotentials for plane-wave calculations". In: *Phys. Rev. B* 43 (3 1991), pp. 1993–2006. DOI: 10.1103/PhysRevB.43.1993. URL: https://link.aps.org/doi/10.1103/PhysRevB.43.1993 (cit. on pp. 128, 156, 163).

[188] John P. Perdew, Kieron Burke, and Matthias Ernzerhof. "Generalized Gradient Approximation Made Simple". In: *Phys. Rev. Lett.* 77 (18 1996), pp. 3865–3868. DOI: 10.1103/PhysRevLett.77.3865. URL: https://link.aps.org/doi/10.1103/PhysRevLett.77.3865 (cit. on pp. 128, 156, 163).

[189] Thibault Sohier, Matteo Calandra, and Francesco Mauri. "Density functional perturbation theory for gated two-dimensional heterostructures: Theoretical developments and application to flexural phonons in graphene". In: *Phys. Rev. B* 96 (7 2017), p. 075448. DOI: 10.1103/PhysRevB.96.075448. URL: https://link.aps.org/doi/10.1103/PhysRevB.96.075448 (cit. on p. 129).

[190] Yiming Pan and Fabio Caruso. "Vibrational Dichroism of Chiral Valley Phonons". In: *Nano Letters* 23.16 (2023), pp. 7463–7469. DOI: 10.1021/acs.nanolett.3c01904. URL: https://doi.org/10.1021/acs.nanolett.3c01904 (cit. on p. 131).

[191] Li-Dong Zhao, Shih-Han Lo, Yongsheng Zhang, Hui Sun, Gangjian Tan, Ctirad Uher, C. Wolverton, Vinayak P. Dravid, and Mercouri G. Kanatzidis. "Ultralow thermal conductivity and high thermoelectric figure of merit in SnSe crystals". In: *Nature* 508.7496 (2014), pp. 373–377. ISSN: 1476-4687. DOI: 10.1038/nature13184. URL: https://doi.org/10.1038/nature13184 (cit. on pp. 137, 138, 143).

[192] Li-Dong Zhao, Gangjian Tan, Shiqiang Hao, Jiaqing He, Yanling Pei, Hang Chi, Heng Wang, Shengkai Gong, Huibin Xu, Vinayak P. Dravid, Ctirad Uher, G. Jeffrey Snyder, Chris Wolverton, and Mercouri G. Kanatzidis. "Ultrahigh power factor and thermoelectric performance in hole-doped single-crystal SnSe". In: *Science* 351.6269 (2016), pp. 141–144. DOI: 10.1126/science.aad3749. eprint: https://www.science.org/doi/pdf/10.1126/science.aad3749. URL: https://www.science.org/doi/abs/10.1126/science.aad3749 (cit. on p. 137).

[193] Li-Dong Zhao, Cheng Chang, Gangjian Tan, and Mercouri G. Kanatzidis. "SnSe: a remarkable new thermoelectric material". In: *Energy Environ. Sci.* 9 (10 2016), pp. 3044–3060. DOI: 10.1039/C6EE01755J. URL: http://dx.doi.org/10.1039/C6EE01755J (cit. on p. 137).

[194] T. J. Seebeck. "Ueber die magnetische Polarisation der Metalle und Erze durch Temperatur-Differenz". In: *Annalen der Physik* 82.2 (1826), pp. 133–160. DOI: https://doi.org/10.1002/andp.18260820202 (cit. on p. 138).

[195] Jean Charles Athanase Peltier. *Nouvelles expériences sur la caloricité des courans électriques*. Vol. 56. Annales de chimie et de physique, 1834 (cit. on p. 138).

[196] William Thomson. "4. On a Mechanical Theory of Thermo-Electric Currents". In: *Proceedings of the Royal Society of Edinburgh* 3 (1857), pp. 91–98. DOI: 10.1017/S0370164600027310 (cit. on p. 138).

[197] H. Julian Goldsmid. *Introduction to Thermoelectricity*. Berlin, Heidelberg: Springer Berlin Heidelberg, 2018. ISBN: 978-3-662-49255-0. DOI: 10.1007/978-3-662-49256-7. URL: https://doi.org/10.1007/978-3-662-49256-7 (cit. on p. 140).

[198] D.M. Rowe. *Thermoelectrics handbook: macro to nano*. CRC/Taylor & Francis, 2006, pp. 55–65. ISBN: 0849322642 (cit. on p. 141).

[199] R. J. Cava. "Structural Chemistry and the Local Charge Picture of Copper Oxide Superconductors". In: *Science* 247.4943 (1990), pp. 656–662. DOI: 10.1126/science.247.4943.656. eprint: https://www.science.org/doi/pdf/10.1126/science.247.4943.656. URL: https://www.science.org/doi/abs/10.1126/science.247.4943.656 (cit. on p. 141).

[200] M.S. Dresselhaus, G. Chen, M.Y. Tang, R.G. Yang, H. Lee, D.Z. Wang, Z.F. Ren, J.-P. Fleurial, and P. Gogna. "New Directions for Low-Dimensional Thermoelectric Materials". In: *Advanced Materials* 19.8 (2007), pp. 1043–1053. DOI: https://doi.org/10.1002/adma.200600527. eprint: https://onlinelibrary.wiley.com/doi/pdf/10.1002/adma.200600527. URL: https://onlinelibrary.wiley.com/doi/abs/10.1002/adma.200600527 (cit. on pp. 141, 143).

[201] Do Duc Cuong, S. H. Rhim, Joo-Hyong Lee, and Soon Cheol Hong. "Strain effect on electronic structure and thermoelectric properties of orthorhombic SnSe: A first principles study". In: *AIP Advances* 5.11 (Nov. 2015), p. 117147. ISSN: 2158-3226. DOI: 10.1063/1.4936636. eprint: https://pubs.aip.org/aip/adv/article-pdf/doi/10.1063/1.4936636/12829370/117147_1_online.pdf. URL: https://doi.org/10.1063/1.4936636 (cit. on p. 142).

[202] C. W. Li, J. Hong, A. F. May, D. Bansal, S. Chi, T. Hong, G. Ehlers, and O. Delaire. "Orbitally driven giant phonon anharmonicity in SnSe". In: *Nature Physics* 11.12 (2015), pp. 1063–1069. ISSN: 1745-2481. DOI: 10.1038/nphys3492. URL: https://doi.org/10.1038/nphys3492 (cit. on p. 142).

[203] Jonathan M. Skelton, Lee A. Burton, Stephen C. Parker, Aron Walsh, Chang-Eun Kim, Aloysius Soon, John Buckeridge, Alexey A. Sokol, C. Richard A. Catlow, Atsushi Togo, and Isao Tanaka. "Anharmonicity in the High-Temperature *Cmcm* Phase of SnSe: Soft Modes and Three-Phonon Interactions". In: *Phys. Rev. Lett.* 117 (7 2016), p. 075502. DOI: 10.1103/PhysRevLett.117.075502 (cit. on p. 144).

[204] Fabio Caruso, Maria Troppenz, Santiago Rigamonti, and Claudia Draxl. "Thermally enhanced Fröhlich coupling in SnSe". In: *Phys. Rev. B* 99 (8 2019), p. 081104. DOI: 10.1103/PhysRevB.99.081104. URL: https://link.aps.org/doi/10.1103/PhysRevB.99.081104 (cit. on p. 144).

[205] Yijing Huang, Shan Yang, Samuel Teitelbaum, Gilberto De la Peña, Takahiro Sato, Matthieu Chollet, Diling Zhu, Jennifer L. Niedziela, Dipanshu Bansal, Andrew F. May, Aaron M. Lindenberg, Olivier Delaire, David A. Reis, and Mariano Trigo. "Observation of a Novel Lattice Instability in Ultrafast Photoexcited SnSe". In: *Phys. Rev. X* 12 (1 2022), p. 011029. DOI: 10.1103/PhysRevX.12.011029. URL: https://link.aps.org/doi/10.1103/PhysRevX.12.011029 (cit. on p. 144).

[206] L. D. Landau. "Über die Bewegung der Elektronen in Kristallgitter". In: *Phys. Z. Sowjetunion* 3 (1933), pp. 644–645 (cit. on p. 147).

[207] S. I. Pekar. In: *Zh. Eksp. Teor. Fiz* 16 (1946), p. 341 (cit. on p. 147).

[208] J. D. Jackson. "Electrodynamics, Classical". In: *digital Encyclopedia of Applied Physics*. John Wiley & Sons, Ltd, 2003. ISBN: 9783527600434. DOI: https://doi.org/10.1002/3527600434.eap109. URL: https://onlinelibrary.wiley.com/doi/abs/10.1002/3527600434.eap109 (cit. on p. 147).

[209] Satoru J. Miyake. "Strong-Coupling Limit of the Polaron Ground State". In: *Journal of the Physical Society of Japan* 38.1 (1975), pp. 181–182. DOI: 10.1143/JPSJ.38.181. eprint: https://doi.org/10.1143/JPSJ.38.181. URL: https://doi.org/10.1143/JPSJ.38.181 (cit. on p. 148).

[210] Jozef T Devreese and Alexandre S Alexandrov. "Fröhlich polaron and bipolaron: recent developments". In: *Reports on Progress in Physics* 72.6 (2009), p. 066501. DOI: 10.1088/0034-4885/72/6/066501. URL: https://dx.doi.org/10.1088/0034-4885/72/6/066501 (cit. on p. 148).

[211] C. Verdi and F. Giustino. "Frohlich Electron-Phonon Vertex from First Principles". In: *Phys. Rev. Lett.* 115 (2015), p. 176401. DOI: 10.1103/PhysRevLett.115.176401 (cit. on pp. 148, 156).

[212] R. P. Feynman. "Slow Electrons in a Polar Crystal". In: *Phys. Rev.* 97 (3 1955), pp. 660–665. DOI: 10.1103/PhysRev.97.660. URL: https://link.aps.org/doi/10.1103/PhysRev.97.660 (cit. on p. 148).

[213] Weng Hong Sio, Carla Verdi, Samuel Poncé, and Feliciano Giustino. "Ab initio theory of polarons: Formalism and applications". In: *Phys. Rev. B* 99 (23 2019), p. 235139. DOI: 10.1103/PhysRevB.99.235139. URL: https://link.aps.org/doi/10.1103/PhysRevB.99.235139 (cit. on pp. 148, 156, 157).

[214] Weng Hong Sio, Carla Verdi, Samuel Poncé, and Feliciano Giustino. "Polarons from First Principles, without Supercells". In: *Phys. Rev. Lett.* 122 (24 2019), p. 246403. DOI: 10.1103/PhysRevLett.122.246403. URL: https://link.aps.org/doi/10.1103/PhysRevLett.122.246403 (cit. on pp. 152, 156).

[215] G. Makov and M. C. Payne. "Periodic boundary conditions in ab initio calculations". In: *Phys. Rev. B* 51 (7 1995), pp. 4014–4022. DOI: 10.1103/PhysRevB.51.4014. URL: https://link.aps.org/doi/10.1103/PhysRevB.51.4014 (cit. on pp. 152, 157).

[216] Babak Sadigh, Paul Erhart, and Daniel Åberg. "Variational polaron self-interaction-corrected total-energy functional for charge excitations in insulators". In: *Phys. Rev. B* 92 (7 2015), p. 075202. DOI: 10.1103/PhysRevB.92.075202. URL: https://link.aps.org/doi/10.1103/PhysRevB.92.075202 (cit. on p. 156).

[217] Ferenc Karsai, Paul Tiwald, Robert Laskowski, Fabien Tran, David Koller, Stefanie Gräfe, Joachim Burgdörfer, Ludger Wirtz, and Peter Blaha. "F center in lithium fluoride revisited: Comparison of solid-state physics and quantum-chemistry approaches". In: *Phys. Rev. B* 89 (12 2014), p. 125429. DOI: 10.1103/PhysRevB.89.125429. URL: https://link.aps.org/doi/10.1103/PhysRevB.89.125429 (cit. on p. 156).

[218] Mark R. Pederson and Barry M. Klein. "Improved theoretical methods for studies of defects in insulators: Application to the F center in LiF". In: *Phys. Rev. B* 37 (17 1988), pp. 10319–10331. DOI: 10.1103/PhysRevB.37.10319. URL: https://link.aps.org/doi/10.1103/PhysRevB.37.10319 (cit. on p. 156).

[219] G. Mallia, R. Orlando, C. Roetti, P. Ugliengo, and R. Dovesi. "F center in LiF: A quantum mechanical ab initio investigation of the hyperfine interaction between the unpaired electron at the vacancy and its first seven neighbors". In: *Phys. Rev. B* 63 (23 2001), p. 235102. DOI: 10.1103/PhysRevB.63.235102. URL: https://link.aps.org/doi/10.1103/PhysRevB.63.235102 (cit. on p. 156).

[220] A L Shluger and A M Stoneham. "Small polarons in real crystals: concepts and problems". In: *Journal of Physics: Condensed Matter* 5.19 (1993), p. 3049. DOI: 10.1088/0953-8984/5/19/007. URL: https://dx.doi.org/10.1088/0953-8984/5/19/007 (cit. on p. 156).

[221] Jacob L. Gavartin, Peter V. Sushko, and Alexander L. Shluger. "Modeling charge self-trapping in wide-gap dielectrics: Localization problem in local density functionals". In: *Phys. Rev. B* 67 (3 2003), p. 035108. DOI: 10.1103/PhysRevB.67.035108. URL: https://link.aps.org/doi/10.1103/PhysRevB.67.035108 (cit. on p. 156).

[222] O F Schirmer. "O- bound small polarons in oxide materials". In: *Journal of Physics: Condensed Matter* 18.43 (2006), R667. DOI: 10.1088/0953-8984/18/43/R01. URL: https://dx.doi.org/10.1088/0953-8984/18/43/R01 (cit. on p. 156).

[223] Lewis D. Miller and Richard H. Bube. "Luminescence, Trapping, and F Centers in Lithium Fluoride Crystals". In: *Journal of Applied Physics* 41.9 (Nov. 2003), pp. 3687–3697. ISSN: 0021-8979. DOI: 10.1063/1.1659493. eprint: https://pubs.aip.org/aip/jap/article-pdf/41/9/3687/7946635/3687_1_online.pdf. URL: https://doi.org/10.1063/1.1659493 (cit. on p. 156).

[224] F. Giustino, M. L. Cohen, and S. G. Louie. "Electron-phonon interaction using Wannier functions". In: *Phys. Rev. B* 76 (2007), p. 165108. DOI: 10.1103/PhysRevB.76.165108 (cit. on p. 156).

[225] S. Poncé, E.R. Margine, C. Verdi, and F. Giustino. "EPW: Electron-phonon coupling, transport and superconducting properties using maximally localized Wannier functions". In: *Computer Physics Communications* 209 (2016), pp. 116 –133. DOI: https://doi.org/10.1016/j.cpc.2016.07.028 (cit. on p. 156).

[226] H. Lee, S. Poncé, K. Bushick, S. Hajinazar, J. Lafuente-Bartolome, J. Leveillee, C. Lian, J. Lihm, F. Macheda, H. Mori, H. Paudyal, W.H. Sio, S. Tiwari, M. Zacharias, X. Zhang, Nicola N. Bonini, E. Kioupakis, E.R. Margine, and F. Giustino. "Electron–phonon physics from first principles using the EPW code". In: *npj Computational Materials* 9 (2023), p. 156. DOI: 10.1038/s41524-023-01107-3 (cit. on p. 156).

[227] Giovanni Pizzi et al. "Wannier90 as a community code: new features and applications". In: *Journal of Physics: Condensed Matter* 32.16 (2020), p. 165902. DOI: 10.1088/1361-648x/ab51ff (cit. on p. 156).

[228] Stefan Grimme, Jens Antony, Stephan Ehrlich, and Helge Krieg. "A consistent and accurate ab initio parametrization of density functional dispersion correction (DFT-D) for the 94 elements H-Pu". In: *The Journal of Chemical Physics* 132.15 (Apr. 2010), p. 154104. ISSN: 0021-9606. DOI: 10.1063/1.3382344 (cit. on p. 163).

[229] Axel D. Becke and Erin R. Johnson. "A density-functional model of the dispersion interaction". In: *The Journal of Chemical Physics* 123.15 (Oct. 2005), p. 154101. ISSN: 0021-9606. DOI: 10.1063/1.2065267 (cit. on p. 163).

[230] Stefan Grimme, Stephan Ehrlich, and Lars Goerigk. "Effect of the damping function in dispersion corrected density functional theory". In: *Journal of Computational Chemistry* 32.7 (2011), pp. 1456–1465. DOI: https://doi.org/10.1002/jcc.21759 (cit. on p. 163).

[231] Bogdan Guster, Vasilii Vasilchenko, Maryam Azizi, Matteo Giantomassi, and Xavier Gonze. "Large cylindrical polaron in orthorhombic SnSe: A theoretical study". In: *Phys. Rev. Mater.* 7 (6 2023), p. 064604. DOI: 10.1103/PhysRevMaterials.7.064604. URL: https://link.aps.org/doi/10.1103/PhysRevMaterials.7.064604 (cit. on p. 165).

[232] Léon Van Hove. "Correlations in Space and Time and Born Approximation Scattering in Systems of Interacting Particles". In: *Phys. Rev.* 95 (1 1954), pp. 249–262. DOI: 10.1103/PhysRev.95.249. URL: https://link.aps.org/doi/10.1103/PhysRev.95.249 (cit. on p. 167).

[233] N.N. Syrbu and V.V. Zalamai. "Excitonic and band parameters in SnSe crystals". In: *Journal of Luminescence* 221 (2020), p. 117093. ISSN: 0022-2313. DOI: https://doi.org/10.1016/j.jlumin.2020.117093 (cit. on p. 167).

[234] Chen W. Li, Xiaoli Tang, J. A. Muñoz, J. B. Keith, S. J. Tracy, D. L. Abernathy, and B. Fultz. "Structural Relationship between Negative Thermal Expansion and Quartic Anharmonicity of Cubic ScF_3". In: *Phys. Rev. Lett.* 107 (19 2011), p. 195504. DOI: 10.1103/PhysRevLett.107.195504. URL: https://link.aps.org/doi/10.1103/PhysRevLett.107.195504 (cit. on p. 173).

[235] Zherui Han, Xiaolong Yang, Wu Li, Tianli Feng, and Xiulin Ruan. "FourPhonon: An extension module to ShengBTE for computing four-phonon scattering rates and thermal conductivity". In: *Computer Physics Communications* 270 (2022), p. 108179. ISSN: 0010-4655. DOI: https://doi.org/10.1016/j.cpc.2021.108179. URL: https://www.sciencedirect.com/science/article/pii/S0010465521002915 (cit. on pp. 173–176).

[236] Shin-ichiro Tamura. "Isotope scattering of dispersive phonons in Ge". In: *Phys. Rev. B* 27 (2 1983), pp. 858–866. DOI: 10.1103/PhysRevB.27.858. URL: https://link.aps.org/doi/10.1103/PhysRevB.27.858 (cit. on p. 177).

[237] A. Matthiessen and C. Vogt. "Ueber den Einfluss der Temperatur auf die elektrische Leitungsfähigkeit der Legirungen". In: *Annalen der Physik* 198.5 (1864), pp. 19–78. DOI: https://doi.org/10.1002/andp.18641980504. URL: https://onlinelibrary.wiley.com/doi/abs/10.1002/andp.18641980504 (cit. on p. 177).